

Rochester Institute of Technology

**RIT Digital Institutional Repository**

---

Theses

---

6-5-2024

## **Clinical Validation of Patient-Specific Inverse Modeling with Surface Temperatures and Physiological and Geometrical Factors in Breast Cancer Detection**

Carlos Gutierrez  
cg9804@rit.edu

Follow this and additional works at: <https://repository.rit.edu/theses>

---

### **Recommended Citation**

Gutierrez, Carlos, "Clinical Validation of Patient-Specific Inverse Modeling with Surface Temperatures and Physiological and Geometrical Factors in Breast Cancer Detection" (2024). Thesis. Rochester Institute of Technology. Accessed from

This Dissertation is brought to you for free and open access by the RIT Libraries. For more information, please contact [repository@rit.edu](mailto:repository@rit.edu).

# RIT

## **Clinical Validation of Patient-Specific Inverse Modeling with Surface Temperatures and Physiological and Geometrical Factors in Breast Cancer Detection**

by

Carlos Gutierrez

A Dissertation Submitted in Partial Fulfillment of the Requirements for the  
degree of Doctor of Philosophy in Engineering

Department of Mechanical Engineering

Kate Gleason College of Engineering

Rochester Institute of Technology

Rochester, NY

June 5<sup>th</sup>, 2024

**Clinical Validation of Patient-Specific Inverse Modeling with Surface Temperatures  
and Physiological and Geometrical Factors in Breast Cancer Detection**

**By**

**Carlos Gutierrez**

**Committee Approval:**

We, the undersigned committee members, certify that we have advised and/or supervised the candidate on the work described in this dissertation. We further certify that we have reviewed the dissertation manuscript and approve it in partial fulfillment of the requirements of the degree of Doctor of Philosophy in Engineering.

---

Dr. Satish G. Kandlikar (Advisor) Date  
James E. Gleason Professor, Mechanical Engineering

---

Dr. Isaac Bernabe Perez-Raya Date  
Assistant Professor, Mechanical Engineering

---

Dr. Cristian Linte Date  
Associate Professor, Biomedical Engineering

---

Dr. Pradyumna Phatak Date  
Executive Medical Director, Lipson Cancer Center, RRH

Certified by:

---

Dr. Edward Hensel, P.E. Date  
Associate Dean, Research and Graduate Studies

## Acknowledgements

I would first like to thank Dr. Satish Kandlikar for all his kindness, guidance, and support throughout my five years at RIT. I am truly grateful to have been given the opportunity to be part of the Thermal Analysis, Microfluids, and Fuel Cell Lab conducting such groundbreaking research. His constant commitment to helping others and innovation inspires a fire in me that has helped me reach this final milestone. I will never forget the day he took me under his wing, as it was a day I lost and gained a role model. There are not enough words to describe my gratitude towards his help in achieving my academic goals.

Thank you to my committee members, Dr. Isaac Perez-Raya, Dr. Christian Linte, and Dr. Phatak, for all their support and mentorship that has helped move this thesis forward. Their thoughtful insights, questions, and feedback have helped ensure the quality and impact of this thesis. I would also like to thank Dr. Edward Hensel and Rebecca Ziebarth for their constant support and guidance in the Engineering PhD program.

Thank you to all my previous and current lab members, Dr. Alyssa Owens, Maharshi Shukla, Chirag Goel, Shriya Musuku, Brandon Cappon, Divyprakash Pal, and Winston James, for all the good times, conversations, friendships, advice, inspirations, and support. Thank you to all the undergraduate and graduate students that have worked in the lab dedicating their time to conduct all types of impactful research and that have shown constant commitment to their academic and professional goals.

Thank you to my LRDC and Tango Club friends for their consistent kindness and commitment to spreading the love of dance. Your efforts in helping create safe and inclusive spaces for everyone to enjoy dance regardless of anything has been such an inspiration. I am grateful to have been able to teach and perform dance with such wonderful individuals. My time in these clubs has shown me that my love for teaching and mentoring others expands beyond academics. To my performance teammates, thank you for all your commitment, hard work, and kindness. Although the name list is long, I want you all to

know that you have all made an impact on my life and have helped me look forward to dancing every week. I would especially like to thank Krzysztof Kamil Jarosz for the wonderful friendship, kindness, and inspiration.

To my SHPE Familia, thank you for the constant support and inspiration, as well as for providing me with various opportunities to grow professionally. I am so grateful to have been able to be part of the Region 4 Team, Regional Graduate Leadership Committee, and National Graduate Committee, helping create programs for graduate students and those interested in graduate school. I would like to especially thank Adrian Davila, P.E. and Dr. Ana Rodriguez for their kindness, friendship, mentorship, leadership, and support. You guys have been staples of inspiration for what I do in and outside of SHPE.

Last but not least, thank you to my family and friends that have been there for me through this journey. The list is extensive, but you all know who you are, and I want to thank you deeply. Thank you to Ana Llopis for believing in me and giving me the slap of reality I needed to continue pursuing my dream. Your friendship has been truly valuable, and your kindness will always be cherished. To my parents who have sacrificed so much for me to get where I am today and supported me in many ways through this dream, gracias. Their compassion towards others, resilience to challenges they faced being immigrants, their value for education, and the values installed in me from childhood has helped me become the person I am today. Losing my father to cancer was one of the biggest tragedies in my life, but it also ignited a fire in my help in the fight against cancer. My passion, dedication, and commitment to this thesis is a testament to that and to the sacrifices needed to help others. To my mother, Diana Gil, who has been nothing but the most supporting role model, I want to thank you for always being there for me and believing in me.

Finally, thank you to my partner in crime, soulmate, dance partner, and best friend, Viktoria Koscinski. From the day we met you have shown me nothing but kindness and support. It has not been easy, but your constant love and support has helped me so much on this journey. I have learned so much about myself and I have grown as a person because of you. Thank you from the bottom of my heart.

## Dedication

This work is dedicated towards the fight against cancer and the women who were a part of this research. This work is also dedicated to all the immigrant families that have or are currently making the sacrifices to for their loved ones to succeed. Additionally, I would like to dedicate this work to my mother, grandparents, my family in the US, and my family in Peru who have supported me through my journey. Finally, I would like to give a special dedication to the people I have lost but I have never forgotten. May your souls rest in peace.

*My Grandmother, Marina Vera de Gutierrez*

(May 25th, 1937 – January 2nd, 2013)

*My dearest friend, Mohamed “Mo” Elshafey*

(May 25th, 1992 – July 20th, 2014)

*My Father, Juan Carlos Gutierrez Vera*

(April 15th, 1964 – August 23rd, 2019)

## Abstract

Breast cancer is one of the most common cancers affecting the lives of many women and taking over 683,000 lives worldwide. Early detection of breast cancer through screening has been instrumental in reducing the mortality rate. However, current screening methods based on mammography have issues with patient discomfort, invasiveness, cost and low accuracy, mainly due to dense breast tissue in approximately 40% of women population. Infrared imaging (IRI) is shown to be noninvasive, cost effective, comfortable, and not affected by breast density. The present work describes a novel patient-specific IRI inverse heat transfer algorithm based on the digital model of the breast generated from MRI images and the IRI-Numerical Engine (IRI-NE). Validation of the IRI-NE is conducted with clinical IR images of 23 biopsy-proven breast cancer patients (24 breasts with cancer) through patient-specific inverse heat transfer modeling. This is a continuation of a collaborative study between RIT and Rochester General Hospital. The IRI-NE was able to accurately detect the presence and absence of breast cancer in all patients regardless of breast density, cancer type, tumor size, and tumor depth. The tumor size prediction was compared with actual size obtained from MRI and patient reports and showed a predicted size within 2.4 mm of the actual size. This shows the potential of IRI as an effective adjunct to mammography.

Additionally, this work evaluates the effect breast size, shape, tissue density, vascularity, tumor size and location on the detectability with the IRI-NE. Surface temperature data for various scenarios related to these factors are generated through numerical simulation on the actual digital model of the breast. The IRI-NE was able to predict the presence or absence of cancer for all the cases studied. The detectability limit of the IRI-NE is shown to be dependent on the thermal sensitivity of the IR camera, and a higher sensitivity camera is needed to detect deep tumors in large breasts. Finally, the thermal effects of vascularity and tumor angiogenesis on the detection accuracy are investigated. The blood perfusion rate was shown to significantly influence the heat transfer in small growing tumors due to angiogenesis. This shows the ability to further study cancer through a thermal perspective.

# Table of Contents

<b>Acknowledgements</b> .....	iii
<b>Dedication</b> .....	v
<b>Abstract</b> .....	vi
<b>Table of Contents</b> .....	vii
<b>List of Figures</b> .....	xi
<b>List of Tables</b> .....	xvii
<b>Chapter 1: Introduction</b> .....	1
1.1    Motivation.....	1
1.2    Breast Cancer.....	1
1.2.1    Female Breast Anatomy.....	2
1.2.2    Types of Breast Cancer.....	3
1.2.3    Breast Cancer Stage and Grade .....	5
1.2.4    Risk Factors .....	6
1.3    Cancer Biology .....	8
1.3.1    Cancer Growth.....	8
1.3.2    Tumor Angiogenesis.....	10
1.4    Breast Cancer Screening .....	13
1.4.1    Imaging Modalities.....	14
a.    Mammography .....	14
b.    Ultrasound.....	15
c.    Magnetic Resonance Imaging.....	16
1.4.2    Sensitivity and Specificity .....	17
1.4.3    Factors Affecting Detection .....	19
a.    Breast Density .....	19
b.    Tumor Size.....	21
c.    Tumor Position.....	23
d.    Cancer Type .....	24
1.5    Technological Advancements in Breast Cancer Screening.....	25
1.5.1    Contrast-Enhance Mammography.....	25
1.5.2    Computer Aided Detection/Diagnosis .....	26

1.5.3	Infrared Thermography and Infrared Imaging.....	27
1.6	Conclusion.....	28
<b>Chapter 2: Background</b>	.....	<b>29</b>
2.1	Infrared Thermography of Breast Cancer .....	29
2.1.1	Early Clinical Thermography .....	29
2.1.2	Computer Aided Thermography.....	35
2.2	Bioheat Transfer in Breast Cancer .....	40
2.2.1	Bioheat Transfer Models .....	41
2.2.2	Thermal Characteristics of Breast Cancer.....	49
2.2.3	Bioheat Transfer Studies in Different Breast Geometries .....	56
a.	Idealized Breast Geometries .....	57
b.	Realistic Breast Geometries .....	61
c.	Patient-Specific Breast Geometries.....	63
2.2.4	Inverse Heat Transfer Modeling of Breast Cancer .....	64
2.3	Clinical IRI Patient-Specific Breast Cancer Detection.....	66
2.4	Research Needs.....	72
2.5	Objectives.....	73
<b>Chapter 3: Approach</b>	.....	<b>75</b>
3.1	Overview.....	75
3.2	Patient-Specific Bioheat Transfer .....	75
3.2.1	Clinical Setup and Imaging.....	76
3.2.2	Generation of Patient-Specific DBMs.....	78
3.2.3	Bioheat Transfer Simulation Setup.....	82
3.3	Development of IRI-Numerical Engine .....	85
3.3.1	Enhancement of IR Image Registration .....	85
3.3.2	CFD-Inverse Heat Transfer Interfacing.....	90
3.3.3	Incorporation of CFD Parallel Processing.....	95
3.3.4	Verification and Validation using Clinical Data.....	96
3.4	Detectability of IRI-Numerical Engine .....	97
3.4.1	Bioheat Parametric Study of Breast Cancer .....	97
i.	Breast Shape and Size .....	98
ii.	Tumor Size and Depth .....	100

iii.	Breast Density (Thermal Conductivity) .....	105
3.4.2	Parametric Study Numerical Setup .....	107
3.4.3	Generation of Synthetic IR Surface Temperatures .....	110
3.4.4	Modified IRI-Numerical Engine .....	113
3.4.5	Establishing Detectability Metrics .....	115
i.	Detecting the Presence of Breast Cancer .....	116
ii.	Tumor Size Error.....	117
iii.	Internal Temperature Distribution.....	117
iv.	Maximum Surface Thermal Contrast.....	118
3.5	Physiological Factors in Breast Cancer Detection.....	119
3.5.1	Modeling Thermal Artifacts .....	119
3.5.2	Tumor Perfusion Heat Source Parametric Study.....	124
<b>Chapter 4:</b>	<b>Results</b> .....	<b>126</b>
4.1	Breast Model Generation .....	126
4.2	Detection of Breast Cancer on Twenty-Three Patients .....	127
4.3	Breast Cancer Detection using Surface Temperature Data .....	132
4.3.1	Verification with Eight Patients.....	132
4.3.2	Effect of Noise .....	135
4.4	Detectability Limits of IRI-Numerical Engine .....	136
4.4.1	Error in Tumor Size .....	137
4.4.2	Effect of Tumor Diameter and Depth.....	143
4.4.3	Effect of Breast Shape and Size.....	149
4.4.4	Effect of Breast Density.....	156
4.5	Effects of Physiological Factors.....	158
4.5.1	Effect of ROI Selection.....	158
4.5.2	Effect of Tumor Perfusion Heat Source .....	161
<b>Chapter 5:</b>	<b>Conclusions</b> .....	<b>164</b>
5.1	Summary of Work Done.....	164
5.2	Conclusions.....	167
5.3	Research Contributions .....	169
5.3.1	Societal Contributions .....	169
5.3.2	Technical Contributions .....	170

<b>Chapter 6: Recommendations</b> .....	175
6.1 Integration IRI Numerical-Based Methods with PACS .....	175
6.2 Experimental Detectability Testing.....	178
6.3 Effective Thermal Conductivity Bioheat Transfer Modeling .....	179
6.4 Removal of Thermal Artifacts in IR Images .....	180
<b>Chapter 9: References</b> .....	181

## List of Figures

Figure 1. Illustration of the female breast anatomy obtained from [10].	3
Figure 2. Illustration of the Hallmarks of Cancer reproduced from Hanahan and Weinberg [38,39], adapted from [41].	10
Figure 3. Illustration depicting the comparison between a normal vasculature structure and a tumor vessel structure [43].	13
Figure 4. Example of the different levels of breast density [57].	15
Figure 5. Example of breast ultrasound capturing a (a) malignant and (b) benign tumor [59].	16
Figure 6. Example of CE-MRI at various enhancements including (A) pre-enhanced, (B) homogeneously enhanced, and (C) ultra-high resolution enhanced CE-MRI [70].	17
Figure 7. Example of models for mammography sensitivity as a function of tumor size, reproduced using models from [83,84].	22
Figure 8. Methods utilize to classify tumors in terms of (a) clock positioning, (b) tumor depth, and (c) quadrant localization. Redrawn from [96].	24
Figure 9. Number of scientific publications related to AI-based methods utilized for IR thermography for breast cancer detection.	37
Figure 10. Thermal profiles of the liver obtained using (A-C) Pennes' bioheat model and (D-F) the CCD model from He and Liu [351].	47
Figure 11. Measured temperatures and effective thermal conductivity for (a) healthy and cancerous breast comparison, (b) tumor progression, and (c) treatment monitoring, replicated from Gautherie [113].	54

Figure 12. Plot of the hyperbolic law relation between the metabolic heat production and the tumor doubling time, replicated from Gauterie [112–114].	56
Figure 13. Example (a) concentric and (b) non-concentric hemispherical models developed by Osman and Afify [375] and Sudharsan et al. [378], respectively, and utilized in various literature. Geometries were redrawn and adapted from [116].	59
Figure 14. Examples of cartesian (a) 2D and (b) 3D models utilized in literature, redrawn and adapted from [116,118].	60
Figure 15. Example of realistic 2D (outline of breast from anatomic breast illustration) and 3D (deformed hemisphere due to gravity) models utilized in literature, redrawn and adapted from [387,390].	63
Figure 16. Example of (a) patient-specific digital breast model and (b) thermal simulation of breast cancer.	67
Figure 17. <i>Flowchart showing the process for the inverse heat transfer approach for breast cancer detection</i> [150].	69
Figure 18. Validation results for the inverse heat transfer approach through (a) qualitative comparisons of surface temperature distributions, and (b) quantitative comparisons of the predicted tumor size to actual size from MRI [149,150].	71
Figure 19. Depiction of IRI image capture of patients in the prone position with an (a) illustration of the camera position for imaging, and (b) an example set of IR images of a patient’s left breast in the same positions.	77
Figure 20. Example of DBM generation process from MRI using the method developed by Gonzalez-Hernandez et al. [395].	80

Figure 21. Front and side views of a patient-specific DBM showing the measurement locations of the breast surface width $W$ , height $H$ , and length $L$ .....	82
Figure 22. Labeled boundary condition locations in a patient-specific DBM utilized for bioheat transfer simulations of breast cancer.....	84
Figure 23. Example of the reference and sensed images, the registered image after IR image registration, and the ROI selected from the registered image.....	87
Figure 24. (Top) Illustration of IR image registration process and (Bottom) example of associated GUIs developed in MATLAB.....	90
Figure 25. Flowchart of the IRI-NE utilized for breast cancer detection on 23 patients..	94
Figure 26. Developed GUIs for the IRI-NE's main analysis (top) and (bottom) in case of hardware or software crashes.....	95
Figure 27. Illustration and patient-specific DBM representation of a (a) concave breast and (b) convex breast models. Illustrations reproduced from the work conducted by Hsia and Thomson [409].....	99
Figure 28. 2D view of the inside of the DBM and 3D view of the DBM for the (Top) concave and (Bottom) convex models with labels of the various regions and areas.....	101
Figure 29. Illustration of tumor placement in the (A) concave and (B) convex base models.....	103
Figure 30. Flowchart of parametric study process conducted in ANSYS Fluent.....	110
Figure 31. Example of simulated, synthetic IR, and clinical IR surface temperature distributions for patient 13L.....	112
Figure 32. Example of various noise levels (0 mK, 20 mK, and 40 mK) for the generation of synthetic IR surface temperatures for patient 17L.....	113

Figure 33. Flowchart process of the modified IRI-NE utilized to detect breast cancer using 3D surface temperatures.....	115
Figure 34. Example thermal contrast between a breast with cancer and the same breast without cancer, also known as the healthy breast. ....	119
Figure 35. Example IR images of patients with superficial vasculature for patients 4, 5, and 17.....	121
Figure 36. Vessel model placed inside patient 17L’s DBM for a case with cancer and without cancer. ....	122
Figure 37. Selected ROI for the ROI cases for the 1-vessel model. ....	123
Figure 38. Validation results of the IRI-NE for the (a) seven previous cases and (b) 16 additional cases. ....	129
Figure 39. Predicted tumor size vs actual tumor size obtained from MRI for all cases. ....	132
Figure 40. Verification results and comparison for patient case 1R.....	133
Figure 41. Comparison of surface temperature distribution of the ground truth and predicted data for patient 9L case without cancer. ....	135
Figure 42. Effect of noise level on the detection of breast cancer.....	136
Figure 43. Prediction results for the concave base model with a (a) 10 mm tumor with 20 mK noise, (b) 10 mm tumor with 40 mK noise, (c) 20 mm tumor with 20 mK noise, and (d) 20 mm tumor with 40 mK noise.....	138
Figure 44. Prediction results for the convex base model with a (a) 10 mm tumor with 20 mK noise, (b) 10 mm tumor with 40 mK noise, (c) 20 mm tumor with 20 mK noise, and (d) 20 mm tumor with 40 mK noise.....	140

Figure 45. Effect of noise level at the centerline tumor position on the tumor size prediction error.....	143
Figure 46. Internal temperature distribution plotted against the distance along the center line for patient 1R with varying tumor sizes.....	145
Figure 47. Effect of tumor size and position on the maximum thermal contrast for the (a) concave and (b) convex base models.....	147
Figure 48. Plotted results showing the effect of breast size on the thermal contrast for the concave model with a 10 mm tumor placed along the centerline positions. ....	150
Figure 49. Plotted results showing the effect of breast size on the thermal contrast for the concave model with a 20 mm tumor placed along the centerline positions. ....	151
Figure 50. (Top) Plotted results of the thermal contrast for a 10 mm tumor at tumor positions along the centerline for the convex base and scaled models. (Bottom) Zoomed in plot of the results for tumor positions 1-4 to show the maximum thermal contrast below the 20 mK threshold. ....	153
Figure 51. Plotted results of the thermal contrast for a 20 mm tumor at tumor positions along the centerline for the convex base and scaled models. ....	155
Figure 52. Plot of maximum surface thermal contrast as a function of tumor size (diameter) for three breast sizes.....	156
Figure 53. Plot of the maximum surface thermal contrast as a function of breast density (thermal conductivity of tissue) for varying tumor sizes (diameters) conducted on patient 1R. The breast density ranges are labeled as predominantly fatty (PF) for 0.1 W/m-K to 0.25 W/m-K, scattered fibroglandular (SF) for 0.25 W/m-K to 0.35 W/m-K,	

heterogeneously dense (HD) for 0.35 W/m-K to 0.5 W/m-K, and extremely dense (ED) for 0.5 W/m-K to 0.7 W/m-K. ....	158
Figure 54. Comparison of (first row) ground truth and (second row) predicted ROI temperatures for each case. The last row shows the predicted surface temperatures for each case. ....	160
Figure 55. Plotted perfusion rate values associated with an equivalent heat source to a metabolic heat source for tumors of various sizes for patients 1R and 17L. ....	162
Figure 56. Plotted perfusion rate values associated with an equivalent heat source to a heat source utilized in bioheat transfer modeling of breast cancer for tumors of various sizes for patients 1R and 17L. ....	163
Figure 57. Example PACS architecture with an integrated IRI numerical-based system for breast cancer detection. ....	177
Figure 58. Breast phantom model made of tissue mimicking material using a patient-specific DBM mold with an artificial heat source and chest wall heater. ....	179
Figure 59. Example of (a) IR surface temperature with visible thermal artifacts and (b) smoothen IR temperatures attempting to remove the thermal artifact surface temperature. ....	180

## List of Tables

Table 1. Breast cancer staging with descriptions compiled from [30–33].	6
Table 2. Breast cancer risk factors [3,13,34].	8
Table 3. Comparison of common breast cancer imaging modalities, adapted from [73].	19
Table 4. Comparison of sensitivity and specificity for different imaging modalities and breast density, adapted from [73].	20
Table 5. Sensitivity and specificity of thermography from 1961-1972 literature.	32
Table 6. Thermal sensitivity progression from 1972-2020, adapted from [116,118,120].	35
Table 7. Mean effective thermal conductivity value of different tissue types measured in both healthy and cancerous breast in vivo and in vitro, replicated from Gautherie [112–114].	52
Table 8. Clinical patient data collected from pathology reports at RGH for twenty-three patients.	78
Table 9. Thermal physical properties of breast tissue and breast cancer for bioheat transfer modeling [395].	85
Table 10. Geometric lengths for the based and scaled models.	100
Table 11. Coordinate values for the breast domains, breast centers, surface points, and separation boundaries.	104
Table 12. Tumor position coordinates for points along the centerline and in the x-direction.	104
Table 13. Distance from chest and tumor depth values for the concave and convex models.	105

Table 14. Effective thermal conductivity ranges for the different breast density types from Gautherie [112–114]. .....	107
Table 15. Parametric study parameters, and total cases and iteration amounts for N = 200.....	110
Table 16. Patient data utilized for verification of the modified IRI-NE.....	117
Table 17. Values for the upper and lower coordinates for each ROI case.....	123
Table 18. Parametric study overview including total number of parametric cases, total simulation iteration number, and parameters under study for each case for N = 200...	125
Table 19. Breast surface measurements of the right and left breast for each patient case. ....	127
Table 20. Results for tumor size prediction error, absolute error, and percent error for all patient cases. ....	131
Table 21. Comparison of tumor size prediction error between results obtained using synthetic IR and clinical IR surface temperatures. ....	134
Table 22. Error in tumor size at various depths in the concave base model for the 10 mm and 20 mm tumor cases at 20 mK and 40 mK noise levels. ....	139
Table 23. Error in tumor size at various depths in the convex base model for the 10 mm and 20 mm tumor cases at 20 mK and 40 mK noise levels. ....	141
Table 24. Distances from the tumor positions to the nearest surface point for both models. ....	148
Table 25. Comparison of predicted parameters and prediction error between each case. ....	159

# Chapter 1: Introduction

## 1.1 Motivation

Cancer is one of the leading causes of death before the age of 70 worldwide, having an estimated 9.9 million deaths in 2020 [1]. Breast cancer is the most common cancer among women, making 24.5% of all cancers and taking the lives of over 683,000 women, surpassing lung cancer in incidence and mortality rates [1,2]. In the United States, breast cancer makes up 29% of new cancer cases each year and has moved up to be the leading cause of cancer deaths among women [3]. By the end of 2023, over 297,000 new cases of invasive breast cancer have been diagnosed in the United States alone [4]. Studies have shown that advancements in early detection and treatment decreased the mortality rate of breast cancer by 40% from 1989 to 2017 [5]. This shows the importance of breast cancer research and the technological developments needed to further reduce this mortality rate, eventually eliminating it. The work conducted in this thesis aims to evaluate a novel technology developed for accurate breast cancer detection and evaluate its potential in early detection.

## 1.2 Breast Cancer

According to the CDC, breast cancer is defined as a disease that causes the abnormal growth of mutated cells within the breast [6]. The most common types of breast cancer occur in the lobules or in the ducts (glandular tissue), but may occur in other areas such as the nipple, fat and connective tissue, or in the lining of blood and lymph vessels [6,7]. Although breast cancer most commonly occurs in women, ~1% of breast cancers occur in men [7–9]. Early detection of breast cancer has played a major role in guiding treatment

and in reducing the mortality rate. Therefore, it is important to understand breast cancer in terms of the anatomy of the breast, the types of breast cancers, and risk factors that are of importance to clinicians.

### 1.2.1 Female Breast Anatomy

Figure 1 shows the anatomy of the female breast with labels of the different regions, organs, and components within the breast. As the figure shows, the breast is composed of tissue layers that go over the chest wall. The tissue layers are made of three different types: (i) glandular tissue, (ii) fibrous tissue, also known as connective tissue, (iii) and fatty tissue which fills up the remaining space of the breast [10]. The glandular tissue region of the breast consists of 15 to 20 lobules that are arranged in a cluster-like manner. The lobules are made up of smaller lobules which are the main location where milk is produced. Additionally, the glandular tissue region contains the breast ducts which connect to the nipples through a thin tube that carries the milk. In the fibrous tissue, the ligaments are there to help secure the breast in place by stretching the skin to the chest wall. The amount of fatty tissue that makes up the breast determines the size of the breast. Breast density is the measurement of fibroglandular tissue with respect to the amount of fat tissue, where denser breasts have a higher percentage of fibroglandular tissue [11]. The breast also contains blood vessels that provide oxygen to the surround tissue and carry away waste, as well as the lymph nodes, which defends the body against infections through the lymphatic system [7,10].

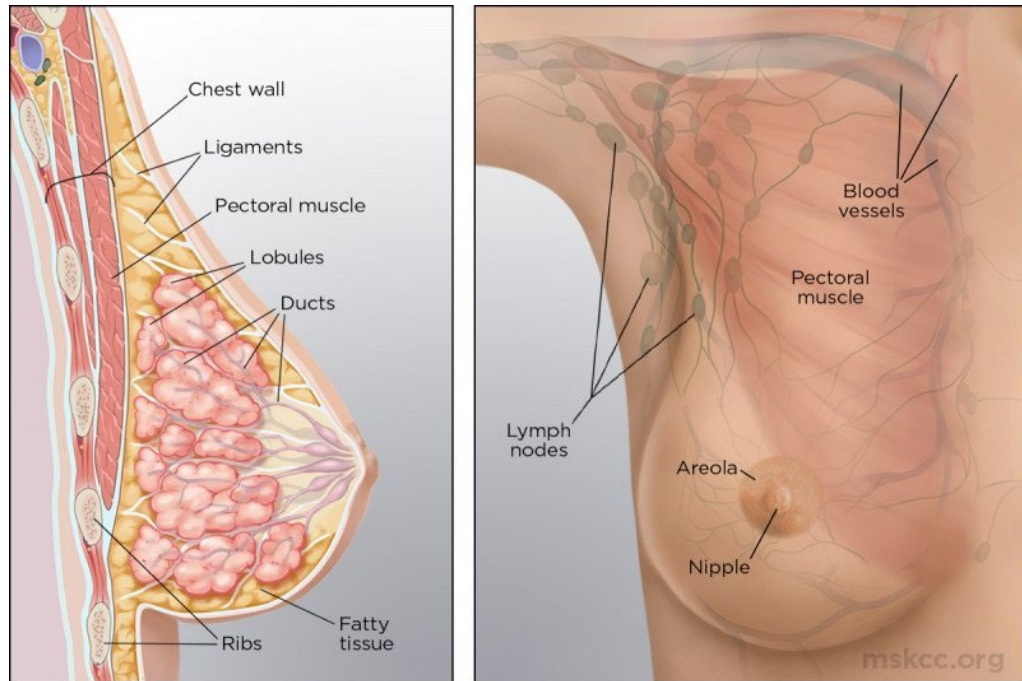


*Figure 1. Illustration of the female breast anatomy obtained from [10].*

### 1.2.2 Types of Breast Cancer

The type of breast cancer is dependent on which cells have been affected and whether the cancer has become invasive or noninvasive. Breast cancer primarily occurs in the ducts or lobules as carcinomas, or tumors, but can occur in other areas [12,13]. Breast tumors can be classified as malignant if they grow abnormally and uncontrollably or as benign if the cells are shown to grow normally. Breast cancer can be referred to as in situ (noninvasive) or as invasive depending on histological markers and the spreading of the diseased cells [3,13]. Ductal carcinoma in situ (DCIS) is the most common noninvasive form of breast cancer making up 20% of all breast cancers [14]. Researchers have found DCIS to be a precursor to invasive breast cancer, where the cancerous cells in a localized region in the ducts migrates to any other region in the breast [15,16]. Lobular carcinoma in situ (LCIS) is not as common as DCIS and is typically classified as a neoplasia, meaning it can be benign or malignant [17,18]. Similar to DCIS, LCIS is a precursor to invasive breast cancer

but has a higher chance to become an invasive breast than DCIS (7-11 times higher) and has demonstrated risk of bilateral breast cancer [18,19]. There are two main invasive carcinomas that can be formed from DCIS and LCIS: (i) invasive ductal carcinoma (IDC) and (ii) invasive lobular carcinoma (ILC). The most common invasive breast cancer is IDC which makes up 70-80% of all invasive breast cancers [13,20]. The second most common invasive breast cancer is ILC making up 10-15% of all invasive breast cancers [20–22].

Breast cancers can be further classified by the presence of estrogen, progesterone, and HER2 receptors in the cancer cells [3,23]. If cancer cells do not have any of these receptors, or test negative for them, then it is classified as triple-negative breast cancer (TNBC), which makes up 10-15% of all breast cancers [3]. When invasive breast cancers are classified as TNBC, treatment becomes limited to chemotherapy due to its aggressive nature [23]. Sarcomas are rare types of breast cancers that make up less than 1% of all breast cancers and form in regions outside of the lobules and ducts [23–25]. One of the more aggressive sarcomas is angiosarcoma, which is a malignant cancer that develops in the blood vessels with an incidence rate of 0.002%-0.05% [24,25]. Although the formation of this type of aggressive cancer is unknown, researchers believe angiosarcomas may arise after treatment of DCIS or of invasive cancers [24]. Other rare forms of breast cancers include inflammatory breast cancer, metaplastic carcinoma, Paget disease, and phyllodes tumors [23,26,27]. The overall goal in treating any type of breast cancer is to ensure the cancer is dealt with before it goes metastatic. When breast cancer becomes metastatic, it means that the cancer has spread to other parts of the body such as the liver, bones, or lungs [26].

### 1.2.3 Breast Cancer Stage and Grade

In addition to categorizing breast cancer by the affected region, invasiveness and hormone receptor presence, breast cancer is also classified and diagnosed with a grade and stage. The grade of cancer investigates how much the cancer cells look like normal cells, which aids in the prognosis and treatment of the cancer [28,29]. In breast cancer, the grade will depend on whether the cells come from invasive breast cancer cells or DCIS, but both have grading scores of 1-3 [29]. For invasive breast cancer, grade 1 indicate slow growing cancer cells that look like normal cells (well differentiated), grade 2 indicates faster growing cancer cells that may not look normal (moderately differentiated), and grade 3 indicates cancer cells that are very distinct from normal cells (poorly differentiated). In the grading of DCIS, these grades are utilized to determine if the cancer is a low-grade DCIS (grade 1), an intermediate grade DCIS (grade 2), or a high-grade DCIS (grade 3). There are two types of staging which are pathological (surgical) staging that occurs after the removal of tissue, and clinical staging that occurs during examinations [30]. The TNM classification system is utilized to stage breast cancer in terms of the tumor size (T stage), number of nearby lymph nodes the cancer has spread to (N stage), and the metastatic spread to other organs (M stage) [23]. Table 1 gives the TNM staging categories and description for each stage compiled from various sources [30–33]. The TNM staging, receptor presence, and cancer grade are utilized in fully staging breast cancer [30].

Table 1. Breast cancer staging with descriptions compiled from [30–33].

<b>T Stage: Tumor Size</b>	
<b>Category</b>	<b>Description</b>
TX	Unknown or cannot be assessed
T0	No tumor
Tis	In situ carcinoma (DCIS or Paget’s disease with no tumor mass)
T1	≤ 20 mm
T1a	≤ 5 mm
T1b	> 5 mm and ≤ 10 mm
T1c	> 10 mm and ≤ 20 mm
T2	> 20 mm and ≤ 50 mm
T3	> 50 mm
T4	Tumor of any size grown into the skin or chest wall
T4a	Tumors that have reached the chest wall
T4b	Tumors that reached the skin
T4c	Tumors that have reached both the skin and chest wall
T4d	Inflammatory breast cancer
<b>N Stage: LNs Spread Number</b>	
NX	Unknown or cannot be assessed
N0	No spread
N1	1-3 axillary LNs
N1mi	Micrometastases under the arm with a spread ≥ 0.2 mm and < 2 mm
N1a	Spread to 1-3 LNs under the arm with a spread ≥ 2 mm
N1b	Spread to internal mammary LNs same side as cancer, but not found by sentinel lymph node biopsy
N1c	Spread is like N1a and N1b
N2	4-9 LNs
N2a	Spread to 4-9 LNs under the arm with at least one area spread ≥ 2 mm
N2b	Spread to one or more inter mammary lymph nodes
N3	10+ LNs
N3a	Spread to 10 + axillary LNs with at least one area spread ≥ 2 mm or LNs under collarbone with at least one area spread ≥ 2 mm
N3b	Spread at least 1 axillary LN with at least one area spread ≥ 2 mm and enlarged internal mammary LNs, or 4+ axillary LNs with at least one area spread ≥ 2 mm and internal mammary LNs
N3c	Spread to LNs above collarbone same side as cancer with at least one area spread ≥ 2 mm
<b>M Stage: Metastatic Spread to Distant Organs</b>	
MX	Unknown or cannot be assessed
M0	No distant spread
M1	Cancer has spread to distant organs

#### 1.2.4 Risk Factors

In diagnosing breast cancer, a risk factor is identified as anything that can increase the chances of obtaining cancer [3,13,34]. There are various risk factors for breast cancer that

have been well identified and documented over the years [3,13]. These factors can be categorized as modifiable factors, sometimes known as lifestyle-related factors, and non-modifiable factors, which can be separated into unalterable factors and historic-based factors [3,34]. Table 2 shows these modifiable and non-modifiable risk factors. The severity of these risk factors can be categorized as high-risk, intermediate-risk and average-risk, which help decide the appropriate screening tool needed. The modifiable risk factors relate to the lifestyle behaviors and choices made by the person at risk for cancer. However, one of the higher modifiable risk factors is hormone alteration procedures that can affect both men and women [13]. One factor that plays a major role in increasing the risk of breast cancer and relates to the majority of other risk factors is being a woman. This is due to women having higher hormonal stimulation that can affect breast cells that can present an imbalance in the body [3]. This is why men are at lower risk of obtaining breast cancer and the majority of the non-modified risk factors increase the risk of breast cancer in women. For the non-modifiable risk factors, women are tested for genetic mutations such as the BRCA1 gene mutation or the BRCA2 gene mutation. The risk of developing breast cancer by age 70-80 is 55-72% for women with a BRCA1 mutation and 45-69% for women with a BRCA2 mutation [35]. In comparison, women with normal BRCA1 and BRCA2 have a 13% risk which shows that these mutations increase the risk about 5 times more. This leads to women being considered high-risk if either of the genetic mutations are present and also leads for an increased number of screening and monitoring procedures. In addition, women with denser breast tissue are also considered high risk and have to go through additional screening due to this factor [11].

Table 2. Breast cancer risk factors [3,13,34].

<b>Modifiable Risk Factors</b>	Lifestyle-related factors	Alcohol and tabaco consumption
		Weight and diet
		Physical activity
		Hormone alteration procedures
		Chemical and environmental exposure
<b>Non-Modifiable Risk Factors</b>	Historic-based factors	History of cancer or other breast diseases
		Menstrual period and menopause timeline
		Radiation therapy history
		Pregnancy and breastfeeding
	Unalterable factors	Gender
		Breast density
		Age
		Height
		Race/ethnicity
		Family history
		Genetic mutations and other genetic factors

### 1.3 Cancer Biology

Cancer is defined as a disease with abnormal and uncontrollable cell growth which can spread to other parts of the body through metastasis [36]. The study of cancer can be traced as far back as 3000 BC to ancient Egypt, but it was not until the 19th century where oncology studies through scientific methods and instrumentation were established [37]. The major scientific method that helped progress cancer research is the establishment of cellular pathology. This led to the advancement in research in understanding the mechanics of cellular cancer growth including the contribution of tumor angiogenesis.

#### 1.3.1 Cancer Growth

The study of cellular cancer growth is a complex phenomenon which entails many factors. Hanahan and Weinberg [38,39] have established the Hallmarks of Cancer in 2000, further refined in 2011, which describe the complexity of cancer growth through ten hallmarks, or principles. These principles include: (1) sustaining proliferating signaling, (2) evading

growth suppressors, (3) avoiding immune destruction, (4) enabling replicative immortality, (5) tumor-promoting inflammation, (6) activating invasion and metastasis, (7) inducing angiogenesis, (8) genome instability and mutation, (9) resisting cell death, and (10) deregulating cellular energetics. Figure 2 shows an illustration of these principles and is a remake of the illustration provided by Hanahan and Weinberg [38,39]. Principles (1)-(4) and (9) have to do with excessiveness, uncontrollability, and abnormality of cancer cell growth, which is similar to normal cell growth but with the mission of metastasis. More importantly, these principles also describe how cancer cells avoid detection, mortality, and growth control. The remaining principles relate to how the cancer cells grow, mutate, and spread as well as factors that happen after growth. In 2017, Fouad and Aanei [40] generated their own hallmark list that renamed, combined, or repurposed the principles from the original Hallmarks of Cancer [38,39]. Currently Hanahan [41] has extended the Hallmarks of Cancer to include other factors such as nonmutational epigenetic reprogramming and senescent cells. Although many of these principles have motivated and guided many cancer research projects, there is one principle that has played a big role in cancer detection and hyperthermia research, tumor vascularity.

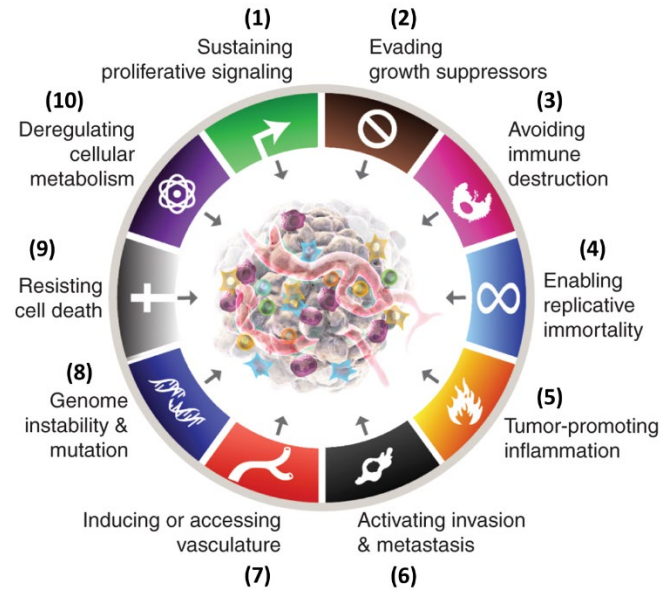


Figure 2. Illustration of the Hallmarks of Cancer reproduced from Hanahan and Weinberg [38,39], adapted from [41].

### 1.3.2 Tumor Angiogenesis

Angiogenesis is defined as the development of new blood vessels through various molecular and biological mechanisms [42]. Vasculogenesis is the formation of new blood vessels and may be conducted simultaneously with angiogenesis to create vasculature networks [43]. Angiogenesis plays a major role in tumor growth through tumor angiogenesis, which has been researched extensively ever since the findings by Folkman [44] and has been established as one of the hallmarks of cancer [38,39]. Although vasculogenesis can play a role in the formation of tumor vasculature, it only contributes from 0.1 to 50% of the formation depending on the tumor and it is mostly seen in the formation of hematological tumors and lymphomas [43].

There are several angiogenic mechanisms, but there are three common mechanisms that have been observed in tumor angiogenesis: (i) sprouting angiogenesis, (ii) intussusception, and (iii) vasculogenic mimicry as described by Marmet [43]. Sprouting angiogenesis is the

formation of new vascular networks from preexisting blood vessels and is utilized by tumors by generating new capillary sprouts from preexisting nearby capillaries. The main driver for sprouting angiogenesis is the migration and proliferation of endothelial cells, the cells that make up the lining of the vessels, regulated by inhibitors and proangiogenic factors, or growth factors. Intussusception (IMG) is the process of splitting preexisting vessels into two new branches of vessels through bridging neighboring vessels with a connective tissue column and has been observed to happen after sprouting angiogenesis or even after vasculogenesis. IMG has been shown to work faster than sprouting angiogenesis as it does not go through endothelial proliferation to form new vessels, making it less metabolically demanding, in comparison. Studies have shown that changes in blood flow dynamics and shear stress on endothelial cells have played a role in influencing the start of IMG. IMG provides more structure for sprouting angiogenesis by aiding with increasing the density of tumor vasculature [43,45]. Vasculogenic mimicry (VM) is the process of creating a new vasculature network without the use of endothelial cells, which acts as a secondary circulatory system to tumors. Studies have yet to uncover the exact drivers of VM, but it has been observed to occur in aggressive tumors. Furthermore, VM has been shown as a key contributor to tumor growth and metastasis [43,46]. All three mechanisms play a vital role in tumor growth as the formation of the tumor vascular network creates the tumor microenvironment, which is needed by the tumor to receive nutrients and to be able to spread. Without angiogenesis, a tumor can grow to no more than 1-2 mm<sup>3</sup> reaching a steady state and balanced phase known as the avascular phase where there is not net increase in the tumor volume.

In angiogenesis, there are many pro- and anti-angiogenic regulators that help balance and stabilize vascular network formation. A primary proangiogenic factor that plays a major role in tumor angiogenesis, is the vascular endothelial growth factor (VEGF). VEGF has a major role in the formation and remodeling of vasculature through sprouting angiogenesis to increase vessel branching and create vessel abnormalities. This regulator is a major contributor to the angiogenic switch for tumors, where the tumor goes from the avascular phase to the angiogenic state to create a vascular network [43,47]. Another contributor to the angiogenic switch is hypoxia, or the low level of oxygen in tissue, which has been observed to occur due to the rapid growth of the tumor and formation of the inefficient tumor vascular network, in comparison to a normal vascular network. The main difference between normal and tumor vasculature is the morphology and the characteristics associated with it due to the uncontrolled and imbalanced angiogenesis regulators and high proliferation of endothelial cells [43,48]. Figure 3 shows a comparison between normal and tumor vasculature including the structural and physiological differences. In Fig. 3, the structural comparison is clear as the normal blood vessels are well-organized while the tumor blood vessels are more chaotic. There are three main components in vasculature structure and stability which are the endothelial cells, pericytes, and the vascular basement membrane. Tumor vasculatures have less compacted endothelial cells and supportive pericytes making the vessels have higher permeability which invokes leakiness and impaired blood flow. The pro-angiogenic factors, such as VEGF, make it so that the tumor vasculature has more variety of dense areas, vessel size and shape, and branching patterns, but without the defined hierarchy associated with normal vasculature. The lack of

unbalanced structure and physiological conditions both play a major factor in tumor growth [43,49].

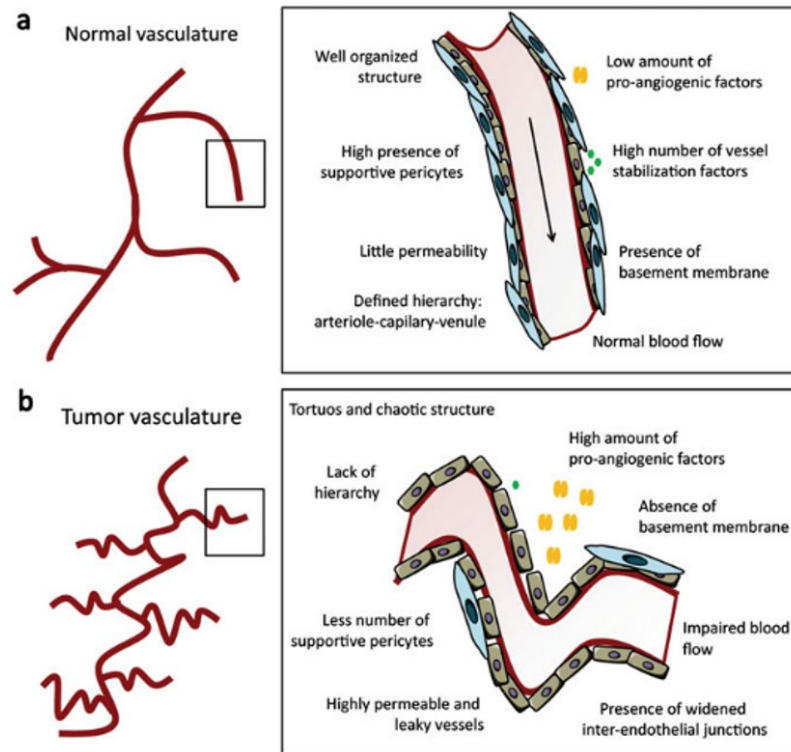


Figure 3. Illustration depicting the comparison between a normal vasculature structure and a tumor vessel structure [43].

## 1.4 Breast Cancer Screening

Medical screening and imaging have played a huge role in the screening and diagnosis of breast cancer. Screening for breast cancer entails conducting tests and examinations on individuals that have no symptoms in hopes of detecting cancer early. The American Cancer Society recommends that women over 40 should get screened for breast cancer, if they are at average risk. Women who are considered high risk are recommended to start screening at the age of 30 [50]. Early detection of breast cancer through screening plays a major role in improving the 5-year relative survival rates up to 99% and reducing mortality rates, if the cancer is detected early enough and is in its earlier stages [5]. In breast cancer,

screening is conducted through imaging with the common imaging modalities being mammography, breast ultrasound, and breast magnetic resonance imaging (MRI).

#### 1.4.1 Imaging Modalities

The main imaging modalities utilized in the detection of breast cancer through screening are mammography, breast ultrasound, and breast magnetic resonance imaging (MRI). The following paragraphs give a brief description, a short history, as well as the pros and cons of these technologies.

##### a. Mammography

Mammography (MG) is considered the gold standard imaging modality for breast cancer screening. In MG, patients have each of their breasts compressed between two plates in a machine which imparts low dose x-rays to each breast tissue [51]. The breast compression spreads the tissue out to give a better picture and to use less x-ray radiation. Images are taken at different angles to obtain different views and cover a wider area of coverage. Digital MG, also known as digital breast tomosynthesis is a machine that compresses the breast once and captures multiple mammograms that are stitched into a three-dimensional (3D) image with the aid of a computer [52]. The concept of utilizing such radiological studies was first observed in 1913 by Albert Salomon and was further developed during the late 1940s to the late 1990s [53]. However, it was not until the 2000s where digital MG was established and approved by the U.S Food and Drug Administration (FDA) [53,54]. Although MG is utilized as the gold standard, it creates discomfort to the patients due to the breast compressions. In addition, MG is suboptimal in image dense breast tissue in comparison to fatty tissue. This is clearly shown in Fig. 4 which shows the different levels of breast density: fatty, scattered fibroglandular, heterogeneously dense, and extremely

dense. Denser breast tissue creates a masking effect which can lead to missed tumors, as well as false-negative or false-positive results [11,55]. Both false-negative and false-positive results create psychological and financial issues due to further testing that is needed, depending on the individual outcome. Some factors that may give false-positive results are patient age (younger vs older patients), surgical history, family medical history, or the use of estrogen medication [11,54,56,57].

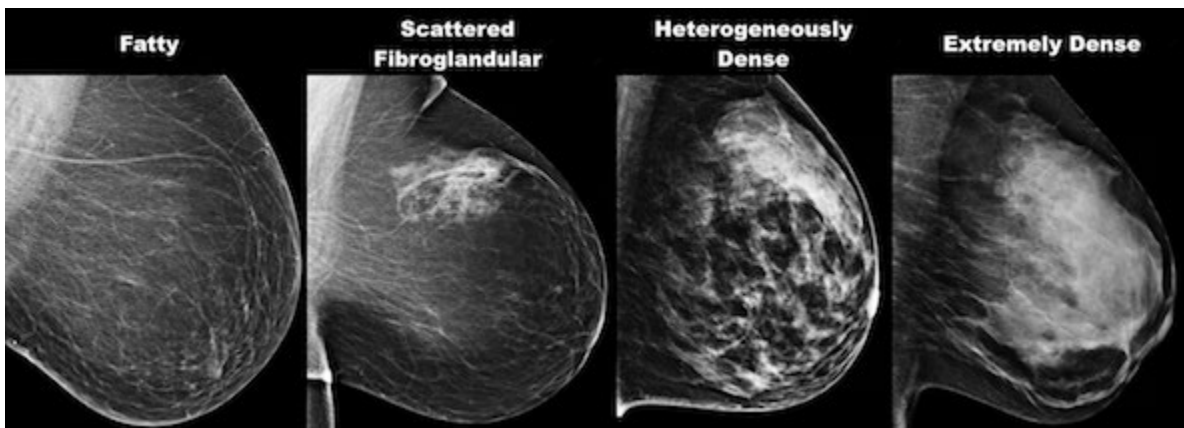


*Figure 4. Example of the different levels of breast density [57].*

#### b. Ultrasound

Breast ultrasound (US) imaging is the technique of using sound waves emitted by a transducer that are utilized to generate digital images of the tissue inside the breast by capturing the echoes created by the sound waves [58–60]. This technique is utilized as an adjunct to mammography to image patients with dense breast tissue. Breast US are especially useful in surgical procedures such as biopsies by guiding biopsy needles to reach the tumor [60,61]. Additionally, this technique does well in capturing both cysts and tumors present within the breasts. A cyst is the accumulation of fluid inside of tissue which forms a lump that that is sometimes mistaken for cancer [62]. Benign tumors can also be captured in a breast US, which can be difficult to differentiate from a malignant tumor. Figure 5

shows US images of a malignant and benign tumor found in two different breasts. The use of breast US in a clinical setting can be traced back to 1954 and the development of digital breast US can be traced to the 1980s and 1990s [58,61]. Although this technique does well in imaging dense breasts, the interpretation of the results is dependent on the radiologist and the modality has been seen to be difficult to standardize [61]. This leads to an increase in psychological impact on patients and their families as they may need to conduct additional testing.

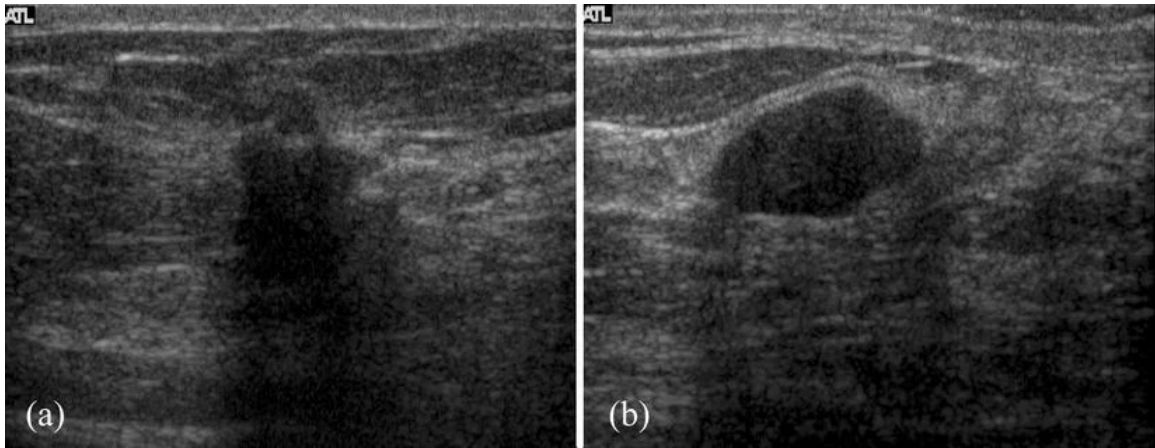


*Figure 5. Example of breast ultrasound capturing a (a) malignant and (b) benign tumor [59].*

### c. Magnetic Resonance Imaging

Breast magnetic resonance imaging (MRI) is an imaging technique that obtains detailed image slices of the inside of the breast with the use of low-energy electromagnetic waves and strong magnetic fields [60,63]. The development of MRI came from a 1973 study by Dr. Lauterbur where nuclear magnetic resonance signals were being resolved by magnetic field gradients into pixels or voxels [64]. This modality was implemented on breast tissue in the 1980s by Dr. Heywang using contrast medium intravenously injected into the breast tissue area [61]. Currently, contrast-enhanced MRI (CE-MRI) is utilized for diagnosing breast cancer due to the neovascularity of tumors created by angiogenesis regardless of

breast density [60]. Additionally, CE-MRIs and dynamic CE-MRIs play a huge role in studying the angiogenesis process and the tumor vascularity structure through obtaining kinetic curves [65–69]. The type of contrast material and image processing method will provide different enhancements and resolutions [70]. Figure 6 shows an example of MRIs of a breast with a tumor going through various enhancements such as pre-enhancement (Fig. 6A), homogeneous enhancement (Fig. 6B), and ultra-high-resolution enhancement (Fig. 6C). Although CE-MRI is well suited to image patients with dense breast tissue, it is only utilized for screening of high-risk patients and not necessarily the rest of the screening population [60,61,71].

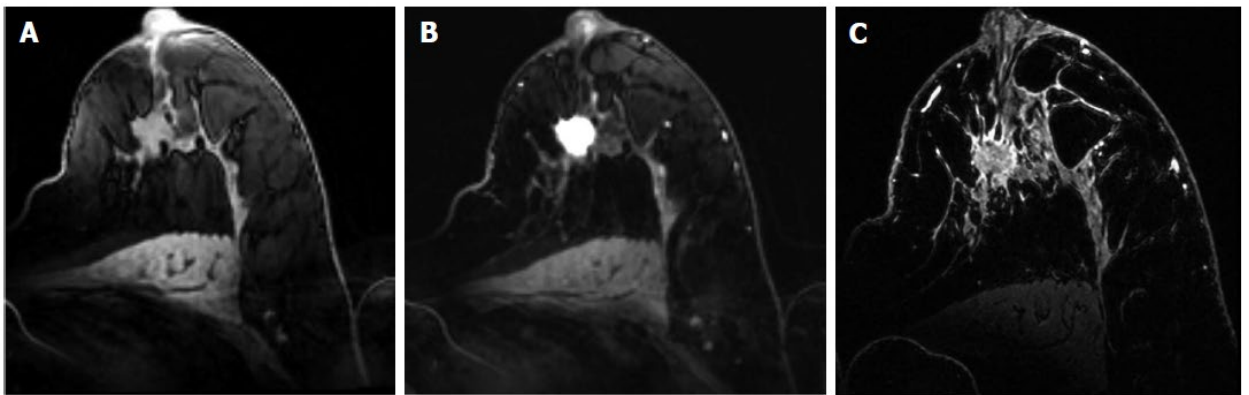


*Figure 6. Example of CE-MRI at various enhancements including (A) pre-enhanced, (B) homogeneously enhanced, and (C) ultra-high resolution enhanced CE-MRI [70].*

#### 1.4.2 Sensitivity and Specificity

The comparison of imaging modalities in the biomedical field is conducted using the sensitivity and specificity of a system [72]. The sensitivity (Eq. 1) is the measure of the accuracy of the modality based on positive diagnosis rate, while the specificity (Eq. 2) measures how well the modality identifies patients without a disease. These values are utilized to quantify the difference between different modalities.

$$\text{Sensitivity} = \frac{\text{true positive}}{\text{true positive} + \text{false negative}} \quad (1)$$

$$\text{Specificity} = \frac{\text{true negative}}{\text{true negative} + \text{false positive}} \quad (2)$$

Table 3 shows a comparison of the sensitivity and specificity values for mammography (MG), ultrasound (US), MRI, and combinations of the modalities, reproduced [73]. From the table it can be observed that MRI has the highest overall sensitivity at 94.6%, but lowest overall specificity at 74.2% in comparison to MG and US. The combination of MG and US has shown to improve the overall sensitivity and specificity in comparison to their standalone counterparts. However, the combination of MRI with MG, US, or MG + US has shown to only improve the sensitivity but decrease the specificity, which is why US is utilized as an adjunct to MG more commonly than MRI. The range values for the sensitivity and specificity of MG, US, and MRI in Table 3 show the effects of various factors such as breast density and tumor type as described by Aristoki et al. [73]. The next section will go over some of these factors that would affect the detection of breast cancer through screening.

Table 3. Comparison of common breast cancer imaging modalities, adapted from [73].

Modality	Sensitivity (%)		Specificity (%)	
	Overall	Range	Overall	Range
MG	54.5	27-86.8	85.5	62.9-98.8
US	67.2	26.9-87.5	76.8	18.8-96.9
MRI	94.6	85.7-100	74.2	25-100
MG + US	72.2	-	87.8	-
MG + MRI	95.8	-	70.1	-
US + MRI	92.3	-	76.8	-
MG + US + MRI	97.7	95-100	63.3	37.1-87.5

### 1.4.3 Factors Affecting Detection

There are various factors that affect the detection of breast cancer including breast density, tumor size (T stage), tumor position, and cancer type. Each of these factors affect the sensitivity and/or specificity of the imaging modalities utilized in breast cancer screening. The details of their effects are described below.

#### a. Breast Density

In the current screening population, it is estimated that more than 40% of women have dense breast tissue [74,75]. Women with dense breast tissue have a higher risk of developing cancer (4 to 6 times more) than women with fatty breast tissue [11]. Also, studies have shown that women with dense breast tissue who have developed cancer in one breast are at higher risk of obtaining cancer in the contralateral breast [76]. Dense breast tissue has made it difficult to screen for breast cancer through MG due to masking effects from the tissue causing almost 38% of tumors to be missed [11,75]. Studies have shown that the sensitivity decreases from 78% to 47% as breast density increase from fatty to extremely dense breast tissue, respectively [77]. Adjunctive screening is utilized to improve the detection of breast cancer for patients with dense breasts. Table 4 shows a

comparison of the sensitivity and specificity for the various imaging modalities presented in Table 3 with the sensitivity and specificity for dense breast tissue, reproduced from [73]. As the table shows, the sensitivity decreases for all standalone modalities when screening for dense breast tissue (MG: 54.5% decreased to 48.7%, US: 67.2% decreased to 63%, MRI: 94.6% decreased to 92.8%). However, when combining methods the sensitivity increases showing the benefits of adjunctive screening. Studies have shown that screening of dense breast tissue increases the recall rates from 11.2% for fatty breast tissue to 23.8% for extremely dense breast tissue, but decrease when utilizing adjunctive technologies [11,78–82]. For specificity, a decrease in value is observed for all of the standalone imaging modalities, except US, and the combination modalities. The US standalone modality shows an increase in specificity from 76.8% to 82.5% regardless of the decrease of sensitivity from 67.2% to 63%. Therefore, there is a need for an imaging modality that can overcome these detectability hardships created by dense breast tissue.

*Table 4. Comparison of sensitivity and specificity for different imaging modalities and breast density, adapted from [73].*

<b>Modality</b>	<b>Sensitivity (%)</b>		<b>Specificity (%)</b>	
	Overall	Dense	Overall	Dense
MG	54.5	48.7	85.5	76.9
US	67.2	63	76.8	82.5
MRI	94.6	92.8	74.2	62.1
MG + US	72.2	78	87.8	76.5
MG + MRI	95.8	96.2	70.1	61
US + MRI	92.3	94.5	76.8	65.7
MG + US + MRI	97.7	99.1	63.3	51.3

#### b. Tumor Size

Studies have shown that the tumor size has a significant impact on the detectability of breast cancer through screening modalities [33,83–86]. There have been various models developed that specify the sensitivity of MG as a function of the tumor size. Figure 7 shows some examples of established models such as the model developed by Weedon-Fekjaer et al. [83] and the model developed by Isheden and Humphreys [84]. Weedon-Fekjaer et al. [83] utilized a logistic function to model the sensitivity as a function of tumor size due to the nature of the function being an increasing function. This property allowed for the researchers to conduct backwards calculations from available data to obtain the necessary parameters to obtain this function. The authors were able to create this model for all age groups in their dataset as well as subset age groups. The model shown in Fig. 7 represents the model the authors developed for their entire age group data. Isheden and Humphreys [84] developed a similar logistic model that accounts for both the tumor size and the breast density percentage. This model showed that breast density has a negative effect on the sensitivity of MG, which has been verified in previous studies [85,87]. These models are great representations of the relationship between MG sensitivity and tumor size. However, other studies have shown that the sensitivity for tumors  $\leq 10$  mm is below 70% and the sensitivity of tumors  $> 10$  mm but  $\leq 20$  mm is below 80% [86]. This is different than the models shown in Fig. 7, as they all reach close to 100% sensitivity for a 20 cm tumor. A better representation of the sensitivity obtained in previous literature has been shown by the model developed by Wang et al. [33]. The authors model utilized both true negative and false positive outcomes to obtain the appropriate parameters for their sensitivity model. This model shows the sensitivity of MG for a tumor size of 20 mm to be about 80% while a 10 mm tumor has a sensitivity of about 65%, which matches with other findings.

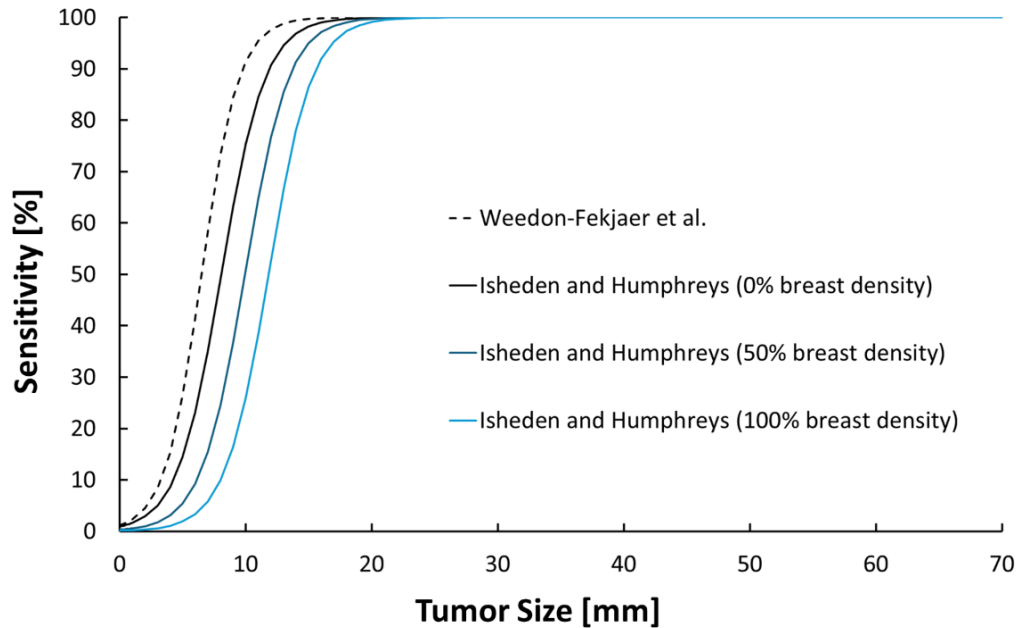


Figure 7. Example of models for mammography sensitivity as a function of tumor size, reproduced using models from [83,84].

Chen et al. [86] compared the sensitivity of MG, US, MG + US, and MG + US + MRI for tumor sizes  $\leq 10$  mm and tumor size  $> 10$  mm but  $\leq 20$  mm showing that sensitivity increased as the tumor size increased. Additionally, the authors showed an increase in sensitivity when comparing MG with US or the combination modalities (MG + US and MG + US + MRI). This lines up with the sensitivity studies discussed in Section 1.4.2. Other studies have investigated the accuracy of tumor size detected in comparison to the size obtained from histology reports and its impact on the detection of breast cancer [88–95]. Various studies have shown that both MG and US tend to underestimate the predicted size especially for Tis and T1 stage tumors (DCIS tumors and tumors  $\leq 20$  mm) while MRI tends to overestimate the predicted size [89–95]. In terms of detectability of cancer, a study conducted by Lee et al. [88] had 37.7%, 26.0%, and 10.3% of Tis, T1, and T2 ( $> 20$  mm but  $\leq 50$  mm) tumors missed, respectively, while T3 and T4 tumors were not missed. This

shows the need to obtain more accurate detection of tumors  $\leq 50$  mm, but especially  $\leq 20$  mm for early detection. However, studies have shown that larger tumors  $> 50$  mm have been missed by MG and US which further calls for an accurate and reliable imaging modality for breast cancer.

### c. Tumor Position

The positioning, depth, and location of a tumor within a breast is categorized utilizing the O'clock position, tumor depth, and quadrant localization criteria, respectively, in according to the World Health Organization [96]. Figure 8 shows example illustrations for each of these categories reproduced from [96]. For the tumor position, a clock pattern is utilized to describe the general position of the tumor as shown in Fig. 8a. Additionally, the center of the breast is utilized as an additional reference position in the case the tumor is not in any particular clock position. For the tumor depth, the breast is split into thirds: posterior (deep and close to the chest wall), middle (or mid), and anterior (closest to the surface) as shown in Fig. 8b. For the tumor location, the breast is first split into upper and lower which then is split into quadrants using the inner and outer categories, as shown in Fig. 8c. The breast side will determine the locations of the inner and outer category which then decides the tumor location based on the quadrant it is located in. The tumor position, depth, and location are important as some tumors are more difficult to image than others due to variability of breast density throughout the breast [97]. Wadhwa et al. [98] showed some cases of tumors in the posterior region that were missed in mammograms due poor technique in alignment prior to imaging. This gives an additional challenge for mammography in addition to breast density and tumor size.

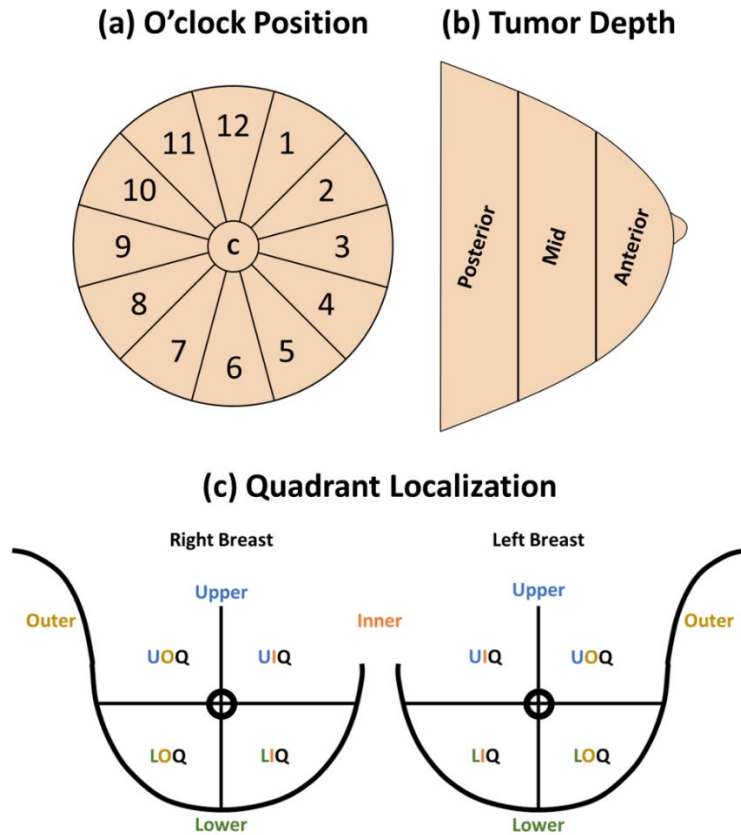


Figure 8. Methods utilize to classify tumors in terms of (a) clock positioning, (b) tumor depth, and (c) quadrant localization. Redrawn from [96].

#### d. Cancer Type

The last factor that can affect the detection of breast cancer is the cancer type, due to their correlation with tumor location, growth, and histology. As discussed in Section 1.2.2, breast cancer occurs primarily in the ducts or in the lobules with the most common cancer being IDC. Both invasive cancers, IDC and ILC, become invasive mostly from DCIS but can also occur from LCIS. Several studies have shown that DCIS and ILC tend to be underestimated the most compared to other cancer types by mammograph and ultrasound [90–92]. Lee et al. [88] has shown that 35.8% and 20.8% of DCIS and ILC cancer type tumors were missed in their study. The one cancer type that has been the most difficult to detect and has a high number of false negative rate has been ILC [98]. This type of cancer

is typically found and diagnosed through biopsy with some cases being found by accident in a different surgical procedure [17–22]. This calls for the need for an imaging modality or technique that can detect breast cancer regardless of breast density, tumor size, tumor position, and cancer type.

## 1.5 Technological Advancements in Breast Cancer Screening

Although there are established technologies and methods for breast cancer detection, there have been various technological breakthroughs in imaging and computational methods. One important advancement in breast cancer research is the advancement in existing technologies. Due to mammography being the gold standard of breast cancer screening, some researchers have investigated ways to improve and automate mammography to conduct more efficient imaging. Contrast-enhanced mammography (CE-MG) has shown great promise in utilizing the contrast-enhanced technology conduct in CE-MRI with mammography especially for imaging patients with dense breasts. The use of advanced computation techniques including artificial intelligence (AI) has helped developed advanced computer aided detection/diagnosis (CAD) systems for efficient breast cancer detection and clinical workflow. In addition to utilizing emerging technologies such as CE-MG for screening dense breast tissue, infrared (IR) thermography has also shown great promise as a screening modality.

### 1.5.1 Contrast-Enhance Mammography

Current studies have investigated the use of contrast-enhanced (CE) technology, such as CE mammography and CE-MRI, to help improve the current imaging protocol. In CE imaging, the patient is injected with contrast material that makes the tumor neovascular more visible in imaging. Studies have shown an increase in detection accuracy with the use

of CE mammography in comparison to tomosynthesis and digital mammography [99]. Cozzi et al. [100] showed that CE mammography can improve the specificity up to 84%, while keeping the sensitivity at about 92%. However, there have been concerns with the use of CE mammography due to having an increased dose of radiation and possible adverse reaction to the CE materials being injected. The use of CE -MRI has shown better outcomes in terms of improving detection accuracy even more than CE mammography [101,102]. However, the cost efficiency that typically comes with MRI imaging does not improve with CE-MRI. Therefore, in order to improve the accuracy of breast cancer screening and diagnosis while decreasing costs, computer-aided detection/diagnosis (CAD) tools have been developed.

### 1.5.2 Computer Aided Detection/Diagnosis

Some researchers have investigated the various CAD tools utilized with mammography images for breast cancer detection [103,104]. The authors have shown that CAD tools are utilized for image enhancement, image segmentation, feature extraction, and image classification. Image enhancement techniques are conducted to improve image quality and are typically used as pre-processing tools in CAD software. Image segmentation and feature extraction techniques try to isolate the areas and key features that are helpful for the CAD tools [105]. Finally, the image classifier utilizes the enhanced segmented images to detect breast cancer and is typically an AI-based method [106]. There has been a major breakthrough in improving AI-based methods for improved classification, especially in breast cancer detection and classification [107–109]. Moreover, AI-based methods have been developed to work with other adjunctive modalities such as ultrasound, CE mammography, and CE-MRI [108]. The aim of having these AI-based CAD tools is to

improve the accuracy of breast cancer detection, which has been shown to be true in some cases [110]. However, all medical decisions must be guided by a radiologist according to the Food and Drug Administration (FDA) and not solely based on the CAD tools or any AI-based method [111]. This means that the detection of breast cancer not only relies on the radiologist, but on the ease of use and reliability of their tools.

### 1.5.3 Infrared Thermography and Infrared Imaging

Thermography is the technique utilized to capture the heat distribution of an object through its emitted IR radiation captured by an IR camera. The IR camera captures the IR radiation and displays it through an image array of temperatures also known as an IR image. In breast cancer, IR thermography is utilized to study the surface heat distribution of the breast caused by a metabolically active and highly perfused malignant tumor [112–114]. In the 1980s, IR thermography was cleared by the Food and Drug Administration (FDA) as an adjunct screening tool to mammography [115]. This method is a noninvasive, cost-efficient, and comfortable technique that relies on the thermal signatures obtained from images. Additionally, this method works very well with dense breast tissue and any other tissue density. However, there has been some backlash over the years due to a lack of proper imaging protocols, evaluation procedures, and low thermal sensitive IR technology from previous studies [116–123]. Another name for IR thermography is infrared imaging (IRI) which was adapted after more advanced IR technology and computational methods for breast cancer detection. Current studies have shown great promise in the detection of breast cancer using AI-based methods [123–141], such as machine learning and deep learning, as well as bioheat transfer-based computational methods [142–156], such as inverse heat transfer modeling and physics-based AI. The AI-based methods have been

able to utilize larger clinical data to test the efficacy of IRI, but variability in sensitivity and specificity suggest further testing is needed. This is the same for the bioheat transfer-based computational methods as there have been very few that have applied their methods to clinical data. The work by Gonzalez-Hernandez et al. [150], Recinella et al. [149] and Perez-Raya et al. [144] have shown great promise in the detection of breast cancer using this method with clinical IR temperatures.

## 1.6 Conclusion

Breast cancer is a complex disease that has taken the lives of over 600,000 women and effecting millions of lives each year. Early detection of breast cancer is the key to helping save lives, but the current screening paradigm has further to evolve. Although mammography is the gold standard for screening of breast cancer, the added difficulty imaging patients with dense breasts has shown the importance of adjunctive screening. However, the current methods also need further enhancements to improve the sensitivity and specificity for better detection of breast cancer. Additionally, the current modalities have been shown to be uncomfortable for many women due to their invasive nature or pain provoking methods that are utilized for imaging. Last, there is a need for a modality that can surpass the additional challenges added on by tumor size, tumor position, and cancer type. Infrared imaging shows great promise in answering the issues established by the current screening paradigm as it is a noninvasive and comfortable modality that does well in imaging dense breast tissue. However, further investigation is needed on the efficacy and the detectability of breast cancer for IRI-based methods.

## Chapter 2: Background

This chapter covers the literature background in the research areas of IR thermography (Section 2.1), bioheat transfer modeling (Section 2.2), and inverse heat transfer modeling (Section 2.3). Sections 2.4 and 2.5 cover the research needs established from the literature and the objectives the current work aims to meet based on the research needs, respectively.

### 2.1 Infrared Thermography of Breast Cancer

Infrared (IR) thermography in breast cancer is a noninvasive and cost-efficient imaging modality that relies on the surface temperature captured by an IR camera. An IR camera captures the thermal radiation emitted by an object which then generates an IR image to depict the thermal distribution of the surface of the object [157–161]. Thermography in breast cancer has been studied extensively since the 1950s and has shown great potential in the detection of breast cancer from IR temperatures. However, this method has had various pushbacks due to a lack of clear protocol and inadequate clinical validation. Researchers would associate hotspot regions captured in an IR camera with the presence of a tumor within a breast and develop methods to screen for breast cancer. There has been a current increase of interest in this research area especially after recent IR technological breakthroughs. This section goes over literature in IR thermography including early clinical studies, current state-of-the-art computer aided methods, and imaging protocols utilized in these studies.

#### 2.1.1 Early Clinical Thermography

In the late 1950s, R. N. Lawson, M.D. and his research group was one of the first researchers that investigated the effects of breast cancer on the surface temperature through

temperature measurements [162–164]. The research group saw the potential of utilizing IR thermography, previously developed by the military for surveillance applications, as a means to screen for breast cancer through temperature readings [164,165]. In the early 1960s (1960-1965), researchers started utilizing IR thermography to identify and classify malignancy of breast diseases from the surface temperatures [165–169]. Studies were conducted on patients with cysts, benign tumors, and malignant tumors to understand how the various rises in temperature correlate with the respective disease. Although the results showed that utilizing IR thermography for temperature measurement is an objective process, Williams [169] suggested further investigation was needed to obtain the efficacy of the modality in a clinical setting. Various researchers investigated the use of IR thermography and liquid crystal thermography as potential screening tools. However, many researchers preferred IR thermography due to its better accuracy in measuring temperatures especially after further imaging advancements [164,168,170–176]. Regardless of the method, researchers started to investigate the sensitivity and specificity of thermography in the clinical setting.

Table 5 shows the reported sensitivity and specificity of thermography for various studies conducted from 1961-1972. The sensitivity and specificity of thermography ranged from 25%-100% and 6%-95%, respectively. Prior to 1967, the average sensitivity value was 89% with the minimum and maximum sensitivity values being 66% and 100%, respectively. The average, minimum, and maximum specificity values were 73.4%, 45%, and 93%, respectively. However, the patient sample sizes were relatively small with the highest number of patients studied coming in at 176 patients with 100 cancer cases. From 1967 to 1969, there was an increase in clinical research and patient recruitment to further

conduct studies on the efficacy of thermography. The average sensitivity and specificity values were 76.5% and 74.7%, respectively, due to the findings of Hitchcock et al. [177] who obtained sensitivity and specificity values of 25% and 6 %, respectively. The reason for these low results are suggested to be due to inexperience of the researchers in interpreting the thermography data [178]. Excluding these results from the average obtains a new average of 80.8% for the sensitivity and 83.3% for the specificity. Although the sample size increased to over 4,700 patients, the number of cancer cases was still small in comparison with the maximum cancer cases coming in at 250 for a sample size of 3518. Then in 1970-1972, the average sensitivity and specificity values of 78.3% and 74.2%, respectively, were obtained, but with only one research group having a decently sized sample size and cancer cases. This research group was led by Isard et al. [179] who conducted screening on 10,055 patients with 300 patients having cancer. This research group was well experienced with thermography and their findings accumulated from their 1969 work [174]. The overall sensitivity and specificity for 1961-1972 was 80.3% and 73.1%, respectively. This showed that the thermography in this time period was comparable to the sensitivity and specificity values for mammography, ultrasound, and MRI shown in Table 3.

Table 5. Sensitivity and specificity of thermography from 1961-1972 literature.

Author	Year	Sample Size	Cancer Cases	Sensitivity	Specificity
Williams et al. [167]	1961	100	57	95%	74%
Williams [169]	1964	176	100	95%	-
Brasfield et al. [180]	1965	150	38	66%	45%
Swearingen [181]		100	19	100%	80%
Notter et al. [182]	1966	154	56	98%	-
Harris [183]		100	60	89%	-
Gershon-Cohen [184]	1967	4,000	200	94%	75%
Hoffman [185]		1,924	24	75%	93%
Wallace [178]	1968	4,413	130	87%	-
Hitchcock et al. [177]		2,523	4	25%	6%
Wallace and Dodd [186]		565	69	87%	81%
Haberman [178]		510	32	84%	82%
Madsen [178]		173	8	75%	-
Seaman [178]		-	80	79%	-
Dodd et al. [187]		1969	4,726	195	85%
Lilienfeld et al. [188]	3,518		250	72%	80%
Isard et al. [174]	2,696		76	72%	-
Draper and Jones [189]	304		38	68%	86%
Williams [190]	300		167	92%	80%
Jones and Draper [191]	1970	170	60	82%	69%
Nathan et al. [192]		97	16	69%	70%
Farrell et al. [193]	1971	126	-	87%	90%
Isard et al. [179]	1972	10,055	306	71%	71%
Nathan et al. [194]		359	34	79%	50%
Davison et al. [176]		193	17	82%	95%

The various researchers shown in Table 5 saw the potential of thermography but suggested that larger clinical studies, better imaging protocols, and better interpretation protocols were needed. The main reason for many of these researchers wanting to continue with thermography has to do with the bioheat transfer advancements that were being conducted by various other researchers. From 1968-1983, researchers C. Gros and M. Gautherie conducted various clinical studies on over 57,000 patients to further investigate breast cancer from a thermal perspective using IR and liquid crystal thermography, and internal temperature measurements [112–114,195–216]. Their research established correlations

between temperature measurements, metabolic activity, tumor doubling time, and high levels of blood perfusion of tumors. Their work highlighted the usefulness of utilizing a thermal approach with thermography to aid in early detection, prognosis, and treatment of breast cancer. In order to answer the need for a large-scale clinical study to investigate the efficacy of thermography, the breast cancer demonstration project (BCDP) was established by the American Cancer Society and the National Cancer Institute [217,119,120]. In the BCDP, over 280,000 patients were screened for breast cancer using various screening methods including thermography and mammography. The study lasted for about 9 years from 1973-1981 with 29 health centers participating in the study, resulting in over 4443 breast cancers detected. However, thermography was pulled from the study after 5 years due to low performance and many centers being unprepared to screen with thermography [119,120]. Many researchers had to be trained in utilizing thermography, which led to inconsistent testing and resulting in poor outcomes. Following these outcomes resulted in thermography having a poor reputation within the medical community and being seen as an inaccurate modality [218,219]. However, many other researchers saw that the negative results should not influence the future of thermography and saw the opportunity to come up with better criteria for interpreting thermography [220,221]. Additionally, others looked into the future of utilizing computational techniques to further improve the accuracy of the modality [222,223]. In 1982, the FDA approved thermography as an adjunct to mammography and has since been recommended it as an adjunctive breast cancer screening modality [224,225].

Various technological advancements gave tools to researchers to further investigate the use of thermography as screening and diagnosis tools. After the 1990s, researchers leaned away

from liquid crystal thermography and towards IR thermography due to all the technological advances in IR technology. One of the advancements comes in terms of improving detector array through decreasing the pixel pitch, which determines the pixel resolution of the IR image [226–229]. Over the years, it was observed that the pixel pitch of IR detector arrays have decreased from 30  $\mu\text{m}$  in 2000 to about 5  $\mu\text{m}$  in 2020 for mid-wave IR sensors [157–161]. This has given pixel resolutions to go from 64 x 64 pixels to 1280 x 1024 pixels with advancements coming out with 2000 x 2000 pixels. In addition to increasing pixel resolution, the thermal sensitivity of IR cameras has increased consequently. The thermal sensitivity of an IR camera is measured through the noise equivalent temperature difference (NETD) which is the lowest temperature difference that can be captured above a certain noise level [157,158,227,228]. In the early 1970s to late 1980s, the thermal sensitivity of IR cameras was 100 mK and above [116,118,120,161,228]. This highly improved starting in the mid-1990s where the thermal sensitivity has gone from 50 mK to 7 mK [116,118,120,230]. Table 6 shows the progression of the IR thermal sensitivity from 1972-2020 with the most current value of 7 mK being achieved by Wang et al. [230]. The first part of the table (1972-2010) was replicated from previous literature on IR thermography [116,118,120]. Current commercial IR camera companies report a thermal sensitivity of <20 mK, such as FLIR and ICI, but do not give the exact value. This leaves this value ambiguous for many researchers but the value of 20 mK is typically taken as the thermal sensitivity of the camera. Due to the success of creating low thermal sensitivity IR cameras, many researchers have developed unique imaging systems to improve imaging of patients. These include the Mammary Rotational Infrared Thermogram (MAMRIT) system

[231,232], three-dimensional infrared imaging (3DIRI) system [233], NoTouch Breast Scan [234], and many other commercial options [118,120,235,236].

*Table 6. Thermal sensitivity progression from 1972-2020, adapted from [116,118,120].*

<b>IR Camera</b>	<b>Year</b>	<b>Thermal Sensitivity [mK]</b>
AGA 750	1972	230
ISI Videotherm	1980	150
Inframetrics 500M	1987	100
Inframetrics 600M	1995	50
Amber PM	2000	39
FLIR A8300	2005	20
FLIR SC 6000	2010	<20
T2SLS Qmagiq	2020	7

### 2.1.2 Computer Aided Thermography

In addition to advancements in IR technology, a variety of computational methods were being developed in conjunction with the newly developed imaging systems. The reason for these computational methods was to conduct more efficient interpretation of the thermal patterns observed in IR images. Thermography techniques often relied on an individual to observe and inspect the thermal patterns on the breast surface generated by an anomaly. In breast cancer, breast tumors generate heat due to their metabolic activity and highly perfused vasculature, which affects the heat distribution on the breast surface [112,114,215,237]. Researchers have recognized this phenomenon and have developed techniques to identify these thermal patterns associated with breast cancer through image features. Various review and survey papers have been conducted by researchers in various fields that studied breast cancer detection with IR thermography through a variety of computational techniques [116,118–124,131,134,148,236,238,239]. Artificial intelligence (AI) has played a major role in the advancement of infrared imaging as an adjunctive screening modality through traditional machine learning-based and deep learning-based

methods [109,239–241]. These methods have been utilized for either image segmentation and enhancement or classification for screening. Traditional machine learning-based methods include classification techniques such as support vector machines (SVM), genetic algorithms (GA), artificial neural networks (ANN), and many other techniques. Deep learning-based methods include convolutional neural networks (CNN), generative adversarial networks (GAN), transfer learning models, as well as other methods. A brief literature search of scientific publications that utilize AI-based methods in IR thermography from 2019-2023 was conducted [109,118,121–125,127–142,148,153,236,238,239,241–322]. Figure 9 shows the results of conducting the search when a limit is set on the search to the first five pages in a scientific publication search engine. As the figure shows, there has been an increase in the number of scientific publications since 2019 and it is expected to continue rising. IR thermography can be separated into steady-state, or static, and dynamic thermography. In static thermography, patients are imaged once after an acclimation time so that the body reaches a steady-state temperature with the environment. In dynamic thermography, a cold stress is applied to the body and the effect over time is captured by multiple IR images [118]. Thermography datasets such as the DMR dataset [323] and DBT-TU-JU dataset [324] have been developed over the years. These datasets have been utilized in almost all AI-based methods and are the main source of training and validation for many AI models. For AI models to detect the features that best correlate with malignancy, it is trained using ground truth data which in many cases is through the DMR and DBT-TU-JU datasets. These datasets come with IR images and labels indicating which patients have proven breast cancer, as well as

which breast tumor is located in. The DMR and DBT-TU-JU datasets contain 1062 and 1100 IR images in patients in the upright position, respectively.

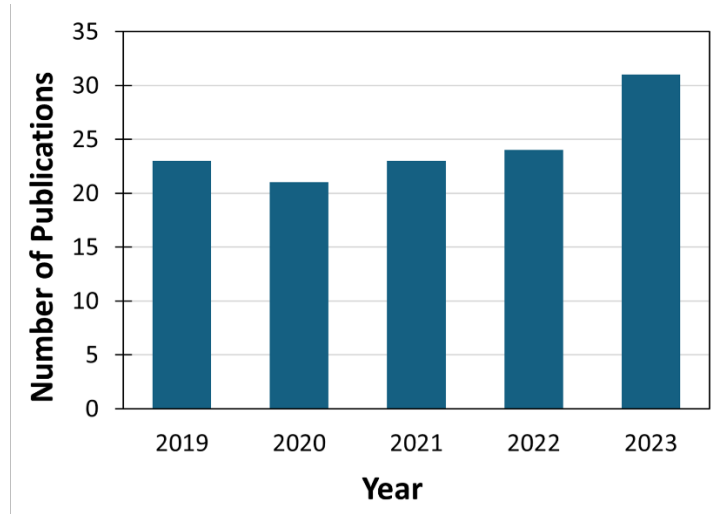


*Figure 9. Number of scientific publications related to AI-based methods utilized for IR thermography for breast cancer detection.*

There are various machine learning-based methods that have been utilized for breast cancer detection using IR thermography. Resmini et al. [294] showed the use of dynamic and static IR thermography to create a hybrid computational method to detect the presence of breast cancer. The dynamic data was used in feature computation through a K-means unsupervised learning algorithm in conjunction with a K-star supervised classifier. Then, an additional cancer diagnosis feature used a genetic algorithm (GA) and support vector machine (SVM) to classify if the breast had cancer or not. The results of this study showed that their technique was able to obtain a sensitivity and specificity of 94.61% and 94.87%, respectively, using IR thermography. The researchers further improved their diagnosis algorithm to an accuracy of 97.8% and tested on both the DMR and UFPE datasets [293]. Hossam et al. [325] developed a technique that performs automatic segmentation of the breast from IR images and detects breast cancer from a region of interest (ROI). The

automatic segmentation method uses color intensity and edge detection to segment the breast. The method then detects the ROI on the segmented breast using a Hough transform algorithm and increases the contrast of detected boundaries of the ROI. The features of the ROI were used as inputs into two classifiers, an SVM classifier and an Artificial Neural Network (ANN) classifier, to predict the presence of a tumor. The results showed that the accuracy of the SVM classifier was 96.7% while the accuracy of the ANN classifier was 96.1% in comparison. Sathish et al. [313] trained a classifier for breast cancer detection using asymmetry features caused by the tumor and captured in the IR images. Temperature values rather than pixel intensity values were used to perform normalization, preprocessing and segmentation. The workflow consisted of extracting features from segmented images using sequential floating forward feature selection, random subset feature selection, and GAs. These features were used to train a SVM Gaussian classifier on normalized images which produced a classification accuracy of 91%. These methods showed the use of machine learning-based classification techniques to detect the presence of breast cancer using IR images.

In deep learning-based methods for breast cancer detection with IR thermography, classification is conducted using convolutional neural networks (CNN), as these techniques are well suited for image-based data. The work by de Freitas Oliveira Baffa and Grassano Lattari [326] utilized CNN with IR images for breast cancer detection through binary classification (healthy or unhealthy/sick). The researchers conducted nine tests on the DMR dataset (2 for static and 7 for dynamic) and compared their results with other studies that utilized the same dataset with traditional machine learning-based classification. The overall performance of their network showed an accuracy of above 95% on the static

dataset, which performed better than the other methods, and above 92% on the dynamic dataset. Fernández-Ovies et al. [321] conducted binary classification on the DMR dataset by applying transfer learning on well-established state-of-the-art CNNs: (i) ResNet18, ResNet34, ResNet50 and ResNet152 [327], and (ii) Vgg16 and Vgg19 [328]. The method considered 5 testing sets and 1 blind validation test, where the Resnet architectures achieved accuracy values of 97.5% and above for all tests. The studies conducted in [326] and [321], utilized augmentation to the IR images to balance and increase the dataset for training, testing, and validation. Farooq and Corcoran [308] utilized the state-of-the-art pre-trained CNN InceptionV3 [329] for binary classification with the DMR dataset. This CNN utilized the pre-trained weights and retrained only the last layer to obtain an accuracy of 80% and the sensitivity of 83.33% for validation.

Further studies have been conducted to improve the use of CNNs on the DMR dataset. Yadav and Jadhav [266] worked on finding the optimal tuning parameters and augmentation method to improve the accuracy of Vgg16 and InceptionV3. The study showed that fewer augmentation, keeping the last convolutional layer unfrozen, and having a learning rate of 0.005 obtained the best accuracy of 98.5% for InceptionV3. Gonçalves et al. [279] investigated using bio-inspired meta-heuristic algorithms (GA and particle swarm optimization) to find the optimal architecture and tuning parameters. The researchers aimed to improve the F1-scores of Vgg16 (from 0.66 to 0.92) and ResNet50 (from 0.83 to 0.90) using GA while maintaining an accuracy of around 91.6%. Tiwari et al. [290] focused on the input data by utilizing the multi-view IR images instead of one view that is typically used from the DMR dataset on pre-trained CNN. The researchers found that the multi-view IR images increased the accuracy from 93% to 98% for static

images, and 94% to 99% for dynamic images when compared to only using the frontal view. Sánchez-Cauce et al. [291] also worked on a multi-input CNN by studying the effect of multi-view IR images, and a combination of IR images with patient and clinical text data as the inputs. The researchers found that utilizing multi-view IR images further enhances the CNN accuracy when compared to using only one view, but further studies are needed on utilizing a combination of IR images and text data. Additionally, there have been studies by Araujo et al. [262,285] have shown the use of IR thermography as a monitoring technique for breast cancer treatment. Their work consisted of an AI-based method with IR images to assess the effects of treatment on breast cancer. This shows the novelty of utilizing IR thermography to study breast cancer and its ability to be utilized in treatment and detection. Although these studies show great promise on the use AI with IR thermography for breast cancer detection, the lack of large datasets make it difficult to conduct unbiased studies without the use of augmentation.

## 2.2 Bioheat Transfer in Breast Cancer

Techniques that move away from the classification and feature-based approaches with IR thermography are numerical methods that utilize bioheat transfer modeling. In the context of this work, IR imaging (IRI) is utilized instead of IR thermography to differentiate between bioheat transfer approaches described in this section and the empirical methods described above. Malignant breast tumors have high metabolic activity and are highly perfused which alters the temperature distribution on the breast surface [112,114,215,237]. Various works have investigated the thermal characteristics of breast cancer and their effect on surface temperatures. These factors have been modeled as heat sources, thermal properties, and thermal parameters through bioheat transfer modeling using models such

as the Pennes' bioheat equation [330]. The Pennes bioheat equation has accurately reproduced the experimental thermal response in breast cancer [116,118,120,148,151]. It accounts for the metabolic heat generated within the tissue and the heat transfer between the tissue and the blood flow. This section goes over the various bioheat models (Section 2.2.1), the thermal characteristics of breast cancer (Section 2.2.2), bioheat transfer modeling using breast geometries (Section 2.2.3), and parametric studies of bioheat transfer models for breast cancer (Section 2.2.4).

### 2.2.1 Bioheat Transfer Models

Thermal modeling is the process of creating an analytical model of a system using the fundamental laws of thermodynamics and heat transfer through experimentation or known theory. This modeling process can be implemented in biological systems as all living things are governed by these same laws. There have been various models that have tried to study and incorporate the complex system of the human body or of a particular organ [142,151,331–334].

In 1948, Bazett et al. [335,336] explored the temperature of blood flow inside of a person as well as external parameters that affect the cooling of the system through invasive measurement tools. The authors concluded that the temperature in the limbs is not constant, or uniform, regardless of external conditions. In the same year, Pennes [330] conducted thermal experiments on the forearm of various individuals establishing the effects of perfused tissue and blood flow on the heat transfer within the forearm. From his results, the Pennes' bioheat equation was developed which has played a major role in bioheat transfer modeling. Pennes' bioheat equation is as follows:

$$\rho_t c_t \frac{\partial T_t}{\partial t} = \nabla \cdot (k_t \nabla T_t) + \rho_b c_b \omega_b (T_a - T_t) + q_m \quad (3)$$

where  $\rho$  is density,  $c$  is the specific heat,  $T$  is temperature,  $t$  is time,  $k$  is the thermal conductivity,  $\omega_b$  is the blood perfusion rate, and  $q_m$  is the metabolic heat generation rate, while the subscripts  $t$ ,  $b$  and  $a$  stand for tissue, blood, and artery respectively. In 1961, Wissler [337] incorporated Pennes' bioheat equation to model the heat transfer within the human body by modeling the human body as multiple cylinders with blood vessels. His model aimed to incorporate the effects of the blood vessels within each cylindrical body part. However, due to the simplicity of the model it was not the most accurate way to model the heat transfer within the body especially as more available thermal information was being available from experiments. Throughout the 1960s various researchers studied the thermal properties of tissues, blood vessels, and diseases through experiments with tools such as IRI to understand their significance in the heat transfer within the body [165,169,195–197,338–341]. Seeing the need for a more accurate model that incorporates the effect of the blood vessels Wulff [342] replaced the blood perfusion term  $\rho_b c_b \omega_b (T_a - T_t)$  by a convective term  $\rho_b c_b U_h \nabla T_t$ . In this mode,  $U_h$  is the local mean blood velocity in the capillaries which adds to the complexity of the system. This model was proven to be an inaccurate representation as the author assumes the blood and tissue are at equilibrium at the capillary level. Studies by Priebe and Betz [341], Draper and Boag [173], and Gautherie et al. [202] a few years prior proved that this was not the case through experimentation.

Chen and Holmes [343] developed a model that incorporated both the blood perfusion term and convective term as well as a diffusion term due to the blood perfusion  $\nabla \cdot (k_p \nabla T_t)$ ,

where  $k_p$  is the thermal conductivity due to blood perfusion. Their model utilized a thermal equilibrium assumption at medium sized blood vessels with diameters of 50-300  $\mu\text{m}$  instead of the capillaries. Also, their model assumed that the arterial temperature  $T_a$  was not the core temperature but instead the temperature of the arterial blood in the largest artery. Some researchers split the blood and tissue thermal interaction into a model called the two-compartment bioheat transfer model. These models divided the domain into sub-domains with the tissue making up one of the domains and the blood making up the other domain [151,331,334]. Xuan and Roetzel [344] proposed a model that considers the heat exchange between the tissue and blood vessels as a porous medium. Their model is as follows:

$$(1 - \varepsilon)\rho_t c_t \frac{\partial T_t}{\partial t} = \nabla \cdot (k_t \nabla T_t) + h_{tb}(T_b - T_t) + (1 - \varepsilon)q_m \quad (4)$$

$$\varepsilon\rho_b c_b \left[ \frac{\partial T_b}{\partial t} + \mathbf{u}_b \cdot \nabla T_b \right] = \nabla \cdot (k_b \nabla T_b) + h_{tb}(T_t - T_b) \quad (5)$$

where  $\varepsilon$  is the porosity,  $T_b$  is temperature in the blood,  $h_{tb}$  is the local volumetric heat transfer coefficient, and  $\mathbf{u}_b$  is the blood flow velocity. The blood flow velocity  $\mathbf{u}_b$  may be obtained through experimental measurements, the continuity and Navier-Stokes equations, or any other means. An extension of the Chen and Holmes and two-compartment models was developed by Weinbaum et al. [345,346] who suggested a three-compartment model in order to capture the complex heat transfer interaction between the tissue, arterial blood, and venous blood sub-domains. This model splits up Eq. 5 into two equations to model the arterial blood temperature  $T_{ar}$  and venous blood temperature  $T_{vn}$ . In addition, the convective heat transfer interaction between the tissue and blood  $h_{tb}(T_b - T_t)$  is split into

two to model the interaction between the tissue with the arterial blood  $h_{t-ar}(T_{ar} - T_t)$  and the tissue with the venous blood  $h_{t-vn}(T_{vn} - T_t)$ . These terms are also incorporated in the additional blood temperature equations in the appropriate heat flow direction. Last, the heat exchange between the arterial blood and venous blood is modeled with the term  $h_{ar-vn}(T_{ar} - T_{vn})$  which is added to the blood temperature equations in the appropriate heat flow direction.

Following these models, various researchers aimed to further model the thermal interaction between the tissue and blood vessels through additional terms, assumptions, and geometric interpretations. In 2008, Nakayama and Kuwahara [347] suggested adding the perfusion effects to the three-compartment models in order to better model the countercurrent heat exchange from the vessels and the heat transfer towards the skin surface. These perfusion effects were added through perfusion terms due to the arterial blood  $\rho_b c_b \omega_{ar} T_{ar}$  and venous blood  $\rho_b c_b \omega_{vn} T_{vn}$  phases, where  $\omega_{ar}$  and  $\omega_{vn}$  are the arterial and venous blood perfusion rates, respectively. Additionally, these perfusion effects were incorporated in the tissue phase through the perfusion term  $\rho_b c_b \omega_{ar}(T_{ar} - T_{vn})$  with the counter current assumption that  $\omega_{ar} = -\omega_{vn}$ . This led to various researchers conducting further testing and modeling of more complex systems. Mahjoob and Vafai [348] later developed a more complex model with analytical solutions for dual layer biological media in relation to porous-media theory. The authors derived their models for two types of dual layer geometric models, an isolated boundary model and a uniform core temperature model. The goal of their model was to obtain better representation of the thermal interactions between the tissue and blood through the appropriate boundary conditions. Although their work showed great promise in developing an accurately simplified model, they did not test their

models against any experimental data. Wang and Fan [349] conducted a study on both the continuum, or mixture theory, and porous-media bioheat transfer models to identify their characteristics and discuss fundamental theories based on their involvement with a macroscopic model. The authors concluded that both models take advantage of simplicity, but do not offer connections between microscale and macroscale properties and they do not accurately model the blood and tissue interaction. The porous-media models have recently overcome these issues, which points in the direction of developing a closure theory for these equations. A current mode by Wang et al. [350] has shown the ability to model the effects of blood flow utilizing the porous-media models in the hand and foot provided the vasculature structure. Their work shows the ability to utilize known vasculature geometries with models described above to show the thermal effects of the vessels.

Another important model that aimed to improve the complex bioheat modeling of the vasculature in organs was the coupled continuum-discrete (CCD) model developed by He and Liu [351]. The CCD model utilized the concept of modeling the various vascular from Eqs. 4 and 5 while extending the heat transfer contribution of any available size vessels. This was conducted by incorporating additional heat sources contributed by large visible vessels, small visible vessels, and invisible vessels through the following:

$$\hat{\rho}_t c_t \frac{\partial T_t}{\partial t} = \nabla \cdot (\hat{k}_t \nabla T_t) + Q_{tl} + Q_{ts} + Q_{tc} + \hat{Q}_m \quad (6)$$

$$\rho_b c_b \left[ \frac{\partial T_b}{\partial t} + \frac{q_b}{A_b} \frac{\partial T_b}{\partial l} \right] = k_b \frac{\partial^2 T_b}{\partial l^2} + Q_b + Q_m \quad (7)$$

$$\frac{\partial A_b}{\partial t} + \frac{\partial q_b}{\partial l} = 0 \quad (8)$$

$$\frac{\partial q_b}{\partial t} + \frac{\partial}{\partial l} \left( \frac{q_b^2}{A_b} \right) + \frac{A_b}{\rho_b} \frac{\partial p_b}{\partial l} = - \frac{K}{A_b} q_b \quad (9)$$

where  $\hat{\rho}_t$ ,  $\hat{k}_t$  and  $\hat{Q}_m$  are the volume average tissue density, thermal conductivity and metabolic heat generation, respectively,  $Q_{tl}$ ,  $Q_{ts}$  and  $Q_{tc}$  are the thermal interactions from blood to tissue due to large visible vessels, small visible vessels and invisible vessels, respectively,  $q_b$  is the blood flow flux,  $A_b$  is the vessel tube cross-sectional area,  $l$  is the direction of the vessel along the centerline,  $Q_b$  is the thermal interaction between tissue and blood for large and small visible vessels,  $p_b$  is the blood pressure, and  $K$  is the flow parameter. The authors used their developed parallel alternating direction explicit finite difference method [352] to obtain numerical solutions for the 3D thermal-transport equations (Eqs. 6 and 7), and 1-D transport equations (Eqs. 8 and 9). Validation of the CCD model was performed on a liver model domain reconstructed from MRI data where they were able to evaluate the thermal effect of the liver vasculature and a tumor heat source. A comparison study was conducted between the CCD model and the Pennes' bioheat model to understand the difference in the thermal profile. Figure 10 shows the thermal distribution in the liver for Pennes' bioheat model (A-C) and the CCD model (D-F). As the figure shows, the CCD model provides a more complex thermal profile due to the different levels of vasculature. Although this is a detailed profile that includes various levels of vascularity, the thermal interaction between the capillary flow and interstitial solid region. Tang et al. [353] conduct a study on a model that incorporates the models discussed above but also incorporates thermal interactions in the microvasculature level. The microvasculature, or microcirculation, system involves the transport between the capillaries and the interstitial space made up of interstitial fluid [354]. This then changes the transport equations to

incorporate fluid flow in both the blood and the interstitial space. Although this method allows for bioheat transfer modeling of organs, tissue, blood vessels, and microvasculature, there have not been many models that incorporate all these concepts into one model. This is due to the high level of modeling complexity that also increases the numerical and computational complexity needed to solve these types of problems. Furthermore, it can be difficult to obtain the vasculature structure, let alone the organ structure of most body parts.

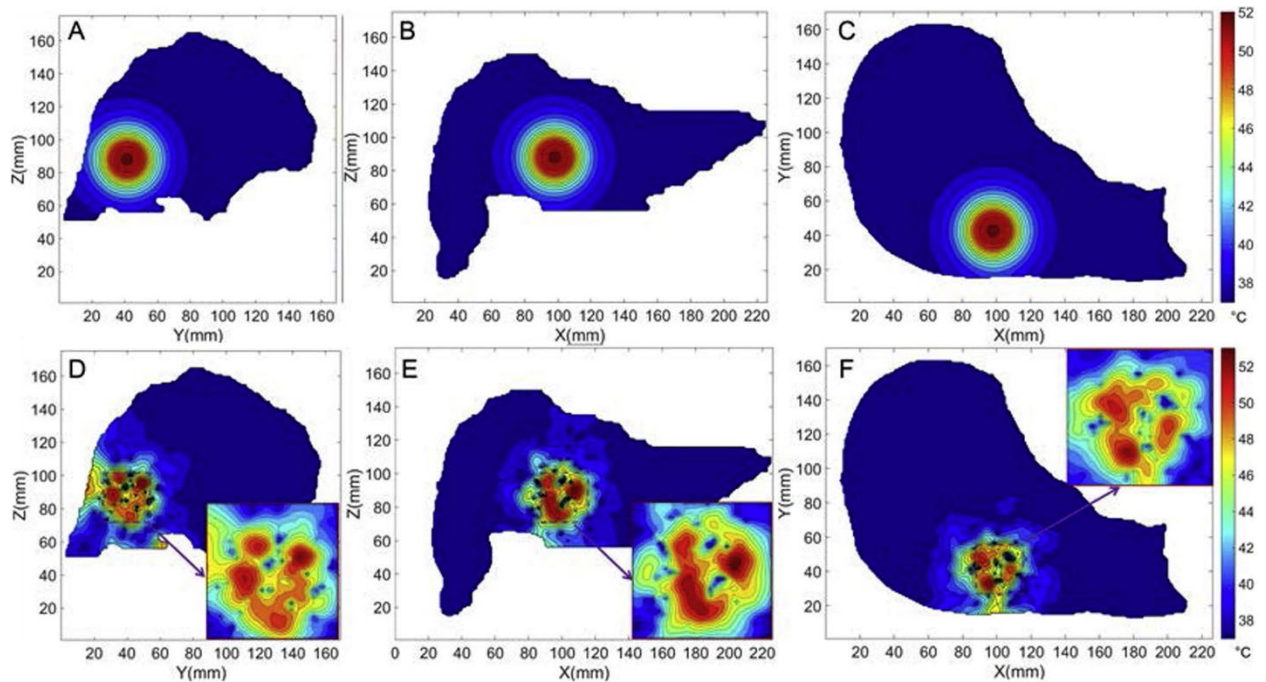


Figure 10. Thermal profiles of the liver obtained using (A-C) Pennes' bioheat model and (D-F) the CCD model from He and Liu [351].

Although all these models can model the bioheat transfer of different regions of the body, Pennes' bioheat model has shown to adequately model the overall bioheat transfer. For this reason, many researchers have preferred to use it as its simplest form or through a higher level of simplicity while holding true to the model. One of the simplified models that aimed to achieve this has been the effective thermal conductivity bioheat model developed by Weinbaum and Jiji [355]. Effective thermal conductivity models have been utilized in

various applications such as in nanofluids modeling [356,357], porous media modeling [358–360], two-phase material modeling [361], multiphase composite materials [362], and heterogenous materials [363]. The effective thermal conductivity is obtained through Fourier’s law of conduction in an elementary control volume such that the total heat flux is given by:

$$Q_T = k_{eff} A \frac{\Delta T}{L} \quad (10)$$

where  $Q_T$  is the total heat,  $k_{eff}$  is the effective thermal conductivity,  $A$  is the cross-sectional area of the elementary control volume perpendicular to the direction of the heat flux,  $L$  is the length of the elementary control volume in the direction or opposing the heat flux, and  $\Delta T$  is the total change in temperature in the elementary control volume. Weinbaum and Jiji [355] utilized this concept to model the heat transfer from the tissue and blood vessels into the following model:

$$\rho_t c_t \frac{\partial T_t}{\partial t} = \nabla \cdot (k_{eff} \nabla T_t) + q_m \quad (11)$$

$$k_{eff} = k_t \left( 1 + \frac{n\pi^2 R^2 k_b^2 Pe^2}{4\sigma k_t^2} \right) \quad (12)$$

$$Pe = \frac{2\rho_b c_b \omega_b(x, y, z)}{k_b} \quad (13)$$

where  $n$  is the total number of vessels crossing each other in a unit surface area in a given geometry,  $R$  is the vessel radius,  $\sigma$  is a shape factor relating the cross-section of the given geometry, and  $Pe$  is the dimensionless Peclet number. This gives the effective thermal conductivity to be rewritten as  $k_{eff} = k_t [1 + f(\omega_b, \sigma)]$ , where  $f(\omega_b, \sigma)$  is function that

depends on the local blood perfusion rate  $\omega_b$  and local vasculature structure  $\sigma$ . Another version of this model was developed by Rojas-Altamirano et al. [359] for a tissue domain that was assumed to be a porous medium. Their effective thermal conductivity model incorporated the structure of their porous medium tissue domain. This was done by including the pore size and fractal scaling method in order to conduct numerical simulations using the Monte Carlo simulation method [364–366]. Both these effective thermal conductivity models showed the possibility to utilize an accurately simplified model given some information on the vasculature structure within a tissue domain. The issue is that this information is crucial for the model and cannot be modeled otherwise.

### 2.2.2 Thermal Characteristics of Breast Cancer

In 1956, Lawson [162] conduct a study on 26 patients with proven breast cancer where temperature measurements were taken of the breast with cancer and the contralateral healthy breast. Temperature measurements of the surface using thermocouples were taken near the tumor and at a mirroring location within the contralateral breast. The author reported that the average, maximum, and minimum rise in temperatures due to the presence of a tumor were found to be 2.27 °C, 3.5 °C, and 1.3 °C, respectively. This lead Lawson and Chugtai [165] to further investigate the thermal effects of breast cancer on the breast surface and its correlation to tumor malignancy. on additional women with proven malignant and benign tumors. The authors found that patients with malignant tumors had an average temperature increase of 2 °C while patients with benign tumors had an average temperature increase of 0.19 °C. This showed the potential of utilizing surface temperatures to determine malignancy and the presence of breast cancer. In the late 1960s, researchers were showing the potential in utilizing IRI to obtain the thermal properties of human tissue

and saw potential in extending this work to breast cancer [195–197]. Also, some researchers were showing that an increase in vascularity appearing in a thermogram was a secondary indicator of the presence of breast cancer [339,340,367]. This increase in vascularity was due the tumor and its microenvironment generated through tumor angiogenesis feeding from the surround blood vessels [44,368,369]. This led researchers to investigate the thermal characteristics of breast tumors that influenced the thermal profiles captured in IRI through heat transfer experiments in live tissue.

One researcher that was able to conduct various experiments on patients and obtain numerous amount of insight on the thermal characteristics of breast cancer was Gautherie [112–114]. He conducted a 16-year-long clinical and fundamental study to find thermopathological correlations of breast tumors using IRI and thermal experiments. In the study, 85,000 symptomatic women were recruited for mass screening where all patient information and history were obtained. Each patient underwent physical, thermographic, and mammographic examinations as well as additional testing and surgeries when prompted. In the patient group, there were approximately 6,600 diagnosed breast cancer cases which were treated by specialists. Any patients with a benign diseases or flagged abnormality by any of the examinations were carefully monitored and reexamined periodically. Some of the patients with cancer (418 cases) were selected for further testing that consisted of in situ internal thermal measurements of the breast, or intramammary thermal measurements. These patients were separated into three groups with each group going through tumoral and peritumoral thermal measurements but at specific procedures. The first group with 236 cases went through a single series of measurements before obtaining any treatment. The second group with 128 cases went through multiple

measurements to capture the natural evolution of the cancer. This group went through this procedure due to patients either refusing treatment or having external factors that prevented them from obtaining treatment. The last group with 54 cases went through multiple measurements while going through treatment to study the effect of treatment on the thermal measurements. The tumor sizes for the 418 cancer cases were in the Tis, T1, or T2 stages and ranged from 0.6 cm to 4.1 cm.

The thermal measurements were conducted in the breast with cancer and the contralateral healthy breast using a sterile 0.8 mm diameter fine-needle thermoelectric probe. Due to the low thermal capacity of the needle, there was no disruption in measurements which was further proven through histological studies and experimentation on rheoelectrical phantom models. These models were hemispherical breast models that mimicked the breast structure, thermal characteristics, external heat exchange, and vascularity as seen in breast cancer. The thermal measurements were implemented through an ethical clinical agreement and were limited by the length and fragility of the needle. Patients were given local skin anesthesia and measurements were taken at approximate symmetrical locations in both breasts. The measurements were taken about every 5 mm interval for a maximum depth of 65 mm, the probe length. Two types of thermal measurements were obtained in each patient: temperature measurements and effective thermal conductivity measurements. The temperatures of the tumor were shown to be significantly higher than the venous and arterial blood temperatures in each patient case. The effective thermal conductivity  $\lambda_e$  considers both the tissue conduction and the convection due to capillary vessels, assuming the heat flow is isotropic. Both in vivo and in vitro  $\lambda_e$  measurements were taken of each breast (cancerous breast and healthy breast). The values of  $\lambda_e$  was dependent on the breast

density which was classified into three categories: fat, fibrous, or glandular. Table 7 shows the values recorded for the mean values of  $\lambda_e$  for the various breast tissue types in healthy and cancerous tissue obtained in vivo and in vitro. In addition to thermal measurements, the surface temperature distribution of each of patients' breasts were captured using IR thermography and liquid crystal thermography. Thermography was utilized to conduct qualitative analysis on thermovascular patterns on any region of interest on the surface of the breast. Quantitative evaluations of temperature differences in local areas of hyperthermia were also obtained and compared with the contralateral breast.

*Table 7. Mean effective thermal conductivity value of different tissue types measured in both healthy and cancerous breast in vivo and in vitro, replicated from Gautherie [112–114].*

Tissue Type	Healthy Breast [W/m-K]		Cancerous Breast [W/m-K]	
	in vitro	in vivo	in vitro	in vivo
Fat	0.120	0.171	-	-
Fibrous	0.253	0.286	-	-
Glandular	0.322	0.370	-	-
Cancerous	-	-	0.280	0.511

Figure 11 shows some of the thermal measurement results for all three groups. Figure 11a shows that the presence of the tumor generated an increase in the temperature and effective thermal conductivity when compared to the contralateral healthy breast. This was shown regardless of the cancer type as results were captured for ILC case and IDC cases. The results showed that the healthy tissue measured temperature gradually increases with the depth into the breast tissue, but a major spike in temperature can be seen when a tumor is present. Similarly, the effective thermal conductivity is approximately constant in a healthy breast while the introduction of a tumor gives an abnormal increase in its vicinity. This increase in effective thermal conductivity value was correlated to an increase of blood supply from the tumor region, or hypervascularization. This is due to the

physiopathological concept that an increase in blood supply from the tumor is due to an increase in metabolism [38,39]. From the second group, the results showed that the distribution in temperature and effective thermal conductivity increased as the tumor grew. Figure 11b shows the progression of a tumor for a patient with lobular cancer for measurements taken about a month apart. As tumor grows to about 20 mm, the effective thermal conductivity value begins to drop in the region inside the tumor. This has to do with larger tumors becoming necrotic and growing in a shell-like manner. Figure 11c shows the measured results from the last group which investigated the effect of treatment on the temperature and effective thermal conductivity. As the results showed, the treatment helped reduce the tumor size and decrease the thermal measurement values. From this study, it was concluded that a tumor can be considered a highly perfused and metabolically active heat source that highly effects the surrounding tissue. The next step was to calculate the metabolic heat production and obtain a correlation from the collected data.

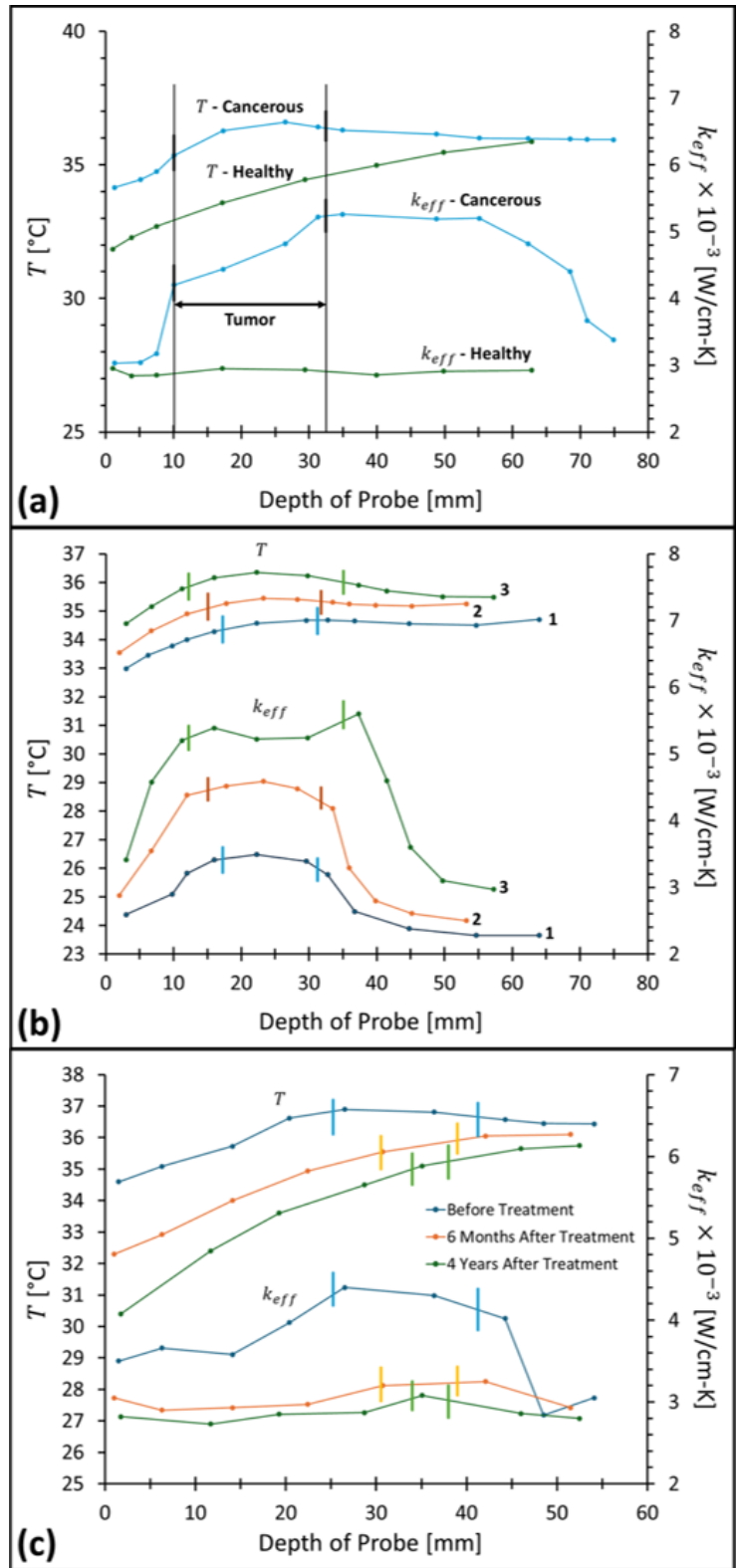


Figure 11. Measured temperatures and effective thermal conductivity for (a) healthy and cancerous breast comparison, (b) tumor progression, and (c) treatment monitoring, replicated from Gautherie [113].

The metabolic heat production ( $q^*$ ) was further evaluated throughout the period of tumor evolution with the rate of growth, the doubling time (DT), and was recorded for 128 patients that had tumor sizes of 0.6-4.1 cm. It was observed that during growth the metabolic heat production changed with the the DT, as shown in Fig. 12. This indicates that the faster a tumor grows, more heat is generated and similarly the slower it grows, less heat is generated. As shown by the figure, the DT ranged from 49-676 days with metabolic heat production going from  $68 - 3.8 \times 10^{-3} \text{ W/cm}^3$ . For fast growing tumors the  $DT \leq 150$  days have a metabolic heat production  $q^* \geq 20 \times 10^{-3} \text{ W/cm}^3$ , and for slow growing tumors the  $DT \geq 250$  days have a metabolic heat production  $q^* \leq 10 \times 10^{-3} \text{ W/cm}^3$ . Also, it was observed that this relationship between DT and metabolic heat production applied to malignant tumors in the range from ~10 mm to 50 mm. This correlation can be a helpful tool to obtaining DT when knowing the metabolic heat production at the time of diagnosis. This shows the ability of utilizing the thermal characteristics of a tumor to provide key information about the tumor such as the size and DT. Additionally, these factors showed the possibility of detecting cancer through a thermal perspective and that thermography may be the key tool to aid in this effort.

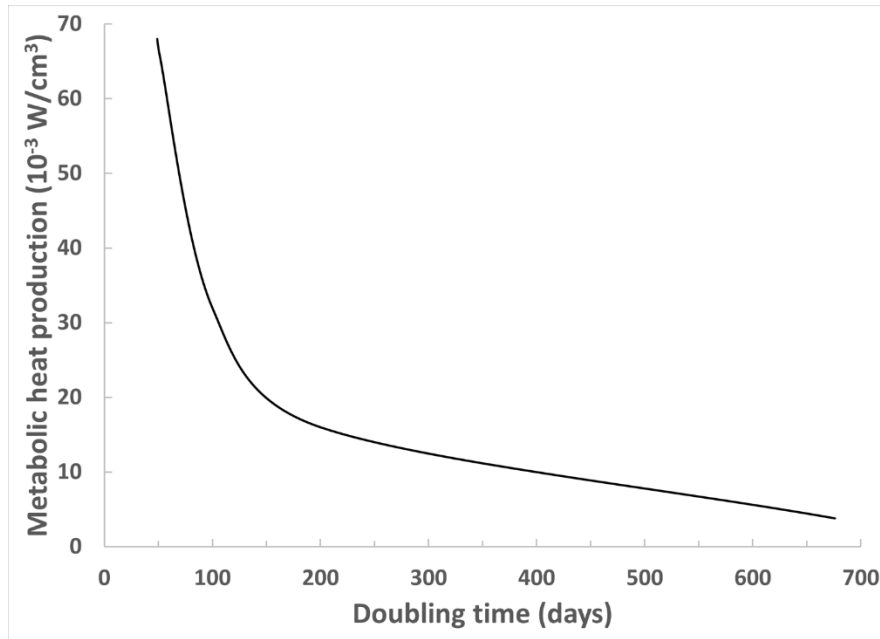


Figure 12. Plot of the hyperbolic law relation between the metabolic heat production and the tumor doubling time, replicated from Gautherie [112–114].

### 2.2.3 Bioheat Transfer Studies in Different Breast Geometries

Utilizing the thermal characteristics of metabolically active highly perfused malignant tumors and the aiming to conduct noninvasive studies, encouraged researchers to conduct bioheat transfer modeling of breast cancer. Bioheat transfer modeling of breast cancer has been studied extensively with the use of computational methods, Pennes' bioheat equation, and various types of breast geometry models [116,118,120,142,148,370]. There are two main methods that have utilized for bioheat transfer modeling of breast cancer: finite difference methods (FDM) or finite volume methods (FVM) [334,371] and physics-informed neural networks (PINNs) [372]. There are various commercial and open-source software such as ANSYS Fluent and OpenFOAM, respectively, that utilize FDM and FVM for computational fluid dynamics (CFD) and numerical heat transfer modeling. For physics-based AI modeling through PINNs, in-house algorithms have been developed to conduct various heat transfer problems [144,373,374]. Kandlikar et al. [116] and

Mashekova et al. [148] have conducted in depth literature reviews on the topic of bioheat transfer of breast cancer and have shown that there are three types of breast geometries that have been utilized: (a) idealized, (b) realistic, and (c) patient-specific breast geometries. Further details of each breast geometry type are discussed below.

#### a. Idealized Breast Geometries

The idealized breast geometries are simplified models in the form of hemispherical and cartesian models. These models can be easily generated using any computer aided design software or through any numerical scheme as the important factors of these geometries relate to the size and the placement of the tumors. Figure 13 and 14 show examples of the hemispherical and cartesian models utilized in literature, respectively. There are two types of hemispherical models which are concentric (Fig 13a) and non-concentric (Fig 13b) hemispherical models. The first hemispherical model was developed by Osman and Afify [375] to conduct bioheat transfer modeling in a healthy breast. Their model was a three-dimensional (3D) concentric hemisphere with 4 concentric layers made up of skin and areola layer, fat layer, muscle layer, and core layer, as shown in Fig. 13a. The bottom of the hemisphere was assigned a constant temperature, or isothermal, boundary condition and the top surface was set to a convection boundary condition. The authors utilized a countercurrent bioheat model similar to Wulff [342] which added convective heat transfer terms to model the effects of the thermal exchange between the blood vessels and tissue at the fat and muscle layers. The perfusion rate was modeled as a non-homogenous distribution due to the different layers and thermal exchange. The thermal properties and boundary condition values were obtained from previous studies including experimental studies conducted from Pennes [330] and Keller [376]. The thermal distribution on the surface showed agreement with the temperatures captured of a healthy with an IR camera.

The authors extended their work to model breast cancer utilizing values obtained from Gautherie's experiments [377]. Their results showed good agreement with experimental data and their model was able to capture the effect of the different layers on the temperature distribution. However, the addition of layers created a non-homogeneous distribution with larger temperature gradients near the surface. Furthermore, the assumptions made on the bioheat transfer model added to the to the uncertainties of utilizing this concentric model for breast cancer as there was a lot of debate on the use of the countercurrent model. Although their model was not as commonly used for bioheat transfer modeling of breast cancer, the boundary conditions, thermal properties, and the hemispherical breast shape were utilized by others. More importantly, their model inspired Sudharsan et al. [378] to develop the non-concentric hemispherical model shown in Fig. 13b. This model reduced the number of layers from 5 to 4 removing the skin layer and added a gland layer that made up the majority of the breast. The authors utilized the same boundary conditions from Osman and Afify [377], but did not utilized the countercurrent bioheat model or the non-homogeneous perfusion rate distribution. Their model has been widely used in various work due to the surface temperature distribution coming in close agreement with available experimental data [379]. However, the symmetric nature of the hemisphere creates symmetric temperature distributions that disagree with the experimental data. The breast is a more complex curved shape than what is depicted in a hemispherical mode. Regardless of this fact, this model has been extensively utilized by various researchers to conduct parametric studies and inverse modeling to better understand the effect of the tumor on the heat transfer within the breast. The parametric studies have shown that the tumor depth and size have the most significant impact on the surface temperature distribution [116,148,380–

382]. Several studies on the effect of the heat transfer coefficient and cold stress on the thermal contrast have aided in obtaining the appropriate boundary condition for the respective IRI case comparison [383].

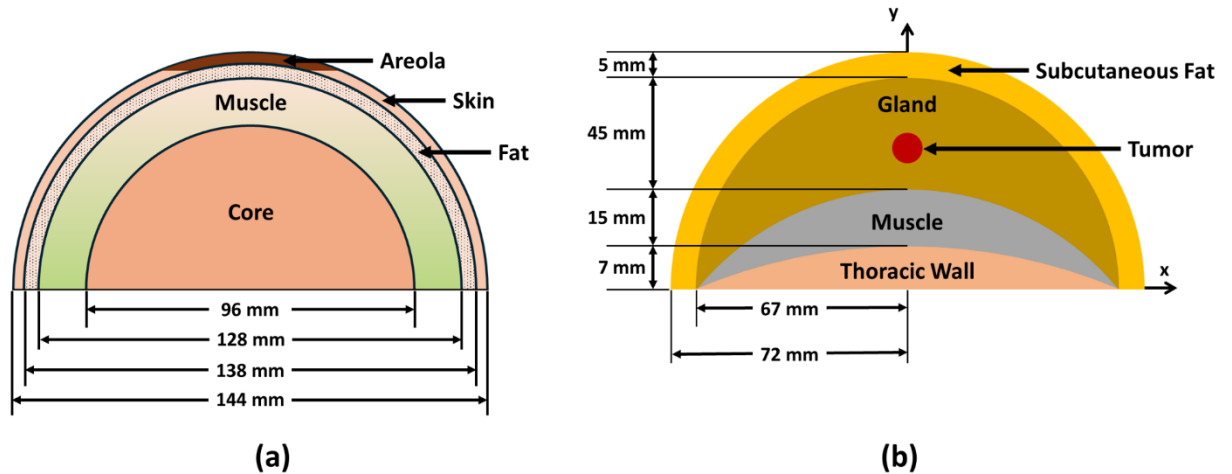


Figure 13. Example (a) concentric and (b) non-concentric hemispherical models developed by Osman and Afify [375] and Sudharsan et al. [378], respectively, and utilized in various literature. Geometries were redrawn and adapted from [116].

The cartesian models are rectangular models with one or more layers. A 2D cartesian model (Fig. 14a) was first developed by Zhang [384] to conduct bioheat transfer modeling of breast cancer using their developed Lattice Boltzmann method. Their model assumed an adiabatic boundary condition at the side walls representing the heat transfer to the connecting tissue, a convective boundary condition at the top wall representing the surface of the breast exposed to the atmosphere, and an isothermal boundary condition representing the constant temperature from the chest wall. The dimensions of the 2D cartesian domain were 10 cm wide by 5 cm long and with the tumor modeled as a square of size 1.25 cm. The author utilized the principles obtained from Gautherie [112–114] to model the tumor with higher perfusion and metabolic heat generation using the a steady-state Pennes’ bioheat equation. Later, Amri et al. [385] developed a 3D cartesian model with two layers

and a spherical tumor. The authors also utilized the steady-state Pennes' bioheat equation but derived the metabolic heat generation value as a function of the tumor diameter based on the findings from Gautherie [112–114]. They utilized the following relationships to obtain the metabolic heat generation in terms of the tumor size:

$$d_t = 0.01 \times \exp[0.00213(DT)] \text{ (m)} \quad (14)$$

$$Q_m \times DT = 3.27 \times 10^6 \text{ (W} \cdot \text{day/m}^3\text{)} \quad (15)$$

where  $d_t$  is the tumor diameter,  $DT$  is the doubling time in days, and  $Q_m$  is the metabolic heat generation. These cartesian models have been utilized extensively in parametric studies and inverse modeling due to their ease of use and computational efficiency [116,148,385,386]. However, they do not give a good representation of the breast shape and have not been validated with experimental data unlike the hemispherical models.

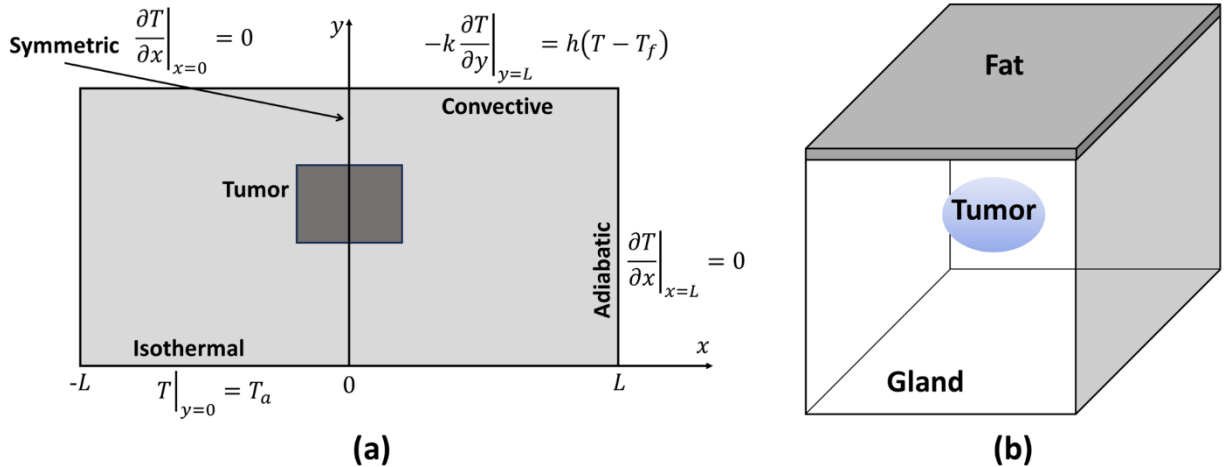


Figure 14. Examples of cartesian (a) 2D and (b) 3D models utilized in literature, redrawn and adapted from [116,118].

#### b. Realistic Breast Geometries

In response to the need for more accurate modeling of the breast, several researchers utilized several tactics to generate realistic breast geometries. Figueiredo et al. [387] developed a 2D realistic model shown in Fig. 15 by utilizing the outlines from an anatomy breast illustration from [388]. Their model incorporated layers similar to the non-concentric hemispherical models to separate the fat and skin tissue layers, as well as the lymph node, the milk ducts, and lobules. The authors utilized the steady-state Pennes' bioheat equation with thermal physical properties specific to each layer and biological region. The tumor was modeled to be highly perfused with a high metabolic heat generation using Gautherie's principles [112–114]. Additionally, cases were conducted where the tumor was placed in the lobular and milk duct regions to simulate lobular and ductal carcinomas, respectively. Although this model gave a more accurate representation of the breast with tumors being placed at accurate locations, this model has to be validated against experimental data or other studies. Additionally, the breast being a 3D object may play a bigger role in the temperature distribution which cannot be depicted in this 2D model. This method was utilized by Barros and Figueiredo [389] to generate 3D geometries based on the 2D outlines. A glandular tissue region replaced the area where the lobules and milk ducts were previously modeled given a more simplistic approach. However, the exact method utilized to generate these 3D models is unknown and the breast geometry is symmetric about the xy-plane. This symmetry may play a major role in the temperature distribution similar to the hemispherical models, but further studies are needed to understand its effects. Jiang et al. [390] developed a 3D realistic model generated by deforming a concentric hemispherical breast due to gravity, as shown in Fig. 15b. The authors conducted an anisotropic Pennes' bioheat transfer model with the tumor being

modeled with a higher perfusion rate and metabolic heat generation than the rest of the breast. The boundary conditions and thermal properties utilized in hemispherical models were utilized. The deformation of the breast was conducted using nonlinear elastic deformation model that was coupled with the thermal model using the concentric hemispherical model developed by Osman and Afify [375,377]. The deformation of the breast helped show the asymmetric temperature distribution with a warmer region in one end and a colder region on the other end of the breast. This temperature distribution was in agreement with the temperature distribution observed in IR images from previous experiments [379]. However, further clarification is needed on the temperature distribution due to the coupling of the deformation with the thermal model. Furthermore, validation of the breast shape is needed to ensure their coupled model generates an accurate breast model. Other methods that have been utilized by researchers to generate realistic breast models have been through the breast outlines from IR images [145,391] and 3D scans, or traces, of breast mannequins [147,392–394]. The methods that utilized the IR images gave complex symmetric 3D models similar to the one discussed by Barros and Figueiredo [389], which has yet to be validated. The 3D scans of mannequins show great promise as the actual breast shape can be utilized for bioheat transfer modeling, but this method limits the breast sizes and shapes that can be imaged for comparison.

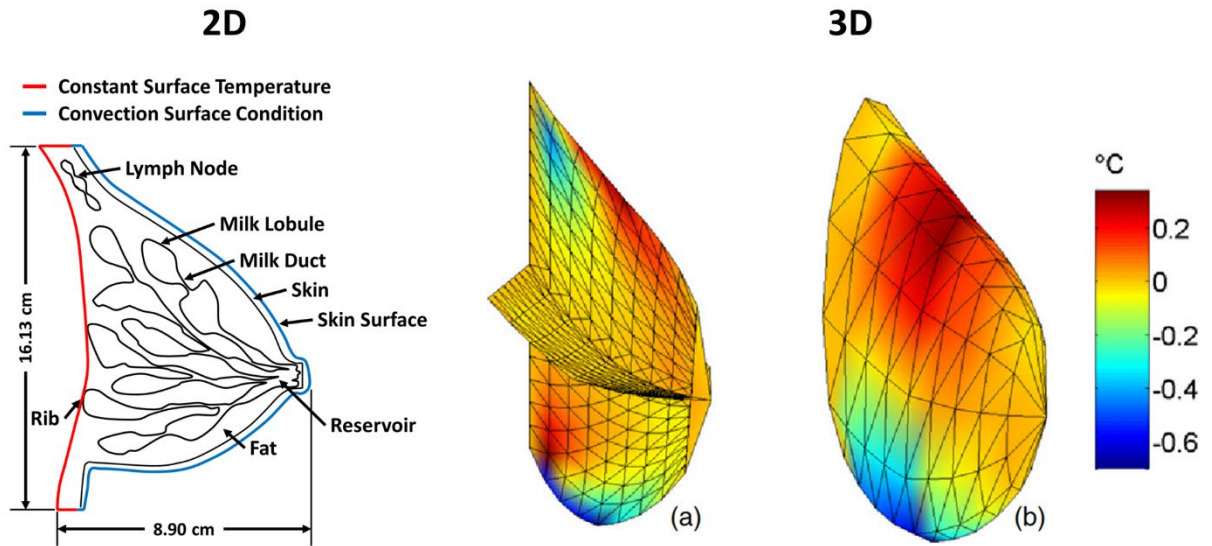


Figure 15. Example of realistic 2D (outline of breast from anatomic breast illustration) and 3D (deformed hemisphere due to gravity) models utilized in literature, redrawn and adapted from [387,390].

### c. Patient-Specific Breast Geometries

Patient-specific breast geometries are breast geometries of patients obtained using patient images with 3D reconstruction techniques or 3D scanners. Gonzalez-Hernandez et al. [395] developed a method to generate patient-specific digital breast models using MRI slices, image registration, and 3D reconstruction. The steady-state bioheat model was utilized with similar boundary conditions and thermal properties utilized in literature. The tumor was modeled with higher perfusion rate and metabolic heat generation than the surrounding tissue. The authors did not utilize multiple layers as these layers played little to no effect on the total heat transfer [116,118,120]. Also, the authors did not model a physical tumor like most breast geometry models of breast cancer. The tumor heat source was added numerically by assigning the tumor characteristics to a tumor spherical region of size  $d_t$ . The temperature distributions were compared against experimental data as well as with clinical IR images and showed great results [150,396]. Lozano et al. [397] and Mukhmetov et al.

[154] both utilized 3D scanners to generate patient-specific breast geometries for bioheat transfer modeling. Their methods showed the usefulness of conducting studies with patient-specific models and the validity of their model by comparing their results to the patient's IR images. Both patient-specific geometries utilized layers within their models, but only Lozano et al. [397] modeled the actual tumor topography as well as used a steady-state bioheat model. Mukhmetov et al. [154] modeled the tumor as a sphere while also conducting a transient simulations. Regardless of the method, patient-specific geometries are able to encapsulate the thermal effects on the complex geometries and should be utilized to conduct any thermal study including inverse modeling.

#### 2.2.4 Inverse Heat Transfer Modeling of Breast Cancer

In relation to breast cancer detection, inverse heat transfer approaches utilizing the bioheat transfer models and IRI data have shown great promise in the detection of tumors. Researchers have utilized traditional finite element methods [149,150,387,391] and AI-based [144,145,147,154,398–400] algorithms to conduct inverse modeling. Figueiredo et al. [387] showed that a finite element-based inverse heat transfer approach has the ability to localize tumors in a realistic 2D breast model. The authors generated surface temperatures using thermal modeling for a 3 mm DCIS tumor in the anterior region, a 3 mm DCIS tumor in the posterior region, a 10 mm IDC tumor in the anterior region, and a 10 mm ILC tumor in the posterior region. Their algorithm utilized the temperature difference between the breast model with a tumor and a breast model without a tumor (healthy breast) to conduct inverse modeling to obtain the tumor centers. These tumor centers are the x- and y- coordinates of the tumor location within the breast model. This work showed great promise in utilizing inverse heat transfer to detect breast tumors within

a breast geometry. However, due to the breast being a 3D object with no exact symmetry, a method is needed that utilizes 3D patient-specific breast models. Additionally, the metabolic heat generation rate utilized for the tumors did not correlate with the findings of Gautherie [112–114], especially for the 3mm tumor cases. Gautherie's [112–114] model is utilized to obtain the metabolic heat generation rate of a tumor through its diameter size for tumors in the range 10-50 mm. The exact values for the metabolic heat generation rate of tumors < 10 mm are not known and require further investigation. Finally, this method utilized simulated ground truth data instead of actual IR data to conduct the inverse modeling.

In a similar manner, Hossain and Mohammadi [399] utilized a generative algorithm (GA), AI-based method, to conduct inverse modeling on 3D breast models utilizing bioheat modeling. Similar to Figueiredo et al. [387], thermal modeling of breast cancer was conducted to obtain ground truth surface temperature data to utilize with their GA. Their method predicted tumor depth, tumor radius, and the metabolic heat generation of the tumor. Although their work showed great results, they utilized 3D hemispherical breast models to conduct the thermal simulation instead of 3D patient-specific breast models. Also, similar to Figueiredo et al. [387], they did not utilize IR temperature data to conduct their inverse modeling. Conversely, Saniei et al. [400] utilized IR images with bioheat transfer modeling and Gautherie's experimental findings [112–114]) with a dynamic neural network, AI-based method, for inverse modeling. Their algorithm was able to estimate the tumor size and depth using the IR temperatures that were correlated with bioheat transfer modeling. Although their work showed great promise in utilizing IR temperatures to predict the presence of breast tumors, the IR images were taken in the upright position.

This could mean that tumors hidden in the inframammary fold could be missed, as this under region is not imaged. This shows the need for a method that can utilize the IR temperatures of patients to accurately predict the presence of tumors. Additionally, the method should be able to indicate the absence of breast cancer. This would allow for IRI to be evaluated for its efficacy to detect the presence and absence of breast cancer.

### 2.3 Clinical IRI Patient-Specific Breast Cancer Detection

Inverse heat transfer approaches utilizing bioheat transfer modeling have been shown to be effective and accurate methods for detecting the presence of breast cancer using IRI and patient-specific breast models [149,150]. Through a collaborative study between Rochester Institute of Technology (RIT) and Rochester General Hospital (RGH) a computerized IRI program for the detection and localization of breast cancers was created called the IRI-numerical engine. This collaborative study started under an Institutional Review Board (IRB) on March of 2018, where thirty biopsy-proven breast cancer patients were imaged with IRI in the prone position with seven patients being analyzed by the program [149,150,396,401]. This program utilized a method for creating patient-specific digital breast models from the MRI images, a numerical simulation of the heat transfer within the breast, image processing techniques, and an inverse heat transfer approach. Gonzalez-Hernandez et al. [395] conducted numerical thermal simulations of breast cancer using Pennes' bioheat equation [330] and Gautherie's experimental findings [112–114]. An example of a patient-specific digital breast model and the thermal simulation associated with a breast tumor on the model is shown in Fig. 16. Using this method to create patient-specific digital breast models and simulating a cancerous breast, an inverse heat transfer approach was used with IRI images to detect and localize a tumor [150]. In this method,

computed temperature images of the simulated model were obtained and compared with corresponding IRI images through image registration and an iterative inverse heat transfer approach.

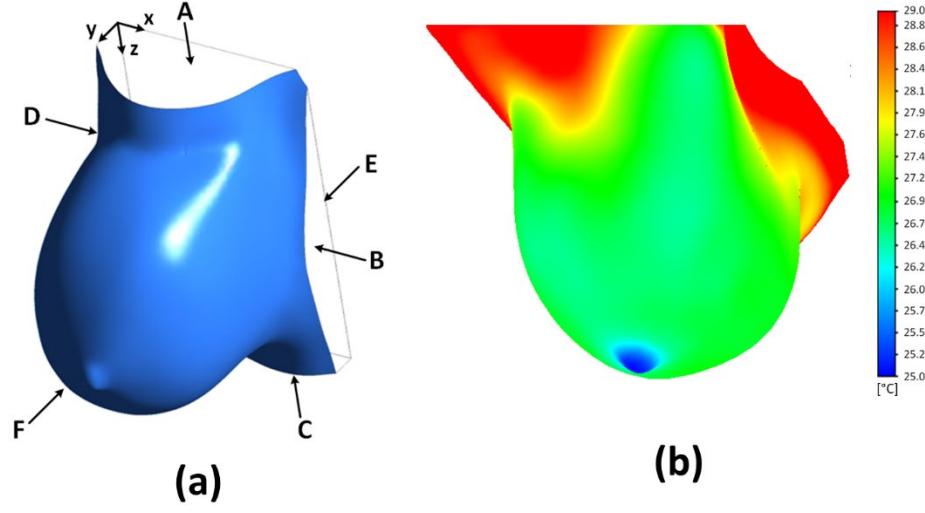


Figure 16. Example of (a) patient-specific digital breast model and (b) thermal simulation of breast cancer.

The inverse heat transfer approach utilized the Levenberg-Marquardt algorithm (LMA) [402] which minimized the objective function:

$$S(\boldsymbol{\beta}) = \|\mathbf{T}_{IR} - \mathbf{T}(\boldsymbol{\beta})\| \quad (16)$$

$$\boldsymbol{\beta} = [d_t \quad x_t \quad y_t \quad z_t] \quad (17)$$

where  $S$  is the objective function dependent on the tumor parameter vector  $\boldsymbol{\beta}$ ,  $\mathbf{T}_{IR}$  is the IR surface temperature, and  $\mathbf{T}$  is the surface temperature from the thermal simulation dependent on the tumor parameter vector  $\boldsymbol{\beta}$ . The tumor parameter vector  $\boldsymbol{\beta}$  (Eq. 17) contains the tumor diameter  $d_t$  and tumor center coordinates  $(x_t, y_t, z_t)$ . Minimization of the objective function is conducted through the gradient descent method applied to the tumor parameter through the following:

$$\boldsymbol{\beta}^{n+1} = \boldsymbol{\beta}^n + [(\mathbf{J}^n)^T \mathbf{J}^n + \eta^n \boldsymbol{\Omega}^n]^{-1} (\mathbf{J}^n)^T [\mathbf{T}_{IR} - \mathbf{T}(\boldsymbol{\beta}^n)] \quad (18)$$

$$\boldsymbol{\Omega} = \text{diag}(\mathbf{J}^T \mathbf{J}) \quad (19)$$

$$\mathbf{J} = \left[ \frac{\partial \mathbf{T}(\boldsymbol{\beta})}{\partial \boldsymbol{\beta}} \right]^T \quad (20)$$

where the indices  $n$  and  $n + 1$  refer to the current and updated values of the tumor parameter  $\boldsymbol{\beta}$ ,  $\mathbf{J}$  is the Jacobian matrix with respect to the tumor parameter vector  $\boldsymbol{\beta}$ ,  $\boldsymbol{\Omega}$  is a diagonal matrix made using the Jacobian matrix, and  $\eta$  is a dampening parameter. The algorithm takes the tumor parameter vector  $\boldsymbol{\beta}^{n+1}$  to obtain the surface temperature  $\mathbf{T}(\boldsymbol{\beta}^{n+1})$  that is utilized in the object function for comparison with the given IR surface temperature  $\mathbf{T}_{IR}$ . If the objective function tends to zero, or to a given convergence value, then there is a match between temperatures and the algorithm gives the final tumor parameter vector. This convergence value  $\varepsilon_1$  is compared to the objective function by checking to see if  $S(\boldsymbol{\beta}^{n+1}) < \varepsilon_1$ . In addition, other stopping criteria are imposed such as the algorithm stopping when a maximum number of iterations is reached ( $n > n_{max}$ ) or when the difference between the tumor parameter vectors is small ( $\|\boldsymbol{\beta}^{n+1} - \boldsymbol{\beta}^n\| < \varepsilon_2$ ). This is implemented to obtain the best estimates and to prevent the algorithm from running without termination due to the ill-posed nature of the problem. Figure 17 shows the flow chart for the inverse heat transfer approach for breast cancer detection using IRI data.

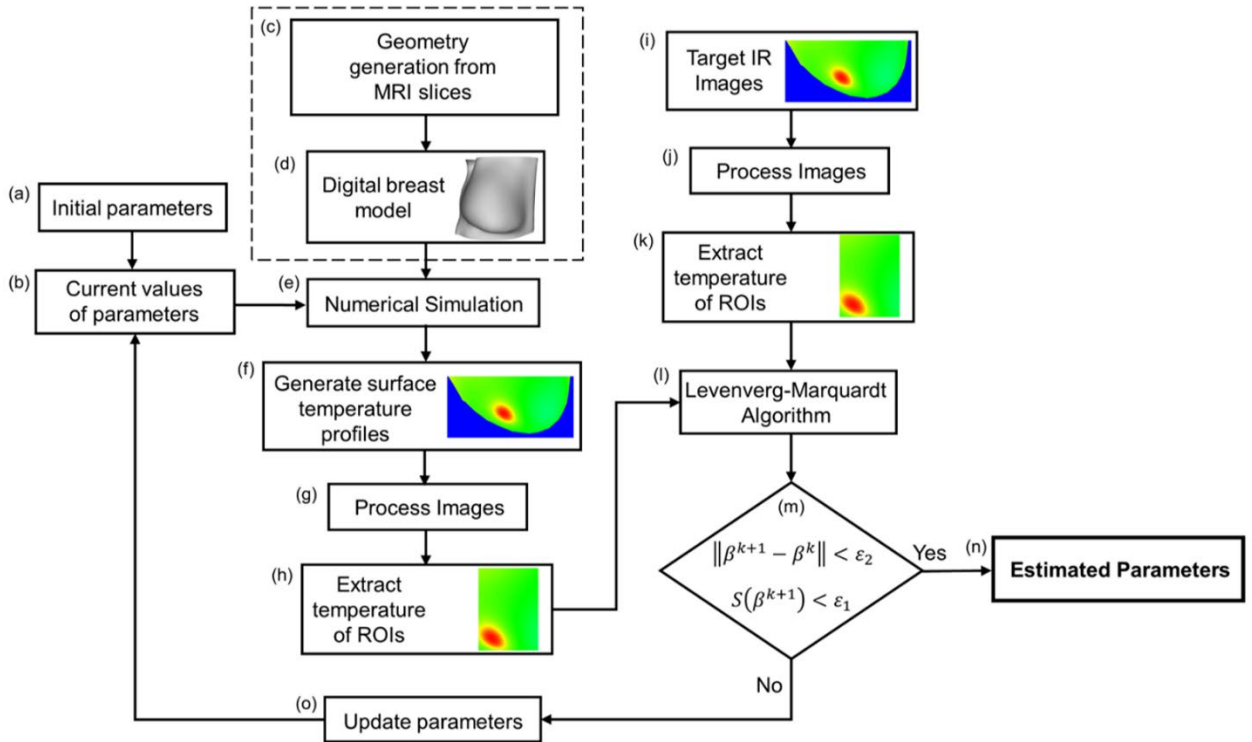


Figure 17. Flowchart showing the process for the inverse heat transfer approach for breast cancer detection [150].

The inverse heat transfer approach was validated with seven biopsy-proven breast cancer patients [149,150]. The results from the studies were in the form of computed surface temperatures which were compared with the IR images of the patient. Figure 18a shows an example of the comparison between the IR images and the computed surface temperatures, also known as the IRI results. Figure 18b shows the overall results of this study, which shows that the inverse heat transfer approach was able to capture the presence of a tumor for all cases. Not shown in these figures is the ability of the algorithm to detect the absence of a tumor in a healthy breast. For each patient, both breasts were imaged and modeled using the methods by Gonzalez-Hernandez et al. [395] and were categorized as left (L) or right (R). This category was based on the patient's orientation such that their right breast is the breast on their right side of their body, and not based on the common medical

nomenclature for viewing of patient images. Therefore, the results of the two patients shown in Fig. 18a are of patient 1 left breast and patient 7 left breast, which means the contralateral breasts, patient 1 right breast and patient 7 right breast, have no tumor and are labeled as the healthy breasts. As Fig. 18b shows, patient 6 was detected to have cancer in both their left and right breasts, or in other words having bilateral breast cancer. This study has shown great promise of the use of IRI as a reliable, accurate, and noninvasive breast cancer screening modality. Further studies of the remaining patients are currently under investigation and will be described in the upcoming chapter.

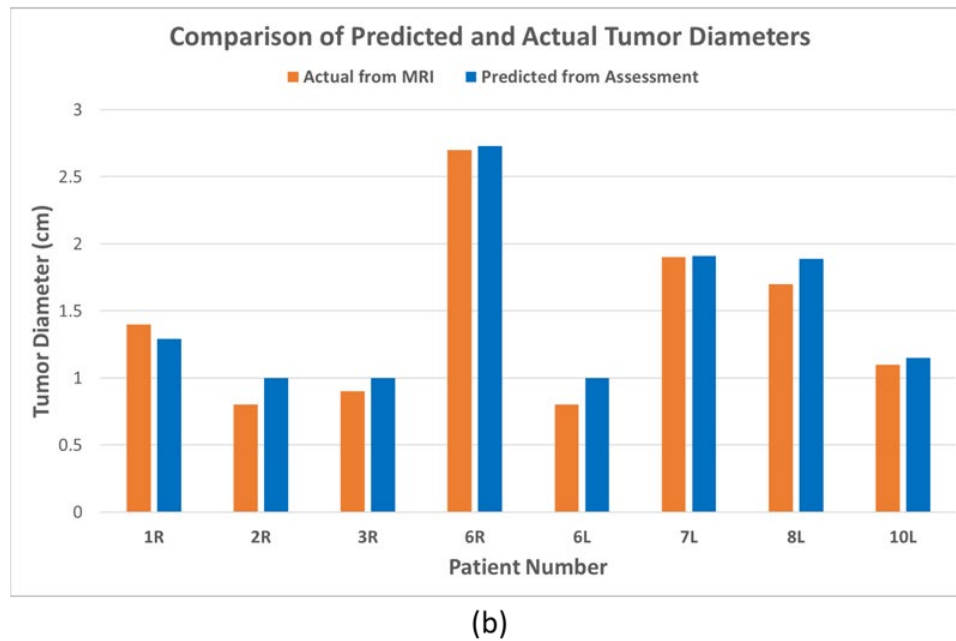
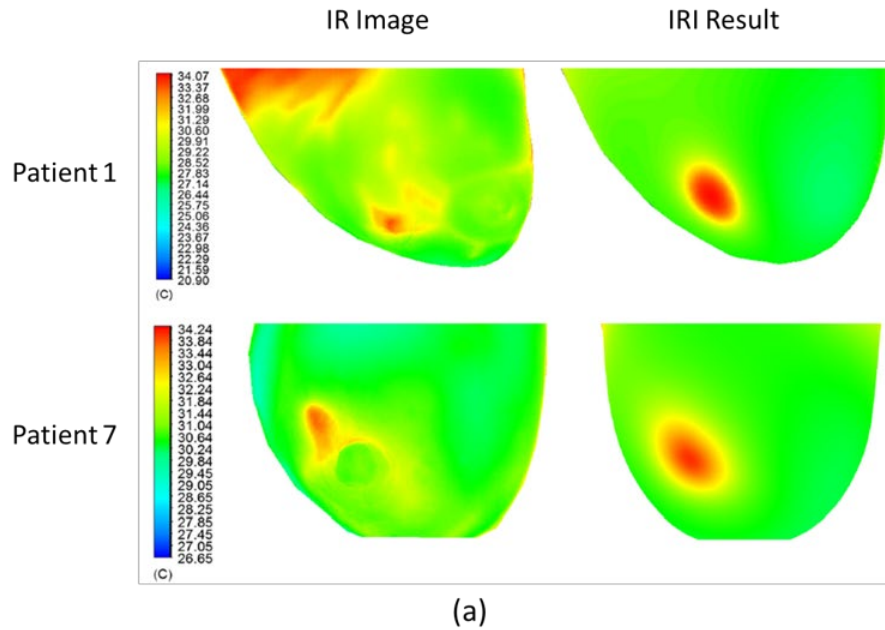


Figure 18. Validation results for the inverse heat transfer approach through (a) qualitative comparisons of surface temperature distributions, and (b) quantitative comparisons of the predicted tumor size to actual size from MRI [149,150].

## 2.4 Research Needs

The work by Gautherie [112–114] has shown the need to investigate breast cancer detection through a thermal perspective. Previous methods to investigate the presence of cancer have been empirically driven regardless of the use of advanced AI techniques. Incorporating the thermal characteristic findings from Gautherie with bioheat transfer modeling shows the ability to conduct noninvasive investigation of breast cancer using IRI. The overlying physics is key, but there have been too few cases of conducting further thermal investigation of breast cancer with accurate breast models. Additionally, few bioheat models have looked at further understanding the vascularity effects on the surface temperature and their effect on detection. Previous investigations of vasculature have only been through empirical methods. The preliminary collaborative study, described in Section 2.3, for breast cancer detection using the inverse heat transfer approach has shown great promise in the creation of a noninvasive breast cancer detection system. The algorithm was able to detect the presence of a tumor for all patients and the absence of a tumor in the healthy breast regardless of cancer type, breast density, tumor size, and tumor depth. However, several patients are left to be tested with this approach and there is a need to optimize the algorithm to be able to conduct a larger study. With a larger data sample, the thermal characteristics of breast cancer can be analyzed in various patients. This shows that the tools are in place for conducting further analysis for this inverse heat transfer approach with IRI as well as conduct further thermal analysis of breast tumors on the breast surface temperature.

## 2.5 Objectives

The overall objectives of this study are to develop and validate an accurate and efficient methodology to analyze infrared surface temperatures of a patient's breast for detecting the presence of a malignant tumor. In order to use it as a screening tool, it is also expected to indicate if there is no malignant tumor present in non-cancerous breasts. The effect of vasculature on tumor detection will also be established. Another objective of this study is to evaluate the detectability limits for detecting cancer as a function of geometric and physiological factors of the breast. The final objective is to determine the thermal effects of tumor angiogenesis and breast vascularity in relation to early detection of breast cancer. These objectives are further described in more detail below.

1. Develop an optimized and autonomous algorithm to conduct a larger clinical study with the inverse heat transfer approach in an efficient and timely manner. This includes enhancements to the previous algorithm validated against 7 biopsy-prove breast cancer patients. This also includes processing the additional data of 16 patients collected from the previous study including the IR images and MRI data. This includes 24 breasts with cancer and 22 without cancer in contralateral breasts.
2. Validate the developed algorithm with 23 biopsy proven breast cancer patient to determine the accuracy in the detection of breast cancer through an IRI inverse heat transfer-based approach. Comparison with tumor sizes obtained from MRI data is utilized to validate the developed algorithm.
3. Establish the detectability limit of the developed algorithm and IRI detection process using various geometric and physiological factors that impact the bioheat transfer of the breast due to the presence of breast cancer. These factors include

breast shape, breast size, breast density, tumor size, and tumor location. The thermal effects of these factors on the breast surface temperature distribution and detection accuracy need to be quantified.

4. Determine the impact of angiogenesis through the tumor blood perfusion on the heat transfer within the breast tissue. Quantify the effects of vascularity on the surface temperature distribution and on the detection accuracy of breast cancer using the developed algorithm.

## Chapter 3: Approach

### 3.1 Overview

This chapter goes over the methods developed to conduct breast cancer detection robustly and efficiently, as well as the methods to study the thermal effects of breast cancer in patient-specific geometries. Section 3.2 goes over the patient-specific bioheat transfer modeling process including the data collection and patient-specific model generation that is the foundation for this work. Section 3.3 goes over the enhancements conducted on the inverse heat transfer approach utilized for breast cancer detection using IR temperatures packaged into the IRI-Numerical Engine (IRI-NE). This section also goes over the process for efficient detection workflow and validation of the algorithm with 23 biopsy-proven breast cancer patients. Section 3.4 goes over the detectability study conducted on the IRI-NE to test the ability of the algorithm to detect cancers of different sizes, at different locations, and in any breast regardless of breast density, size, or shape. Additionally, this section goes over a modified version of the IRI-NE developed to work with 3D surface temperatures and generated patient-specific synthetic IR temperatures. Finally, Section 3.5 goes over the methods utilized to study the effects of tissue and tumor vascularity on bioheat transfer modeling of breast cancer and the impact it has on the detection of breast cancer.

### 3.2 Patient-Specific Bioheat Transfer

The basis for this work is bioheat transfer modeling of breast cancer using patient-specific geometry. This work utilizes the method developed by Gonzalez-Hernandez [396] for the generation of patient-specific digital breast models (DBMs). These patient-specific DBMs

were utilized in conducting bioheat transfer modeling of breast cancer using ANSYS Fluent simulation software [395]. This section goes over the model generation method as well as the method to conduct bioheat transfer simulation in ANSYS Fluent.

### 3.2.1 Clinical Setup and Imaging

The work in this dissertation is a continuation of a collaborative study between Rochester General Hospital (RGH) and Rochester Institute of Technology (RIT). The work entailed an approved Institutional Review Board (IRB) non-invasive clinical IRI breast cancer detection study with biopsy-proven breast cancer patients. For this clinical study, thirty patients were recruited for IRI screening at RGH through an approved IRB consent procedure. The patients recruited for this clinical study were woman over 40 years old with BIRADS 4 or 5 from initial mammography screening or with detected abnormalities through physical examinations. Prior to biopsy, MRI images of the breasts for each patient were taken in the prone position under an IRB approved protocol. Pathology reports were collected at RGH, and all patient data was de-identified as per the approved IRB protocol. Multi-view IR images were captured of each breast in the same prone position as MRI for each patient using an inhouse imaging system and a sturdy retrofitted imaging table with a 23 cm hole developed by Owens [401]. The IR images were captured with a FLIR SC6700 IR camera with a thermal sensitivity of  $< 20$  mK and 640x512 pixel resolution. The images were captured at  $45^\circ$  intervals around a single breast for 8 views at a  $25^\circ$  vertical tilt starting after 10 minutes of acclimation time. This allowed for the surface temperature of the breast to reach a steady-state condition. Figure 19 shows an illustration of the imaging procedure and example IR images of a patient in the prone position after 10 minutes of acclimation.

Further details of the imaging protocol and clinical study can be found in Recinella et al. [149].

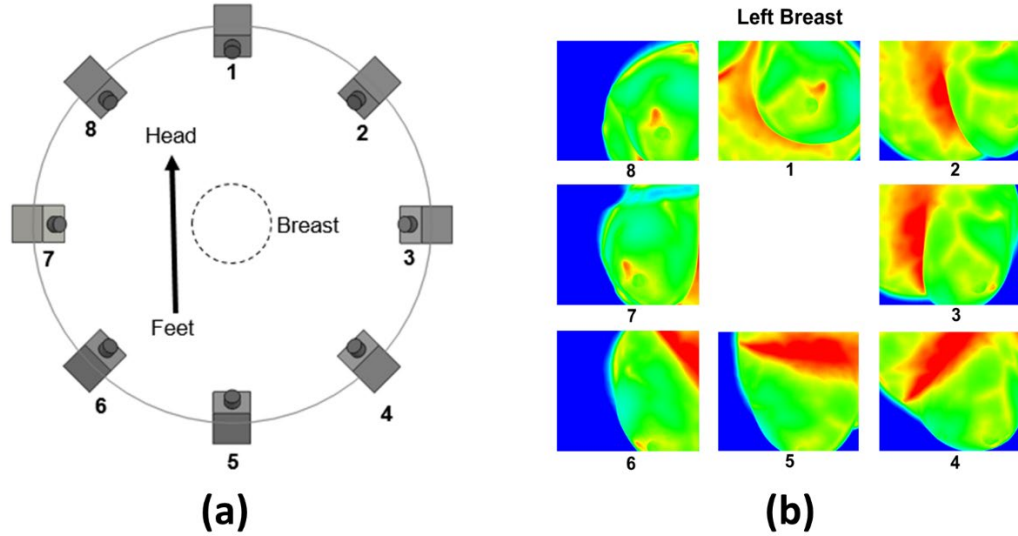


*Figure 19. Depiction of IRI image capture of patients in the prone position with an (a) illustration of the camera position for imaging, and (b) an example set of IR images of a patient's left breast in the same positions.*

In this work, twenty-three patients were utilized for breast cancer detection analysis due to two main factors: (i) MRI data was available and (ii) IR images of each breast were available. For six patients in the thirty-patient cohort, MRI data was either corrupted or not available, but IR images were available. For one patient, MRI data was available but only IR images of one breast were available. Table 8 shows the pathology report for the twenty-three patients that were analyzed in this work. The first seven patients were previously utilized by Gonzalez-Hernandez et al. [150] to validate the inverse heat transfer breast cancer detection approach. These patients were utilized to verify and validate the work developed in this dissertation. The remaining sixteen patients were utilized to further validate the proposed work. There was a total of 24 breasts with cancer, with one patient having bilateral breast cancer, and 22 breasts without cancer. The patient cohort showed

four different breast densities (PF, SF, HD, and ED) and five different cancer types (ADH, DCIS, LCIS, IDC, and ILC). The tumor grade varied from 1-3, with one patient having an unknown grade (patient 18), and the tumor depth ranged from 0.95 cm – 5.45 cm.

Table 8. Clinical patient data collected from pathology reports at RGH for twenty-three patients.

Patient	Age	*BWT	Breast Density	Tumor Grade	Cancer type	Tumor Depth [cm]
Previous Validated Cases						
1	60	R	HD	2	DCIS	1.18
2	70	R	SF	2	IDC	2.14
3	71	R	PF	1	IDC	2.26
4	68	R	SF	3	IDC	2.93
4	68	L	SF	1	ILC	2.72
5	51	R	SF	2	IDC	0.95
6	67	L	SF	1	IDC	2.40
7	67	L	SF	1	IDC	2.28
New Cases						
8	62	L	PF	3	ILC	5.45
9	46	R	HD	2	IDC	2.96
10	48	R	SF	1	IDC	2.23
11	64	R	PF	1	IDC	4.95
12	68	L	HD	1	ADH	2.91
13	68	L	SF	3	IDC	2.43
14	70	R	SF	3	IDC	3.76
15	42	R	HD	3	IDC	2.42
16	49	R	SF	3	IDC	4.30
17	70	L	SF	2	ILC	2.27
18	67	L	ED	X	LCIS	1.29
19	72	R	SF	2	IDC	2.74
20	72	L	SF	3	IDC	1.14
21	64	L	SF	2	IDC	2.93
22	63	L	SF	2	IDC	3.90
23	57	L	SF	2	IDC	2.00

\*BWT: Breast with tumor

### 3.2.2 Generation of Patient-Specific DBMs

Gonzalez-Hernandez [396] developed a method to generate patient-specific DBMs from MRI slices of a patient’s breasts. The method utilizes image processing, 3D reconstruction, and computer graphic methods through various software. The MRI data went through the following image processing technique in ImageJ software: noise filtering, edge detection,

and segmentation. The ImageJ software was also utilized to conduct 3D reconstruction for the generation of a 3D solid geometry. The 3D geometry was then smoothed out using Autodesk Meshmixer and Autodesk Recap, which was then transferred to Autodesk Fusion to generate a 3D model comparable for ANSYS. The model was then imported into ANSYS SpaceClaim where the two breasts were split into their own separate geometries. Finally, each breast model was meshed using ANSYS Meshing with a tetrahedron cell size of 1.5 mm. This method did not generate any tumors or tumor outlines, but instead focused on the generation of the entire breast domain. Figure 20 shows an example of this process on a biopsy-proven patient. A detailed step-by-step process is given in Gonzalez-Hernandez et al. [395], but an overview of the steps are as follows:

1. Select and crop the breast with a region that connects to the chest wall in ImageJ.
2. Conduct a median noise filtering to remove noise in ImageJ.
3. Conduct edge detection to outline the breast shape in ImageJ.
4. Segment the breast using the outlines in ImageJ.
5. Generate a 3D volume geometry using the volume generation tool in ImageJ.
6. Conduct 3D smoothing in Autodesk Meshmixer and Autodesk Recap.
7. Format geometry into an .iges file in Autodesk Fusion.
8. Import geometry into ANSYS SpaceClaim.
9. Separate the breast model into two breast models in ANSYS SpaceClaim.
10. Conduct meshing of each breast model in ANSYS Meshing.

## Patient-Specific Digital Breast Model Generation Process

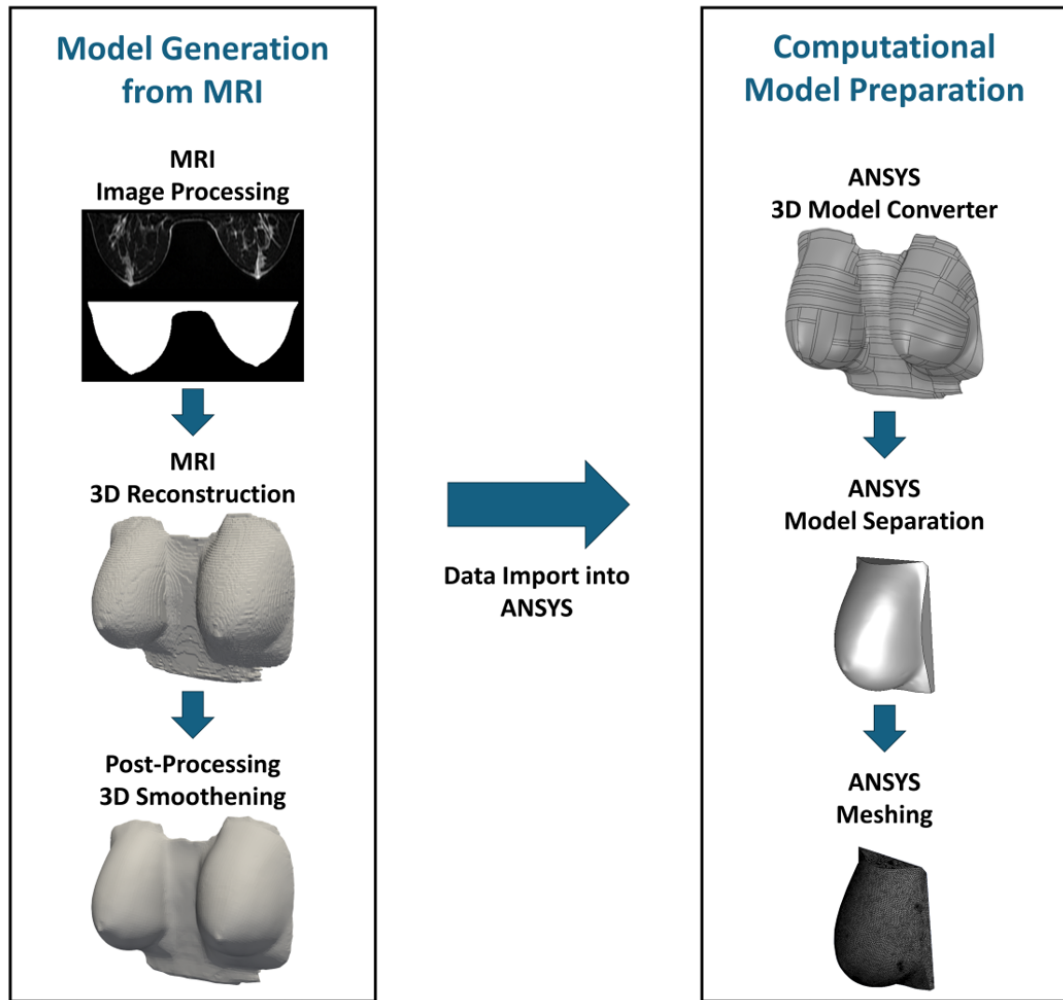


Figure 20. Example of DBM generation process from MRI using the method developed by Gonzalez-Hernandez et al. [395].

This method was previously utilized by Gonzalez-Hernandez et al. [150] to generate patient-specific DBMs of seven biopsy-proven breast cancer patients for inverse heat transfer-based breast cancer detection. The authors conducted a mesh sensitivity analysis to find optimal mesh for thermal modeling of breast cancer. The authors found that an element size of 1.5 mm was optimal to conduct thermal modeling. The current work utilized this method to generate sixteen additional patient-specific DBMs for bioheat

transfer modeling of breast cancer and inverse heat transfer-based breast cancer detection. To verify the method is being conducted correctly, the DBMs of the previous seven patients are generated. This gives a total of twenty-three patients to be modeled and a total of fourth-six DBMs (23 left breasts and 23 right breasts). The left breast relates to the patient's left side and the right breast relates to the patient's right side. The coordinate system is set up such that: the x-direction points from the left to the right side of the patient, the z-directions points from the head to the legs of the patient, and the y-direction points from the chest wall to the surface of the breast. This gives the following geometric lengths:

$$L_x = |x_{max} - x_{min}| \quad (21)$$

$$L_y = |y_{max} - y_{min}| \quad (22)$$

$$L_z = |z_{max} - z_{min}| \quad (23)$$

where  $L_x$ ,  $L_y$ , and  $L_z$  are the geometric lengths in the x-, y-, and z-directions, respectively. The geometric lengths are obtained using the domain of the DBMs, from  $(x_{min}, y_{min}, z_{min})$  to  $(x_{max}, y_{max}, z_{max})$ . These geometric lengths were obtained for each DBM and each patient, which were later utilized to categorize the breast models into small, small-medium, medium, medium-large, and large breast models. In addition, the width  $W$ , height  $H$ , and length  $L$  of the breast surface shown in Fig. 21 were obtained to solidify the categorization. In Fig. 21,  $W$  and  $H$  are the breast surface width and height, respectively, which were measured using the front view of the breast model. The breast surface length  $L$  was measured using the side view of the breast model. All breast surface measurements were obtained from the point of contact between the breast and the chest wall in ANSYS SpaceClaim after each breast was separated (step 8 from above).

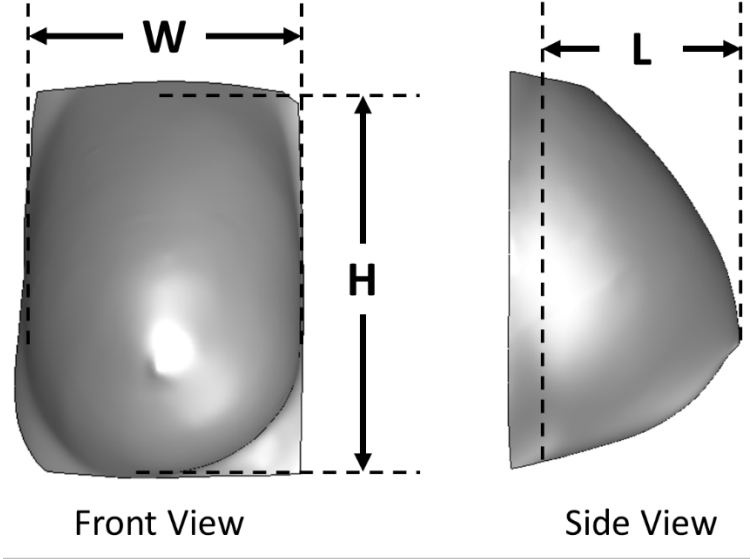


Figure 21. Front and side views of a patient-specific DBM showing the measurement locations of the breast surface width  $W$ , height  $H$ , and length  $L$ .

### 3.2.3 Bioheat Transfer Simulation Setup

This work utilizes the method from Gonzalez-Hernandez et al. [395] to conduct bioheat transfer simulation of breast cancer using patient-specific DBMs in ANSYS Fluent. This method utilizes Pennes' bioheat equation [330] and the fact that a tumor is a metabolically active and highly perfused heat source. Additionally, this method did not use different layers due to their effects having minimal impact on the heat transfer [395]. The Pennes' bioheat equation is utilized to model the tumor heat source within the breast and the surrounding healthy tissue region. This gives the following governing equations:

$$\nabla \cdot (k_h \nabla T) + \rho_b c_b \omega_h (T_a - T) + Q_h = 0 \quad (24)$$

$$\nabla \cdot (k_t \nabla T) + \rho_b c_b \omega_t (T_a - T) + Q_t = 0 \quad (25)$$

where the subscripts  $h$  and  $t$  refer to the healthy and cancerous tissue regions of the breast. This governing equation has a perfusion source term and a metabolic heat generation source term. In the healthy region, the perfusion source term  $\rho_b c_b \omega_h (T_a - T)$  acts as a

heat sink that ensures the body is regulated mimicking the body's circulatory system. In the cancerous region, the perfusion source term  $\rho_b c_b \omega_t (T_a - T)$  acts as an additional heat source due to the presence of the highly perfused tumor. The metabolic heat generation source terms in the healthy and cancerous regions act both as heat sources within the breast due to the metabolic activity of the breast tissue and tumor, respectively. However, the tumor metabolic heat generation source term correlates with the size of a malignant tumor through the following relation provided by Gautherie [112–114]:

$$Q_t = \frac{3.27 \times 10^6}{468.5 \ln(100d_t) + 50} \quad (26)$$

where  $d_t$  is the tumor diameter in the range of 10 mm – 50 mm. Although benign tumors also generate heat, they are not modeled or accounted for in this work as the goal is to detect malignant tumors. The source terms in the healthy and cancerous regions are implemented in ANSYS Fluent through a user-defined function (UDF).

The following boundary conditions were applied to the locations shown in Fig. 22 in order to solve Eqs. 24 and 25:

$$k_h \left. \frac{\partial T}{\partial \mathbf{n}} \right|_{A,B,C,D} = 0 \quad (27)$$

$$T_E = T_{body} \quad (28)$$

$$-k_h \left. \frac{\partial T}{\partial \mathbf{n}} \right|_F = h(T - T_\infty) \quad (29)$$

where  $\mathbf{n}$  is the unit normal vector,  $T_{body}$  is the core body temperature,  $h$  is the heat transfer coefficient, and  $T_\infty$  is the ambient temperature. The adiabatic boundary condition (Eq. 27)

was implemented on the side walls (labels A-D in Fig. 22), the constant temperature condition (Eq. 28) was implemented on the chest wall (label E in Fig. 22), and the convective boundary condition (Eq. 29) was implemented on the breast surface (label F in Fig. 22). The thermal physical properties utilized in this work for bioheat transfer simulations of breast cancer in patient-specific DBMs are shown in Table 9. These properties are based on established literature on bioheat transfer modeling of breast cancer [148,151,370] and have shown to be effective for breast cancer detection through inverse modeling [144,150]. For thermal modeling of the 23 patients utilized in breast cancer detection studies, the thermal conductivity is uniform throughout ( $k_h = k_t$ ) at 0.42 W/m-K as utilized by Gonzalez-Hernandez et al. [150,395] in thermal and inverse modeling of breast cancer. Section 3.5.3 will explore the concept of utilized two distinct values for the tumor and tissue thermal conductivity. Some other thermal property values or ranges are dependent on the study that was conducted and are highlighted with an asterisk (\*). Further details and justification are provided in the appropriate study and associated section.

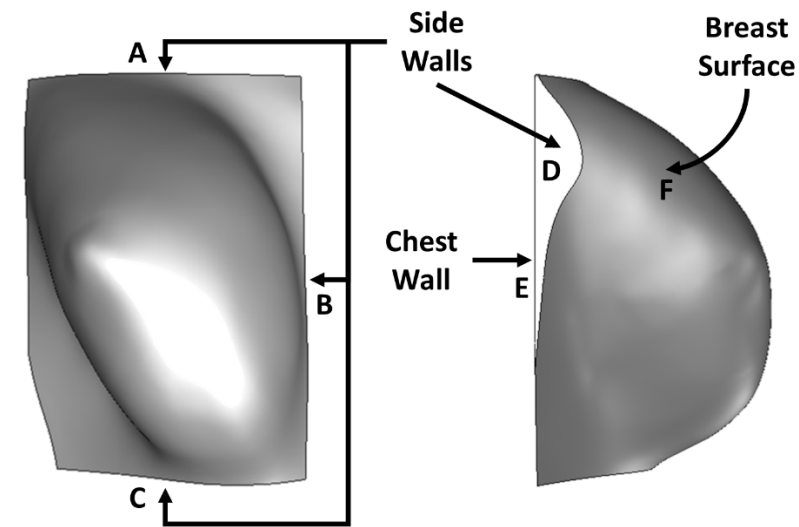


Figure 22. Labeled boundary condition locations in a patient-specific DBM utilized for bioheat transfer simulations of breast cancer.

Table 9. Thermal physical properties of breast tissue and breast cancer for bioheat transfer modeling [395].

Properties	Value	Unit
Thermal conductivity of healthy tissue ( $k_h$ )	*0.1-2.0	$W m^{-1} K^{-1}$
Thermal conductivity of tumor ( $k_t$ )	*0.1-2.0	$W m^{-1} K^{-1}$
Perfusion rate of health tissue ( $\omega_h$ )	$1.8 \times 10^{-4}$	$s^{-1}$
Perfusion rate of tumor ( $\omega_t$ )	* $1.8 \times 10^{-4}$ - $1.8 \times 10^{-2}$	$s^{-1}$
Temperature of arteries ( $T_a$ )	310	K
Specific heat of blood ( $c_b$ )	3840	$J kg^{-1} K^{-1}$
Density of blood ( $\rho_b$ )	1060	$kg m^{-3}$
Metabolic activity of healthy tissue ( $Q_h$ )	450	$W m^{-3}$
Metabolic activity of tumor ( $Q_t$ )	*8,726-65,400	$W m^{-3}$
Core temperature ( $T_{body}$ )	310	K
Heat transfer coefficient ( $h$ )	13.5	$W m^{-2} K^{-1}$
Ambient temperature ( $T_\infty$ )	298	K

\*Thermal property value range based on literature [370].

### 3.3 Development of IRI-Numerical Engine

Gonzalez-Hernandez et al. [150] showed the ability to detect breast cancer using surface temperatures from IR images and an inverse heat transfer-based approach. This work has enhanced and automated this approach into a package algorithm called the IRI-Numerical Engine (IRI-NE). This section goes over the enhancements and additions developed to analyze twenty-three patients efficiently. Finally, this section goes over the methods utilized to validate the IRI-NE using clinical data.

#### 3.3.1 Enhancement of IR Image Registration

The inverse heat transfer breast cancer detection algorithm developed by Gonzalez-Hernandez [396] utilized image registration of multi-view IR images and computed images. The computed images are images captured in ANSYS Fluent of the breast surface temperature. Image registration is the process of aligning two or more images utilizing image processing methods to ensure spatial alignment of the images [403,404]. The process entails having a reference image and a sensed image that goes through an image processing

procedure to align with the reference image. In the case for IR image registration and the inverse heat transfer approach for breast cancer detection, the reference image is the IR image, and the sensed image is the computed image. An intensity-based multimodal affine image registration algorithm was implemented using the MATLAB's Image Processing Toolbox. Gonzalez-Hernandez et al. [150] showed that utilizing an intensity-based multimodal similarity image registration for inverse heat transfer-based breast cancer detection with IR images and computed images was very successful. This is because the IR images were captured in the same prone position that the MRI images were taken. The inverse heat transfer-based breast cancer detection algorithm utilized a region of interest (ROI) to conduct inverse modeling. The ROI is defined as a region with thermal abnormalities and can be identified as the whole breast. Gonzalez-Hernandez et al. [150] tested various sizes of the ROI and the location of selection for inverse modeling. The authors showed that the size of the ROI and the number of divisions of the ROI does not impact on the outcome when selecting an area with little to no vasculature inside the ROI. If there is a denser area of vasculature in the ROI, smaller number of divisions is needed as well as filtering effect to remove the local vasculature effects. This allowed for the focus to be on the heat transfer from a tumor heat source, if present, and not the local vasculature. Figure 23 shows an example of the images utilized in IR image registration, the registered or aligned image, and the ROI extracted from the registered image.

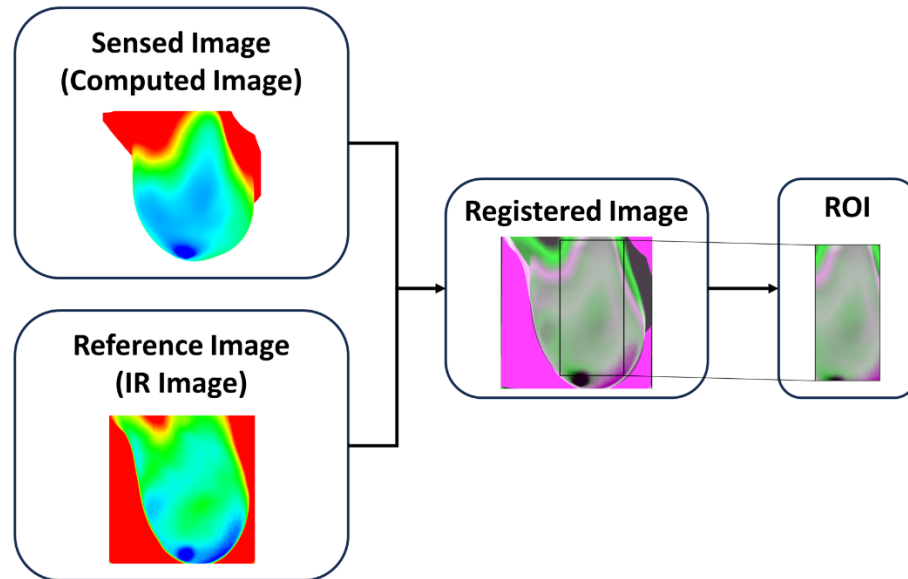


*Figure 23. Example of the reference and sensed images, the registered imaged after IR image registration, and the ROI selected from the registered image.*

The current work enhanced the IR image registration methodology through the following:

- Changed the transformation type from similarity to affine.
- Added various graphical user interfaces (GUIs).
- Added and developed an alignment checking algorithm.
- Added and developed a region of interest (ROI) generator.

In image registration methods, all images are undistorted prior to aligning the images in the same spatial coordinate provided that the camera intrinsic properties are known [403–405]. Since these properties were not known for the IR camera utilized to image the patients, an affine transformation was utilized instead of a similarity transformation to account for the distortion of the IR images. The GUIs were added to allow for users to work along the image registration process and ensure all steps were being conducted correctly. In addition, an alignment checking algorithm was developed with a GUI to allow the user to correct any alignment errors. Last, a ROI generator was developed to allow for

flexible selection of the ROI since every patient had a unique IR image. This IR image registration process differed from the one developed by Gonzalez-Hernandez et al. [150] which needed to be conducted prior to inverse heat transfer modeling. The developed IR image registration process allows the user to run thermal simulations through ANSYS Fluent while conducting inverse heat transfer modeling.

Figure 24 illustrates the process for the developed IR image registration algorithm in a flowchart and provides examples of the GUIs developed in MATLAB. The IR image registration process contains the following five steps:

1. Conduct the thermal simulation of breast cancer and conduct geometry alignment of the breast to obtain computed images in the same orientation as the IR image.
2. Input the image information requested by the Image Info GUI and click the ok button when finished or cancel button to abort the process.
3. Select the region of the breast in both the IR and computed images by drawing a box around the required breast area using the mouse and click ok when done in the Breast Selector GUI.
4. Check to see if the images are aligned and decide to move forward by clicking the yes button, to start over by clicking the no button, or abort the process by clicking on the cancel button in the Alignment GUI.
5. Select the desired ROI using the mouse then click OK when done in the ROI Selector GUI to generate a ROI for analysis.

The first step was conducted using ANSYS Fluent software and the built-in GUIs and macros for geometry alignment. For geometry alignment, the breast is manipulated manually in the GUI until the orientation of the breast relatively matches the breast

orientation captured in the IR image. A macro is activated that saves the orientation of the breast. This is done for the various views when more views desired for detection. After the breast is oriented, a macro is activated to generate and save a computed image at every orientation at the end of a given iteration. Steps 2-5 were conducted using the developed MATLAB GUIs shown in Fig. 24. The GUI for step 2 takes the information relating to the temperature range shown in the images and the number of views. The temperature ranges allow for image intensity values to be transformed into temperature values. The computed images, image information, and IR images are then given to the breast selector GUI (step 3) which brings up the images and asks the user to select the region of the breast. This allows the images to be cropped so that the focus is on the breast instead of the image background. After selecting the breast, the image registration algorithm aligns the images, and the outcome is shown to the user with a GUI that asks the user if the images are registered (step 4). If the images are not aligned, the user can conduct geometry alignment in ANSYS Fluent, obtain new computed images and click on the no button in the Alignment GUI. This is conducted until the alignment of the breasts are satisfactory to the user in every view. Once all views are aligned, the ROI Selector GUI (step 5) asks the user to select the ROI box on the aligned images and the ROI Generator creates the ROI temperatures that will be utilized by the detection algorithm. For the selection of the ROI, the recommendations suggested by Gonzalez-Hernandez [396] were utilized to ensure the appropriate region was selected.

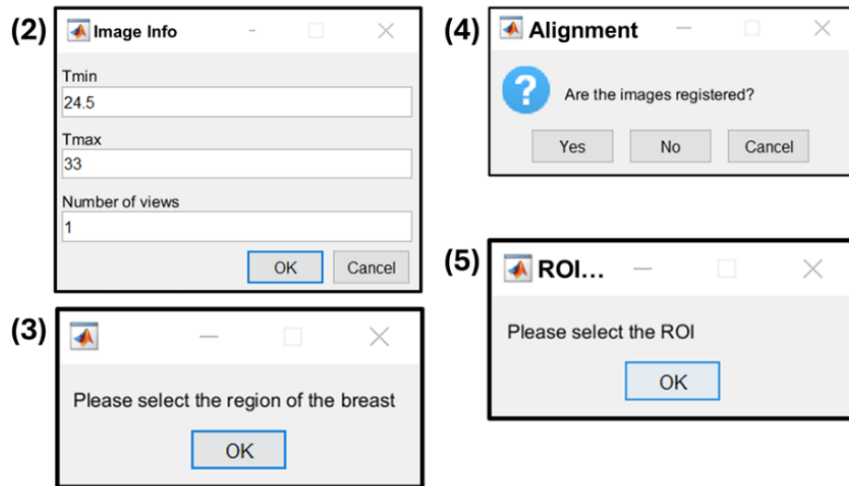
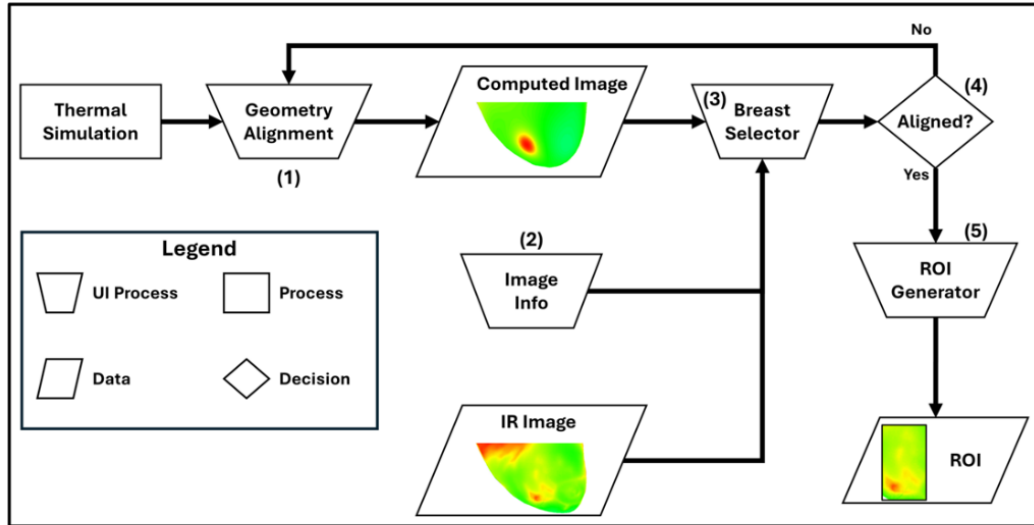


Figure 24. (Top) Illustration of IR image registration process and (Bottom) example of associated GUIs developed in MATLAB.

### 3.3.2 CFD-Inverse Heat Transfer Interfacing

The inverse heat transfer algorithm developed by Gonzalez-Hernandez [396] utilized the patient-specific DBM, bioheat transfer simulations in ANSYS Fluent, clinical IR images, and computed images to detect the presence of breast cancer. The inverse modeling method the author utilized was the Levenberg-Marquardt algorithm [406], which utilizes an iterative gradient decent method to generate the estimated parameters of interest. In terms of breast cancer detection, the three parameters that were estimated by the algorithm were

the tissue thermal conductivity ( $k_h$ ), tumor diameter( $d_t$ ), and tumor location ( $x_t, y_t, z_t$ ). Although this method was validated on 7 biopsy-proven breast cancer patients by Gonzalez-Hernandez et al. [150], the algorithm was only developed for a small sample size. In order for ANSYS Fluent to utilize the predicted parameter from the inverse model and to feed the computed and IR images to the inverse model, the user had to manually go back and forth between the algorithms in order to obtain results. This meant that the inverse model needed to predict the parameters and feed it to ANSYS Fluent to generate new computed images. The inverse model then takes the computed and IR images to compare the temperatures in the ROI to give a new prediction. For the previous method developed by Gonzalez-Hernandez [396], this was conducted by initializing and running ANSYS Fluent after the predicted parameter was created by the inverse model. The algorithm then had to wait for the new computed images to be created, but prior to this the previous computed images needed to be deleted manually so the algorithm could wait for new files. This method would lead to long computational time and be inefficient for large patient sizes. Therefore, an enhanced interface was needed to better communicate between ANSYS Fluent and the inverse model efficiently.

The current work developed a method to automate the communication between ANSYS Fluent and the inverse model in an efficient and robust manner. Figure 25 shows a flowchart for the developed method that automates the process for breast cancer detection through an inverse heat transfer approach. Figure 26. shows the GUIs developed for this method in MATLAB corresponding to the flowchart. To distinguish this method from the previous method developed by Gonzalez-Hernandez [396], the flowchart has been color-coded with the following:

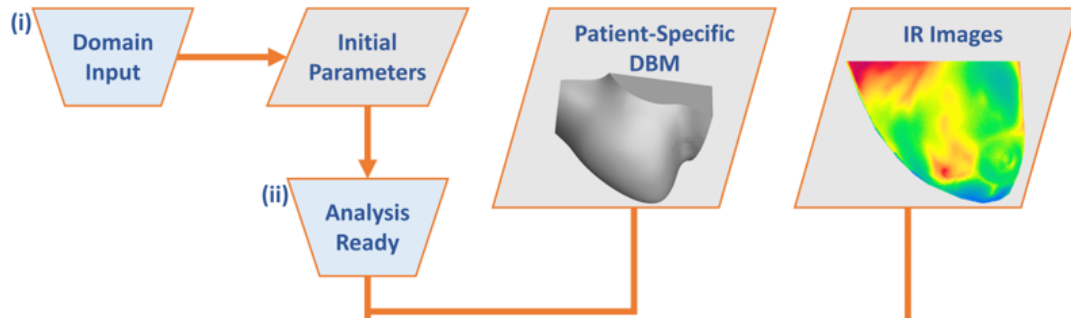
- Grey boxes indicate components utilized from the previous method.
- Blue boxes indicate components that have been added and developed to enhance the detection method.
- Orange lines indicate the initial setup processing flow path.
- Blue lines indicate the main iterative processing flow path.

The method starts with the Domain Input GUI shown in Fig. 25(i) where the user types in the computational domain values in meters which then generates the initial parameter values and saves them into a .txt file. The Analysis Ready GUI shown in Fig. 25(ii) is then executed and tells the user to run the thermal simulation and generate the computed images for image registration. In ANSYS Fluent, the thermal simulation process is conducted utilizing the UDF described in Section 3.2.3 for bioheat transfer of breast cancer. An additional UDF was developed that communicates with the inverse model by creating a pseudo .txt file every 200 iterations, which the inverse model reads in order to send new data to ANSYS Fluent. The UDF also allows the ANSYS Fluent to read in new data after 200 iterations and sends the updated parameters to the required UDFs. Computed images are also saved in the desired views, as described in the previous section, after every 200 iterations. Once the user has generated the computed images and conducted geometry alignment, the IR image registration process described in the previous section (Section 3.3.1) is conducted. After, the ROIs for the IR and computed images are generated and given to the inverse heat transfer algorithm that transforms the images into temperature data. If the temperatures match up to a convergence tolerance, the IRI-NE provides a final assessment output GUI, Fig. 25(iii). This output is either that the IRI-NE has detected the presence or absence of a tumor within the breast. If the temperatures do not match, the

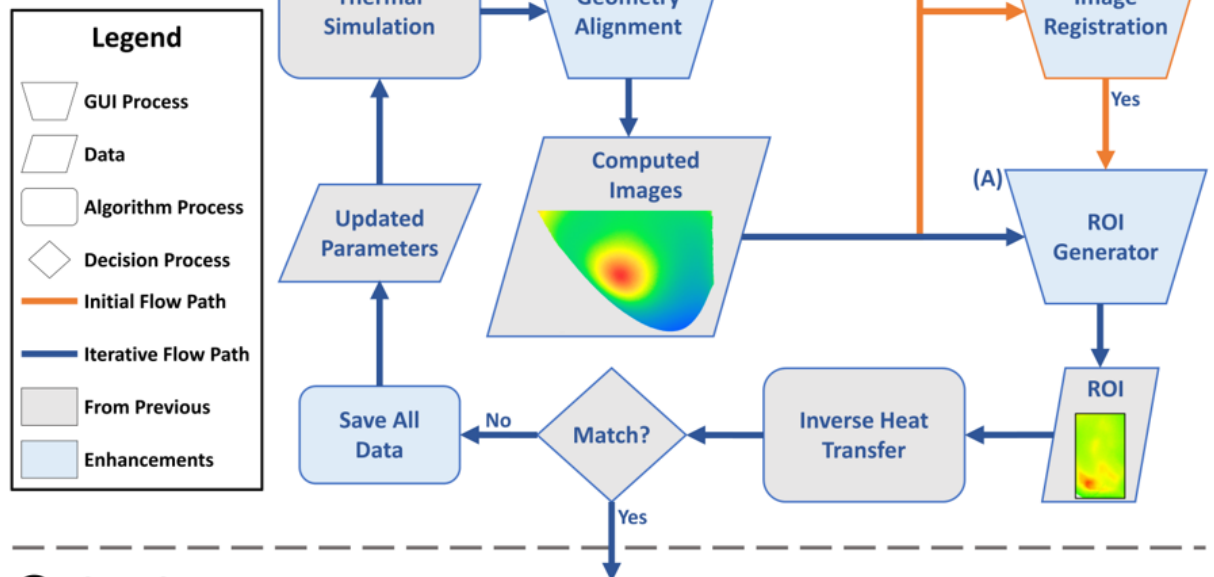
algorithm updates the parameters, saves all data, and generates a new .txt file with the updated parameters for ANSYS Fluent to use. The algorithm only provides this file after deleting the current computed images and reading the pseudo .txt file generated by ANSYS Fluent. The algorithm then conducts an iterative inverse model process (blue path) until there is a match or until the inverse algorithm conducts 50 iterations. The IR image registration process is only required to initiate the algorithm (orange path).

Since this algorithm runs without any human intervention and relies on the computer to conduct all the process, fail-safe procedures were implemented to ensure the algorithm can run smoothly with or without any interruptions. The fail-safe procedures applied to this algorithm are the Save All Data process after the match evaluation between the IR and computed images, and the Warning/Error GUIs shown in Fig. 26(A) implemented at the ROI Generator. The Save All Data process is utilized in the case of a hardware or software crash by saving all relevant data such as the updated parameters, iteration value of the saved data, the image registration ROI, and any other information needed by the algorithm. That way the user can restart the process as the last saved entry and continue the process shown in Fig. 25 until there is a final outcome. The Warning/Error GUIs and procedures are placed before the start of the ROI Generator in the case of ANSYS Fluent software crashing or if the user is starting from last saved. The Warning GUI appears first and after about 10 minutes of runtime the Error GUI appears which will enable the Save All Data procedure and terminate the algorithm. This GUI looks for the pseudo .txt file in order to proceed with the rest of the algorithm, which ensures that the inverse algorithm and ANSYS Fluent software are in constant communication.

## Inputs



## Main



## Output

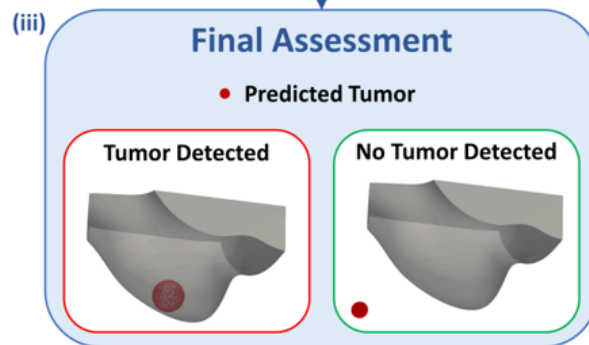
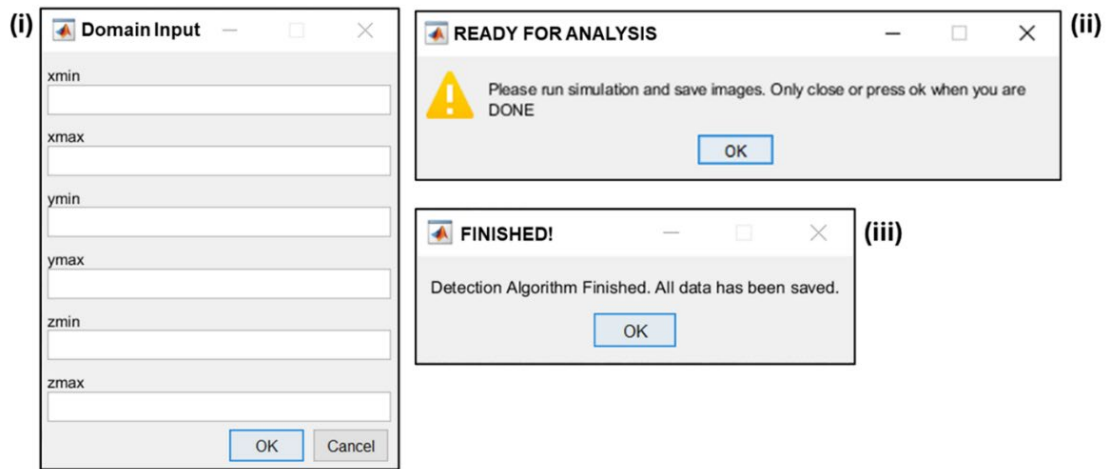


Figure 25. Flowchart of the IRI-NE utilized for breast cancer detection on 23 patients.

## IRI-NE Main Analysis GUIs



### (A) IRI-NE Warning/Error GUIs

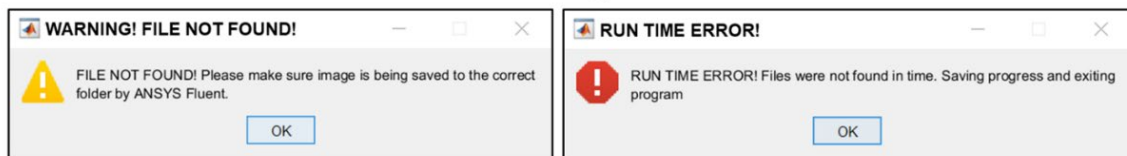


Figure 26. Developed GUIs for the IRI-NE's main analysis (top) and (bottom) in case of hardware or software crashes.

### 3.3.3 Incorporation of CFD Parallel Processing

In addition to the enhancement of the IR image registration, automation of the process, and fail-safe procedures, CFD parallel processing in ANSYS Fluent was implemented. Parallel processing is the method of splitting or partitioning of computational processes that are conducted simultaneously. This is typically done through multithreading in a computer processing unit (CPU), graphics processing unit (GPU), multiple CPUs or GPUs, or a cluster of computers [407]. Parallel processing is utilized to improve computational time and efficiency for complex tasks such as finite element methods and CFD methods. ANSYS Fluent utilizes parallel processing by partitioning the computational mesh and assigning each partition to a thread or compute node for simultaneous processing [408]. For

this reason, it was important that all UDFs contain the appropriate macros to ensure they are executed correctly in parallel. All UDFs for this work were modified to work with parallel processing especially those that write and read files. Simulations were conducted on five machines: (i) Intel® Core™ i7-6700 3.40 GHz workstation with 4 cores, 8 threads and 32 GB RAM, (ii) Intel® Xeon® E5-2630 v4 2.20 GHz workstation with 10 cores, 20 threads and 32 GB RAM, (iii) Intel® Core™ i5-1345U 1.60 GHz workstation with 6 cores, 12 threads and 16 GB RAM, (iv) Intel® Core™ i5-1250P 1.70 GHz workstation with 8 cores, 16 threads and 16 GB RAM and (v) Intel® Core™ i7-9700 3.00 GHz workstation with 8 cores, 8 threads and 16 GB RAM.

### 3.3.4 Verification and Validation using Clinical Data

In order to verify and validate the IRI-NE, the clinical data of the 23 biopsy-proven breast cancer patients presented in Section 3.2.1 and in Table 8 was utilized. A verification study on the IRI-NE was conducted on the 7 patients that were first utilized to validate the inverse heat transfer approach developed by Gonzalez-Hernandez et al. [150]. Then a validation study was conducted on the remaining 16 patients using the IRI-NE. The metrics utilized to verify and validate the method are the assessment outcomes (detection of the presence or absence of breast cancer), and the error in tumor diameter/size (Eqs. 30-32). For Eqs. 30-32,  $d$  is the tumor diameter,  $E_d$  is the error in tumor diameter,  $E_{d,Abs}$  is the absolute error in tumor diameter, and  $E_{d,\%}$  is the percent error in tumor diameter. The subscripts *pred* and *exp* represent the predicted and expected values, respectively. The expected values of the tumor diameter were obtained from MRI utilizing the method described by Gonzalez-Hernandez et al. [150].

$$E_d = d_{pred} - d_{exp} \quad (30)$$

$$E_{d,Abs} = |d_{pred} - d_{exp}| \quad (31)$$

$$E_{d,\%} = \frac{E_{d,Abs}}{d_{exp}} \times 100 \quad (32)$$

### 3.4 Detectability of IRI-Numerical Engine

This section goes over the detectability study conducted on the IRI-NE, where the detectability limits of the algorithm are investigated. The detectability limits of the IRI-NE are defined as the parameters that have an impact on the ability of the algorithm to detect breast cancer using surface temperatures. In Section 1.4.3 in the Introduction Chapter, the factors that heavily affect the detection of breast cancer in the current screening paradigm were discussed. In this work, these same factors are tested to find the detectability limits of the IRI-NE through bioheat parametric studies and inverse modeling using synthetic IR temperatures. Additionally, this section goes over a modified version of the IRI-NE that utilizes surface temperatures to conduct inverse modeling instead of images.

#### 3.4.1 Bioheat Parametric Study of Breast Cancer

In thermal modeling, parametric studies are utilized to study the effects of geometric properties, thermal properties, boundary conditions, heat sources, and other key parameters on the heat transfer of a physical system. The current work investigates effect of the following parameters on the detection of breast cancer and the thermal distribution of a tumor:

- Breast shape
- Breast size

- Tumor size
- Tumor position
- Breast density (thermal conductivity)

The tumor size and position, and the breast density have been shown to play a major role in the detection of breast cancer for mammography and ultrasound. The only factor that was not considered was the cancer type as the modeling of all tumors was conducted through Eq. 26 which relies on the tumor size. The effects of the tumor and breast density on the breast surface temperatures will be studied since the tumor is a heat source dependent on the tumor size and the breast density is measured through the tissue thermal conductivity [112–114]. The breast shape and size were studied as they relate to the other three factors. These geometric factors will show that the relative tumor size and position to the breast geometry have an influence on the heat transfer. This also comes into play when considering the amount of breast density or tissue thermal conductivity material in the breast. The current work conducts four parametric studies to test the thermal effects between the two or more parameters as well as any effects on the detection of breast cancer. The following will go over the setup that was conducted for each parameter under study. Further details of the four parametric studies are discussed in the next section, Section 3.4.2.

- i. Breast Shape and Size

There were two main breast shape categories that were studied in this work which are the convex and concave breast shapes. These two categories were obtained from a measurement system developed by breast surgeons in order to standardize their practice [409,410]. In this work, the concave models were categorized as models that had an inward

indenting feature while the convex model were categorized based on their roundness and lack of this indentation feature. The two patient-specific DBMs that were chosen to represent these categories are patient 17L (concave) and patient 1R (convex). Figure 27 shows an illustration of these breast shapes and the patient-specific DBMs representing these categories. These models were utilized as the base geometries for the various parametric studies conducted in this dissertation.

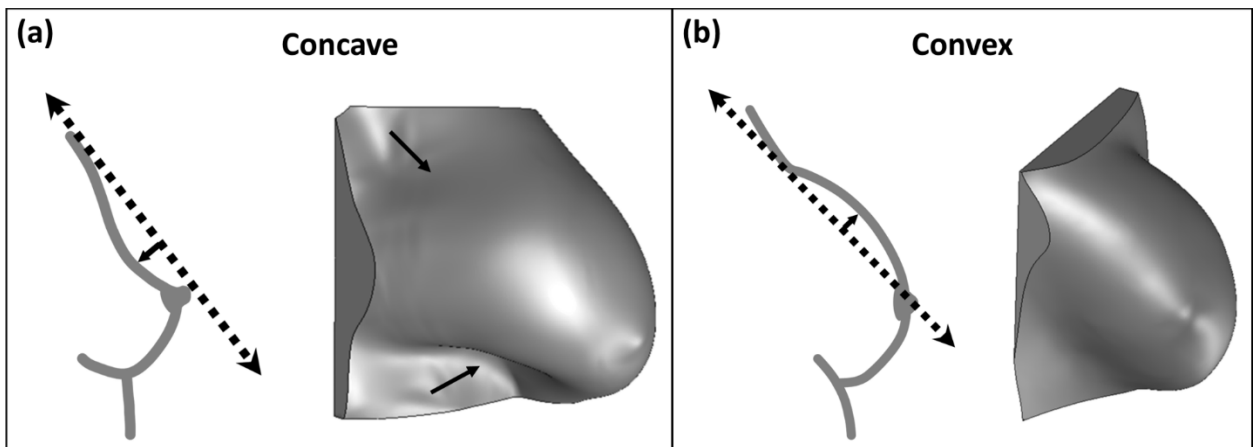


Figure 27. Illustration and patient-specific DBM representation of a (a) concave breast and (b) convex breast models. Illustrations reproduced from the work conducted by Hsia and Thomson [409].

To study the effects of breast size, a standardized method was needed since all breast geometries were unique in terms of sizing. This was conducted by utilizing scaling of the models in ANSYS SpaceClaim and the DBM's geometric lengths in the  $x$ -,  $y$ -, and  $z$ -directions, or  $L_x$ ,  $L_y$ , and  $L_z$ , respectively. The geometric lengths are obtained using Eqs. 21-23 from Section 3.2.2. Scaling was conducted such that three size models were generated known as small, medium, and large models. These models are hereon labeled as scaled models, which were generated with the constraint that the medium and large models are 1.5x and 2x bigger than the small model, respectively. The small model was generated by utilizing dimensions that closely resemble the convex base model. Table 10 provides

the geometric lengths  $L_x$ ,  $L_y$ , and  $L_z$  for the base and scaled models. For each breast shape, parametric studies will be conducted on the base and scaled models which gives a total of 8 breast geometries (4 concave and 4 convex) for bioheat parametric modeling.

*Table 10. Geometric lengths for the based and scaled models.*

Model Type	$L_x$ [cm]	$L_y$ [cm]	$L_z$ [cm]
Concave (17L)	12.0	10.6	12.2
Convex (1R)	7.0	5.9	10.0
Small	8.0	6.0	8.0
Medium	12.0	9.0	12.0
Large	16.0	12.0	16.0

ii. Tumor Size and Depth

For the current work, the tumor size range of 10 mm – 20 mm at 0.5 mm were utilized for parametric studies. This tumor size range is within the 10 mm – 50 mm range that is utilized with Gautherie’s model [112–114] for the metabolic heat generation of a tumor, Eq. 26. This range was selected as the focus of this work is on early detection of breast cancer in particular Tis and T1 stages. Similar to the breast shape and size, a standardized method was needed for the tumor placement. As shown in Fig. 22, the DBMs contains both the chest wall and the breast surface, but with some other parts of the breast that connect the two areas. The current work focuses on glandular tissue carcinomas which occur in the ducts and lobules like the cancer types observed in the 23 patients mentioned in Section 3.2.1 and seen in Table 8. For the patient-specific DBMs there are two main regions within the breast which are the breast tissue region and chest region. The location of the ducts and lobules are in the breast tissue region. The chest wall region contains the pectoral muscles and the tissue region that connects the chest wall to the breast tissue region. To obtain these regions, the separation boundary that separates the regions was found by obtaining the transition point where the chest surface transitions into the breast surface. Figure 28 shows

a 2D view of the inside of the breast and 3D view with the labeled regions and areas on the breast for both concave and convex models. This then allowed for the tumor depth regions to be identified within the breast tissue region for each breast.

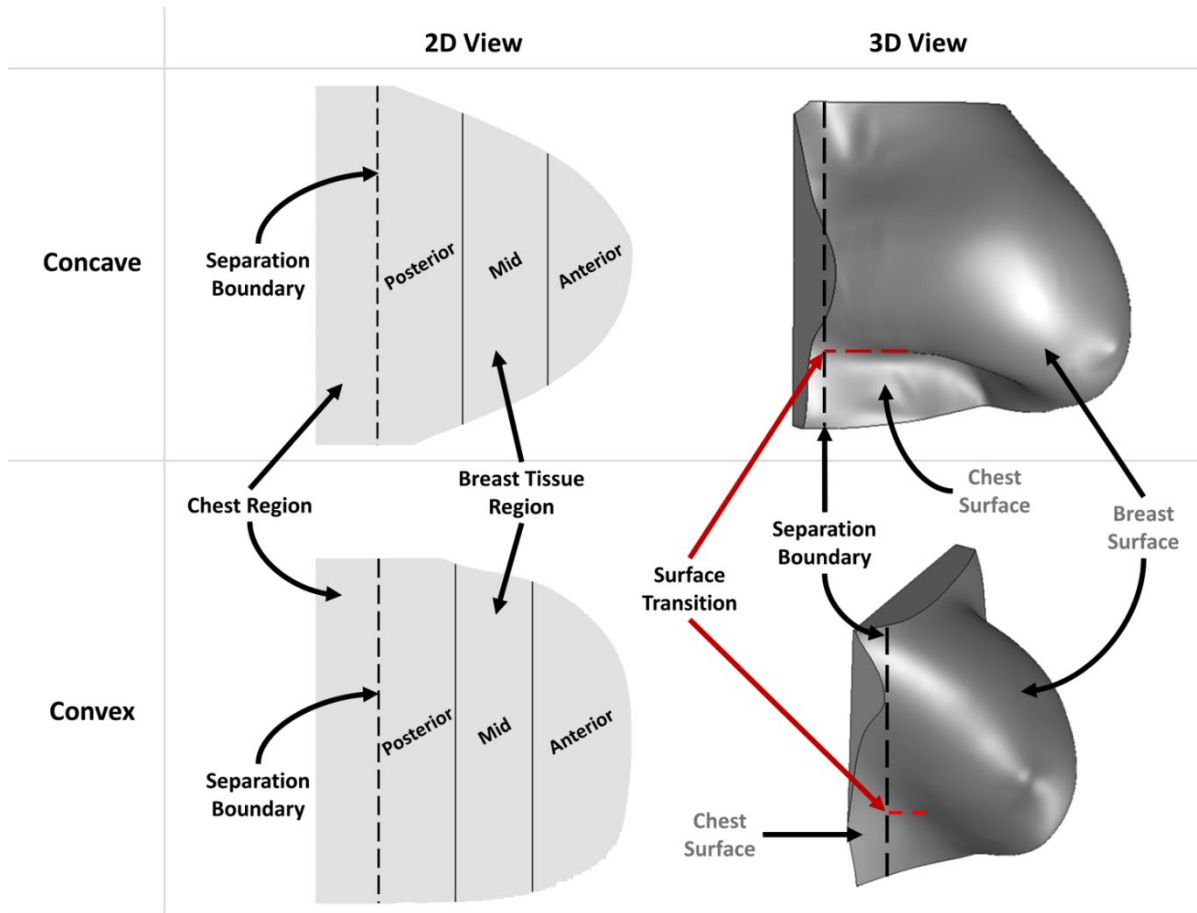


Figure 28. 2D view of the inside of the DBM and 3D view of the DBM for the (Top) concave and (Bottom) convex models with labels of the various regions and areas.

Tumors were placed within these three depth regions at equal distances from each other for each breast model. The tumors were placed using the centerline of the breast, an imaginary line that passes through the coordinates  $(x_{mid}, y_{min}, z_{mid})$  and  $(x_{mid}, y_{max}, z_{mid})$ , where  $x_{mid}$  and  $z_{mid}$  are the x- and z-coordinates of the breast center obtained from the domain through:

$$x_{mid} = \frac{x_{max} - x_{min}}{2} + x_{min} \quad (33)$$

$$z_{mid} = \frac{z_{max} - z_{min}}{2} + z_{min} \quad (34)$$

Then, 10 tumor positions were selected for the base cases with 6 positions placed along the centerline in the y-direction with coordinates  $(x_{mid}, y_m, z_{mid})$  and 4 were along the x-direction with coordinates  $(x_{m,n}, y_m, z_{mid})$ , where  $x_{m,n}$  and  $y_m$  are the x- and y-coordinates of the tumor. Figure 29 shows the placements of the 10 tumors within tumor depth regions of the concave and convex base models. These 10 positions were selected as they covered the three depth regions and deeper tumors. The x- and y-coordinates of the tumor positions were obtained using the following:

$$y_m = \frac{(y_{max} - y_{sb}) - (\Delta y + \Delta y_{ch})}{6} (m - 1) + \Delta y_{ch} + y_{sb} \quad (35)$$

$$x_{m,n} = \frac{(x_{surf,m} - x_{mid})}{3} (n - 1) + x_{mid} \quad (36)$$

where  $\Delta y$  is the spacing in the y-direction between tumor points,  $\Delta y_{ch}$  is the distance between the first point and the chest wall in the y-direction,  $y_{sb}$  is the y-coordinate for the separation boundary,  $m$  is the y-coordinate position case number for  $m = 1, 2, 3, \dots, 6$ ,  $x_{surf,m}$  is the x-coordinate of the farthest surface point at point case  $m$ , and  $n$  is the x-coordinate position case for  $n = 2, 3$ . The x-coordinate values for the tumors along the x-direction utilized the first two points away from the chest as their reference. These points move away from the centerline in the x-direction and have the same y-coordinate value as their reference points. Table 11 gives the x-, y- and z-coordinates of the breast domain, x- and z- coordinates of the breast center, x-coordinates of the surface points for y-coordinate

position cases 1 and 2, and y-coordinates of the separation boundary for each breast model. Table 12 gives the y-coordinates of the tumor positions along the centerline for all breast models obtained from Eq. 35, and the x-coordinates of the tumor positions obtained from Eq. 36 at y-coordinate position cases 1 and 2 for the base models. The  $x_{surf,1}$  and  $x_{surf,2}$  values were obtained using a search algorithm that utilized the shortest distance between the points on the centerline to the nearest surface point.

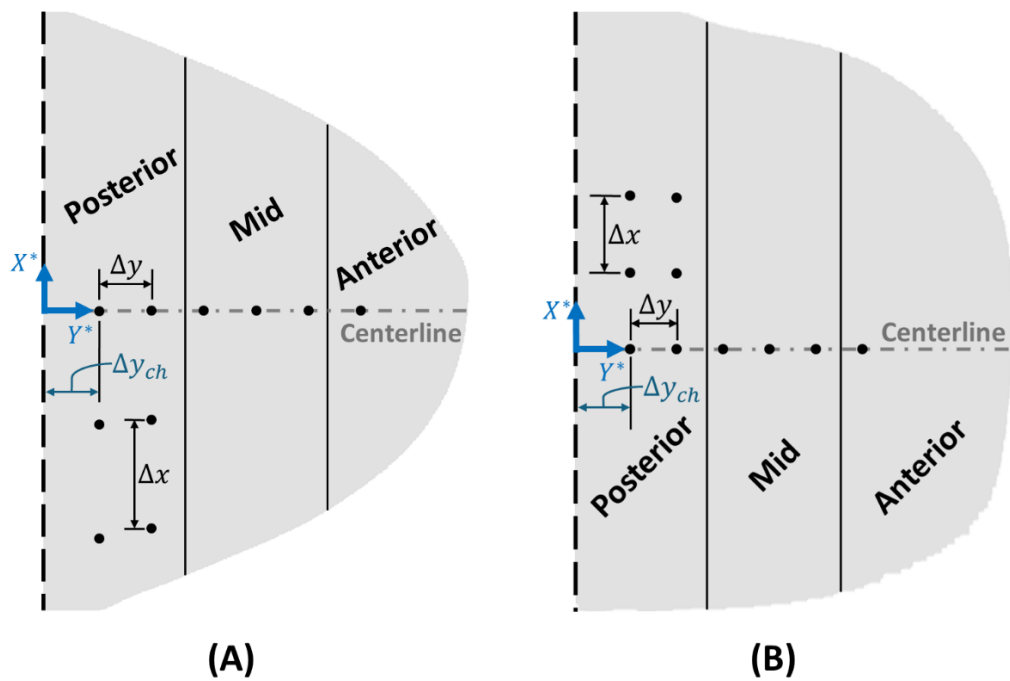


Figure 29. Illustration of tumor placement in the (A) concave and (B) convex base models.

Table 11. Coordinate values for the breast domains, breast centers, surface points, and separation boundaries.

Model	$x_{min}$ [cm]	$x_{mid}$ [cm]	$x_{max}$ [cm]	$x_{surf,1}$ [cm]	$x_{surf,2}$ [cm]	$y_{sb}$ [cm]	$y_{max}$ [cm]	$z_{min}$ [cm]	$z_{mid}$ [cm]	$z_{max}$ [cm]
Concave										
Base	17.6	23.6	29.7	16.7	17.0	2.5	11.0	4.9	11.0	17.1
Small	11.7	15.7	19.7	-	-	1.4	6.2	3.2	7.2	11.2
Medium	17.6	23.6	29.6	-	-	2.1	9.3	4.8	10.8	16.8
Large	23.5	31.5	39.5	-	-	2.8	12.4	6.4	14.4	22.3
Convex										
Base	3.4	6.9	10.4	9.4	9.4	4.0	8.5	6.7	11.7	16.7
Small	8.4	12.4	16.4	-	-	4.1	8.6	5.3	9.3	13.3
Medium	3.3	9.3	15.3	-	-	4.5	11.3	4.6	10.6	16.6
Large	7.8	15.8	23.8	-	-	8.2	17.2	10.6	18.6	26.6

Table 12. Tumor position coordinates for points along the centerline and in the x-direction.

Model	$y_1$ [cm]	$y_2$ [cm]	$y_3$ [cm]	$y_4$ [cm]	$y_5$ [cm]	$y_6$ [cm]	$x_{1,2}$ [cm]	$x_{1,3}$ [cm]	$x_{2,2}$ [cm]	$x_{2,3}$ [cm]
Concave										
Base	3.5	4.6	5.7	6.7	7.8	8.9	21.3	19.0	21.4	19.2
Small	2.2	2.7	3.2	3.7	4.2	4.7	-	-	-	-
Medium	3.0	3.9	4.8	5.7	6.5	7.4	-	-	-	-
Large	3.9	5.1	6.4	7.6	8.9	10.1	-	-	-	-
Convex										
Base	4.5	5.0	5.5	6.0	6.5	7.0	7.7	8.6	7.7	8.5
Small	4.6	5.1	5.6	6.1	6.6	7.1	-	-	-	-
Medium	5.0	5.9	6.8	7.6	8.5	9.4	-	-	-	-
Large	8.7	9.9	11.2	12.4	13.7	14.9	-	-	-	-

In order to ensure that there is a consistent metric throughout each model, a normalized coordinate system was developed by utilizing the intersection between separation boundary and the centerline. This normalized coordinate system  $(X^*, Y^*)$  gives a new representation for the tumor depth  $(X^*)$  and a new metric called the distance from the chest  $(Y^*)$ . Figure 29 shows the location of the new coordinate system within the concave (Fig. 29A) and convex (Fig. 29B) based models. This coordinate is centered in a plane parallel to the xy-plane at a z-coordinate of  $z_{mid}$ . The transformation that was utilized on the tumor coordinates to change them into the normalized coordinate system is as follows:

$$X^* = \frac{x_t - x_{mid}}{x_{max} - x_{mid}} \quad (37)$$

$$Y^* = \frac{y_t - y_{sb}}{y_{max} - y_{sb}} \quad (38)$$

where  $x_t$ , and  $y_t$  are the x-, and y-coordinates of the tumor, respectively. Table 13 shows the values of the normalized coordinates of the tumor positions for the concave and convex models. The tumor depth  $X^*$  is 0 for the tumor positions along the center line since this depth measurement relates to the distance away from the  $Y^*$ -axis. The tumor depth is negative for the concave base model as the tumors were placed in the direction opposite of the  $X^*$ -axis.

Table 13. Distance from chest and tumor depth values for the concave and convex models.

Model	$Y_1^*$	$Y_2^*$	$Y_3^*$	$Y_4^*$	$Y_5^*$	$Y_6^*$	$X_{1,2}^*$	$X_{1,3}^*$	$X_{2,2}^*$	$X_{2,3}^*$
Concave										
Base	0.12	0.25	0.38	0.50	0.63	0.76	-0.39	-0.78	-0.37	-0.75
Small	0.17	0.27	0.37	0.48	0.58	0.69	-	-	-	-
Medium	0.13	0.25	0.37	0.50	0.62	0.74	-	-	-	-
Large	0.11	0.24	0.38	0.51	0.64	0.74	-	-	-	-
Convex										
Base	0.11	0.22	0.33	0.44	0.55	0.67	0.24	0.48	0.24	0.47
Small	0.11	0.22	0.33	0.44	0.56	0.67	-	-	-	-
Medium	0.07	0.20	0.33	0.46	0.59	0.72	-	-	-	-
Large	0.06	0.19	0.33	0.47	0.61	0.75	-	-	-	-

### iii. Breast Density (Thermal Conductivity)

The breast density is a major factor that affects the detection of breast cancer in the current screening paradigm, reducing the sensitivity of mammography from 95-98% to 30-50% [75]. There are four main breast density types which are fatty or predominantly fatty (PF), scattered fibroglandular (SF), heterogeneous dense (HD), and extremely dense (dense). The breast density has been associated with thermal conductivity where an increase in density correlates with an increase in thermal conductivity. Gautherie [112–114] has shown

this correlation through his clinical experiments where he measured the effective thermal conductivity ( $k_{eff}$ ) of breast and tumor tissues. The measured  $k_{eff}$  considers the conduction from Fourier's law and natural convection from the capillary vessels associated with the blood perfusion. Table 14 shows the ranges for the measured  $k_{eff}$  for the various breast density types. According to Priebe and Betz [341], the relationship that a thermal conductivity value of  $5 \times 10^{-4}$  W/m-K resulted in 150 ml/min/(100 g of tissue) or 0.023 1/s of blood perfusion. Utilizing this relationship, the  $k_{eff}$  values in Table 14, and the blood perfusion values from Table 9 the following can be utilized to obtain the tissue thermal conductivity:

$$k = k_{eff} \pm \frac{k_0}{\omega_0} \omega \quad (39)$$

where  $k$  is the tissue thermal conductivity,  $k_0$  and  $\omega_0$  is the thermal conductivity and blood perfusion values from Priebe and Betz [341], respectively, and  $\omega$  is the blood perfusion value from Table 9. This relation assumes a linear relation between the  $k_{eff}$  and  $k$  due to the heat flow from the convection due to the vessels being assumed to be isotropic. The  $\frac{k_0}{\omega_0} \omega$  value for both healthy and cancerous tissue are not significant giving values of about  $4 \times 10^{-8}$  W/m-K and  $2 \times 10^{-6}$  W/m-K. Therefore, the value for  $k$  can be assumed to be the same value as  $k_{eff}$  for any given breast density. The current work utilizes the thermal conductivity range 0.15 W/m-K to 0.7 W/m-K in order to conduct a larger emphasis on studying denser breast tissue.

Table 14. Effective thermal conductivity ranges for the different breast density types from Gautherie [112–114].

Breast Density	$k$ [W/m-K]
PF	0.1-0.25
SF	0.25-0.35
HD	0.35-0.5
ED	0.5-0.7

### 3.4.2 Parametric Study Numerical Setup

There are five main parametric studies that were conducted to test the thermal effect of multiple parameters as well as their effect on breast cancer detection. The first parametric study tested the effects of breast shape (concave vs convex), 2 tumor sizes (10 mm and 20 mm), and the 10 tumor positions, shown in Fig. 29, on the detection. The second parametric study investigated the thermal effects of breast shape (concave vs convex), 5 tumor sizes (10 mm to 20 mm at 2.5 mm increments). The third parametric study tested the thermal effect of breast shape (concave vs convex), breast size (small, medium, and large), 2 tumor sizes (10 mm and 20 mm), and the 6 tumor positions along the centerline. The fourth parametric study tested the thermal effect of breast size (small, medium, and large) and 21 tumor sizes (10 mm – 20 mm at 0.5 mm increments) located at the first centerline tumor position in the posterior region. The fifth parametric study tested the thermal effect of 5 tumor sizes (10 mm to 20 mm at 2.5 mm increments) located at the first centerline tumor position in the posterior region and thermal conductivity (0.15 W/m-K to 0.7 W/m-K at 0.05 W/m-K increments). Parametric studies 1-4 utilize a thermal conductivity of 0.42 W/m-K as utilized by Gonzalez-Hernandez et al. [395] for modeling of breast cancer in patient-specific DBMs. This thermal conductivity value has been utilized in various literature involving bioheat transfer modeling of breast cancer [148,151,370]. Parametric studies 2-5 investigated the effects of their respective parameters on the surface

temperature for each breast model. The first parametric study investigates the effect of its parameters on the detection of breast cancer using inverse modeling. Parametric studies 4 and 5 investigate the thermal effect of its parameters for a deep tumor case. In total there were 20, 30, 12, 21, and 60 parametric cases for the first, second, third, fourth, and fifth parametric studies, respectively.

To simplify the process of conducting the parametric studies, the parameters under study were combined into the following array:

$$\mathbf{B} = \begin{bmatrix} \boldsymbol{\beta}_1 \\ \vdots \\ \boldsymbol{\beta}_j \\ \vdots \\ \boldsymbol{\beta}_M \end{bmatrix} \quad (40)$$

$$\boldsymbol{\beta}_j = [d_j] \quad (41)$$

$$\boldsymbol{\beta}_j = [d_j \quad x_j \quad y_j \quad z_j] \quad (42)$$

$$\boldsymbol{\beta}_j = [k_j \quad d_j \quad x_j \quad y_j \quad z_j] \quad (43)$$

where  $\mathbf{B}$  is the parametric array containing all parameter values for each parametric case,  $j$  is the parametric case number,  $M$  is the total number of parametric cases, and  $\boldsymbol{\beta}_j$  is the parametric vector containing either the tumor size ( $d_j$ ), tumor size and tumor position ( $x_j, y_j, z_j$ ), or the thermal conductivity ( $k_j$ ), tumor size and tumor position at parametric case  $j$ . To utilize the parametric array in ANSYS Fluent a UDF was developed that looped through the parametric vector pairs and switched between them after every  $N$  Fluent iterations. Additionally, surface temperatures for each parametric case were also saved after every  $N$  iterations through a developed surface temperature extraction UDF. Further

details on the surface temperature extraction UDF are provided in the next section, Section 3.4.3. The process for conducting parametric studies in ANSYS Fluent with the developed UDFs is shown in Fig. 30. The process starts with  $\beta_j$  going through the condition that checks whether iteration  $i$  has reached a multiple of  $N$ . If iteration  $i$  has reached a multiple of  $N$ , the parametric case will save the surface temperatures and check if  $i < i_{max}$ , where  $i_{max}$  is the total number of iterations. If it is the algorithm will go from  $j$  to  $j + 1$  for the next parametric case. If  $i$  is not a multiple of  $N$ , the UDF will continue to conduct the thermal simulation at the current parameter case, go from  $i$  to  $i + 1$ , and then continue with the same parameter case. If  $i$  is not a multiple of  $N$ , the process. The value of  $i_{max}$  depends on the total number of parametric cases and the value of  $M$  which gives  $i_{max} = M \times N$ . Each parametric study has their own number of parametric cases. Table 15 shows the total number of parametric cases for each of the five parametric studies including the total number of iterations for  $N = 200$ , as well as the parameters under study.

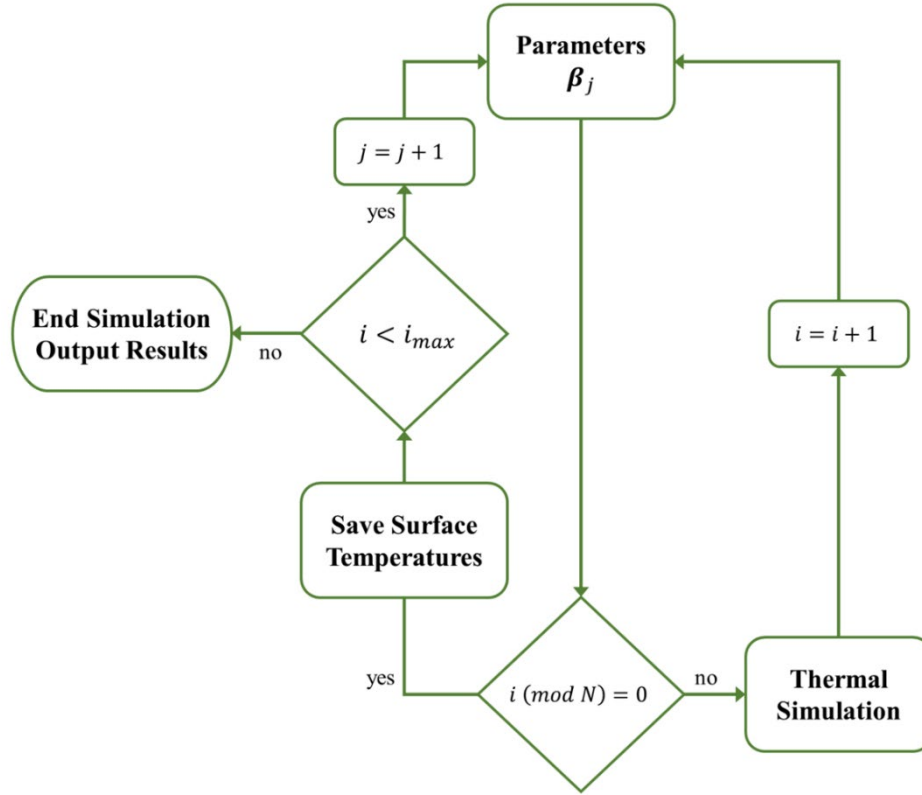


Figure 30. Flowchart of parametric study process conducted in ANSYS Fluent.

Table 15. Parametric study parameters, and total cases and iteration amounts for  $N = 200$ .

Parametric Study	$M$	$i_{max}$	$\beta_j$
First Study	20	4,000	$d_j, (x_j, y_j, z_j)$
Second Study	30	6,000	$d_j, (x_j, y_j, z_j)$
Third Study	12	2,400	$d_j, (x_j, y_j, z_j)$
Fourth Study	21	4,200	$d_j$
Fifth Study	60	12,000	$k_j, d_j, (x_j, y_j, z_j)$

### 3.4.3 Generation of Synthetic IR Surface Temperatures

As mentioned in the previous section, surface temperatures were extracted through a developed UDF in ANSYS Fluent. This was conducted using Fluent's zone IDs which are assigned by the software to each boundary condition location shown in Fig. 22 and the interior breast tissue region. The extraction UDF separates the temperature distribution of each zone and only saves the surface temperature distribution located at the zone ID of the breast surface. This is conducted for all parametric studies described in the previous

section, but for the first parametric study an additional step was implemented. The first parametric study investigates the effect of breast shape, tumor size, and tumor location on the detection of breast cancer using inverse modeling. Inverse modeling of breast cancer was conducted using the IRI-NE and ground truth clinical IR surface temperatures. However, the ground truth data for the parametric studies are simulated surface temperatures extracted from ANSYS Fluent. In order to mimic the noise level captured by an IR camera, a Gaussian noise was added to the simulated temperatures to generate synthetic IR temperatures. This was done through a Gaussian noise filter algorithm that conducted the following:

$$\mathbf{T}_{SIR} = \mathbf{T}_{sim} + \mathbf{T}_{Gauss}(\mu, \sigma) \quad (44)$$

$$\mathbf{T}_{Gauss}(\mu, \sigma) = \frac{T_{IR}}{\sqrt{2\pi\sigma^2}} e^{-\frac{(x-\mu)^2}{2\sigma^2}} \quad (45)$$

where  $\mathbf{T}_{SIR}$  is the vector containing the synthetic IR surface temperatures,  $\mathbf{T}_{sim}$  is the vector containing the simulated surface temperatures,  $\mathbf{T}_{Gauss}$  is the Gaussian noise temperature,  $\mu$  is the mean and center of the Gaussian distribution,  $\sigma$  is the spread and standard deviation of the Gaussian distribution, and  $T_{IR}$  is the thermal sensitivity of an IR camera. This was conducted in python using normal distribution NumPy function with  $\mu = 0$ , and  $\sigma = 1$ , or standard normal distribution. Figure 31 shows an example of a simulated surface temperature, its generated synthetic IR surface temperature, and the clinical IR surface temperature of patient 13L. The thermal sensitivity of an IR camera is known as the smallest temperature difference that can be captured by the IR camera, also known as noise equivalent temperature difference (NETD) [157,158,229]. Since the thermal sensitivity of the IR camera utilized to capture the clinical IR was  $<0.02$  K, a  $T_{IR}$  value of 0.02 K, or 20

mK, was utilized to generate the synthetic IR shown in Fig. 31. As the figure shows, the noise level of the synthetic IR closely resembles the level observed in the clinical IR.

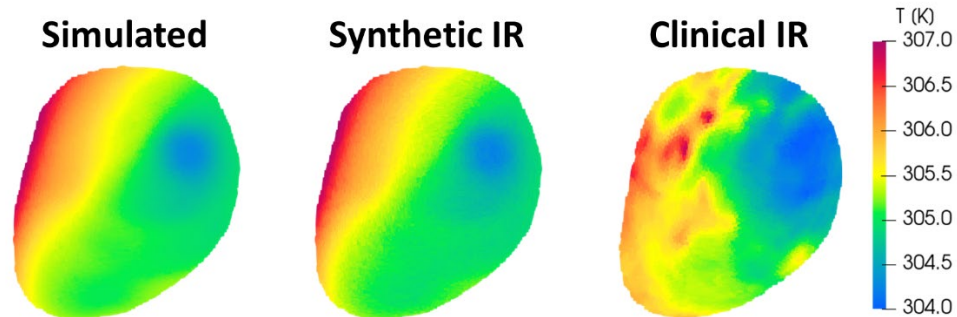


*Figure 31. Example of simulated, synthetic IR, and clinical IR surface temperature distributions for patient 13L.*

In addition to generating synthetic IR temperatures that mimic the noise level of the clinical IR with 20 mK thermal sensitivity noise, other noise levels were tested in the inverse model. Figure 32 shows examples of three noise levels (0 mK, 20 mK, and 40 mK) added to the surface temperatures to generate synthetic IR temperatures. As the figure shows, the noise level has an effect on the surface temperature distribution and may play a role in the detection of breast cancer. Gonzalez-Hernandez et al. [150] showed that the noise level of the data did not affect the detection for the 7 patients utilized in their study. It is expected that the noise level does not only affect detection but also insignificantly affects the predicted tumor size. This work studied the effect on detection with added 20 mK and 40 mK noise levels on the simulated temperatures obtained from the first parametric study. Furthermore, a study was conducted using five noise levels (0 mK, 5 mK, 10 mK, 20 mK, and 40 mK) that were added to the simulated temperatures. This study compared the predicted tumor size with the actual size for each of the noise levels at the tumors placed along the centerline.

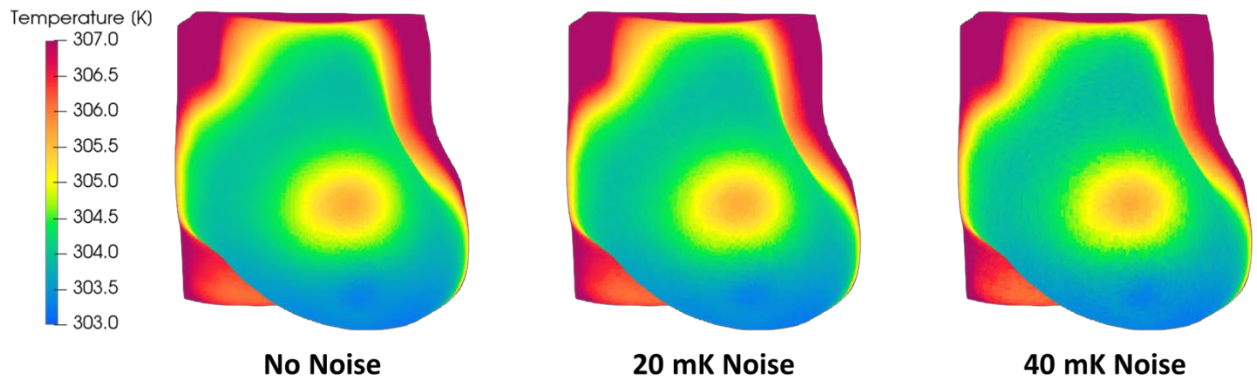


Figure 32. Example of various noise levels (0 mK, 20 mK, and 40 mK) for the generation of synthetic IR surface temperatures for patient 17L.

#### 3.4.4 Modified IRI-Numerical Engine

The IRI-NE was developed to optimize the inverse heat transfer approach so that it could be efficiently implemented on 23 patients. Since the IRI-NE utilizes clinical IR images as ground truth data and the ground truth data from the parametric studies are 3D surface temperatures in the form of point-clouds extracted by ANSYS Fluent, a modified version was developed in python called the modified IRI-NE. Various studies in the area physics-informed neural networks (PINNs) have shown great results in utilizing 2D and 3D temperature data for forward [145,398,411] and inverse [144,398] modeling of breast cancer. The process for generating synthetic IR surface temperatures described in the previous section, Section 3.4.3, was implemented into the modified IRI-NE. Additionally, the IR image registration process was replaced with the surface temperature extraction UDF process also described in Section 3.4.3. Last, the Domain Input GUI was replaced with a domain extraction process that obtained the breast domain from the patient-specific DBMs and generated the initial tumor parameters. Figure 33 shows the flowchart process of the modified IRI-NE with the added Extract Domain process, Add Noise process, and Extract Surface Temperature process. Similar to the IRI-NE described in Section 3.3.2, the

inverse heat transfer algorithm and ANSYS Fluent communicate with each other via pseudo .txt files after every 200 iterations. This allows for the entire process to be completely autonomous only needing to adjust the folder the inverse algorithm needs to read data from and write to, which is the folder ANSYS Fluent is saving data to, as well as manually setting Fluent to run. The output to the modified IRI-NE is the same as the output of the IRI-NE, which is the presence or absence of breast cancer. However, the modified IRI-NE has the additional option to predict the tumor size, tumor location, and tissue thermal conductivity. The user is able to select this option prior to running the algorithm and conducting the entire inverse modeling process.

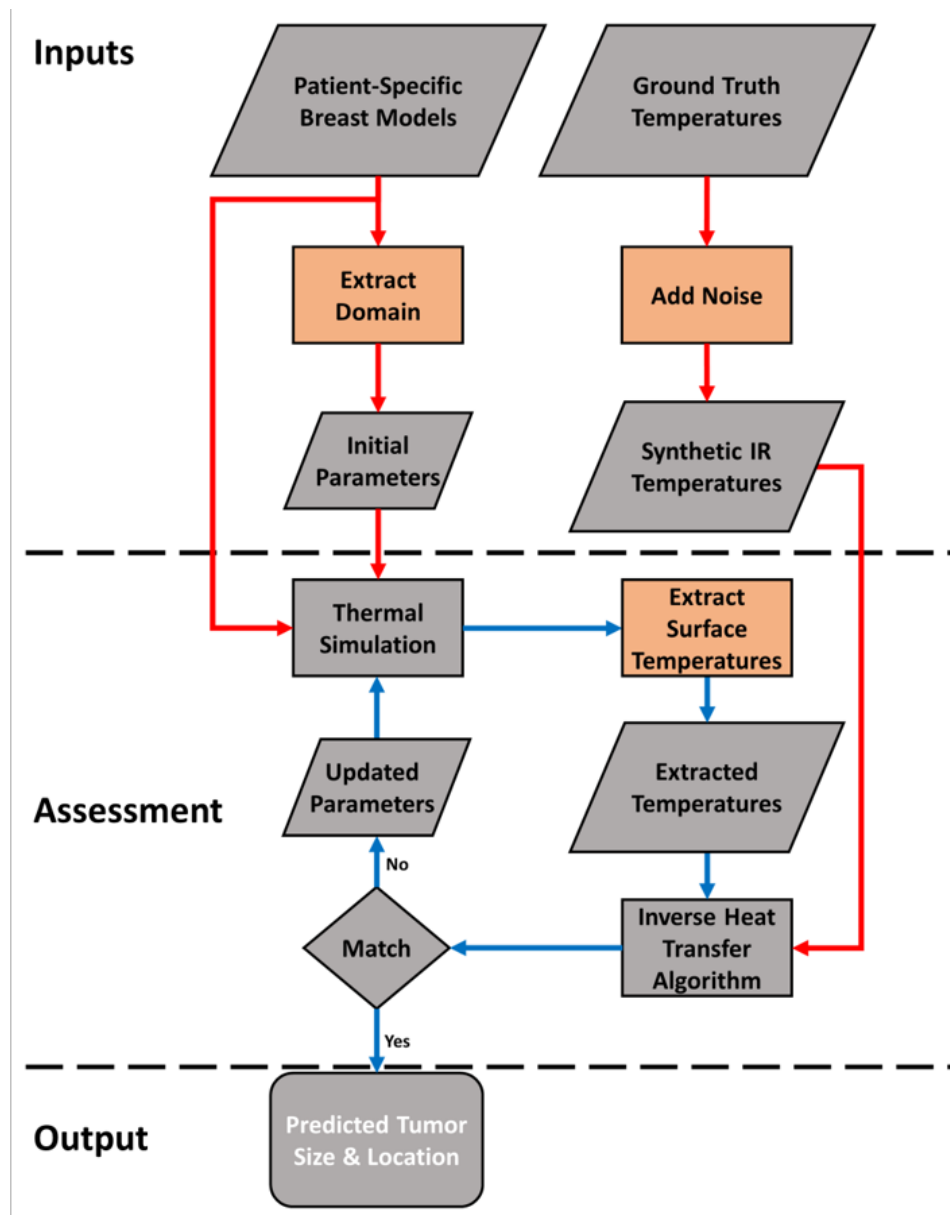


Figure 33. Flowchart process of the modified IRI-NE utilized to detect breast cancer using 3D surface temperatures.

### 3.4.5 Establishing Detectability Metrics

To determine the detectability limit of the IRI inverse heat transfer approach utilized in the IRI-NE and modified IRI-NE, detectability metrics are needed. There were four main metrics utilized to establish the detectability of breast cancer of the IRI inverse heat transfer approach: (i) the ability of the algorithm to detect the presence and absence of breast cancer,

(ii) the error in tumor size, (iii) the internal temperature distribution of the breast, and (iv) the maximum surface thermal contrast. Further details of each detectability metric are described below.

i. Detecting the Presence of Breast Cancer

In Section 3.3.4, a clinical verification and validation study of the IRI-NE for 23 biopsy-proven breast cancer patients was described. That study looked into whether the IRI-NE was able to accurately predict the presence of cancer in breast with certified cancer and the absence of cancer in the contralateral healthy breast. Two similar studies were conducted to verify the modified IRI-NE with patient data and to test the detection of breast cancer on the first parametric study. The first study utilized patient data of 8 biopsy-proven patients (patients 1R, 8L, 9L, 10R, 12L, 13L, 17L, and 19R) from Section 3.2.1. This study required generating synthetic IR temperatures using the known tumor sizes and positions obtained from MRI, except for patient 9L, which was then utilized with the modified IRI-NE. Patient 9L is the only patient breast that which is a contralateral healthy breast. However, the same breast models with cancer were modeled without a tumor to represent additional healthy breasts. Table 16 shows the known cancer type, breast density, tumor sizes, tumor positions, tumor depth, and metabolic activity values for these patients. It is important to note that patient 12L has a 5 mm tumor which is below the range for Eq. 26. For this case, the tumor metabolic heat generation was estimated to be  $70,000 \text{ W/m}^3$  which has been utilized by various researchers in modeling tumors with unknown heat generation [370,387,389]. The second study utilized the ground truth synthetic IR temperature data generated for the first parametric study tumor size and position shown in Table 12 with the modified IRI-NE. Both studies investigated the ability of the algorithm to detect the presence and absence of breast cancer using 3D surface temperature data and the modified

IRI-NE. The modified IRI-NE was set up to predict the tumor size and location as the thermal conductivity of the tissue was set to be 0.42 W/m-K for all for both the ground truth data and output predicted simulation data.

Table 16. Patient data utilized for verification of the modified IRI-NE.

Patient	Cancer Type	Breast Density	$d_t$ [mm]	$(x_t, y_t, z_t)$ [mm]	Depth [cm]	$Q_t$ [W/m <sup>3</sup> ]
1R	DCIS	HD	14	(76,60,118)	1.18	15,749
8L	ILC	PF	12	(274,39,147)	5.45	24,148
9L	-	HD	-	-	-	-
10R	IDC	SF	11	(26,12,109)	2.96	34,547
12L	ADH	HD	5	(27,19,171)	4.95	*70,000
13L	IDC	SF	13	(40,09,144)	2.91	18,911
17L	ILC	SF	21	(236,80,112)	2.27	8,224
19R	IDC	SF	11	(51,32,122)	2.74	34,547

\*Value obtained from literature.

#### ii. Tumor Size Error

The tumor size error was introduced in Section 3.3.4 for the clinical verification and validation study through Eq. 30. This was utilized to describe the error in the size prediction of the IRI-NE in comparison to the expected size from MRI. For this work, the error in the predicted size from the modified IRI-NE for the verification and parametric studies described above was compared to the ground truth size using Eq. 46. In this equation  $d_{GT}$  is the ground truth tumor diameter size either obtained from MRI for the verification study (Table 16) or from the parameters used to generate ground truth data in the first parametric study (Table 12).

$$E_d = d_{pred} - d_{GT} \quad (46)$$

#### iii. Internal Temperature Distribution

In order to quantify and evaluate the thermal effects of parametric studies 2-4, the internal temperature distribution along the centerline was extracted. This was conducted to provide

insight on the effects the tumor size and position had on the temperature distribution within each breast model. For comparison, the internal temperature distribution of the same breast models without a tumor are obtained.

iv. Maximum Surface Thermal Contrast

This final metric investigates the effects of the parameters utilized in parametric studies 2-5 on the surface temperature. To conduct a proper comparison, the maximum thermal contrast  $\Delta T_{max}$  was obtained for all cases using the following:

$$\Delta T_{max} = \max_T \Delta T \quad (47)$$

$$\Delta T = |T_{Cancer} - T_{Healthy}| \quad (48)$$

where  $\Delta T_{max}$  is the maximum thermal contrast,  $\Delta T$  is the surface temperature difference,  $T_{Cancer}$  is the surface temperature of the breast with cancer, and  $T_{Healthy}$  is the surface temperature of the breast without cancer. The thermal contrast, also known as the surface temperature difference between a breast with cancer and a breast without cancer, has been utilized in various studies [116,118–120,151,381,387,412,413]. Figure 34 shows an example of the thermal contrast obtained from a breast with cancer and the same breast without cancer, or the healthy breast. As the figure shows, there is a wide area that is effect by the tumor but what is important is that maximum contrast. The  $\Delta T_{max}$  for every case is compared to the thermal sensitivity value of  $T_{IR} = 20$  mK, the value of the IR camera utilized described in Section 3.2.1. The detectability of the parameters under study was measured by seeing if  $\Delta T_{max}$  was above the threshold value, or  $\Delta T_{max} \geq T_{IR}$ .

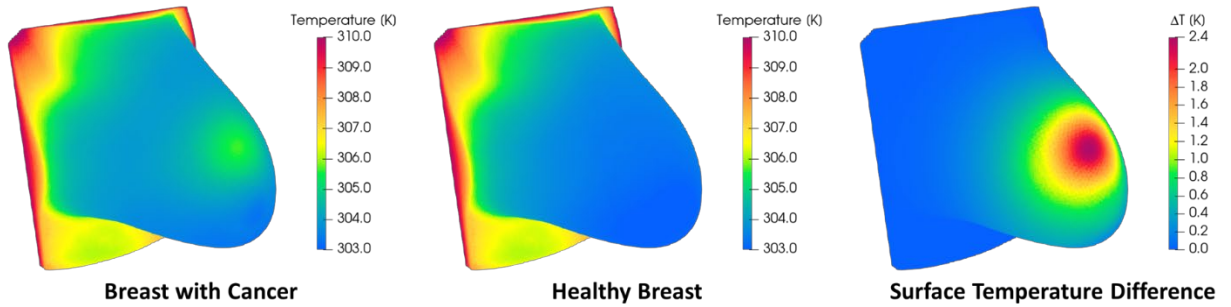


Figure 34. Example thermal contrast between a breast with cancer and the same breast without cancer, also known as the healthy breast.

### 3.5 Physiological Factors in Breast Cancer Detection

Physiological factors are the biological components that make up the functionality of a living organism. In terms of breast cancer, there are three main physiological factors such as breast density, breast vascularity and tumor vascularity. The breast density has been described and studied in the form of detectability (Section 3.4). The vascularity of the breast and of a breast tumor play a major role in the bioheat transfer within breast tissue through the blood perfusion terms. The current work investigates the influence of these physiological factors on surface temperatures and on the detection of cancer. This section goes over the methods utilized to model thermal artifacts such as vessels near the surface and their impact on detection. Finally, parametric studies of the breast tissue and tumor blood perfusion terms were conducted to understand their significance in the heat transfer.

#### 3.5.1 Modeling Thermal Artifacts

The female breast is an accessory reproductive organ and is a complex system made up of various tissue layers, the lobules, the ducts, and blood vessels. The blood vessels play an important role in supplying the breast with all the oxygen and nutrients it needs while regulating the temperature within the breast tissue. When capturing IR images of a breast, thermal artifacts created by superficial veins can be seen in the images along with their

thermal effects. Gershenson and Gershenson [414] showed the significance of superficial veins in a breast with cancer on the heat transfer in the tissue. The authors provided a method to identify and isolate vascularity in IR images to remove thermal effects from the veins. In the multi-view clinical IR images, thermal artifacts due to superficial veins were captured for the 23 biopsy-proven breast cancer patients described in Section 3.2.1. Figure 35 shows some examples of IR images of breasts that capture thermal artifacts for patients 4, 5, and 17. Patient 4 was reported to have bilateral breast cancer while both patients 5 and 17 were reported to have breast cancer in their left respective breasts. In comparison to their contralateral healthy breast for patients 5 and 17, it is hard to distinguish between a breast with and without cancer. Gonzalez-Hernandez et al. [150] showed that the inverse heat transfer approach was able to detect the presence and absence of breast cancer regardless of thermal artifacts caused by vascularity. The IRI-NE was also able to detect the presence and absence of breast tumors regardless of vascularity [415,416]. This was potentially due to the ROI selection method established by Gonzalez-Hernandez et al. [150] that ignored the superficial vessels. This work aims to quantify the effects of thermal artifacts caused by vascularity and ROI selection on the detection of breast cancer.

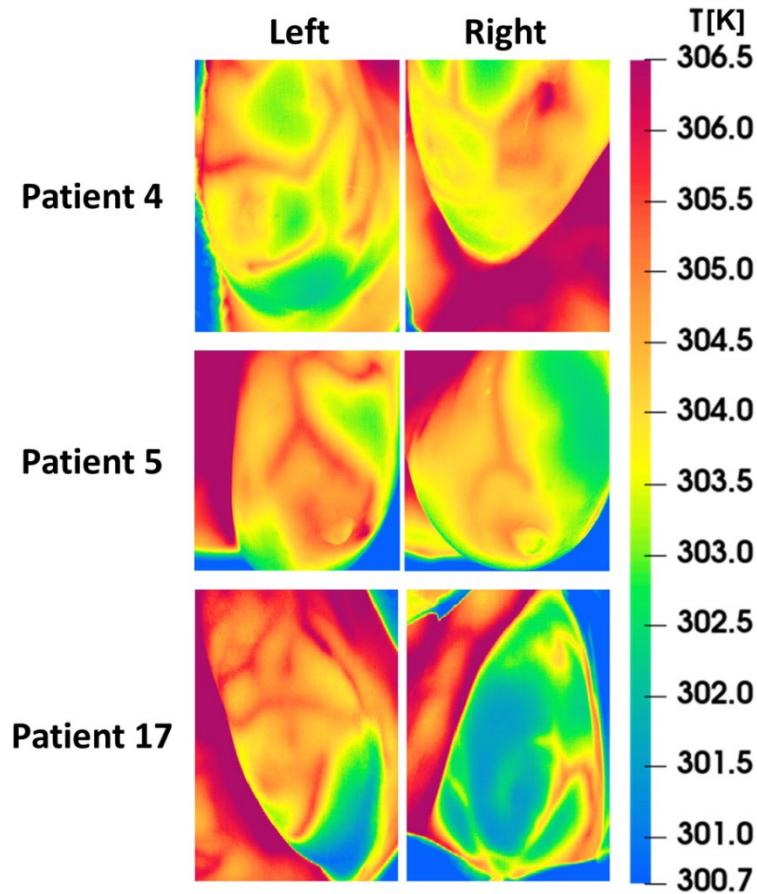


*Figure 35. Example IR images of patients with superficial vasculature for patients 4, 5, and 17.*

A simplistic approach was utilized to generate artificial thermal artifacts to test with the IRI-NE by modeling superficial veins. Superficial veins were modeled and incorporated inside the DBM of patient 17L using ANSYS SpaceClaim and Design Modeler. A 1-vessel model was generated for this work and placed 1.6 mm away from the surface, has a diameter of 1.6 mm, and was modeled to be  $\sim 28.0$  mm long. Figure 36 shows the DBM of patient 17L with the 1-vessel model inside the DBM as well as the individual vessel model with dimensions. This model was utilized for thermal simulations in ANSYS Fluent and inverse modeling for breast cancer detection using the modified IRI-NE. For thermal simulations in ANSYS Fluent the vessel was modeled as a fixed constant temperature of 310 K. At the interface between the vessel and breast tissue the wall is set to be coupled by

the Fluent software for thermal simulations. The thermal conductivity of blood was assigned to the vessel at  $k_b = 0.52$  W/m-K and a thermal conductivity of  $k_h = 0.45$  W/m-K was assigned to the breast and tumor tissues. The rest of the simulation was conducted using the thermal physical properties, bioheat transfer model, tumor heat generation model, and boundary conditions described in Section 3.2.3.

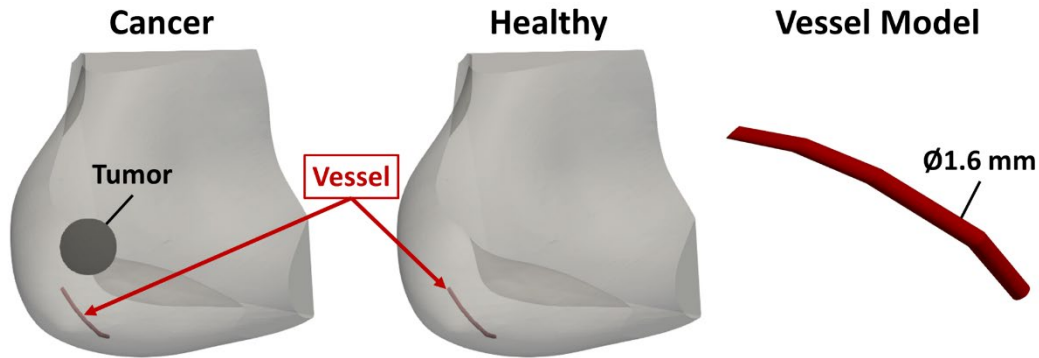


Figure 36. Vessel model placed inside patient 17L's DBM for a case with cancer and without cancer.

Synthetic IR surface temperatures were generated for two cases, a case with cancer and a case without cancer, for both models utilizing the method described in Section 3.4.3. Prior to conducting inverse modeling, ROI selection was conducted for the 3D surface temperatures. This was conducted through a developed algorithm that selected the ROI points  $(x_{ROI}, y_{ROI}, z_{ROI})$  based on the criteria  $x_{upper} \geq x_{ROI} \geq x_{lower}$ ,  $y_{upper} \geq y_{ROI} \geq y_{lower}$ , and  $z_{upper} \geq z_{ROI} \geq z_{lower}$ . These criteria depend on a lower and upper coordinate values that were established based on the method developed by Gonzalez-Hernandez et al. [150]. In order to quantify the effects of the vessel, three different ROI selections were conducted. For the first case (Case 1), the ROI was selected to be in the lower outer quadrant (LOQ) of the breast, based on the quadrant localization tumor classification

method described in Section 1.4.3c and shown in Fig. 8. For the second case (Case 2), the ROI was selected to be in the lower inner quadrant (LIQ) of the breast. The last case (Case 3) had the ROI be the entire breast surface similar to what was conducted in Section 3.4. Figure 37 shows the selected ROI for each ROI case for the 1-vessel model. Table 17 shows upper and lower coordinate values for each of these ROI cases. The 3D ROI selection algorithm was incorporated to the modified IRI-NE in order to select the same ROIs for comparison. The user had to change the values of the upper and lower coordinate criteria for the appropriate case study. Additionally, the modified IRI-NE was set to predict the tumor size, tumor location, and tissue thermal conductivity by the user prior to conducting inverse modeling.

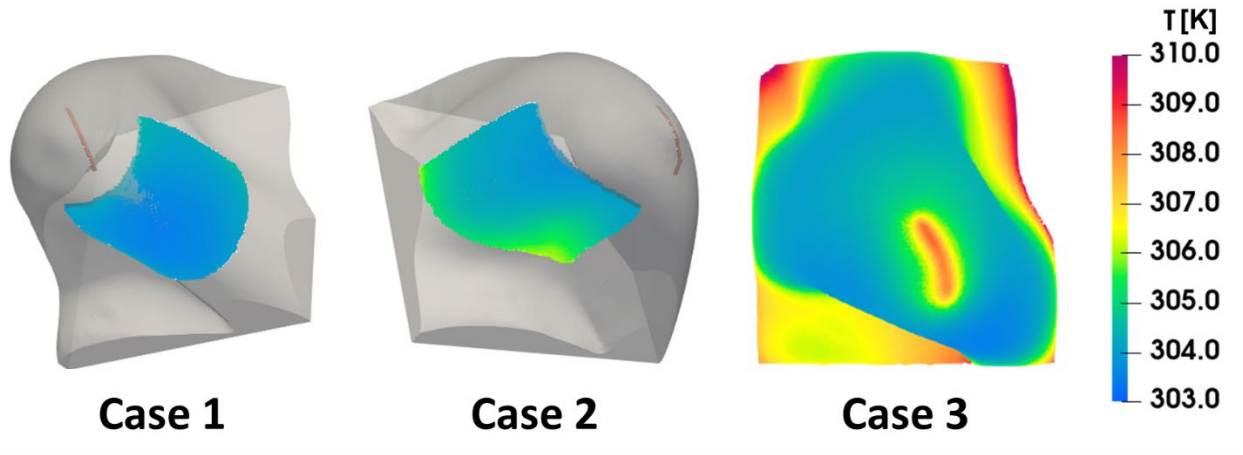


Figure 37. Selected ROI for the ROI cases for the 1-vessel model.

Table 17. Values for the upper and lower coordinates for each ROI case.

ROI Case	$x_{lower}$ [cm]	$x_{upper}$ [cm]	$y_{lower}$ [cm]	$y_{upper}$ [cm]	$z_{lower}$ [cm]	$z_{upper}$ [cm]
Case 1	23.6	29.7	4.7	9.0	4.9	12.0
Case 2	17.6	23.6	3.4	8.5	11.0	17.1
Case 3	17.6	29.7	0.4	11.0	4.9	17.1

### 3.5.2 Tumor Perfusion Heat Source Parametric Study

When cancer cells are present within the breast, a tumor is formed by creating its vascular environment through angiogenesis utilizing the surrounding breast vessels to obtain nutrients. Breast tumors are known to be very metabolically active and highly perfused malignant masses that generate heat. In bioheat transfer modeling, breast tumors are modeled as heat sources through their metabolic heat generation and blood perfusion heat source. However, the contribution of angiogenesis through the blood perfusion heat source is not as well quantified as the metabolic heat generation (Eq. 26). The current work focused on the blood perfusion heat source in patients 1R and 17L by conducting three parametric studies for comparison: (i) variation of tumor blood perfusion rate and no tumor heat generation, (ii) no tumor blood perfusion rate and variation of tumor heat generation, and (iii) variation of tumor heat generation and fixed perfusion rate. The first parametric study investigated the effect of only having the tumor blood perfusion as the tumor heat source by varying the blood perfusion term from  $1.8 \times 10^{-4}$  1/s to  $3.6 \times 10^{-2}$  1/s at  $1.8 \times 10^{-4}$  1/s increments and having  $Q_t = 0$  W/m<sup>3</sup> for tumor sizes of 10 mm to 20 mm at 0.5 mm increments. The range of the blood perfusion term was taken from literature that has reported a perfusion rate of  $1.3 \times 10^{-5}$  1/s to  $9.5 \times 10^{-4}$  1/s for healthy breast tissue and  $9.3 \times 10^{-4}$  1/s to  $2.1 \times 10^{-2}$  1/s for cancerous tissue [370]. The range for the tumor size was kept at 10 mm to 20 mm similar to the detectability study in order to test early detection and the effect of Tis and T1 stage tumors. Thermal simulations were conducted using ANSYS Fluent with the UDF utilized in Section 3.4.2 for parametric studies with the varying parameters being  $d_t$  and  $\omega_t$ . Additionally, the surface temperature extraction UDF was utilized to extract the surface temperature for each parametric case. The tumor was

placed at tumor position  $(x_{mid}, y_6, z_{mid})$  in the anterior region of the breast shown in Fig. 29 of the breast with a thermal conductivity of  $k_h = 0.42$  W/m-K.

The second parametric study had the tumor blood perfusion term as  $\omega_t = 0$  1/s and the  $Q_t$  for the same tumor sizes from the first parametric study (10 mm to 20 mm at 0.5 mm increments). The last parametric study utilized a fixed tumor perfusion heat source and variable metabolic activity for the same values utilized in the first and second parametric studies. Thermal simulations of the parameter cases were conducted using the parametric UDF from Section 3.4.2. Table 18 shows a summary of the parametric studies including the total number of parametric cases and total number of simulation iterations for each study for  $N = 200$ . Surface temperatures were also obtained for these parametric cases and compared using the following:

$$RMSE_{1,2} = \|\mathbf{T}_1 - \mathbf{T}_2\|_2 \quad (49)$$

$$RMSE_{1,3} = \|\mathbf{T}_1 - \mathbf{T}_3\|_2 \quad (50)$$

where  $RMSE$  is the root mean square error,  $\mathbf{T}_1$ ,  $\mathbf{T}_2$  and  $\mathbf{T}_3$  are the extracted surface temperatures for parametric studies 1, 2 and 3, respectively, and  $\|\cdot\|_2$  is the L2-norm. This metric was utilized to quantify the thermal effects of tumor angiogenesis on the surface temperature.

*Table 18. Parametric study overview including total number of parametric cases, total simulation iteration number, and parameters under study for each case for  $N = 200$ .*

Parametric Study	$M$	$i_{max}$	$\beta_j$
First Study	4200	840,000	$d_j, \omega_j$
Second Study	21	4,200	$d_j$
Third Study	21	4,200	$d_j$

## Chapter 4: Results

### 4.1 Breast Model Generation

The generation of patient-specific DBMs was conducted on all 23 biopsy-prove breast cancer patients described in Section 3.2.1 using the method developed by Gonzalez-Hernandez et al. [395] described in Section 3.2.2. These DBMs were generated for the use of bioheat transfer modeling of breast cancer through ANSYS Fluent simulation software. Although DBMs were available for the first seven patients, they were replicated to verify the method. Table 19 shows the size of the height  $H$ , width  $W$ , and length  $L$  of the breast surface for each patient case. The average  $H$ ,  $W$ , and  $L$  values for the right breast were 12.37 cm, 10.32 cm, and 8.66 cm, respectively. For the left breast the average  $H$ ,  $W$ , and  $L$  values for the right breast were 12.16 cm, 10.40 cm, and 8.68 cm, respectively. Patients that have  $L < 10$  cm in both breasts are patients 1, 4, 7, 9, 10, 12-14, 17-20, 22, and 23 while patients that have  $L \geq 10$  cm are patients 2, 3, 5, 6, 8, 11, 15, 16, and 21.

Table 19. Breast surface measurements of the right and left breast for each patient case.

Patient	Right Breast			Left Breast		
	H [cm]	W [cm]	L [cm]	H [cm]	W [cm]	L [cm]
1	8.82	5.69	5.19	8.96	5.51	5.06
2	9.10	6.00	10.38	9.10	5.95	10.19
3	10.24	7.25	10.13	10.10	6.88	10.45
4	9.66	11.65	9.01	9.52	11.71	9.40
5	12.60	11.82	12.53	12.88	11.41	12.51
6	10.06	11.06	12.02	10.06	10.73	11.73
7	11.34	4.78	7.10	10.92	5.27	6.26
8	14.89	14.36	10.03	16.41	16.15	10.34
9	13.97	10.04	7.08	13.57	10.37	7.01
10	13.49	13.25	5.18	10.84	12.88	5.26
11	15.14	14.26	10.78	15.00	14.45	11.37
12	12.81	8.81	9.15	14.33	9.03	7.20
13	11.74	13.32	7.36	12.50	11.89	4.66
14	10.46	8.27	6.68	10.43	9.12	7.86
15	14.80	13.53	10.82	13.89	12.76	11.19
16	17.04	15.72	11.64	16.87	14.96	11.17
17	12.16	10.89	7.79	10.85	10.29	8.83
18	11.98	7.81	6.26	12.28	8.24	7.54
19	14.19	8.05	6.10	15.96	8.65	7.62
20	8.76	8.79	7.35	8.18	8.98	7.84
21	14.57	9.78	10.39	11.55	9.86	10.51
22	15.58	9.08	6.87	14.97	9.07	6.49
23	11.16	13.04	9.34	10.40	14.93	9.26

#### 4.2 Detection of Breast Cancer on Twenty-Three Patients

The IRI-NE was developed to detect the presence of breast cancer on 23 biopsy-proven patients utilizing their respective IR surface temperatures captured by an in-house IRI system. The first seven patients were utilized to verify the algorithm worked effectively and efficiently. An additional 16 patients were utilized for validation of the algorithm to detect breast cancer. Figure 38 shows the comparison of the predicted tumor size from the IRI-NE and the tumor size obtained through MRI for the seven previous patients (Fig. 38a) and 16 new patients (Fig. 38b). As the results showed, the algorithm was able to detect the presence of breast cancer for all patients regardless of cancer type, breast density, and tumor depth. The results for the previous seven patients were similar to the results obtained by

Gonzalez-Hernandez et al. [150]. For both the previous and new cases, the IRI-NE was able to predict the presence of cancer for tumors smaller than 1 cm. The algorithm is set to predict tumor size values between 1 cm to 5 cm which means the smallest tumor the IRI-NE was able to detect was 1 cm. This shows that a tumor smaller than 1 cm can provide enough heat generation that would be picked up by the IR camera and the algorithm. In terms of the contralateral healthy breast, except for patient 4 who had bilateral breast cancer, the IRI-NE was able to predict the absence of breast cancer. The algorithm did this by placing the tumor outside of the breast domain or at the chest wall where the heat source did not have a significant impact on the surface temperature. The IRI-NE obtained results after an average time of 2.5h when using a 4 core CPU computer and 30 min when using a 10 core CPU computer.

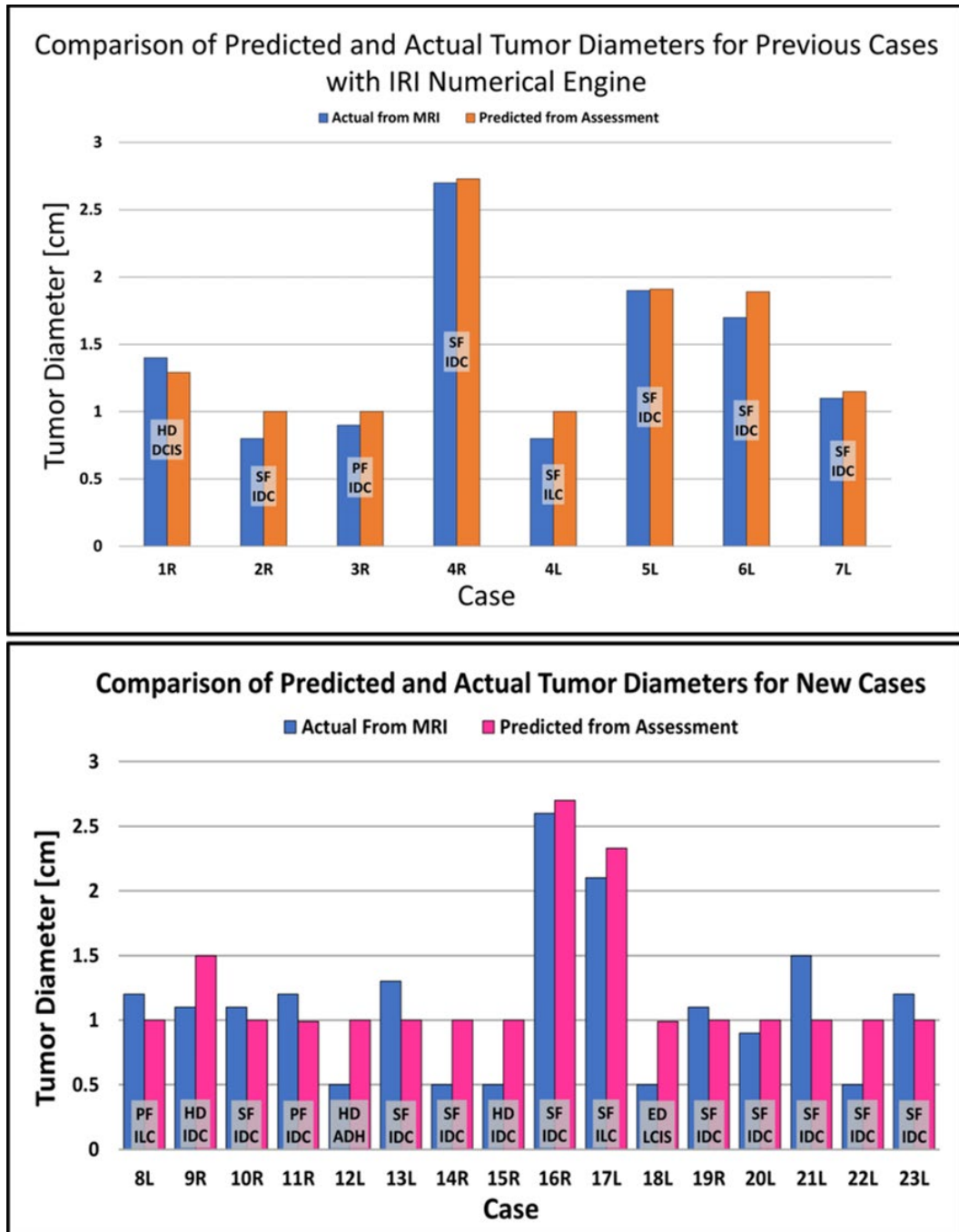


Figure 38. Validation results of the IRI-NE for the (a) seven previous cases and (b) 16 additional cases.

Table 20 provides the error, percent error, and percent error in tumor size prediction from the IRI-NE. Negative error values show an underestimation in prediction while positive error values show an overestimation in prediction. Tumors that give large errors are the 5

mm tumors as they are predicted to be 10 mm due to constraints implemented from Gautherie's relation (Eq. 26). There are five patients that had 5 mm tumors (patient cases 12L, 14R, 15R, 18L, and 22L). Omitting these patients gives the mean, max, and min absolute errors in tumor size as 1.8 mm, 5.0 mm, and 0.1 mm, respectively. Similarly, the mean, max, and min percent errors in tumor size were found to be 14.4%, 36.4%, and 0.5%, respectively. Overall, when comparing the predicted tumor size and actual tumor size for all cases gives a coefficient of determination of  $R^2 = 0.9574$ , as shown in Fig. 39. This shows that the algorithm has good accuracy in predicting the tumor size from IR surface temperature. Although results show that the IRI-NE is able to accurately detect the presence and absence of breast cancer, the sample size of patients is too small to make any definitive conclusions. Therefore, there is a need for a larger clinical study in order to test the efficacy of this approach. Additionally, the ability of the IRI-NE to detect benign tumors is unknown due to all patients having malignant tumors. Further data collection and clinical studies are warranted for understanding the capabilities of the algorithm to detect benign tumors.

Table 20. Results for tumor size prediction error, absolute error, and percent error for all patient cases.

Case	$d_{pred}$ [mm]	$d_{exp}$ [mm]	$E_d$ [mm]	$E_{d,Abs}$ [mm]	$E_{d,\%}$ [%]
1R	12.9	14	-1.1	1.1	7.9
2R	10	8	2.0	2.0	25.0
3R	10	9	1.0	1.0	11.1
4R	27.3	27	0.3	0.3	1.1
4L	10	8	2.0	2.0	25.0
5L	19.1	19	0.1	0.1	0.5
6L	18.9	17	1.9	1.9	11.2
7L	11.5	11	0.5	0.5	4.5
8L	10	12	-2.0	2.0	16.7
9R	15	11	4.0	4.0	36.4
10R	10	11	-1.0	1.0	9.1
11R	10	12	-2.0	2.1	17.5
12L	10	5	5.0	5.0	100
13L	10	13	-3.0	3.0	23.1
14R	10	5	5.0	5.0	100
15R	10	5	5.0	5.0	100
16R	27	26	1.0	1.0	3.8
17L	23.3	21	2.3	2.3	11
18L	10	5	5.0	5.0	100
19R	10	11	-1.0	1.0	9.1
20L	10	9	1.0	1.0	11.1
21L	10	15	-5.0	5.0	33.3
22L	10	5	5.0	5.0	100
23L	10	12	-2.0	2.0	16.7

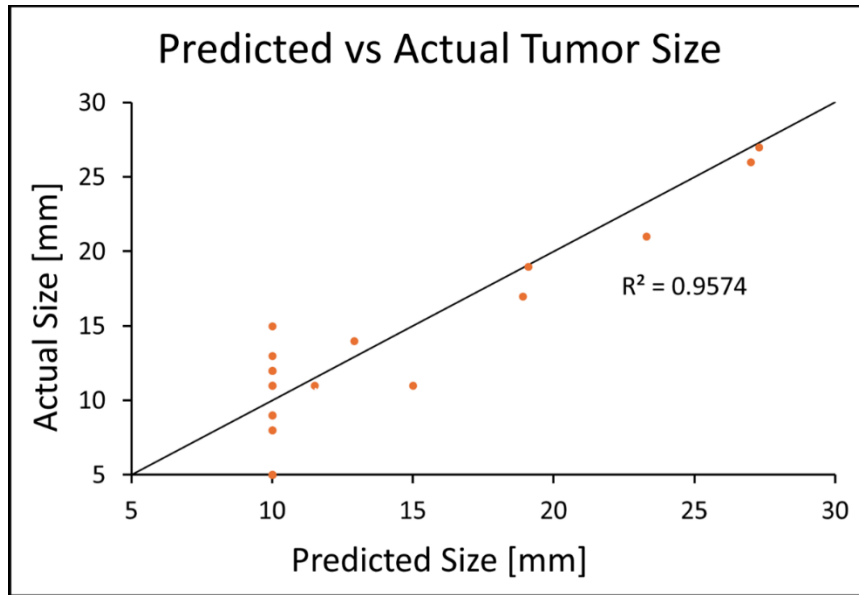


Figure 39. Predicted tumor size vs actual tumor size obtained from MRI for all cases.

### 4.3 Breast Cancer Detection using Surface Temperature

#### Data

Prior to establishing the detectability limits of the IRI-NE through various cases, a method was presented in Section 3.4.3 to generate synthetic IR surface temperatures to conduct inverse modeling using a modified IRI-NE. This section covers two studies utilized to verify the modified IRI-NE and the effect of noise in the detection of breast cancer.

#### 4.3.1 Verification with Eight Patients

To verify that the modified IRI-NE works with synthetic IR surface temperatures, patient cases were utilized to create ground truth data using the properties and approach described in Section 3.4.5. Comparison was conducted between the results obtained using synthetic IR and clinical IR to understand how the data effect detection. Figure 40 shows the surface temperature distribution of the ground truth synthetic IR and clinical IR for patient case 1R, as well as the predicted outcome from the IRI-NE. The rows compare the clinical IR ground truth and predicted surface temperature distribution with their synthetic IR

counterpart. As the results show, the synthetic IR is able to mimic the surface temperature distribution captured in the clinical IR. The columns compare the ground truth IR with the predicted temperature distribution results obtained from the inverse model. In comparison, the predicted temperatures obtained using the synthetic IR had better results than the predicted obtained from the clinical IR. This was true for all cases when comparing the clinical IR and synthetic IR ground truth and prediction.

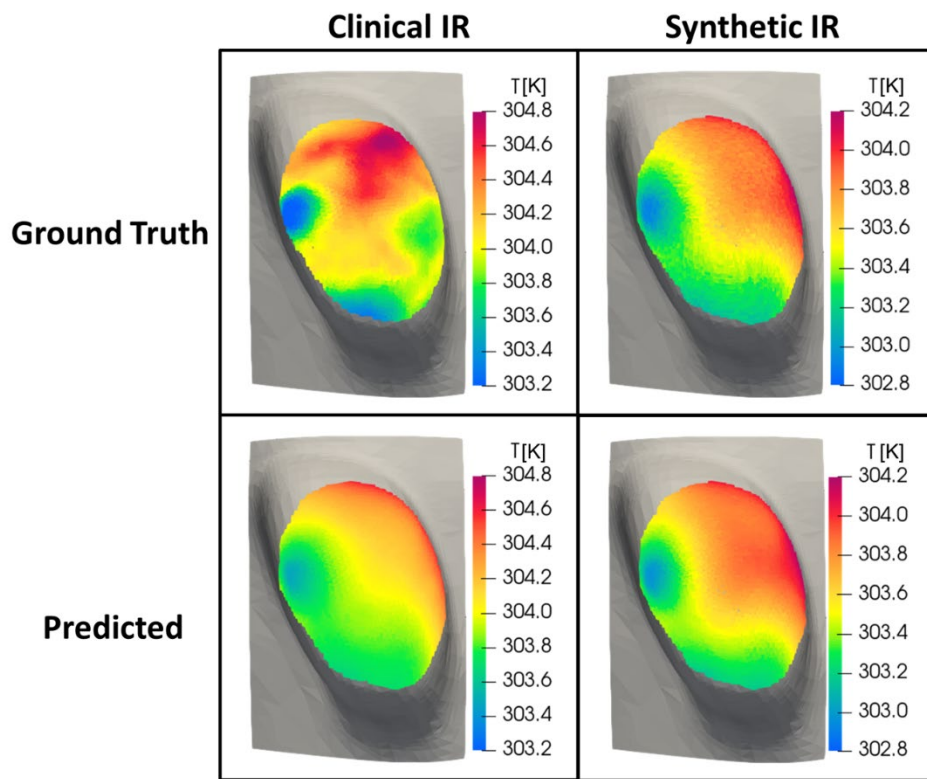


Figure 40. Verification results and comparison for patient case 1R.

Table 21 shows the error in tumor size prediction using synthetic IR and clinical IR surface temperatures with the IRI-NE. For all cases, the algorithm detected the presence of breast cancer with a maximum absolute error of 3 mm, excluding patient case 12L. The prediction errors for the cases that utilized synthetic IR data were very similar to the cases that utilized clinical IR data. The differences in tumor prediction may be due to various factors such as

the tumor position, breast shape, breast size, breast density and the type of noise added to the synthetic data. Patient cases 8L, 10R, 12L, 13L, and 19L were cases of patients with deep tumors, tumors in the posterior region. Patient cases 1R and 17L are cases with tumors closer to the anterior region, or near the breast surface. This shows the importance of conducting the detectability study described in Section 3.4 to determine the factors that affect detection. Patient case 12L was modeled with an artificial 5 mm tumor with an approximate metabolic heat generation value of  $70,000 \text{ W/m}^3$ , unlike the other cases that utilized Eq. 26. This is due to the heat generation rate being unknown for tumors smaller than 10 mm. Additionally, Eq. 26 was developed by Gautherie [112–114] to work for tumor sizes ranging from 10 mm to 50 mm based on the data he collected. The modified IRI-NE utilized this range as a constraint for prediction giving a 10 mm tumor as the smallest possible prediction.

*Table 21. Comparison of tumor size prediction error between results obtained using synthetic IR and clinical IR surface temperatures.*

Patient	Ground Truth	Synthetic IR		Clinical IR	
	$d_{act}$ [mm]	$d_{pred}$ [mm]	Error [mm]	$d_{pred}$ [mm]	Error [mm]
1R	14	12.5	-1.5	12.9	-1.1
8L	12	15	3.0	10	-2.0
10R	11	14	3.0	10	-1.0
12L	5	10	5.0	10	5.0
13L	13	10	-3.0	10	-3.0
17L	21	23.3	2.3	23.3	2.3
19R	11	12	1.0	10	-1.0

To verify the modified IRI-NE can predict the absence of breast cancer, synthetic IR surface temperature data of a patient without cancer was utilized by the algorithm. For this case, the algorithm was able to predict the absence of breast cancer by placing the tumor at the chest wall. Figure 41 shows the surface temperature distribution for the ground truth data and predicted data of the healthy patient case. The maximum and mean absolute

difference in surface temperature between the predicted and ground truth data was 0.18 K and 0.04 K, respectively.

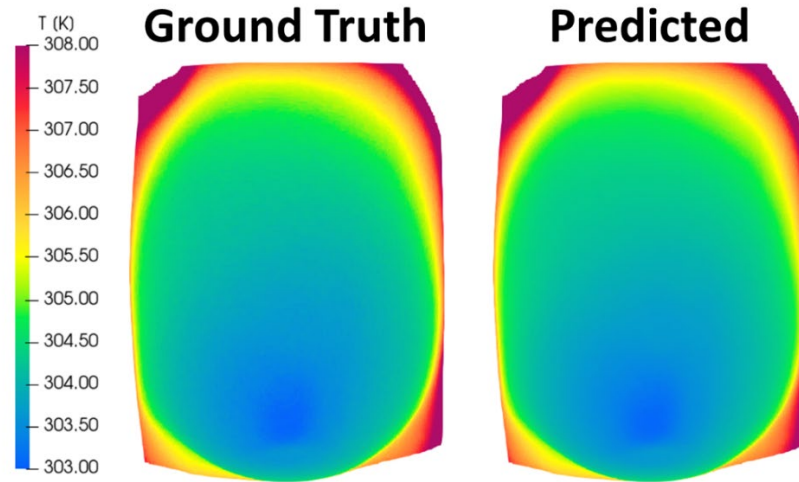


*Figure 41. Comparison of surface temperature distribution of the ground truth and predicted data for patient 9L case without cancer.*

#### 4.3.2 Effect of Noise

Synthetic IR surface temperatures were generated using a Gaussian noise with the noise level representing the thermal sensitivity of an IR camera. To quantify the effect of this noise level on the detection, four other noise levels were utilized to generate ground truth data and tested with the IRI-NE. The four noise levels selected for testing were 0 mK (no noise), 5 mK, 10 mK, and 40 mK in addition to the 20 mK noise utilized in the previous section. Figure 42 shows absolute error in tumor size for the different noise levels. Utilizing ground truth data with no noise gives the best results with an absolute error of 1.48 mm, as expected. All noise levels provide a similar absolute error value giving a mean absolute error of 1.51 mm with a standard deviation of 0.02 mm. The 20 mK noise provides an absolute error of 1.52 which is 0.04 mm higher than the 0 mK noise level and 0.01 mm from the mean value. In comparison with the clinical IR data absolute error of 1.1 mm, the

mean absolute error for all the noises is 0.41 mm higher while the 20 mK noise level is 0.42 mm higher. The difference may be due to the thermal distribution from the clinical IR data having more detail than the synthetic IR due to the vasculature of the breast and tumor. The results show that utilizing synthetic IR data with ground truth tumor size and position can provide a good representation of the clinical IR data. Additionally, the results show that the effect of noise is minimal on the accuracy of detection. However, more tests are needed to evaluate the effect of the other factors described in Section 3.4 that may affect the detectability of the IRI-NE.

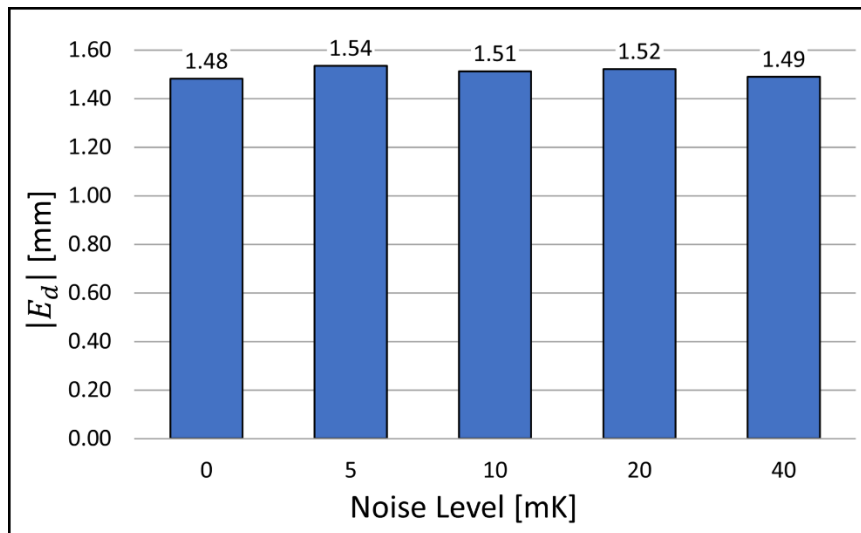


Figure 42. Effect of noise level on the detection of breast cancer.

#### 4.4 Detectability Limits of IRI-Numerical Engine

This section presents all the results for the parametric studies and the detectability study described in Section 3.4. Section 4.4.1 shows the effect of tumor size and position on the tumor size prediction for the two breast shapes (concave vs convex). Section 4.4.2 shows the effect of tumor size and position on the thermal contrast of the two breast shapes (concave and convex). Section 4.4.3 shows the effect of breast shape (concave vs convex)

and size (small, medium, and large) on the thermal contrast for models with tumors of various sizes and locations. Section 4.4.4 shows the effect of breast density through the thermal conductivity on the thermal contrast for tumors of various sizes in the posterior region of the convex geometry.

#### 4.4.1 Error in Tumor Size

The ground truth data generated for the first parametric study described in Section 3.4.2 was utilized with the IRI-NE to conduct inverse modeling using synthetic IR surface temperatures. This was conducted on the two base geometries (concave and convex) for 2 tumor sizes (10 mm and 20 mm) and 10 tumor positions described in Section 3.4.1. The goal of this study was to investigate the effect of tumor size and position in each base geometry on the detection accuracy.

Figure 43 shows the predicted tumor size for the concave geometries at two different noise levels (20 mK and 40 mK). The blue circles represent the actual tumor size while the dark grey circles represent the predicted tumor size from the algorithm. Both the circles are not to scale of their represented sizes, but the sizes of the dark grey circles are with respect to the size of the blue circles. The values inside of the circles are the values of the predicted tumor size in millimeters. The first column provides the predicted tumor sizes for the 10 mm (Fig. 43a) and 20 mm (Fig. 43c) at the 10 tumor positions when utilizing 20 mK noise level on the ground truth data. The second column (Figs. 43b and 43d) provides the results for the cases that utilized a 40 mK noise level on the ground truth data. For all cases, the algorithm was able to predict the presence of breast cancer regardless of tumor size, tumor position, and noise level. As the results show, the noise level does not have a significant impact on the predicted size given that the predicted tumor size is similar between the 20

mK and 40 mK cases. However, the tumor size and position have been shown to have a bigger impact on the prediction size of the algorithm. From Fig. 43, it can be observed that the 20 mm tumors are predicted more accurately than the 10 mm tumors regardless of tumor position. Although the results of the tumor position are not provided as the focus is on the tumor size prediction, the IRI-NE predicted an equivalent tumor size at the appropriate location to match the surface temperatures from the ground truth data.

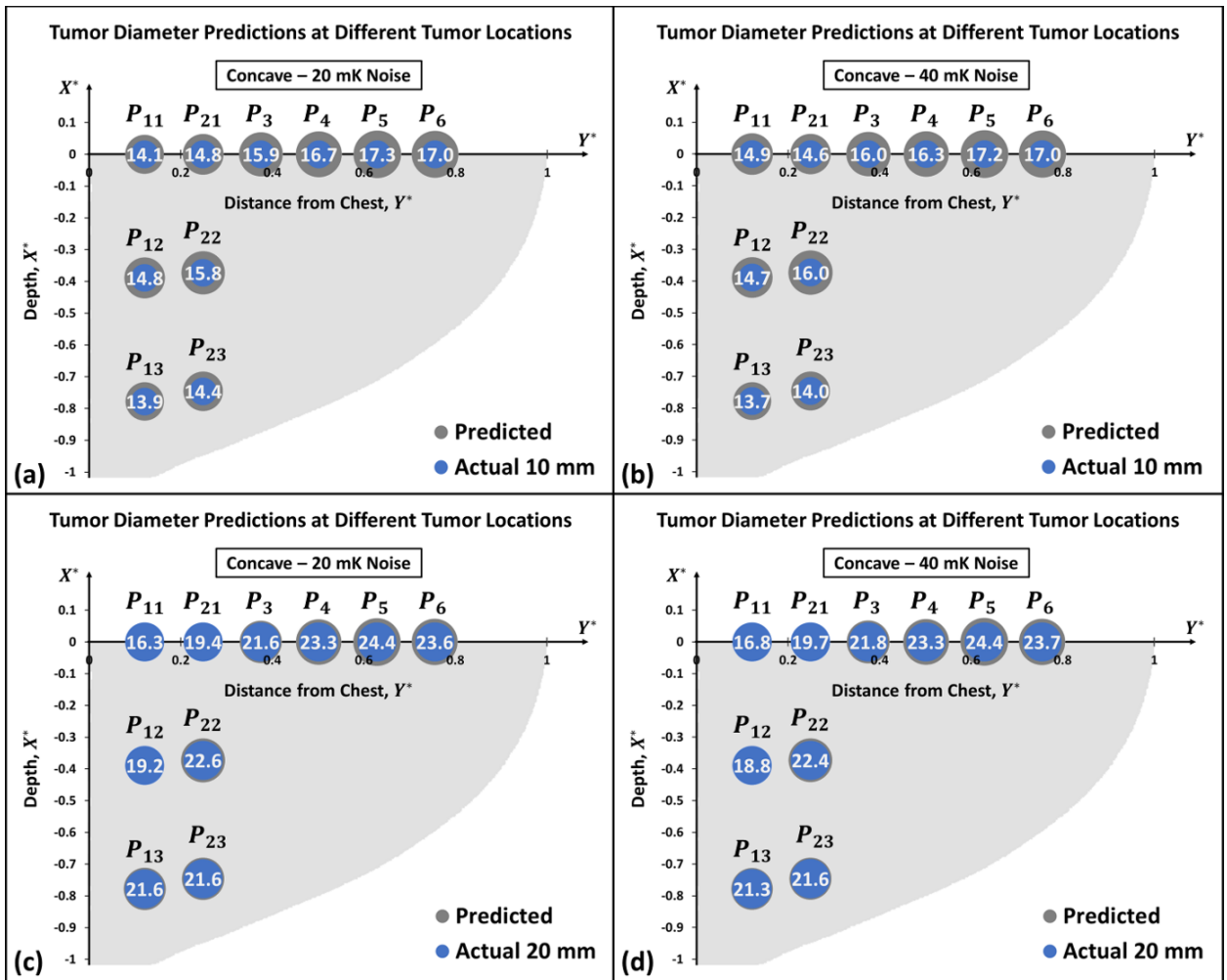


Figure 43. Prediction results for the concave base model with a (a) 10 mm tumor with 20 mK noise, (b) 10 mm tumor with 40 mK noise, (c) 20 mm tumor with 20 mK noise, and (d) 20 mm tumor with 40 mK noise.

Further analysis of the results was conducted to determine the effect of tumor depth on the tumor size prediction on the concave base geometry. Table 22 shows error in tumor size  $E_d$  for the concave base case for the two tumor sizes with the two noise levels. Similar to results shown in Fig. 43, the noise level has no significant impact on  $E_d$ , but the tumor size does have a significant impact. This may be due to the bigger tumors having a wider span of heat transfer than smaller tumors. The median, mean, and max absolute error  $|E_d|$  in tumor size for the 10 mm case with 20 mK noise was 5.3 mm, 5.5 mm, and 7.3 mm. For the 20 mm case with 20 mK noise the median, mean, and max  $|E_d|$  in tumor size was 2.1 mm, 2.4 mm, and 4.4 mm. This shows that the tumor size was more accurately predicted in the 20 mm tumor cases compared to the 10 mm tumor cases. Additionally, the results show that the algorithm can obtain accurate prediction regardless of tumor depth.

Table 22. Error in tumor size at various depths in the concave base model for the 10 mm and 20 mm tumor cases at 20 mK and 40 mK noise levels.

Tumor Depth	Location	10 mm Tumor		20 mm Tumor	
		20 mK Noise	40 mK Noise	20 mK Noise	40 mK Noise
		$E_d$ [mm]		$E_d$ [mm]	
Posterior	$P_{11}$	4.1	4.9	-3.7	-3.2
	$P_{12}$	4.8	4.7	-0.8	-1.2
	$P_{13}$	3.9	3.7	1.6	1.3
	$P_{21}$	4.8	4.6	-0.6	-0.3
	$P_{22}$	5.8	6.0	2.6	2.4
	$P_{23}$	4.4	4.0	1.6	1.6
Mid	$P_3$	5.9	6.0	1.6	1.8
	$P_4$	6.7	6.3	3.3	3.3
	$P_5$	7.3	7.2	4.4	1.1
Anterior	$P_6$	7.0	7.0	3.6	3.7

For the convex case, similar results were observed in terms of the tumor prediction at the various locations for the two tumor sizes (10 mm and 20 mm) and two noise levels (20 mK and 40 mK) as shown in Fig. 44. Just like the concave cases, the algorithm was able to

detect the presence of the tumor for all tumor positions and tumor cases with the noise level playing little to no significance in the predicted tumor size. The tumor size played a role in the accuracy of predicted size with 20 mm tumors having a higher prediction accuracy in comparison to 10 mm tumors.

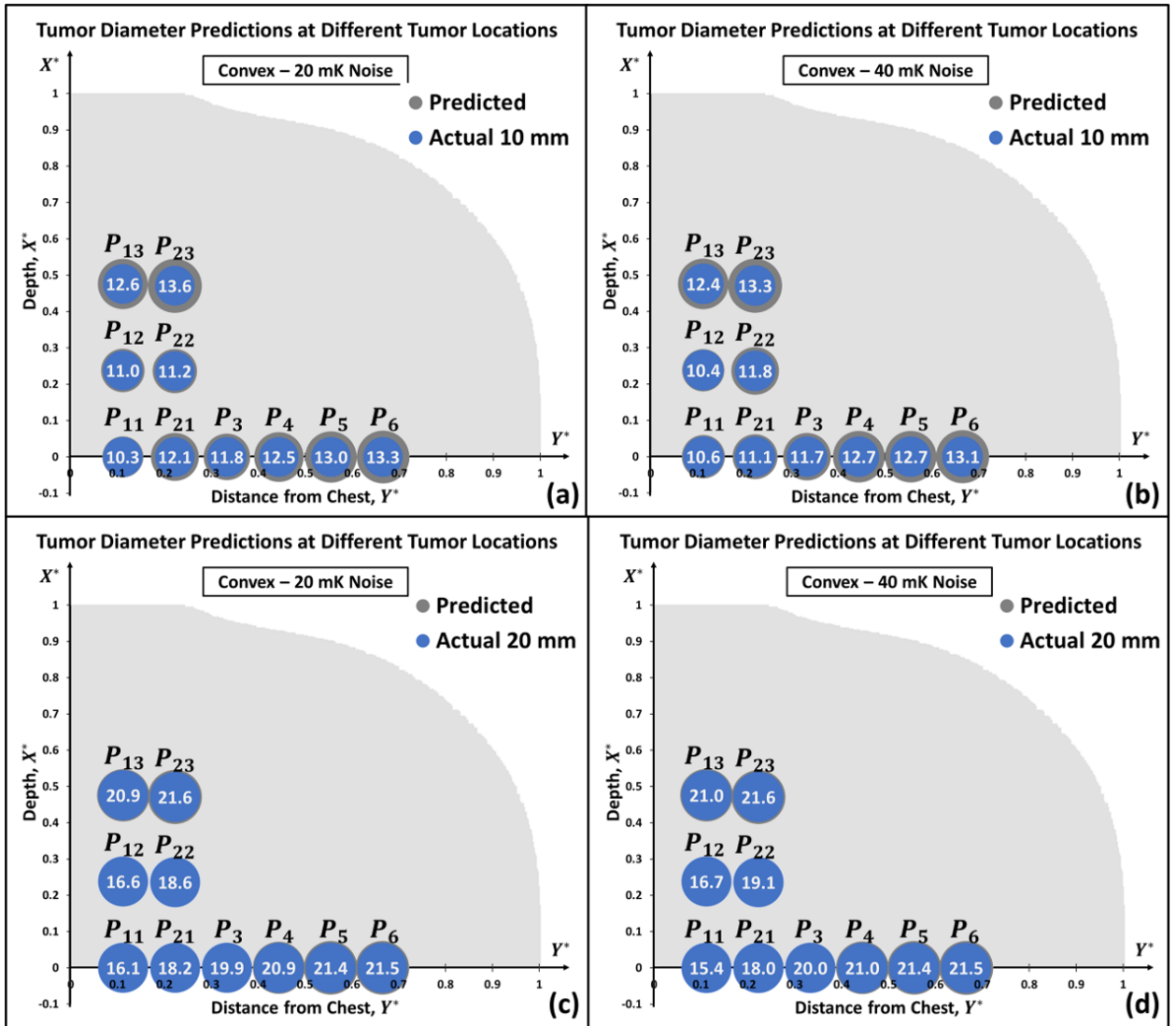


Figure 44. Prediction results for the convex base model with a (a) 10 mm tumor with 20 mK noise, (b) 10 mm tumor with 40 mK noise, (c) 20 mm tumor with 20 mK noise, and (d) 20 mm tumor with 40 mK noise.

Analyzing  $E_d$  for the convex model further shows that the noise level did not affect the accuracy of prediction while the tumor size played a major role. Table 23 provides the error

in tumor size  $E_d$  for the convex base cases at the various tumor depth. The mean, median, and maximum  $|E_d|$  for the 10 mm tumor with 20 mK noise cases were 2.1 mm, 2.3 mm, and 3.6 mm, respectively. For the 20 mm tumor with 20 mK noise cases, the mean, median, and maximum  $|E_d|$  were 1.7 mm, 1.5 mm, and 4.0 mm. As the results show, the mean and median  $|E_d|$  values for the 10 mm tumor cases were larger than the 20 mm cases. However, the maximum  $|E_d|$  values for both cases were similar which shows that breast shape or size may play a bigger role in the prediction. This is due to the fact that the predicted tumor is an equivalent tumor placed at the appropriate tumor location to match the surface temperature. As for the noise level, the  $E_d$  values did not significantly change when utilizing different noise levels, but a higher difference for the 20 mm tumor cases was observed in comparison to the concave base model cases. Further analysis was needed to verify that the noise level impact at the various tumor positions in the convex base model.

*Table 23. Error in tumor size at various depths in the convex base model for the 10 mm and 20 mm tumor cases at 20 mK and 40 mK noise levels.*

Tumor Depth	Location	10 mm Tumor		20 mm Tumor	
		20 mK Noise	40 mK Noise	20 mK Noise	40 mK Noise
		$E_d$ [mm]		$E_d$ [mm]	
Posterior	$P_{11}$	0.3	0.6	-4.0	-4.7
	$P_{12}$	1.0	0.4	-3.4	-3.3
	$P_{13}$	2.6	2.4	0.9	1.0
	$P_{21}$	2.1	1.1	-1.8	-2.0
	$P_{22}$	1.2	1.8	-1.4	-0.9
	$P_{23}$	3.6	3.3	1.6	1.6
Mid	$P_3$	1.8	1.7	-0.1	0.0
	$P_4$	2.5	2.7	0.9	1.0
	$P_5$	3.0	2.7	1.4	1.4
Anterior	$P_6$	3.3	3.1	1.5	1.5

Further analysis was conducted for the 20 mm tumor case placed along the centerline ( $P_1, P_2, P_3, P_4, P_5, P_6$ ) by conducting inverse modeling with the IRI-NE for ground truth

data at various noise levels (0 mK, 5 mK, 10 mK, 20 mK, and 40 mK). Figure 45 shows the  $|E_d|$  for a 20 mm tumor at the different positions with different noise levels including the average  $|E_d|$  at each position. As the figure shows, the noise level had little to no impact on the prediction especially for positions  $P_3$ ,  $P_4$ ,  $P_5$ , and  $P_6$  which had standard deviation values of  $|E_d|$  of 0.05 mm, 0.05 mm, 0.04 mm and 0.02 mm, respectively. The mean  $|E_d|$  values at positions  $P_3$  to  $P_6$  were 0.09 mm, 0.91 mm, 1.39 mm, and 1.51 mm, respectively. The values were 0.02 mm, 0.04 mm, 0.02 mm and 0.03 mm away from the  $|E_d|$  obtained from the 0 mK noise level at their respective positions. The positions that had the most impact by the noise level were at position  $P_1$  and  $P_2$ . At position  $P_1$  the value of  $|E_d|$  goes from 3.98 mm to 4.65 mm and has a mean  $|E_d|$  value of 4.29 mm with standard deviation of 0.25 mm. For  $P_2$  the results show a small impact from the noise level with values of  $|E_d|$  going from 1.65 mm to 2.04 mm and with a mean  $|E_d|$  value of 1.78 mm with a standard deviation of 0.15 mm. The higher standard deviation values may be due to  $P_1$  and  $P_2$  being closer to the chest wall region for the convex base model in comparison to  $P_1$  and  $P_2$  in the concave base model. This shows that breast shape and size may play a bigger role in the accuracy of detection especially for deep tumors. Regardless of the higher standard deviation  $|E_d|$  value, the  $|E_d|$  values for the 20 mK noise level at every position was either better or about the same as the average  $|E_d|$  value and the  $|E_d|$  value for the 0 mK noise level. This further shows the validity of utilizing synthetic IR data made with 20 mK noise with the IRI-NE for accuracy prediction of the presence of breast cancer.

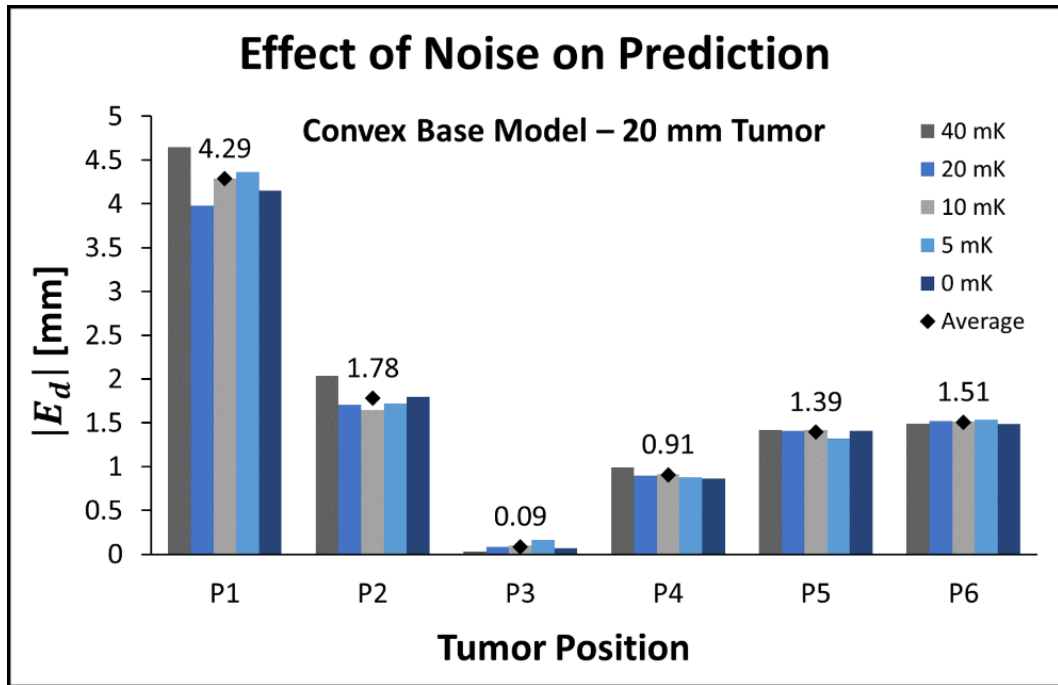


Figure 45. Effect of noise level at the centerline tumor position on the tumor size prediction error.

#### 4.4.2 Effect of Tumor Diameter and Depth

The previous section showed that the IRI-NE is able to predict the presence of tumors regardless of tumor location and tumor size in each base model. Additionally, the results from the previous section showed that a tumor in the first tumor position  $P_1$  in the convex case had a larger prediction error. To understand the reasoning for this, the internal temperature distribution of the breast was investigated using the method described in Section 3.4.5 for the convex base model. For this method, the temperature along the centerline was taken for a tumor in position  $P_1$  for various tumor sizes. Figure 46 shows a plot of the internal temperature distribution along the centerline for varying tumor sizes 1 cm to 2 cm at 0.2 cm increments and for the same breast model without a tumor. The results show an increase in temperature due to the presence of a tumor when compared to the breast with no tumor. The maximum internal temperature increases from 309.97 K for a

breast without a tumor to 310.08 K when introducing a 1 cm tumor. Although the metabolic heat generation of a 1 cm tumor is larger than a 2 cm tumor, the internal temperature increases to 311.35 K when introducing a 2 cm tumor. This is due to larger tumors affecting larger volumes of tissue in comparison to smaller tumors and therefore distributing a larger volume of heat. All tumors introduce a variation to the temperature distribution especially in the region where the tumor spreads (tumor diameter length). The increase occurs gradually as the healthy tissue turns into cancerous tissue and then decreases as the cancer tissue turns back into healthy tissue. This decrease in temperature that matches the trend observed in the breast with no tumor is due to perfusion term in healthy tissue from Eq. 24 acting as a heat sink. This simulates how the body regulates its temperature even after an additional heat source. The temperature distribution continues to drop to the closer surface due to the convective heat transfer from the ambient temperature cooling off the skin. However, the presence of a tumor introduces a slight increase in temperature at the surface. Without the presence of a tumor the temperature at the surface along the centerline is 303.35 K which increases to 303.4 K when a 1 cm tumor is introduced and to 303.6 K when a 2 cm tumor is introduced. The 50 mK difference at the surface between a breast without a tumor and with a 1 cm tumor shows why inverse heat transfer-based detection is able to detect the presence of a tumor heat source. These results show the thermal impact deep tumors have on the internal temperature of the body and on the surface temperature.

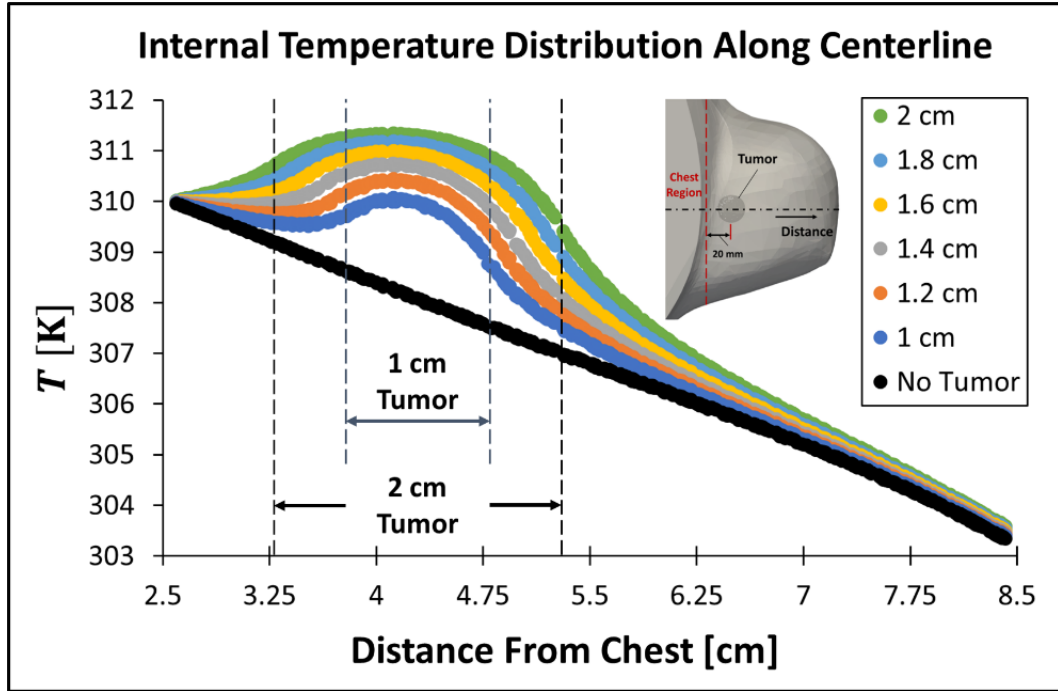


Figure 46. Internal temperature distribution plotted against the distance along the center line for patient 1R with varying tumor sizes.

Further studies were conducted to investigate the effect of the tumor size and location on the surface temperature using the maximum thermal contrast  $\Delta T_{max}$  described in Section 3.4.5. This was done by using the results of the second parametric study described in Section 3.4.2. The value of  $\Delta T_{max}$  for each base model (concave and convex) with tumors of various sizes (10 mm to 20 mm at 2.5 mm increments) at the centerline positions  $P_1$  to  $P_6$  was utilized to observe the effects on the breast surface. The tumor positions were represented using a normalized distance from the chest  $Y^*$  using the method from Eq. 39 described in Section 3.4.1.

Figure 47 shows the calculated  $\Delta T_{max}$  values for the concave (Fig. 47a) and convex (Fig. 47b) base model cases. For both breast models and all parametric cases, the  $\Delta T_{max}$  value was above the 20 mK thermal sensitivity threshold. This shows that an IR camera would be able to capture the surface temperature effected by these size tumors at various depths.

It is important to note that the  $\Delta T_{max}$  values for the convex cases are higher than the  $\Delta T_{max}$  values in the concave cases. An example can be seen for a 10 mm at the first tumor position in the concave base model at  $Y^* = 0.12$  having  $\Delta T_{max} = 0.73$  K, while in a convex base model at  $Y^* = 0.11$  having  $\Delta T_{max} = 0.92$  K. This validates that the breast shape also influences  $\Delta T_{max}$ , but further tests are needed to quantify the influence. The results show that as the tumor size increases or as the tumor is placed further away from the chest wall region, the value of  $\Delta T_{max}$  also increases for both breast models. The increase in  $\Delta T_{max}$  as the tumor is placed further away from the chest wall region was observed to increase nonlinearly. This shows that the tumor size and location highly affect the surface temperature distribution, as well as shows the concept of utilizing equivalent tumors. For example, a 10 mm tumor placed at  $Y^* = 0.67$  can have an equivalent 15 mm tumor at about  $Y^* = 0.52$  in the convex base model that can have the same  $\Delta T_{max}$  according to the plot in Fig. 47b. For the concave base model, a 15 mm tumor at  $Y^* = 0.63$  can have an equivalent 20 mm tumor at about  $Y^* = 0.51$  with the same  $\Delta T_{max}$  according to the plot in Fig. 47a.

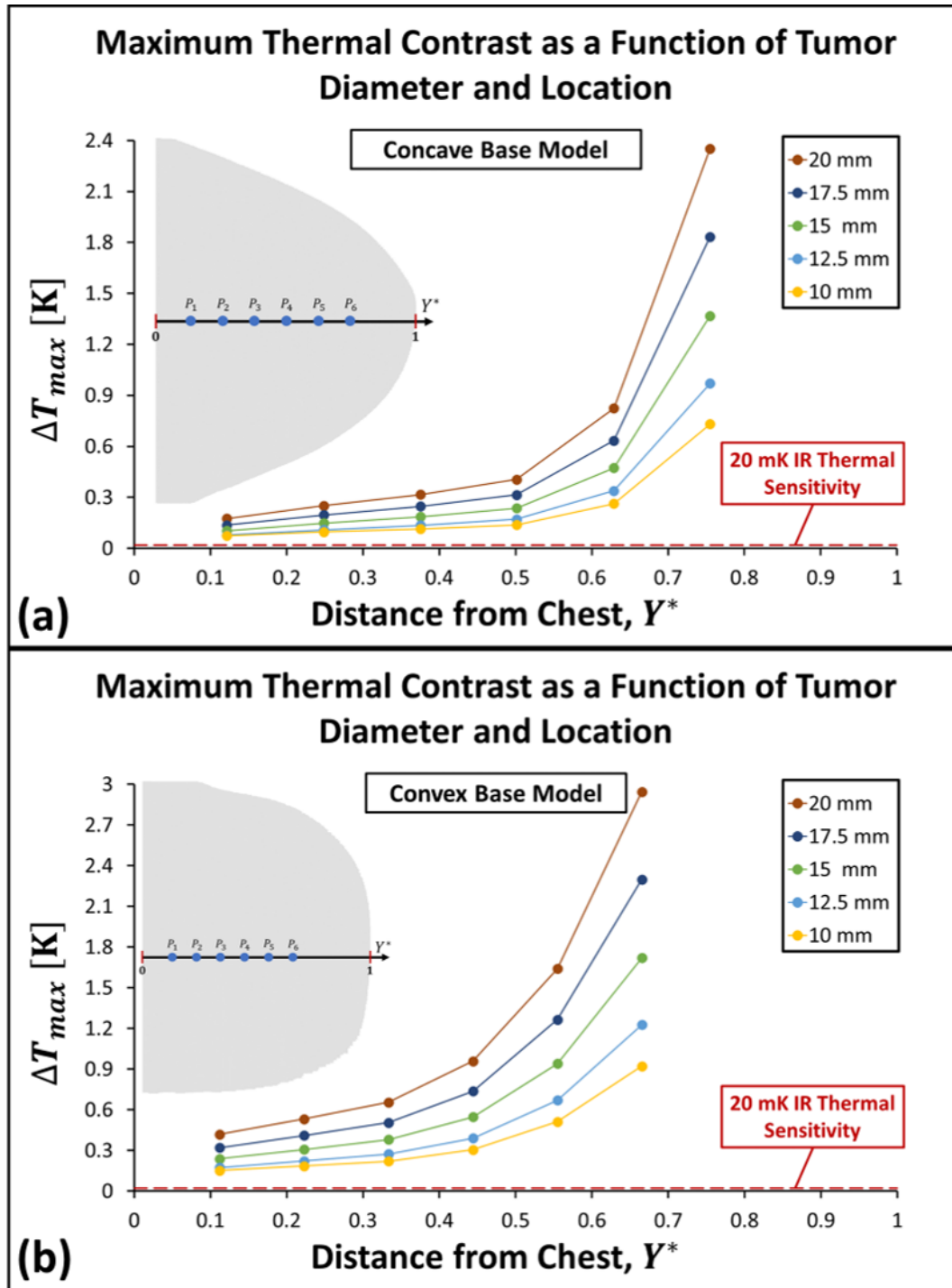


Figure 47. Effect of tumor size and position on the maximum thermal contrast for the (a) concave and (b) convex base models.

The difference between these equivalent tumors is in the area that these tumors affect due to their distance to the nearest surface. Bigger tumors would affect larger areas in comparison to smaller tumors that are in the same tumor position. The distance between a tumor position  $\mathbf{P}_i$  and the nearest surface point  $\mathbf{P}_{surf,i}$  is obtained through the following:

$$S_i = \|\mathbf{P}_{surf,i} - \mathbf{P}_i\| \quad (51)$$

where  $S_i$  is the distance from the surface to tumor position  $i$ , and  $\|\cdot\|$  is the Euclidean norm. Table 24 shows the results of utilizing Eq. 51 using a search function that finds the shortest distance from the tumor center points to the breast surface. As the results show, the convex model has a smaller distance to the surface in comparison to the concave model especially for positions  $P_1$  to  $P_5$ . For position  $P_6$  the distance to the surface for both breast models are close in value. These values make sense as the concave model is larger in size and longer in shape than the convex model. This shows that both the breast shape and size influence the surface temperature distribution from a tumor heat source. However, further investigation is needed to quantify the effect of the breast shape and size on  $\Delta T_{max}$ , which the next section goes over. Overall, the results from this section have shown that the tumor size and location highly impact the surface temperature. Furthermore, these results have shown that these surface temperatures can be picked up by an IR camera with thermal sensitivity of 20 mK.

Table 24. Distances from the tumor positions to the nearest surface point for both models.

Model Type	$S_1$ [cm]	$S_2$ [cm]	$S_3$ [cm]	$S_4$ [cm]	$S_5$ [cm]	$S_6$ [cm]
Concave	3.16	3.06	3.07	3.08	2.52	1.59
Convex	2.43	2.46	2.49	2.35	1.87	1.40

#### 4.4.3 Effect of Breast Shape and Size

In order to quantify the effect of the breast shape and size on the surface temperature distribution and detection of breast cancer, parametric studies were conducted on scaled breast geometries. The concave and convex breast geometries were utilized to generate scaled breast geometries utilizing the method described in Section 3.4.1. The third parametric study from Section 3.4.2 was conducted where 2 tumor sizes (10 mm and 20 mm) were placed at the 6 tumor positions along the centerline for each breast geometry. Similar to the previous section, the  $\Delta T_{max}$  values were utilized to quantify the effect of the breast shape and size.

Figure 48 shows a plot of the  $\Delta T_{max}$  value for a 10 mm tumor placed at the centerline tumor positions  $P_1$  to  $P_6$  in the concave base and scaled models (small, medium, and large). The tumor position number (1-6) was utilized instead of  $Y^*$  to standardize the plotted results. All  $\Delta T_{max}$  values were above the 20 mK threshold value, with the lowest value being  $\Delta T_{max} = 27.6$  mK at  $P_1$  in the large model. This shows that an IR camera with 20 mK thermal sensitivity can capture the temperature distribution of a 10 mm tumor at all of the centerline positions. Additionally, the results show a nonlinear increase in  $\Delta T_{max}$  value as the distance from the chest wall region increases or as the tumor moves from  $P_1$  to  $P_6$ , similar to the previous section. In contrast, it is observed that  $\Delta T_{max}$  decreases nonlinearly as the breast size increases from small to large. This is due to the distance from the surface increasing as the breast size increases for a non-symmetrical geometry. The  $\Delta T_{max}$  values for the medium scaled concave model were very similar to the concave base model with some deviation as the base model is a medium size breast. The deviation is due to scaling changing the  $L_y$  geometric length of the base model from 10.6 cm to 9.0 cm. This is

reflected starting at  $P_4$  as the decrease in this length increased the  $\Delta T_{max}$  value. This shows the importance of utilizing patient-specific breast geometries to better understand the thermal characteristics of breast cancer. Furthermore, this shows the impact of breast size, but further studies are needed to better quantify the effect on the breast surface and detection of breast cancer.

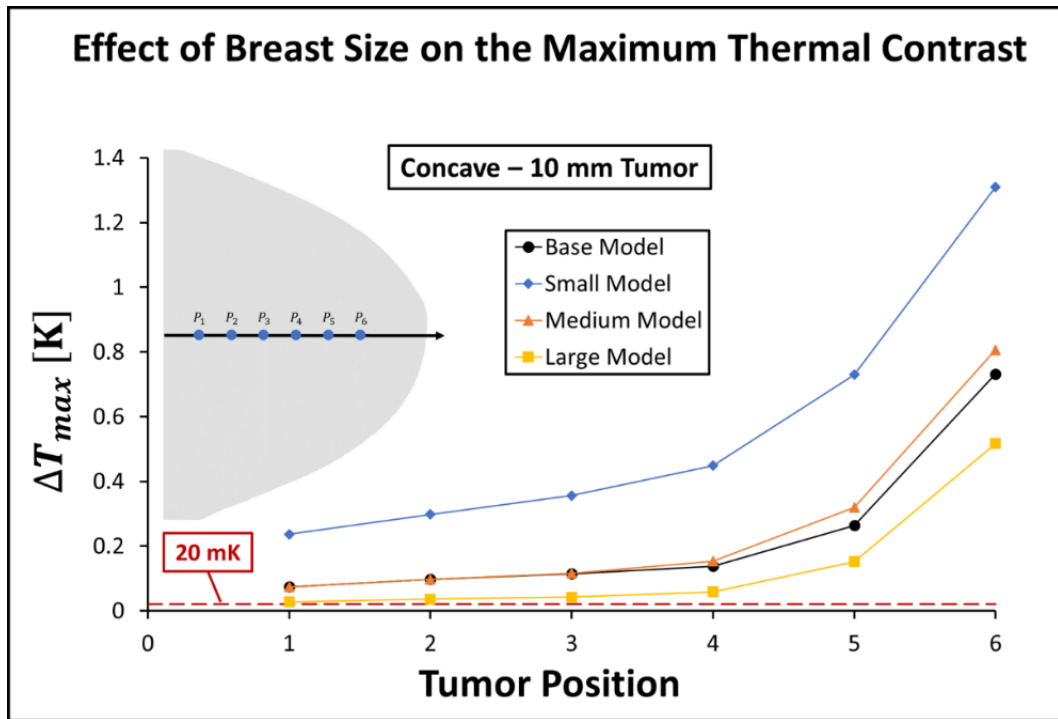


Figure 48. Plotted results showing the effect of breast size on the thermal contrast for the concave model with a 10 mm tumor placed along the centerline positions.

Further investigation on the effect of breast size for the concave breast model on the surface temperature distribution was conducted using a 20 mm tumor at the centerline positions  $P_1$  to  $P_6$ . Figure 49 shows the  $\Delta T_{max}$  values plotted against the tumor position for the base and scaled concave models. The range for the  $\Delta T_{max}$  axis was set to the same range as the one showed in Fig. 48 for comparison. The same trends are observed as the concave cases with a 10 mm tumor, where  $\Delta T_{max}$  increases as the tumor position increases and decreases as

the breast size increases. Also, for all breast sizes the  $\Delta T_{max}$  values are above the 20 mK threshold with the lowest value being  $\Delta T_{max} = 49.5$  mK at  $P_1$  in the large concave model. Similar to what was shown in Section 4.4.2, the 20 mm tumor increases the  $\Delta T_{max}$  values for all breast geometry cases. This is clearly shown in Fig. 49 where some values are not visible due to them being above the max  $\Delta T_{max}$  value in the  $\Delta T_{max}$  axis. The results for the concave cases with 10 mm and 20 mm tumors show that their surface temperature distribution can be captured by an IR camera with a 20 mK thermal sensitivity. Additionally, this shows that tumors of size between 10 mm to 20 mm at the various positions can be detected utilizing a thermal approach for at least the concave models.

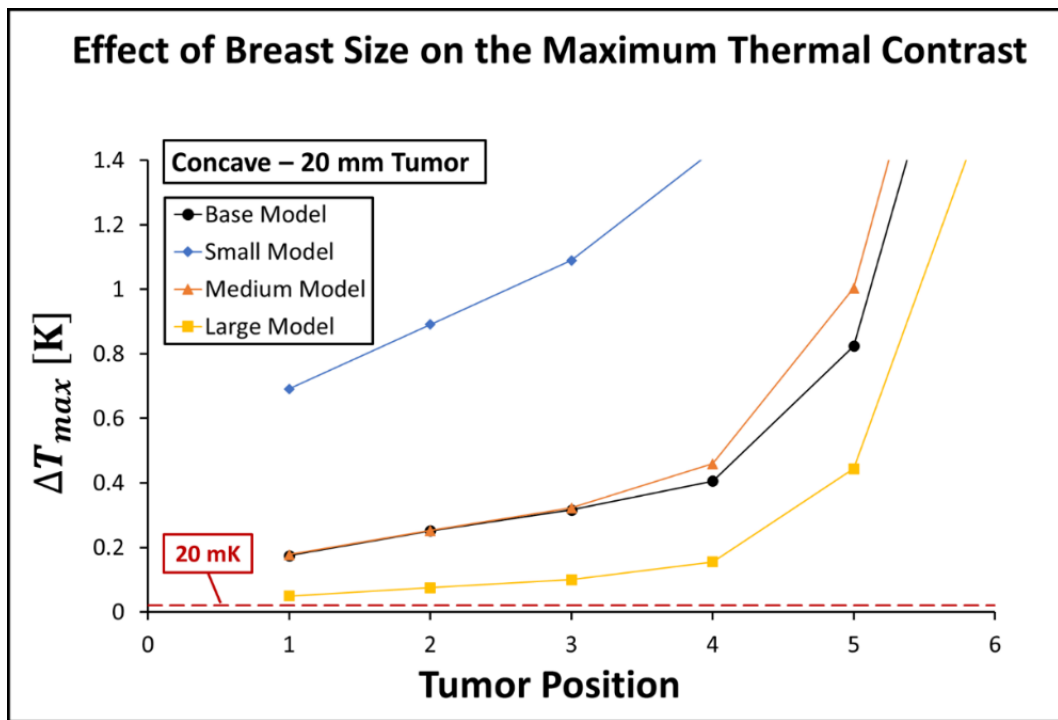


Figure 49. Plotted results showing the effect of breast size on the thermal contrast for the concave model with a 20 mm tumor placed along the centerline positions.

To study the effect of breast shape,  $\Delta T_{max}$  values were obtained for the convex base and scaled models. Figure 50 shows the  $\Delta T_{max}$  plotted for a 10 mm tumor placed along the

centerline positions  $P_1$  to  $P_6$  for the base and scaled convex models. Similar to the concave cases, the  $\Delta T_{max}$  value increases as the tumor position increases and as the breast size decreases. However, the  $\Delta T_{max}$  values are lower than the concave cases with 10 mm tumor with the convex case having 0.96 K as the highest value while the concave case had 1.31 K. This shows that the breast shape has an impact on the surface temperature distribution. The base and small convex models have similar  $\Delta T_{max}$  values for  $P_1$  to  $P_3$  since the base convex model is considered a small breast geometry. The base, small, and medium convex models have  $\Delta T_{max}$  values above the 20 mK threshold for all tumor positions with the lowest value being  $\Delta T_{max} = 43.8$  mK at  $P_1$  in the medium convex model. The large convex model has  $\Delta T_{max}$  values above 20 mK only for tumor positions  $P_4$  to  $P_6$ . Figure 50 also shows a zoomed in version of the plot at  $P_1$  to  $P_4$  which shows that  $\Delta T_{max}$  is below the threshold for  $P_1$  to  $P_3$  with the highest value being  $\Delta T_{max} = 19.9$  mK at  $P_3$  for the large convex model. The smallest  $\Delta T_{max}$  was shown to be  $\Delta T_{max} = 14.4$  mK at  $P_1$  for the large convex model. This shows that tumors at positions  $P_1$  to  $P_3$  in a large breast geometry would not be detectable if utilizing an IR camera with 20 mK thermal sensitivity.

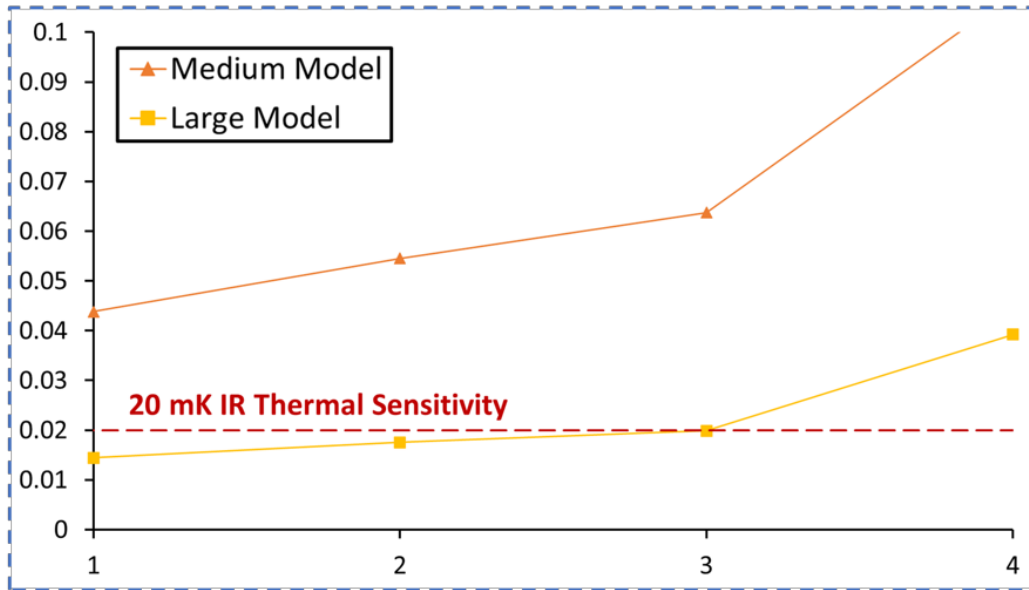
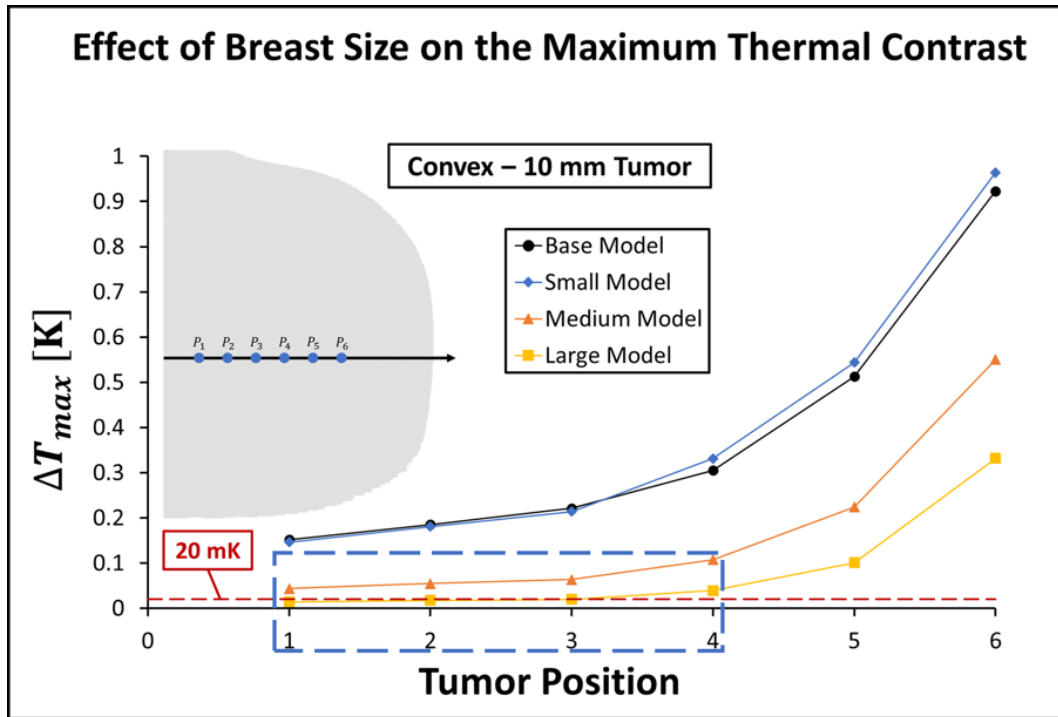


Figure 50. (Top) Plotted results of the thermal contrast for a 10 mm tumor at tumor positions along the centerline for the convex base and scaled models. (Bottom) Zoomed in plot of the results for tumor positions 1-4 to show the maximum thermal contrast below the 20 mK threshold.

To further investigate the effect of breast size on the surface temperature distribution the same parametric studies were conducted on the convex base and scaled model with a 20 mm tumor. Figure 51 shows the  $\Delta T_{max}$  values for a 20 mm tumor at tumor positions  $P_1$  to

$P_6$  for the base and scaled convex models. All previous trends shown in the concave cases and the previous convex case are the same for this parametric case, with an increase of  $\Delta T_{max}$  for an increase in tumor position and decrease in breast size. Additionally, just like the comparison between the 10 mm and 20 mm concave cases the 20 mm convex cases have a higher  $\Delta T_{max}$  values compared to the 10 mm convex cases. This was shown especially with all  $\Delta T_{max}$  values being above the 20 mK threshold for all breast models, unlike the 10 mm convex cases. The lowest  $\Delta T_{max}$  value was found to be  $\Delta T_{max} = 20.4$  mK at  $P_1$  in the large convex model an increase from 14.4 mK. This further validates that the tumor position, tumor size, breast shape, and breast size highly impact the detectability of breast cancer. The IR camera utilized for the clinical validation study presented in Section 4.2 was shown to have a thermal sensitivity of  $< 20$  mK but The exact value for the thermal sensitivity was not disclosed by the manufacturer. The value of the thermal sensitivity may be below the lowest  $\Delta T_{max}$  value of 14.4 mK obtained for the large convex model. There have been studies showing thermal sensitivity values as low as 7 mK [230], which shows that these tumors can be captured using a very thermal sensitive IR camera. This shows the need for improvements in current IR technology in order to improve the detectability of breast cancer through an IRI inverse heat transfer approach.

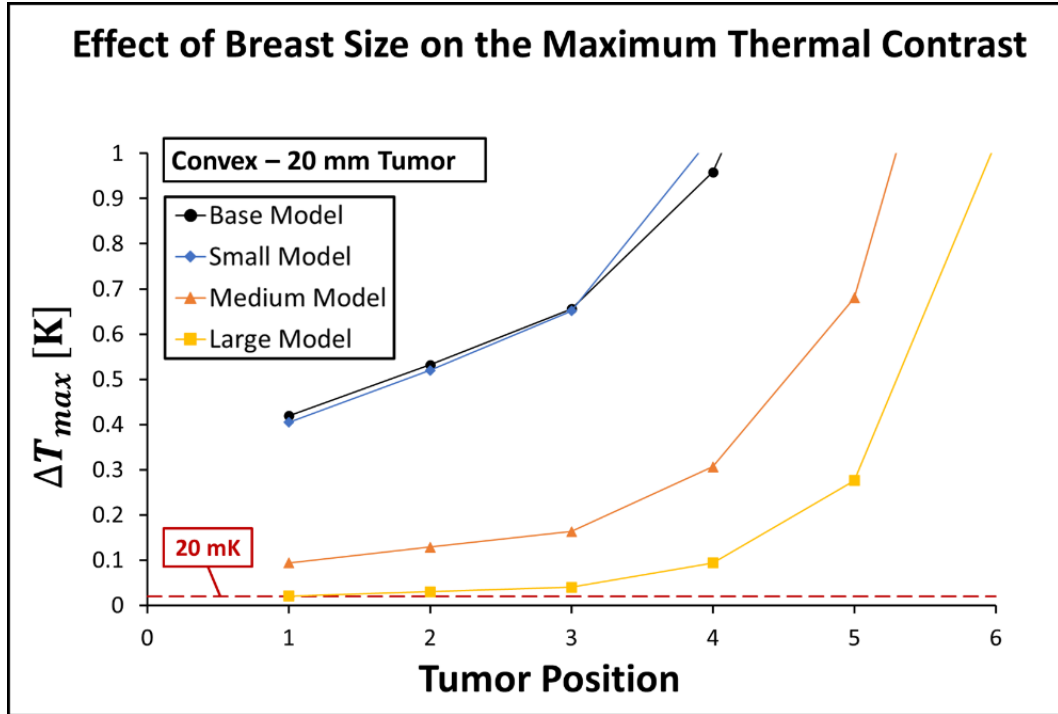


Figure 51. Plotted results of the thermal contrast for a 20 mm tumor at tumor positions along the centerline for the convex base and scaled models.

Focusing on deep tumors, tumors in the posterior region at  $P_1$ , the maximum thermal contrast  $\Delta T_{max}$  of the surface was plotted as a function of tumor size  $d_t$  for the scaled convex models. Figure 52 shows the results for the  $\Delta T_{max}$  vs  $d_t$  plot for the small, medium, and large convex models. The plots show that  $\Delta T_{max}$  increase as  $d_t$  increases for a fixed patient geometry but decreases as the breast size increases for a fixed tumor size. This is due to a larger area of tissue that is being added that surrounds the tumor giving a longer distance for the heat to transfer from the tumor to the surface of the breast. The results for the small breast geometry show that  $\Delta T_{max}$  goes from 0.14 K to 0.60 K for a 1 cm and 2 cm tumor, respectively. For the medium breast geometry,  $\Delta T_{max}$  goes from 0.04 K to 0.19 K for 1 cm and 2 cm tumors, respectively. Finally, the results for a large breast geometry show that  $\Delta T_{max}$  goes from 15.2 mK to 65.3 mK for a 1 cm and 2 cm tumor, respectively. For the small and medium breast cases, all  $\Delta T_{max}$  values are above the 20 mK IR camera

thermal sensitivity threshold. The large breast case starts below this threshold for 1 cm, 1.05 cm, and 1.1 cm tumors, but then reaches 20.7 mK for a 1.15 cm tumor. The FLIR SC6700 IR camera utilized in the clinical validation study has a thermal sensitivity of <20 mK. This indicates that these tumor sizes and their thermal effects may still be captured by the IR camera. A more sensitive IR camera would most definitely pick up the thermal signatures from this tumor. This shows that detectability limits for the IRI inverse heat transfer approach are dependent on the thermal sensitivity of the IR camera.

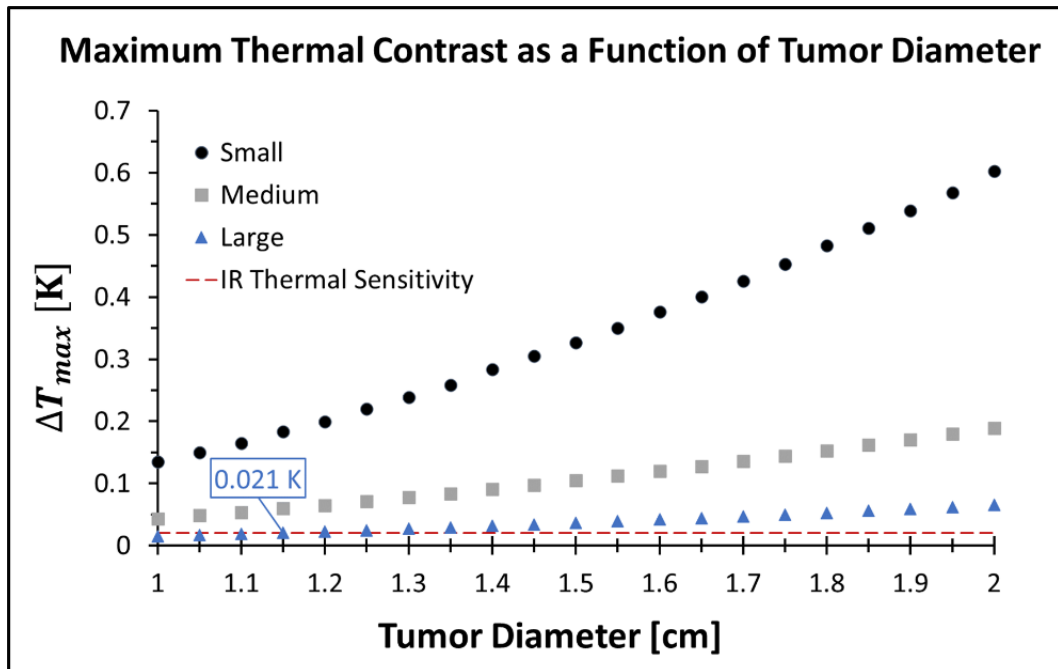


Figure 52. Plot of maximum surface thermal contrast as a function of tumor size (diameter) for three breast sizes.

#### 4.4.4 Effect of Breast Density

The breast density has been shown to provide challenges in the detection of breast cancer in the current screening paradigm, especially in mammography [11,75]. In IR thermography and IRI, breast density has shown to play a role in capturing the thermal abnormality caused by a tumor heat source through the thermal conductivity [112–114].

However, there have not been studies indicating the influence of breast density through thermal conductivity values in the detection of breast cancer. As the results from Sections 4.4.1 to 4.4.3 have shown, factors that affect the surface temperature distribution also affect the detectability of breast cancer. Furthermore, the results have shown that deep tumors may be harder to detect depending on the breast shape and size. Therefore, the fifth parametric study described in Section 3.4.2 on the convex base model for deep tumors of various sizes at  $P_1$  was conducted.

Figure 53 shows the plotted results of  $\Delta T_{max}$  as a function of the thermal conductivity  $k$  for 5 tumor sizes to determine the thermal effect of breast density on breast cancer. The results show that  $\Delta T_{max}$  increases as breast density and tumor size increases but becomes constant as the breast tissue gets denser. This is very apparent in tumor sizes such as the 12.5 mm and 15 mm tumor sizes where their respective  $\Delta T_{max}$  values go from 0.14 K to 0.23 K and from 0.2 K to 0.34 K. The  $\Delta T_{max}$  values become constant at 0.35 W/m-K and 0.45 W/m-K for the 12.5 mm and 15 mm tumor sizes, respectively. Also, the results the constant  $\Delta T_{max}$  value shifts towards the denser breast tissue areas as the tumor sizes increases. The constant  $\Delta T_{max}$  value for a 10 mm tumor starts at 0.3 W/m-K but starts at 0.5 W/m-K for a 20 mm tumor. This shows that breast density has a more significant effect on larger tumors than on smaller tumors, especially on tumors smaller than 15 mm. The 10 mm and 12.5 mm tumor cases show a total  $\Delta T_{max}$  increase of 0.05 K and 0.09 K, respectively. All  $\Delta T_{max}$  values for each case are above the IR camera thermal sensitivity value of 0.02 K described previously. This signifies that the thermal effects of a 10 mm tumor can be captured by a 20 mK thermal sensitive IR camera regardless of breast density. Furthermore, the results show that utilizing a fixed thermal conductivity value in bioheat

transfer modeling and inverse heat transfer modeling would suffice but may provide errors in tumor sizing. Further studies are needed to investigate the effect of having different thermal conductivity values for the breast and tumor tissue.

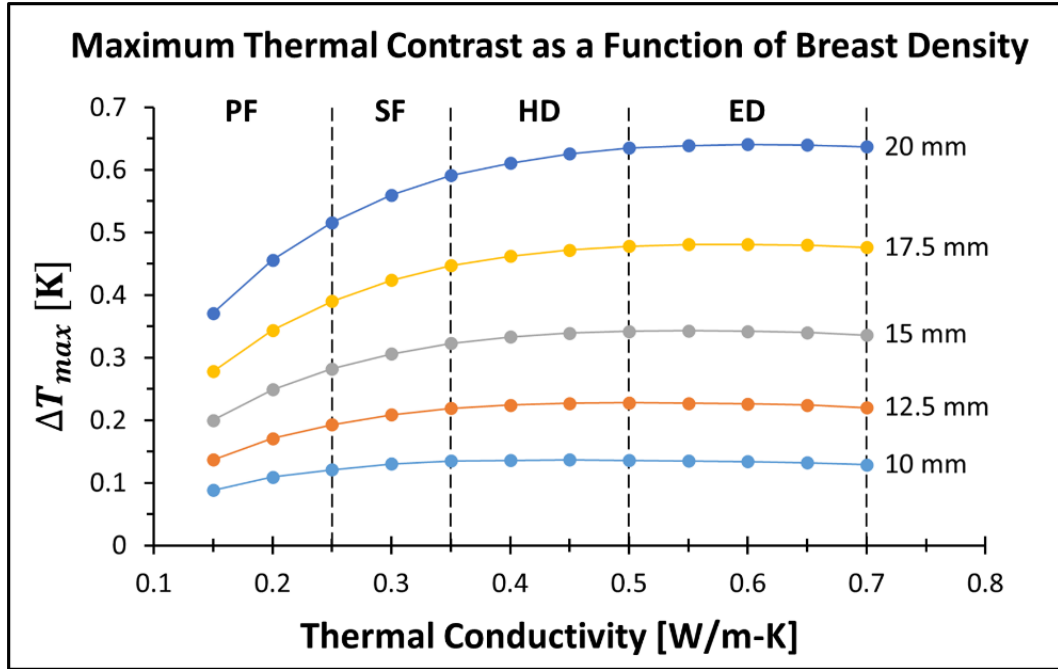


Figure 53. Plot of the maximum surface thermal contrast as a function of breast density (thermal conductivity of tissue) for varying tumor sizes (diameters) conducted on patient IR. The breast density ranges are labeled as predominantly fatty (PF) for 0.1 W/m-K to 0.25 W/m-K, scattered fibroglandular (SF) for 0.25 W/m-K to 0.35 W/m-K, heterogeneously dense (HD) for 0.35 W/m-K to 0.5 W/m-K, and extremely dense (ED) for 0.5 W/m-K to 0.7 W/m-K.

## 4.5 Effects of Physiological Factors

### 4.5.1 Effect of ROI Selection

The effects of thermal artifacts caused by superficial veins captured in IR images on the detection of breast cancer using the IRI-NE have yet to be studied and quantified. The work proposed in Section 3.5.1 was conducted to investigate how the thermal profile of a breast with an artificial thermal artifact affects the accuracy of detection. Table 25 shows the predicted results for each ROI case as well as the comparison error to the ground truth

values in bold. The results show that utilizing ROI cases 1 and 2 provides more accurate results for the predicted tumor size, tumor location, and thermal conductivity. The case that gives the best results is ROI case 2 which has the lowest tumor size and location errors. ROI case 1 has the lowest error in thermal conductivity compared to the other cases. The error in predicted thermal conductivity and tumor size were highest for ROI case 3. The error in the tumor location was similar throughout with the maximum absolute error for the x-, y-, and z-coordinates being 6.1 mm, 9.1 mm, and 8.3 mm, respectively.

Table 25. Comparison of predicted parameters and prediction error between each case.

ROI Case	<b><math>k</math> [W/m-K]</b>	<b><math>d_t</math> [m]</b>	<b><math>x_t</math> [m]</b>	<b><math>y_t</math> [m]</b>	<b><math>z_t</math> [m]</b>
	<b>0.45</b>	<b>0.021</b>	<b>0.236</b>	<b>0.08</b>	<b>0.112</b>
Predicted Results					
Case 1	0.4505	0.0273	0.2421	0.0891	0.1149
Case 2	0.4670	0.0232	0.2380	0.0844	0.1172
Case 3	0.3474	0.0489	0.2400	0.0744	0.1203
Prediction Error					
Case 1	0.0005	0.0063	0.0061	0.0091	0.0029
Case 2	0.0170	0.0022	0.0020	0.0044	0.0052
Case 3	-0.1026	0.0279	0.0040	-0.0056	0.0083

A comparison of the ground truth ROI temperatures for each case with their respective predicted ROI temperatures is shown in Fig. 54. Additionally, the predicted surface temperature associated with the predicted values from Table 26 are shown in Fig. 54. These results show that ROI case 2 provides a better predicted ROI temperature than ROI cases 1 and 3. The RMSE for ROI cases 1, 2, and 3 were 0.17 K, 0.06 K, and 1.63 K, respectively, which further shows that the ROI case 2 provides the most accurate result. Comparing the predicted surface temperatures for each ROI case with the ground truth surface temperature (ground truth ROI for case 3 in Fig. 54), shows that all cases try to capture the hot region on the surface due to superficial vessel. ROI cases 1 and 3 provide a more noticeable hot region than ROI case 2, but with ROI case 3 having a much different temperature

distribution due to predicting a much larger tumor. This shows that superficial vessels have an effect, but further studies are needed to quantify this error and how it affects healthy tissue. A test was conducted with the same breast without a tumor and the IRI-NE was able to predict the absence of the tumor with all ROI cases. The RMSE between the predicted and ground truth was found to be 0.42 K, much lower than ROI case 3 with a tumor. This shows that the IRI-NE is able to predict the presence and absence of breast cancer regardless of superficial vessels with some errors.

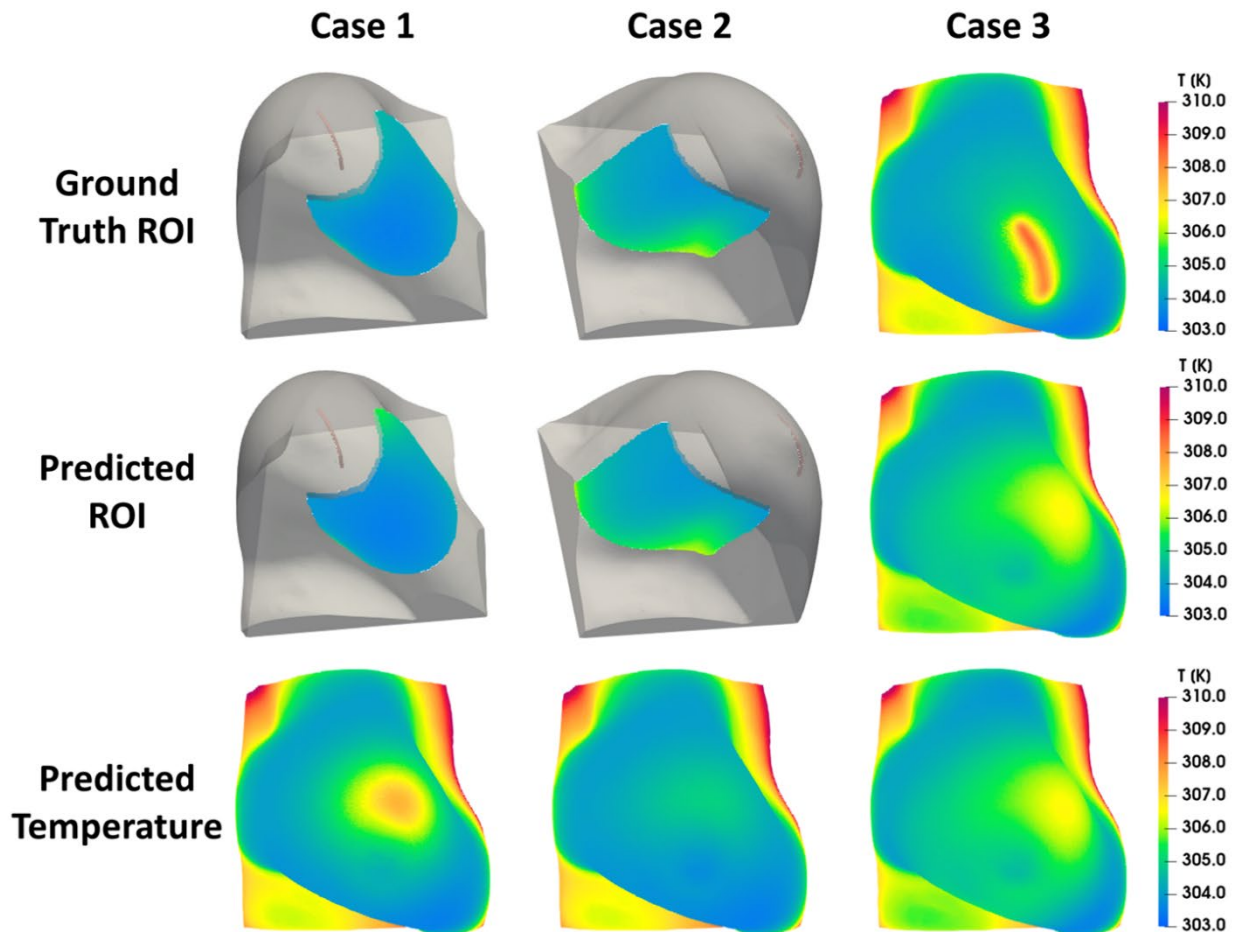


Figure 54. Comparison of (first row) ground truth and (second row) predicted ROI temperatures for each case. The last row shows the predicted surface temperatures for each case.

#### 4.5.2 Effect of Tumor Perfusion Heat Source

Malignant breast tumors are highly metabolically active and highly perfused heat sources that have been shown to heavily affect the thermal distribution on the surface of the breast. The metabolic heat generation of breast tumors have been quantified through the tumor doubling time and volumetric growth. However, the perfusion rate has not been as extensively quantified in comparison to the metabolic heat generation. The method described in Section 3.5.2 was conducted to quantify the effect of the tumor perfusion heat source on the surface temperature. The root mean square error (RMSE) of the surface temperatures was obtained for the parametric cases described in Section 3.5.2. The minimum RMSE value at each tumor size was utilized to identify the contribution of the heat sources to the surface temperatures.

Figure 55 shows the plotted results of perfusion rate values that give equivalent heat sources to a metabolic heat source for various tumor sizes for patients 1R and 17L. The results show that the perfusion term decreases nonlinearly as the tumor size increases. This shows that smaller tumors need a higher perfusion rate to provide an equivalent heat source from the metabolic activity. This matches with what has been presented in literature relating to growing tumors being highly perfused due to tumor angiogenesis [43]. Tumor angiogenesis allows the tumor to create a vasculature network and take nutrients away from the body by connecting to the body's vasculature network. When comparing the two patients, patient 1R requires higher perfusion rate values compared to patient 17L. This shows the effect of the breast shape and size on the heat transfer that has been shown in Section 4.4. The maximum perfusion rate value for patient 1R was  $1.062 \times 10^{-2}$  1/s which is above the value of  $9.0 \times 10^{-3}$  1/s utilized in literature, while patient 17L was

$5.76 \times 10^{-3}$  1/s. The minimum perfusion rate values for patients 1R and 17L were  $9.0 \times 10^{-4}$  1/s and  $5.4 \times 10^{-4}$  1/s, respectively, which are above the value for healthy tissue perfusion ( $1.8 \times 10^{-4}$  1/s) utilized in literature [370,417]. All the perfusion rate values for both patients were above the healthy tissue perfusion rate value which indicates that the tumor needs to be highly perfused to generate significant heat. However, this only compares with the heat source generated by only the metabolic activity of the tumor.

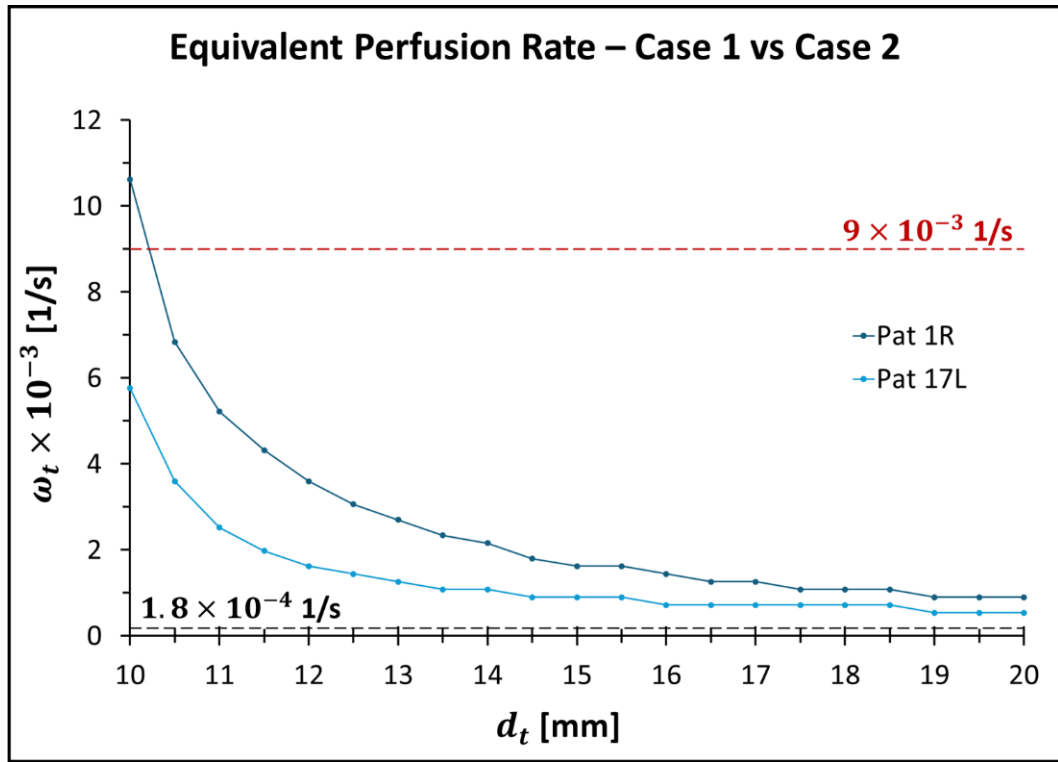


Figure 55. Plotted perfusion rate values associated with an equivalent heat source to a metabolic heat source for tumors of various sizes for patients 1R and 17L.

A comparison of the heat generated by the perfusion heat source with the heat sources utilized in bioheat transfer modeling of breast cancer shown in Section 3.2.3 was conducted through the RMSE. Figure 56 shows the plotted results of the perfusion rate that provides the equivalent heat source as the heat sources utilized in bioheat transfer modeling of breast cancer for various tumor sizes. Similar to the results shown in Fig. 55, the perfusion rate

decreases nonlinearly as tumor diameter increases for both patients. The equivalent perfusion source for patients 1R and 17L for a 10 mm tumor were  $3.6 \times 10^{-2}$  1/s and  $1.8 \times 10^{-2}$  1/s, respectively, which were 200 and 100 times bigger than that of healthy tissue. All perfusion rate values are above the  $9.0 \times 10^{-3}$  1/s tumor perfusion rate term utilized in literature. This shows how much the tumor vascularity has an impact on the heat transfer within the body. Furthermore, the results show that smaller growing tumors may be modeled using the perfusion heat source as the dominating heat source due to angiogenetic growth from the tumor vasculature. However, the values for these perfusion terms are not known for smaller tumors especially tumors smaller than 10 mm, which have metabolic activity values that are also unknown. This shows the need for further studies that focus on tumors smaller than 10 mm.

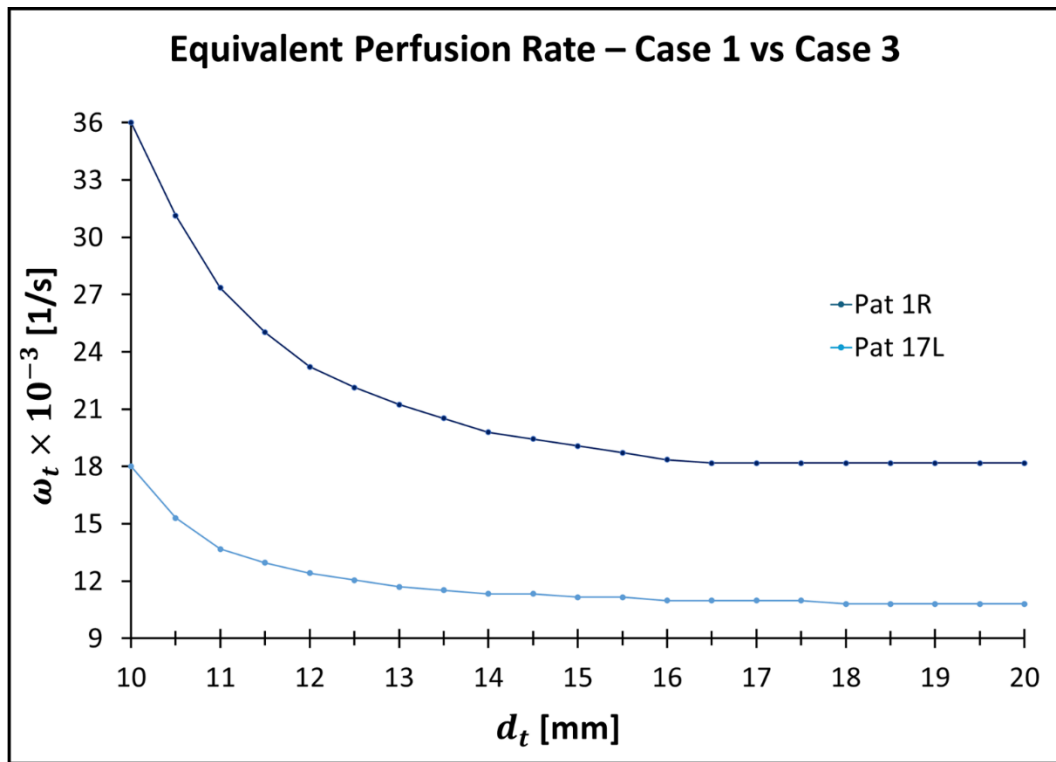


Figure 56. Plotted perfusion rate values associated with an equivalent heat source to a heat source utilized in bioheat transfer modeling of breast cancer for tumors of various sizes for patients 1R and 17L.

## Chapter 5: Conclusions

### 5.1 Summary of Work Done

The work conducted in this thesis focused on early detection of breast cancer through a developed IRI inverse heat transfer approach. This work also focused on the accuracy of this approach when presented with common challenges observed in the current breast cancer screening paradigm. Three major studies were conducted that validated and tested the accuracy of this approach: (1) a clinical study, (2) a detectability study, and (3) a vascularity study. The following provides the work completed in each study.

#### Clinical Study

- An efficient autonomous IRI inverse heat transfer-based algorithm was developed for this thesis called the IRI-Numerical Engine (IRI-NE) to accurately detect the presence and absence of breast cancer. The IRI-NE is a modified and enhanced version of the algorithm developed by Gonzalez-Hernandez et al. [150] utilized to detect breast cancer in 7 biopsy-proven breast cancer patients.
- The modifications and enhancements to the algorithm presented in this work were developed to work with larger clinical data. This included the enhancements to the IR image registration, inclusion of an inverse modeling interface for ANSYS Fluent, inclusion of parallel processing in ANSYS Fluent, and inclusion of a fail-safe procedure.
- The IRI-NE was validated on 23 biopsy-proven breast cancer patients through data collected from a collaborative study between RIT and Rochester General Hospital.

This data included clinical IR images, MRI data, pathology reports, and other patient data.

- The MRI data was utilized to generate patient-specific digital breast models (DBMs) for bioheat transfer modeling of breast cancer using the method developed by Gonzalez-Hernandez et al. [395]. The patient-specific DBMs were utilized as the computational domain for inverse modeling. The tumor size from MRI was utilized only to compare with the predicted tumor size from the algorithm.
- For all patient cases, the algorithm was able to accurately predict the presence and absence of breast cancer regardless of cancer type, tumor size, tumor depth, and breast density.

#### Detectability Study

- Parametric studies were conducted to study the effects of tumor size, tumor position, breast size, breast shape, and breast density on surface temperature distribution and accuracy of detection. The method to conduct these parametric studies and extract surface temperatures for each parametric case through user-defined functions (UDFs) for ANSYS Fluent was presented.
- The IRI-NE was modified and utilized to test the accuracy of detection for synthetic IR ground truth data generated from the parametric studies involving tumor size and position. The synthetic IR ground truth data were generated using the extracted surface temperature and the IR thermal sensitivity through a developed method presented in this work.
- The detectability of the modified IRI-NE was tested using detectability metrics and the surface temperatures obtained from parametric studies. The detectability

metrics were identified as factors that contributed to the accuracy of detection and acquisition of data through tumor size prediction error and the thermal contrast on the breast surface, respectively. The method for obtaining the detectability metrics was presented in this work.

- The detectability limit of the IRI-NE was found to be dependent on the thermal sensitivity of an IR camera. The thermal contrast was utilized for comparison with the thermal sensitivity of a 20 mK IR camera to identify the detectability limits.

### Vascularity Study

- The effects of superficial vessels on the accuracy of detection for the IRI-NE was conducted. A method for modeling a single vessel in patient-specific DBMs for thermal simulations of a breast with and without cancer was presented in this work. Different size ROIs were tested including the entire breast surface to test the accuracy of detection. A method for selecting the ROI for surface temperature data was presented.
- The IRI-NE was able to predict the presence and absence of breast cancer regardless of the superficial vascular. The tumor size prediction was shown to be affected by the type of ROI used in the IRI-NE.
- The thermal effects of the blood perfusion heat source were conducted through parametric studies involving the perfusion term and the tumor size. A comparison study was conducted using surface temperatures between a model with only a perfusion heat source and models with either only a metabolic heat source or both the perfusion and metabolic heat sources.

- The perfusion rate was shown to have a large impact on the heat transfer especially for small growing tumors. The necrosis effect of tumors was shown through the small values of perfusion rate needed to match the metabolic heat generation of larger tumors.

## 5.2 Conclusions

The current work showed a method to conduct breast cancer detection through advanced computational methods (thermal and inverse modeling) using surface temperatures captured through infrared imaging (IRI). This developed method was packaged into an algorithm called the IRI-Numerical Engine (IRI-NE). The IRI-NE was able to accurately predict the presence and absence of breast cancer in 23 biopsy-proven breast cancer patients using inverse heat transfer modeling and IR surface temperatures. Utilizing image processing techniques, such as image registration, to extract surface temperatures for inverse heat transfer modeling was shown to be reliable and accurate. The surface temperatures generated through bioheat transfer modeling were able to match that of IR surface temperatures captured by an IR camera, irrespective of the presence of a tumor. The inverse algorithm in the IRI-NE was able to accurately predict the presence of tumors regardless of breast density, tumor size, tumor depth, and cancer type. This work shows that breast cancer can be detected accurately using IRI and heat transfer-based methods. Additionally, this work showed that the IRI-NE is able to work in a larger clinical setting as a prototype software. A larger clinical study is warranted to obtain the efficacy of this modality as suggested by Owens [401]. Finally, this work showed the ability of utilizing IRI with the IRI-NE as an adjunctive modality to mammography.

The detectability limits of the IRI-NE were obtained through thermal analysis of the surface temperature generated from parametric studies. In this detectability study, a modified IRI-NE was developed that conducted inverse modeling using 3D IR surface temperatures. This was conducted by utilizing bioheat transfer modeling to generate surface temperatures and adding a Gaussian noise mimicking the thermal sensitivity of an IR camera. The synthetic IR surface temperatures were shown to sufficiently represent the heat transfer and noise captured in an IR image. Parametric studies were conducted to study the effect of breast density, breast size, breast shape, tumor size, and tumor location on the surface temperatures and the detection of tumors. The modified IRI-NE was able to predict the presence of breast cancer regardless of breast shape, breast size, tumor size, and tumor location. The thermal contrast was utilized to study the effects of the parameters on the surface temperature and to compare with the thermal sensitivity of a 20 mK IR camera. For many cases, tumors were considered detectable due to the thermal contrast being above 20 mK. Any of the parameters providing a thermal contrast below 20 mK was deemed undetectable by a 20 mK IR camera but could be detected with a 10 mK camera. This showed that the detectability limit of the IRI-NE was dependent on the thermal sensitivity of the IR camera.

Thermal analysis of the surface temperatures was also utilized to study the effects of tumor and tissue vascularity. The effect of vascularity of healthy and cancerous tissue on the heat transfer and detection of breast cancer was investigated. Superficial vessels have been shown to affect the accuracy of detection through the use of various size ROIs. Utilizing small ROIs away from the surface that captures the vascularity provided better results. Although utilizing the entire breast surface as an ROI can include the thermal profiles

created by the superficial vessel, the IRI-NE was able to detect the presence and absence of tumors regardless of the effects. The effects of the tumor vasculature on the heat transfer were conducted through varying the perfusion rate of the tumor to obtain equivalent heat sources. This study showed that the tumor perfusion rate due to angiogenesis plays a major role in the heat transfer for small growing tumors.

## 5.3 Research Contributions

### 5.3.1 Societal Contributions

Early detection of breast cancer is vital in reducing recall rates, treatment management, and reducing the mortality rates. The developed technique in this thesis contributes to early detection of breast cancer which has the potential to help the hundreds of thousands of women going through screening. This technique is noninvasive and has shown high accuracy of detection regardless of breast density, tumor size, tumor depth, and cancer type which shows promise in helping reduce recall and mortality rates. More importantly, this method has the potential of reducing psychological and physical discomfort associated with the current screening paradigm. Many women have discussed the horrendous experiences they had to go through to be screened for breast cancer. This includes the women in my family, my partner's family, as well as many other women I have encountered over the years. From the various discussions, all these women have mentioned the pain they go through during and after a mammogram. Some women who had the experience of being recalled due to their dense breast tissue have spoken about the many hurdles they had to face in the current screening paradigm. They have talked about the financial, psychological, and bureaucratic distress they had to go through just to get re-imaged. When speaking to

these women about the technique that this thesis has developed and clinically validated, all these women have shown nothing but support and praise for such a technology.

In addition, techniques were developed that studied the characteristics of breast cancer through a thermal perspective which shows great promise in improving breast cancer treatment management. This work has shown that research concepts relating to cancer growth can be studied through the developed detection technique with thermal analysis. This provides an opening to utilizing this noninvasive technique as a way to monitor treatment and help in decision making of treatment. There have been many researchers, physicians, and clinicians that have suggested utilizing this technique for cancer treatment at the 2023 San Antonio Breast Cancer Symposium. This shows that this technology and the work conducted in this thesis has the potential to save many lives. Finally, the overall work conducted over the many years on this project has ignited hope in many of us going through the problems caused by cancer. The future looks brighter than ever and hopefully this will push for the necessary steps to utilize this technology as a noninvasive adjunctive modality.

### 5.3.2 Technical Contributions

The technical contributions of this thesis include the development of novel numerical techniques utilized for breast cancer detection and to study the thermal characteristics of breast cancer. The developed breast cancer detection technique was clinically validated with biopsy-proven breast cancer patient data collected through an approved collaborative IRB between RIT and RGH. The thermal characteristics of breast cancer and cancer growth were obtained through thermal analysis using numerical techniques. This showed the ability of conducting noninvasive cancer research through numerical and thermal

techniques with infrared imaging. Details of the major contributions in the fields of breast cancer detection and bioheat transfer modeling of breast cancer, as well as other contributions, are described below.

### Major Contributions

- Developed a novel autonomous patient-specific IRI and inverse heat transfer-based packaged algorithm for large clinical studies called the IRI-Numerical Engine (IRI-NE). The IRI-NE is based on and improves on the breast cancer detection algorithm developed by Gonzalez-Hernandez [396] that utilizes IRI to predict the presence and absence of tumors.
- Clinically validated the IRI-NE with 23 biopsy-proven breast cancer patients and published the findings in Scientific Reports Nature journal [415]. For all patients the IRI-NE accurately predicted the presence and absence of breast cancer regardless of breast density, tumor size, tumor location, and cancer type.
- Predicted tumor diameter of 24 cancerous breasts with a mean absolute error of 2.4 mm and a coefficient of determination of  $R^2 = 0.9574$ .
- Predicted the absence of tumor in 22 non-cancerous breasts using the IRI-NE.
- Generated patient-specific digital breast models (DBMs) using MRI data of each patient using the method developed by Gonzalez-Hernandez et al. [395].
- Enhanced the IR image registration algorithm utilized in the IRI-NE for surface temperature matching through graphical user interfaces (GUIs) and quality checking steps.
- Interfaced an external inverse heat transfer algorithm with ANSYS Fluent for cross platform communication. A user-defined function (UDF) was developed to

interface ANSYS Fluent with the external program written in both MATLAB and Python. The program interacted with the data created by the UDF to conduct inverse modeling and sent prediction data to the ANSYS Fluent for thermal modeling of breast cancer.

- Incorporated fail-safe procedures in the IRI-NE that saved data and the status of the algorithm in case of any crashes or other external factors. This allows users to continue where the IRI-NE left off instead of starting from the beginning.
- Improved computational efficiency of detection by reducing the average run time by half (1h to 30 mins) compared to the method developed by Gonzalez-Hernandez [396] using parallel processing in ANSYS Fluent.
- Developed a method to extract temperature data from various boundary and breast regions in ANSYS Fluent for post processing and inverse modeling through a UDF. Post processing included a method to separate the surface temperature and a method to add noise to the surface temperature to generate synthetic IR data.
- Modified the IRI-NE to conduct inverse modeling using synthetic IR data or any 3D temperature data that can be extracted from the surface of the breast. Validation of the modified IRI-NE was conducted using clinical data of 8 of the 23 patients from the clinical validation study.
- Developed a method to conduct steady-state parametric studies of breast tissue thermal physical properties and tumor thermal characteristics in ANSYS Fluent through a novel and robust UDF. The UDF was utilized to test multiple parameters in a single steady-state thermal simulation and to generate surface temperature data after a given number of iterations.

- Identified detectability metrics that evaluated the effect of breast shape, breast size, tumor size, tumor location, and breast density on the surface temperature and detection accuracy. Identified the detectability limit of the IRI-NE using synthetic IR data generated from the parametric studies and the detectability metrics.
- Determined that the detectability limit of the IRI-NE relies on the thermal sensitivity of the IR camera and not the breast density, which highly affects the current screening modalities. Identified that tumors smaller than 1.15 cm inside the deep posterior region of a large breast would not be detected by a 20 mK thermal sensitive IR camera but would be detected in a 10 mK thermal sensitive IR camera.
- Determined that breast density positively improved the detectability of breast cancer especially in deep tumors.
- Identified the effects of superficial blood vessels on the detection accuracy of the IRI-NE as well as the ROI selection that obtained the best results. Identified that the IRI-NE was able to predict the presence and absence of breast cancer regardless of local vascularity of the breast.
- Determine that the blood perfusion heat source of small growing tumors have a bigger impact on the heat transfer due to high perfusion rates associated with tumor angiogenesis. This work showed that further studies on tumor angiogenesis can be conducted through a thermal perspective using the perfusion rate.

#### Other Contributions

- Became an interdisciplinary researcher learning from various fields by taking courses and self-learning from experts in computer science, imaging science, mathematical modeling, biomedical engineering, and mechanical engineering.

- Presented research at the 2024 San Antonio Breast Cancer Symposium, the 2023 Society of Hispanic Professional Engineers (SHPE) National Convention, and the 2023 Rochester Engineering Society Engineering Symposium.
- Awarded the Outstanding Graduate Student Award and 1<sup>st</sup> place presentation at the 2024 RIT Graduate Education Week – Graduate Showcase. Awarded 3<sup>rd</sup> place poster presentation at the 2023 SHPE National Convention.
- Represented RIT, Rochester, and Upstate NY at the SHPE Hill Day event advocating for funding and resource for STEM outreach initiatives at Capitol Hill.
- Guest lectured in two RIT graduate courses: MECE 731 (Computational Fluid Dynamics) and SWEN 640 (Research Methods).
- Published several peer-reviewed journal articles and a non-provisional patent application.
- Helped develop and write six grant applications: 4 national government grants including the NSF and DOD, and 2 state grants including the Peter T. Rowley Breast Cancer Scientific Research Projects. One NSF grant that was accepted was the Small Business Innovation Research (SBIR) Phase I grant.
- Worked in a doctoral internship at a startup company learning the commercialization process of a medical imaging device under the NSF SBIR Phase I grant.

## Chapter 6: Recommendations

In Chapter 2, it was observed that IR thermography research has increased due to the improvements of AI, but these methods have yet to show results better than the current screening modalities. The IRI-NE has shown great promise in becoming an accurate method that could place IRI as an adjunct to mammography. However, larger clinical studies are warranted to determine the efficacy of the approach due to only a small sample size being validated in this work. Owens [401] has discussed the planning of a large clinical study for IRI-based methods to determine the efficacy in greater detail, which can be applied to the IRI-NE. In addition to conducting this larger clinical study, other studies are needed to further assess the use of the IRI-NE in a clinical setting and alternative data collection methods. Furthermore, studies are needed to further validate the detectability of the IRI-NE as well as improve bioheat transfer modeling and data processing steps. Recommendations for future studies covering these topics are presented in this chapter.

### 6.1 Integration IRI Numerical-Based Methods with PACS

In hospitals and clinics, radiologists use the Picture Archiving and Communication System (PACS) to organize, store, transmit, and display medical images through a hospital information system (HIS) or radiology information system (RIS) [418]. This is important to keep patient medical records safe in an environment doctors and clinicians can access to aid in patient assessment. To ensure the safety of data, PACS systems go through two industry standards, the Health level 7 (HL7) and the Digital Communications in Medicine (DICOM) standards. Breast cancer screening relies heavily on the PACS system in order for radiologists to conduct imaging and broadcast of data throughout the hospital or clinic.

Computer aided detection (CAD) modules are sometimes implemented to enhance the workflow and assist radiologists in assessing the data.

In order for the IRI-NE to be utilized in a clinical environment by a radiologist through the PACS system similar to a CAD module, integration of the system is needed. Figure 57 shows a PACS architecture consisting of hospital server modules and PACS system components integrated with an IRI numerical-based system, which includes an IRI Acquisition System, the IRI-NE, and a Digital Breast Model Generator module. There are several steps required to integrate this IRI numerical-based system to the hospital servers and PACS system. The first step is to integrate the IRI acquisition system to the PACS system via a PACS Broker and Data Grid, and a DICOM Acquisition Gateway. The PACS Broker and Data Grid sends the electronic patient records (ePRs) obtained at screening to the RIS storage database in order to identify the patient. The DICOM Acquisition Gateway formats and compresses the image data with the ePRs utilizing HL7 and DICOM standards. This data is then sent to the DICOM PACS Server and Archive which then becomes the main communicator between the RIS database and any other modules, such as the Breast Imaging Workstation utilized to visualize any image data at the hospital or clinic.

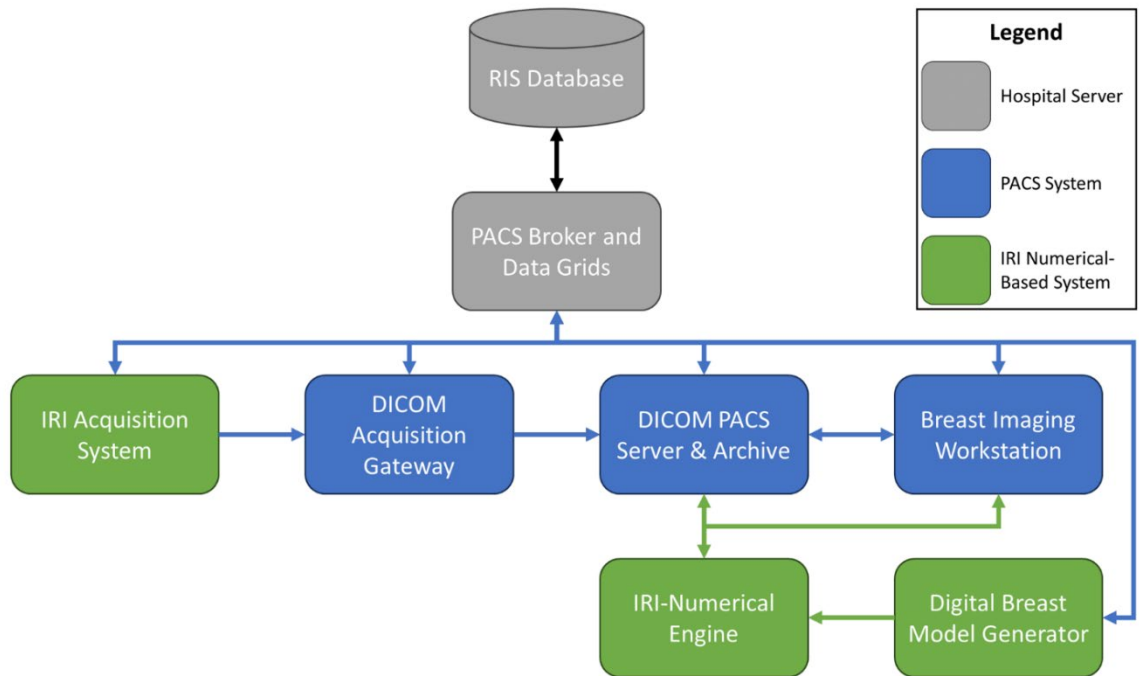


Figure 57. Example PACS architecture with an integrated IRI numerical-based system for breast cancer detection.

For the second step, the IRI-NE will need to be modified in order to communicate and integrate with the DICOM PACS server. This communication would allow the IRI-NE to know which patient to work on and when a request is pulled for the IRI-NE to analyze the patient. For the third step, a digital breast model (DBM) Generator module is needed to remove the dependency of MRI data to generate DBMs for bioheat transfer modeling of breast cancer. Any method to generate 3D breast models may be utilized such as 3D scanners, depth sensors, 3D reconstruction techniques, or any combination of these methods. This DBM Generator will need to be interfaced with the DICOM PACS Server and Archive to be able to pull the necessary data for model generation from the RIS database or from the PACS archives. Finally, the DBM Generator will need to be integrated with the IRI-NE in order to provide it with the data needed to conduct thermal and inverse heat transfer modeling. Further studies will be needed in the areas of software engineering,

medical informatics, and cybersecurity in order to ensure that the IRI-NE and the IRI acquisition system can be properly integrated into a hospital environment.

## 6.2 Experimental Detectability Testing

The detectability of the IRI-NE was conducted in this work through parametric numerical studies and generated synthetic IR data. To extend this work, an experimental detectability study is proposed to further validate the results found in this thesis. This proposed recommendation includes the use of phantom models created from patient-specific breast models. Mukhmetov et al. [147,394] developed a method to create phantom models using 3D scans of a female mannequin, Dragon Skin 10 MEDIUM Set Silicone Rubber to mimic tissue, and a resistor heat source. This allowed for thermal experiments to be conducted using this tissue mimicking phantom model to obtain IR surface temperatures to compare with thermal models and to conduct inverse heat transfer modeling. Other phantom models can be explored such as the agar-agar model proposed by Owens [401] or other breast phantom models utilized in literature [419–421].

The experimental detectability tests should be conducted for a 10 mm artificial tumor heat source made out of a cartridge heater or a resistor placed at the various depths studied in this thesis. To simulate the chest wall condition, a rectangular plate heater can be placed on top of the phantom model. Figure 58 shows an example of a phantom breast model that could be utilized for experimental detectability testing. The heat source should be adjusted to be an equivalent heat generation source using model developed by Gautherie [112–114] for the metabolic heat generation of a malignant tumor (Eq. 26). Power to the heat source and heater wall can be supplied through an external power source via a connecting wire. The artificial tumor can be positioned inside the breast model to test the IRI-NE in detecting

the heat source created by these tumors. This can provide an additional validation study of the IRI-NE for the detection of heat sources inside of breast models.

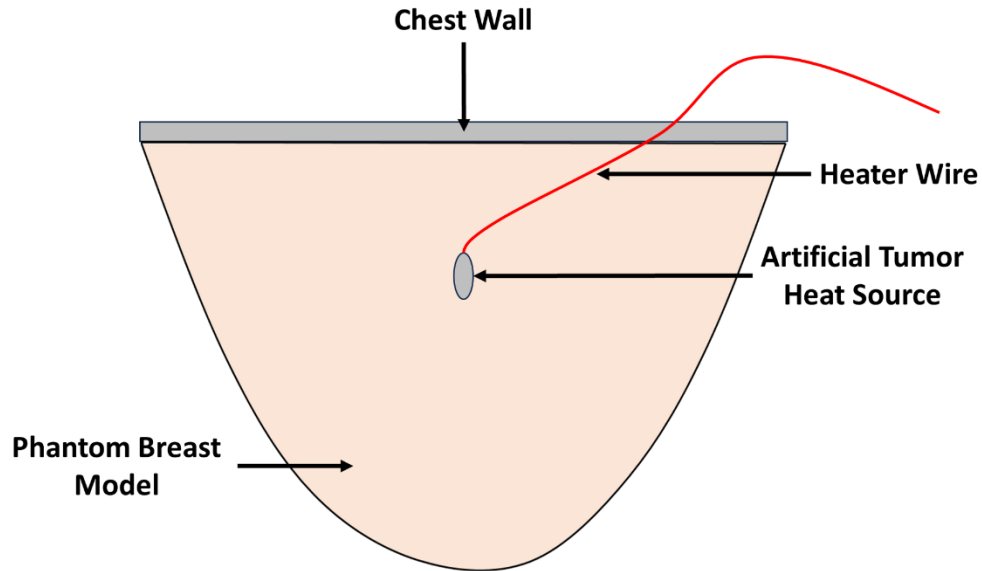


Figure 58. Phantom breast model with an artificial heat source and chest wall heater.

### 6.3 Effective Thermal Conductivity Bioheat Transfer

#### Modeling

Many researchers have investigated various forms of bioheat transfer modeling that would encapsulate the thermal effects provided by the tissue and vessels. The effective thermal conductivity bioheat model (Eq. 11), first developed by Weinbaum and Jiji [355], is able to capture the thermal effects of the tissue and small vessel interactions in a simplified model. This method worked well for a known vascular structure or other known relationship between the vessel and tissue environment. Gautherie [112–114] obtained measurements of the effective thermal conductivity ( $k_{eff}$ ) of patients with cancer and their contralateral healthy breast obtained using a fine-probe needle. Utilizing these principles an effective thermal conductivity model would be a good area to expand this work. This

can be conducted by considering the heat transfer due to large vessels inside a breast tissue region, as well as a tumor and its vasculature.

#### 6.4 Removal of Thermal Artifacts in IR Images

As the results from this work has shown, thermal artifacts affect the accuracy of detection. One method that was explored to improve accuracy was utilizing ROIs that do not include the areas that show the thermal artifacts. Another method that can be explored is the use of image processing techniques to identify thermal artifacts and conduct smoothening of the surface temperature. Smoothening of the thermal artifacts can be conducted by blurring the IR images or through the use of other filters. This smoothening is utilized to remove the hot regions created by thermal artifacts that appear in IR images. Figure 59 shows an example of IR surface temperature with a visible thermal artifact created by superficial veins and the same IR surface temperature gone through smoothening. The smoothen IR temperatures blend in the surface temperature with the rest of the temperatures in the surroundings. Further processing is needed to fully remove the thermal artifact temperatures, which requires further studies in the area of IR image processing.

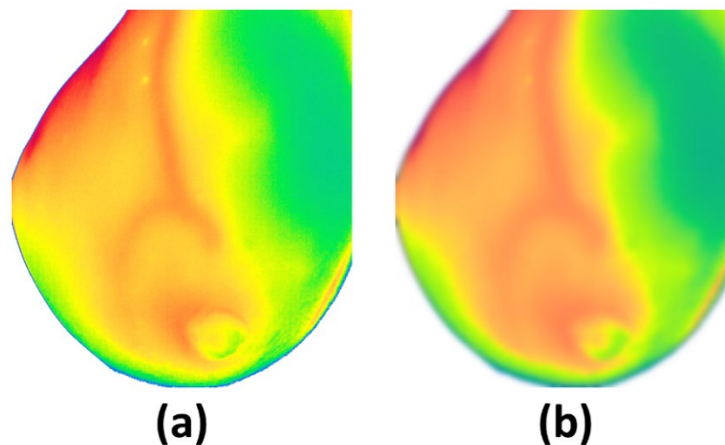


*Figure 59. Example of (a) IR surface temperature with visible thermal artifacts and (b) smoothen IR temperatures attempting to remove the thermal artifact surface temperature.*

## Chapter 9: References

- [1] Sung, H., Ferlay, J., Siegel, R. L., Laversanne, M., Soerjomataram, I., Jemal, A., and Bray, F., 2021, "Global Cancer Statistics 2020: GLOBOCAN Estimates of Incidence and Mortality Worldwide for 36 Cancers in 185 Countries," *CA: A Cancer Journal for Clinicians*, **71**(3), pp. 209–249.
- [2] Hong, R., and Xu, B., 2022, "Breast Cancer: An up-to-Date Review and Future Perspectives," *Cancer Communications*, **42**(10), pp. 913–936.
- [3] Łukasiewicz, S., Czezelewski, M., Forma, A., Baj, J., Sitarz, R., and Stanisławek, A., 2021, "Breast Cancer—Epidemiology, Risk Factors, Classification, Prognostic Markers, and Current Treatment Strategies—An Updated Review," *Cancers*, **13**(17), p. 4287.
- [4] "Breast Cancer Statistics | How Common Is Breast Cancer?" [Online]. Available: <https://www.cancer.org/cancer/types/breast-cancer/about/how-common-is-breast-cancer.html>. [Accessed: 25-Nov-2023].
- [5] Siegel, R., Miller, K., and Jemal, A., 2020, "Cancer Facts & Figures 2020," p. 76.
- [6] CDCBreastCancer, 2023, "What Is Breast Cancer?," Centers for Disease Control and Prevention [Online]. Available: [https://www.cdc.gov/cancer/breast/basic\\_info/what-is-breast-cancer.htm](https://www.cdc.gov/cancer/breast/basic_info/what-is-breast-cancer.htm). [Accessed: 05-Mar-2024].
- [7] 2021, "What Is Breast Cancer?" [Online]. Available: <https://www.cancer.org/cancer/types/breast-cancer/about/what-is-breast-cancer.html>. [Accessed: 05-Mar-2024].
- [8] 2011, "Definition of Breast Cancer - NCI Dictionary of Cancer Terms - NCI" [Online]. Available: <https://www.cancer.gov/publications/dictionaries/cancer-terms/def/breast-cancer>. [Accessed: 05-Mar-2024].
- [9] "Breast Cancer" [Online]. Available: <https://www.who.int/news-room/fact-sheets/detail/breast-cancer>. [Accessed: 05-Mar-2024].
- [10] "Anatomy of the Breast | Memorial Sloan Kettering Cancer Center" [Online]. Available: <https://www.mskcc.org/cancer-care/types/breast/anatomy-breast>. [Accessed: 12-Dec-2021].
- [11] Lian, J., and Li, K., 2020, "A Review of Breast Density Implications and Breast Cancer Screening," *Clinical Breast Cancer*, **20**(4), pp. 283–290.
- [12] Watkins, E. J., 2019, "Overview of Breast Cancer," *JAAPA*, **32**(10), p. 13.
- [13] Ahmad, A., ed., 2019, *Breast Cancer Metastasis and Drug Resistance: Challenges and Progress*, Springer, Cham, Switzerland.
- [14] Salvatorelli, L., Puzzo, L., Vecchio, G. M., Caltabiano, R., Virzi, V., and Magro, G., 2020, "Ductal Carcinoma In Situ of the Breast: An Update with Emphasis on Radiological and Morphological Features as Predictive Prognostic Factors," *Cancers*, **12**(3), p. 609.
- [15] Grimm, L. J., Rahbar, H., Abdelmalak, M., Hall, A. H., and Ryser, M. D., 2022, "Ductal Carcinoma in Situ: State-of-the-Art Review," *Radiology*, **302**(2), pp. 246–255.
- [16] Shehata, M., Grimm, L., Ballantyne, N., Lourenco, A., Demello, L. R., Kilgore, M. R., and Rahbar, H., 2019, "Ductal Carcinoma in Situ: Current Concepts in Biology, Imaging, and Treatment," *Journal of Breast Imaging*, **1**(3), pp. 166–176.
- [17] Sokolova, A., and Lakhani, S. R., 2021, "Lobular Carcinoma in Situ: Diagnostic Criteria and Molecular Correlates," *Modern Pathology*, **34**, pp. 8–14.
- [18] Harris, C. G., and Eslick, G. D., 2021, "Impact of Lobular Carcinoma in Situ on Local Recurrence in Breast Cancer Treated with Breast Conservation Therapy: A Systematic Review and Meta-Analysis," *ANZ Journal of Surgery*, **91**(9), pp. 1696–1703.

- [19] Brock, J., 2022, "Lobular Carcinoma in Situ – A Pragmatic Approach to the Controversies," *Human Pathology Reports*, **27**, p. 300589.
- [20] Zhao, H., 2021, "The Prognosis of Invasive Ductal Carcinoma, Lobular Carcinoma and Mixed Ductal and Lobular Carcinoma According to Molecular Subtypes of the Breast," *Breast Cancer*, **28**(1), pp. 187–195.
- [21] Wilson, N., Ironside, A., Diana, A., and Oikonomidou, O., 2021, "Lobular Breast Cancer: A Review," *Frontiers in Oncology*, **10**.
- [22] Thomas, M., Kelly, E. D., Abraham, J., and Kruse, M., 2019, "Invasive Lobular Breast Cancer: A Review of Pathogenesis, Diagnosis, Management, and Future Directions of Early Stage Disease," *Seminars in Oncology*, **46**(2), pp. 121–132.
- [23] Swaminathan, H., Saravanamurali, K., and Yadav, S. A., 2023, "Extensive Review on Breast Cancer Its Etiology, Progression, Prognostic Markers, and Treatment," *Med Oncol*, **40**(8), p. 238.
- [24] Duncan, M. A., and Lautner, M. A., 2018, "Sarcomas of the Breast," *Surgical Clinics*, **98**(4), pp. 869–876.
- [25] Kokkali, S., Moreno, J. D., Klijanienko, J., and Theocharis, S., 2022, "Clinical and Molecular Insights of Radiation-Induced Breast Sarcomas: Is There Hope on the Horizon for Effective Treatment of This Aggressive Disease?," *International Journal of Molecular Sciences*, **23**(8), p. 4125.
- [26] "Types of Breast Cancer" [Online]. Available: <https://www.breastcancer.org/types>. [Accessed: 25-Nov-2023].
- [27] "Types of Breast Cancer | About Breast Cancer" [Online]. Available: <https://www.cancer.org/cancer/types/breast-cancer/about/types-of-breast-cancer.html>. [Accessed: 25-Nov-2023].
- [28] 2013, "Tumor Grade - NCI" [Online]. Available: <https://www.cancer.gov/about-cancer/diagnosis-staging/diagnosis/tumor-grade>. [Accessed: 06-Mar-2024].
- [29] 2021, "What Is a Breast Cancer's Grade? | Grading Breast Cancer" [Online]. Available: <https://www.cancer.org/cancer/types/breast-cancer/understanding-a-breast-cancer-diagnosis/breast-cancer-grades.html>. [Accessed: 06-Mar-2024].
- [30] 2021, "Stages of Breast Cancer | Understand Breast Cancer Staging" [Online]. Available: <https://www.cancer.org/cancer/types/breast-cancer/understanding-a-breast-cancer-diagnosis/stages-of-breast-cancer.html>. [Accessed: 06-Mar-2024].
- [31] 2015, "Cancer Staging - NCI" [Online]. Available: <https://www.cancer.gov/about-cancer/diagnosis-staging/staging>. [Accessed: 06-Mar-2024].
- [32] Rosen, R. D., and Sapra, A., 2024, "TNM Classification," *StatPearls*, StatPearls Publishing, Treasure Island (FL).
- [33] Wang, J., Gottschal, P., Ding, L., Veldhuizen, Daniëlle W. A. van, Lu, W., Houssami, N., Greuter, M. J. W., and de Bock, G. H., 2020, "Mammographic Sensitivity as a Function of Tumor Size: A Novel Estimation Based on Population-Based Screening Data," *Breast*, **55**, pp. 69–74.
- [34] "Breast Cancer Risk Factors and Prevention Methods" [Online]. Available: <https://www.cancer.org/cancer/types/breast-cancer/risk-and-prevention.html>. [Accessed: 11-Mar-2024].
- [35] 2023, "Chances of Developing Breast Cancer by Age 70 to 80 - NCI" [Online]. Available: <https://www.cancer.gov/research/progress/discovery/brca-cancer-risk-infographic>. [Accessed: 11-Mar-2024].

- [36] 2021, “What Is Cancer? - National Cancer Institute” [Online]. Available: <https://www.cancer.gov/about-cancer/understanding/what-is-cancer>. [Accessed: 11-Dec-2021].
- [37] 2018, “Understanding What Cancer Is: Ancient Times to Present” [Online]. Available: <https://www.cancer.org/cancer/cancer-basics/history-of-cancer/what-is-cancer.html>. [Accessed: 11-Dec-2021].
- [38] Hanahan, D., and Weinberg, R. A., 2000, “The Hallmarks of Cancer,” *Cell*, **100**(1), pp. 57–70.
- [39] Hanahan, D., and Weinberg, R. A., 2011, “Hallmarks of Cancer: The Next Generation,” *Cell*, **144**(5), pp. 646–674.
- [40] Fouad, Y. A., and Aanei, C., 2017, “Revisiting the Hallmarks of Cancer,” *Am J Cancer Res*, **7**(5), pp. 1016–1036.
- [41] Hanahan, D., 2022, “Hallmarks of Cancer: New Dimensions,” *Cancer Discovery*, **12**(1), pp. 31–46.
- [42] 2011, “NCI Dictionary of Cancer Terms - NCI” [Online]. Available: <https://www.cancer.gov/publications/dictionaries/cancer-terms/>. [Accessed: 17-Jan-2023].
- [43] Marmet, D., ed., 2019, *Tumor Angiogenesis: A Key Target for Cancer Therapy*, Springer, Cham.
- [44] Folkman, J., 1971, “Tumor Angiogenesis: Therapeutic Implications,” *New England Journal of Medicine*, pp. 1182–1186.
- [45] Djonov, V., and Makanya, A. N., 2005, “New Insights into Intussusceptive Angiogenesis,” *Mechanisms of Angiogenesis*, M. Clauss, and G. Breier, eds., Birkhäuser Basel, Basel, pp. 17–33.
- [46] Luo, Q., Wang, J., Zhao, W., Peng, Z., Liu, X., Li, B., Zhang, H., Shan, B., Zhang, C., and Duan, C., 2020, “Vasculogenic Mimicry in Carcinogenesis and Clinical Applications,” *J Hematol Oncol*, **13**(1), p. 19.
- [47] Lee, S., Chen, T. T., Barber, C. L., Jordan, M. C., Murdock, J., Desai, S., Ferrara, N., Nagy, A., Roos, K. P., and Iruela-Arispe, M. L., 2007, “Autocrine VEGF Signaling Is Required for Vascular Homeostasis,” *Cell*, **130**(4), pp. 691–703.
- [48] Goel, S., Duda, D. G., Xu, L., Munn, L. L., Boucher, Y., Fukumura, D., and Jain, R. K., 2011, “Normalization of the Vasculature for Treatment of Cancer and Other Diseases,” *Physiological Reviews*, **91**(3), pp. 1071–1121.
- [49] Baluk, P., Hashizume, H., and McDonald, D. M., 2005, “Cellular Abnormalities of Blood Vessels as Targets in Cancer,” *Current Opinion in Genetics & Development*, **15**(1), pp. 102–111.
- [50] 2023, “ACS Breast Cancer Screening Guidelines” [Online]. Available: <https://www.cancer.org/cancer/types/breast-cancer/screening-tests-and-early-detection/american-cancer-society-recommendations-for-the-early-detection-of-breast-cancer.html>. [Accessed: 06-Mar-2024].
- [51] Bailar, J. C., 1976, “Mammography: A Contrary View,” *Ann Intern Med*, **84**(1), pp. 77–84.
- [52] Pisano, E. D., and Yaffe, M. J., 2005, “Digital Mammography,” *Radiology*, **234**(2), pp. 353–362.
- [53] Kalaf, J. M., 2014, “Mammography: A History of Success and Scientific Enthusiasm,” *Radiol Bras*, **47**(4), p. VII–VIII.
- [54] Commissioner, O., 2021, “Mammography: What You Need to Know,” FDA.
- [55] Freer, P. E., 2015, “Mammographic Breast Density: Impact on Breast Cancer Risk and Implications for Screening,” *Radiographics*, **35**(2), pp. 302–315.

- [56] Narayan, A. K., Lee, C. I., and Lehman, C. D., 2020, "Screening for Breast Cancer," *Medical Clinics*, **104**(6), pp. 1007–1021.
- [57] "3D Mammograms | Beverly Hills," Bedford Breast Center [Online]. Available: <https://www.bedfordbreastcenter.com/mammogram-los-angeles/>. [Accessed: 12-Dec-2021].
- [58] Dempsey, P. J., 2004, "The History of Breast Ultrasound," *Journal of Ultrasound in Medicine*, **23**(7), pp. 887–894.
- [59] Sehgal, C. M., Weinstein, S. P., Arger, P. H., and Conant, E. F., 2006, "A Review of Breast Ultrasound," *J Mammary Gland Biol Neoplasia*, **11**(2), pp. 113–123.
- [60] Barba, D., León-Sosa, A., Lugo, P., Suquillo, D., Torres, F., Surre, F., Trojman, L., and Caicedo, A., 2021, "Breast Cancer, Screening and Diagnostic Tools: All You Need to Know," *Critical Reviews in Oncology/Hematology*, **157**, p. 103174.
- [61] Nicosia, L., Gnocchi, G., Gorini, I., Venturini, M., Fontana, F., Pesapane, F., Abiuso, I., Bozzini, A. C., Pizzamiglio, M., Latronico, A., Abbate, F., Meneghetti, L., Battaglia, O., Pellegrino, G., and Cassano, E., 2023, "History of Mammography: Analysis of Breast Imaging Diagnostic Achievements over the Last Century," *Healthcare*, **11**(11), p. 1596.
- [62] Gokhale, S., 2009, "Ultrasound Characterization of Breast Masses," *Indian J Radiol Imaging*, **19**(3), pp. 242–247.
- [63] Hendrick, R. E., 2008, *Breast MRI*, Springer New York, New York, NY.
- [64] Lauterbur, P. C., 1973, "Image Formation by Induced Local Interactions: Examples Employing Nuclear Magnetic Resonance," *Nature*, **242**(5394), pp. 190–191.
- [65] Platt, T., Ladd, M. E., and Paech, D., 2021, "7 Tesla and Beyond: Advanced Methods and Clinical Applications in Magnetic Resonance Imaging," *Investigative Radiology*, **56**(11), p. 705.
- [66] Wu, C., Hormuth, D. A., Oliver, T. A., Pineda, F., Lorenzo, G., Karczmar, G. S., Moser, R. D., and Yankeelov, T. E., 2020, "Patient-Specific Characterization of Breast Cancer Hemodynamics Using Image-Guided Computational Fluid Dynamics," *IEEE Trans. Med. Imaging*, **39**(9), pp. 2760–2771.
- [67] Jayender, J., Gombos, E., Chikarmane, S., Dabydeen, D., Jolesz, F. A., and Vosburgh, K. G., 2013, "Statistical Learning Algorithm for in Situ and Invasive Breast Carcinoma Segmentation," *Computerized Medical Imaging and Graphics*, **37**(4), pp. 281–292.
- [68] Jayender, J., Chikarmane, S., Jolesz, F. A., and Gombos, E., 2014, "Automatic Segmentation of Invasive Breast Carcinomas from Dynamic Contrast-Enhanced MRI Using Time Series Analysis: Segmenting Invasive Breast Carcinomas," *J. Magn. Reson. Imaging*, **40**(2), pp. 467–475.
- [69] Stehouwer, B. L., Klomp, D. W. J., van den Bosch, M. A. A. J., Korteweg, M. A., Gilhuijs, K. G. A., Witkamp, A. J., van Diest, P. J., Houwert, K. A. F., van der Kemp, W. J. M., Luijten, P. R., Mali, W. P. Th. M., and Veldhuis, W. B., 2013, "Dynamic Contrast-Enhanced and Ultra-High-Resolution Breast MRI at 7.0 Tesla," *Eur Radiol*, **23**(11), pp. 2961–2968.
- [70] Menezes, G. L., Knuttel, F. M., Stehouwer, B. L., Pijnappel, R. M., and Bosch, M. A., 2014, "Magnetic Resonance Imaging in Breast Cancer: A Literature Review and Future Perspectives," *World J Clin Oncol*, **5**(2), pp. 61–70.
- [71] Mann, R. M., Cho, N., and Moy, L., 2019, "Breast MRI: State of the Art," *Radiology*, **292**(3), pp. 520–536.
- [72] Swift, A., Heale, R., and Twycross, A., 2020, "What Are Sensitivity and Specificity?," *Evidence - Based Nursing*, **23**(1), p. 2.
- [73] Aristokli, N., Polycarpou, I., Themistocleous, S. C., Sophocleous, D., and Mamais, I., 2022, "Comparison of the Diagnostic Performance of Magnetic Resonance Imaging (MRI),

- Ultrasound and Mammography for Detection of Breast Cancer Based on Tumor Type, Breast Density and Patient's History: A Review," *Radiography*, **28**(3), pp. 848–856.
- [74] Massat, M. B., 2017, "Breast Imaging Update: Guidelines, Recall Rates and Personalized Care," *Applied Radiology*, **46**(9), pp. 28–31.
- [75] Hussein, H., Abbas, E., Keshavarzi, S., Fazelzad, R., Bukhanov, K., Kulkarni, S., Au, F., Ghai, S., Alabousi, A., and Freitas, V., 2023, "Supplemental Breast Cancer Screening in Women with Dense Breasts and Negative Mammography: A Systematic Review and Meta-Analysis," *Radiology*, **306**(3), p. e221785.
- [76] Yuan, W.-H., Hsu, H.-C., Chen, Y.-Y., and Wu, C.-H., 2020, "Supplemental Breast Cancer-Screening Ultrasonography in Women with Dense Breasts: A Systematic Review and Meta-Analysis," *Br J Cancer*, **123**(4), pp. 673–688.
- [77] von Euler-Chelpin, M., Lillholm, M., Vejborg, I., Nielsen, M., and Lynge, E., 2019, "Sensitivity of Screening Mammography by Density and Texture: A Cohort Study from a Population-Based Screening Program in Denmark," *Breast Cancer Res*, **21**(1), p. 111.
- [78] Vourtsis, A., and Berg, W. A., 2019, "Breast Density Implications and Supplemental Screening," *Eur Radiol*, **29**(4), pp. 1762–1777.
- [79] Veenhuizen, S. G. A., de Lange, S. V., Bakker, M. F., Pijnappel, R. M., Mann, R. M., Monninkhof, E. M., Emaus, M. J., de Koekkoek-Doll, P. K., Bisschops, R. H. C., Lobbes, M. B. I., de Jong, M. D. F., Duvivier, K. M., Veltman, J., Karssemeijer, N., de Koning, H. J., van Diest, P. J., Mali, W. P. T. M., van den Bosch, M. A. A. J., van Gils, C. H., Veldhuis, W. B., van Gils, C. H., Bakker, M. F., de Lange, S. V., Veenhuizen, S. G. A., Veldhuis, W. B., Pijnappel, R. M., Emaus, M. J., Peeters, P. H. M., Monninkhof, E. M., Fernandez-Gallardo, M. A., Mali, W. P. T. M., van den Bosch, M. a. a. J., van Diest, P. J., Mann, R. M., Mus, R., Imhof-Tas, M., Karssemeijer, N., Loo, C. E., de Koekkoek-Doll, P. K., Winter-Warnars, H. a. O., Bisschops, R. H. C., Kock, M. C. J. M., Storm, R. K., van der Valk, P. H. M., Lobbes, M. B. I., Gommers, S., Lobbes, M. B. I., de Jong, M. D. F., Rutten, M. J. C. M., Duvivier, K. M., de Graaf, P., Veltman, J., Bourez, R. L. J. H., and de Koning, H. J., 2021, "Supplemental Breast MRI for Women with Extremely Dense Breasts: Results of the Second Screening Round of the DENSE Trial," *Radiology*, **299**(2), pp. 278–286.
- [80] Giess, C. S., Wang, A., Ip, I. K., Lacson, R., Pourjabbar, S., and Khorasani, R., 2019, "Patient, Radiologist, and Examination Characteristics Affecting Screening Mammography Recall Rates in a Large Academic Practice," *Journal of the American College of Radiology*, **16**(4, Part A), pp. 411–418.
- [81] Mullen, L. A., Panigrahi, B., Hollada, J., Panigrahi, B., Falomo, E. T., and Harvey, S. C., 2017, "Strategies for Decreasing Screening Mammography Recall Rates While Maintaining Performance Metrics," *Academic Radiology*, **24**(12), pp. 1556–1560.
- [82] Grabler, P., Sighoko, D., Wang, L., Allgood, K., and Ansell, D., 2017, "Recall and Cancer Detection Rates for Screening Mammography: Finding the Sweet Spot," *American Journal of Roentgenology*, **208**(1), pp. 208–213.
- [83] Weedon-Fekjær, H., Lindqvist, B. H., Vatten, L. J., Aalen, O. O., and Tretli, S., 2008, "Breast Cancer Tumor Growth Estimated through Mammography Screening Data," *Breast Cancer Res*, **10**(3), pp. 1–13.
- [84] Isheden, G., and Humphreys, K., 2019, "Modelling Breast Cancer Tumour Growth for a Stable Disease Population," *Stat Methods Med Res*, **28**(3), pp. 681–702.
- [85] Abrahamsson, L., Isheden, G., Czene, K., and Humphreys, K., 2020, "Continuous Tumour Growth Models, Lead Time Estimation and Length Bias in Breast Cancer Screening Studies," *Stat Methods Med Res*, **29**(2), pp. 374–395.

- [86] Chen, H., Zhou, J., Chen, Q., and Deng, Y., 2021, "Comparison of the Sensitivity of Mammography, Ultrasound, Magnetic Resonance Imaging and Combinations of These Imaging Modalities for the Detection of Small ( $\leq 2$  Cm) Breast Cancer," *Medicine (Baltimore)*, **100**(26), p. e26531.
- [87] Nickson, C., and Kavanagh, A. M., 2009, "Tumour Size at Detection According to Different Measures of Mammographic Breast Density," *J Med Screen*, **16**(3), pp. 140–146.
- [88] Lee, S. H., Jang, M. J., Kim, S. M., Yun, B. L., Rim, J., Chang, J. M., Kim, B., and Choi, H. Y., 2019, "Factors Affecting Breast Cancer Detectability on Digital Breast Tomosynthesis and Two-Dimensional Digital Mammography in Patients with Dense Breasts," *Korean J Radiol*, **20**(1), pp. 58–68.
- [89] Sogunro, O., Cashen, C., Fakir, S., Stausmire, J., and Buderer, N., 2021, "Detecting Accurate Tumor Size across Imaging Modalities in Breast Cancer," *Breast Dis*, **40**(3), pp. 177–182.
- [90] Gruber, I. V., Rueckert, M., Kagan, K. O., Staebler, A., Siegmann, K. C., Hartkopf, A., Wallwiener, D., and Hahn, M., 2013, "Measurement of Tumour Size with Mammography, Sonography and Magnetic Resonance Imaging as Compared to Histological Tumour Size in Primary Breast Cancer," *BMC Cancer*, **13**(1), p. 328.
- [91] Eichler, C., Abrar, S., Puppe, J., Arndt, M., Ohlinger, R., Hahn, M., and Warm, M., 2017, "Detection of Ductal Carcinoma In Situ by Ultrasound and Mammography: Size-Dependent Inaccuracy," *Anticancer Research*, **37**(9), pp. 5065–5070.
- [92] Azhdeh, S., Kaviani, A., Sadighi, N., and Rahmani, M., 2021, "Accurate Estimation of Breast Tumor Size: A Comparison Between Ultrasonography, Mammography, Magnetic Resonance Imaging, and Associated Contributing Factors," *European Journal of Breast Health*, **17**(1), p. 53.
- [93] Ines Ramirez, S., Scholle, M., Buckmaster, J., Paley, R. H., and Kowdley, G. C., 2012, "Breast Cancer Tumor Size Assessment with Mammography, Ultrasonography, and Magnetic Resonance Imaging at a Community Based Multidisciplinary Breast Center," *The American Surgeon™*, **78**(4), pp. 440–446.
- [94] Cuesta Cuesta, A. B., Martín Ríos, M. D., Noguero Meseguer, M. R., García Velasco, J. A., Matías Martínez, M. de, Bartolomé Sotillos, S., and Abreu Griego, E., 2019, "Accuracy of Tumor Size Measurements Performed by Magnetic Resonance, Ultrasound and Mammography, and Their Correlation With Pathological Size in Primary Breast Cancer," *Cirugía Española (English Edition)*, **97**(7), pp. 391–396.
- [95] Püsküllüoğlu, M., Świdarska, K., Konieczna, A., Rudnicki, W., Pacholczak-Madej, R., Kunkiel, M., Grela-Wojewoda, A., Mucha-Małecka, A., Mituś, J. W., Stobiecka, E., Ryś, J., Jarzab, M., and Ziobro, M., 2024, "Discrepancy between Tumor Size Assessed by Full-Field Digital Mammography or Ultrasonography (cT) and Pathology (pT) in a Multicenter Series of Breast Metaplastic Carcinoma Patients," *Cancers*, **16**(1), p. 188.
- [96] "Atlas of Breast Cancer Early Detection" [Online]. Available: <https://screening.iarc.fr/atlasbreastdetail.php?Index=050&e=>. [Accessed: 17-Dec-2023].
- [97] Mousa, D. A., Ryan, E., Lee, W., Nickson, C., Pietrzyk, M., Reed, W., Poulos, A., Li, Y., and Brennan, P., 2013, "The Impact of Mammographic Density and Lesion Location on Detection," *Medical Imaging 2013: Image Perception, Observer Performance, and Technology Assessment*, SPIE, pp. 205–213.
- [98] Wadhwa, A., Sullivan, J. R., and Gonyo, M. B., 2016, "Missed Breast Cancer: What Can We Learn?," *Current Problems in Diagnostic Radiology*, **45**(6), pp. 402–419.
- [99] Jochelson, M. S., and Lobbes, M. B. I., 2021, "Contrast-Enhanced Mammography: State of the Art," *Radiology*, **299**(1), pp. 36–48.

- [100] Cozzi, A., Magni, V., Zanardo, M., Schiaffino, S., and Sardanelli, F., 2022, "Contrast-Enhanced Mammography: A Systematic Review and Meta-Analysis of Diagnostic Performance," *Radiology*, **302**(3), pp. 568–581.
- [101] Pötsch, N., Vatteroni, G., Clauser, P., Helbich, T. H., and Baltzer, P. A. T., 2022, "Contrast-Enhanced Mammography versus Contrast-Enhanced Breast MRI: A Systematic Review and Meta-Analysis," *Radiology*, **305**(1), pp. 94–103.
- [102] Mann, R. M., Kuhl, C. K., and Moy, L., 2019, "Contrast-Enhanced MRI for Breast Cancer Screening," *Journal of Magnetic Resonance Imaging*, **50**(2), pp. 377–390.
- [103] Ramadan, S. Z., 2020, "Methods Used in Computer-Aided Diagnosis for Breast Cancer Detection Using Mammograms: A Review," *Journal of Healthcare Engineering*, **2020**, p. e9162464.
- [104] Zebari, D. A., Ibrahim, D. A., Zeebaree, D. Q., Haron, H., Salih, M. S., Damaševičius, R., and Mohammed, M. A., 2021, "Systematic Review of Computing Approaches for Breast Cancer Detection Based Computer Aided Diagnosis Using Mammogram Images," *Applied Artificial Intelligence*, **35**(15), pp. 2157–2203.
- [105] Zahoor, S., Lali, I. U., Khan, M. A., Javed, K., and Mehmood, W., 2020, "Breast Cancer Detection and Classification Using Traditional Computer Vision Techniques: A Comprehensive Review," *Current Medical Imaging Reviews*, **16**(10), pp. 1187–1200.
- [106] Hassan, N. M., Hamad, S., and Mahar, K., 2022, "Mammogram Breast Cancer CAD Systems for Mass Detection and Classification: A Review," *Multimed Tools Appl*, **81**(14), pp. 20043–20075.
- [107] Bai, J., Posner, R., Wang, T., Yang, C., and Nabavi, S., 2021, "Applying Deep Learning in Digital Breast Tomosynthesis for Automatic Breast Cancer Detection: A Review," *Medical Image Analysis*, **71**, p. 102049.
- [108] Jones, M. A., Islam, W., Faiz, R., Chen, X., and Zheng, B., 2022, "Applying Artificial Intelligence Technology to Assist with Breast Cancer Diagnosis and Prognosis Prediction," *Frontiers in Oncology*, **12**.
- [109] Nassif, A. B., Talib, M. A., Nasir, Q., Afadar, Y., and Elgendy, O., 2022, "Breast Cancer Detection Using Artificial Intelligence Techniques: A Systematic Literature Review," *Artificial Intelligence in Medicine*, **127**, p. 102276.
- [110] Henriksen, E. L., Carlsen, J. F., Vejborg, I. M., Nielsen, M. B., and Lauridsen, C. A., 2019, "The Efficacy of Using Computer-Aided Detection (CAD) for Detection of Breast Cancer in Mammography Screening: A Systematic Review," *Acta Radiol*, **60**(1), pp. 13–18.
- [111] Potnis, K. C., Ross, J. S., Aneja, S., Gross, C. P., and Richman, I. B., 2022, "Artificial Intelligence in Breast Cancer Screening: Evaluation of FDA Device Regulation and Future Recommendations," *JAMA Internal Medicine*, **182**(12), pp. 1306–1312.
- [112] Gautherie, M., 1980, "Thermopathology of Breast Cancer: Measurement and Analysis of in Vivo Temperature and Blood Flow," *Annals of the New York Academy of Sciences*, **335**(1), pp. 383–415.
- [113] Gautherie, M., 1982, "Temperature and Blood Flow Patterns in Breast Cancer during Natural Evolution and Following Radiotherapy," *Prog Clin Biol Res*, **107**, pp. 21–64.
- [114] Gautherie, M., 1983, "Thermobiological Assessment of Benign and Malignant Breast Diseases," *American Journal of Obstetrics & Gynecology*, **147**(8), pp. 861–869.
- [115] Commissioner, O. of the, 2023, "Breast Cancer Screening: Thermogram No Substitute for Mammogram," FDA.
- [116] Kandlikar, S. G., Perez-Raya, I., Raghupathi, P. A., Gonzalez-Hernandez, J.-L., Dabydeen, D., Medeiros, L., and Phatak, P., 2017, "Infrared Imaging Technology for Breast Cancer

- Detection – Current Status, Protocols and New Directions,” *International Journal of Heat and Mass Transfer*, **108**, pp. 2303–2320.
- [117] Sarigoz, T., Ertan, T., Topuz, O., Sevim, Y., and Cihan, Y., 2018, “Role of Digital Infrared Thermal Imaging in the Diagnosis of Breast Mass: A Pilot Study: Diagnosis of Breast Mass by Thermography,” *Infrared Physics & Technology*, **91**, pp. 214–219.
- [118] Gonzalez-Hernandez, J.-L., Recinella, A. N., Kandlikar, S. G., Dabydeen, D., Medeiros, L., and Phatak, P., 2019, “Technology, Application and Potential of Dynamic Breast Thermography for the Detection of Breast Cancer,” *International Journal of Heat and Mass Transfer*, **131**, pp. 558–573.
- [119] Lozano, A., and Hassanipour, F., 2019, “Infrared Imaging for Breast Cancer Detection: An Objective Review of Foundational Studies and Its Proper Role in Breast Cancer Screening,” *Infrared Physics & Technology*, **97**, pp. 244–257.
- [120] Owens, A., Kandlikar, S. G., and Phatak, P., 2021, “Potential of Infrared Imaging for Breast Cancer Detection: A Critical Evaluation,” *Journal of Engineering and Science in Medical Diagnostics and Therapy*, **4**(041005).
- [121] Rakhunde, M. B., Gotarkar, S., and Choudhari, S. G., 2022, “Thermography as a Breast Cancer Screening Technique: A Review Article,” *Cureus*, **14**(11), p. e31251.
- [122] Godfrey, M., and Godfrey, P., 2023, “Breast Thermography: A 20-Year Retrospective Review of Infra-Red Breast Thermal Imaging in New Zealand and Its Potential Role in Breast Health Management,” *Advances in Breast Cancer Research*, **12**(4), pp. 129–141.
- [123] Jacob, G., Jose, I., and S., S., 2023, “Breast Cancer Detection: A Comparative Review on Passive and Active Thermography,” *Infrared Physics & Technology*, **134**, p. 104932.
- [124] Tsietsos, D., Yahya, A., and Samikannu, R., 2022, “A Review on Thermal Imaging-Based Breast Cancer Detection Using Deep Learning,” *Mobile Information Systems*, **2022**, p. e8952849.
- [125] Husaini, M. A. S. A., Habaebi, M. H., Hameed, S. A., Islam, Md. R., and Gunawan, T. S., 2020, “A Systematic Review of Breast Cancer Detection Using Thermography and Neural Networks,” *IEEE Access*, **8**, pp. 208922–208937.
- [126] Mahoro, E., and Akhloufi, M. A., 2024, “Breast Cancer Classification on Thermograms Using Deep CNN and Transformers,” *Quantitative InfraRed Thermography Journal*, **21**(1), pp. 30–49.
- [127] Wang, X., Chou, K., Zhang, G., Zuo, Z., Zhang, T., Zhou, Y., Mao, F., Lin, Y., Shen, S., Zhang, X., Wang, X., Zhong, Y., Qin, X., Guo, H., Wang, X., Xiao, Y., Yi, Q., Yan, C., Liu, J., Li, D., Liu, W., Liu, M., Ma, X., Tao, J., Sun, Q., Zhai, J., and Huang, L., 2023, “Breast Cancer Pre-Clinical Screening Using Infrared Thermography and Artificial Intelligence: A Prospective, Multicentre, Diagnostic Accuracy Cohort Study,” *International Journal of Surgery*, **109**(10), p. 3021.
- [128] Pramanik, R., Pramanik, P., and Sarkar, R., 2023, “Breast Cancer Detection in Thermograms Using a Hybrid of GA and GWO Based Deep Feature Selection Method,” *Expert Systems with Applications*, **219**, p. 119643.
- [129] Nogales, A., Pérez-Lara, F., and García-Tejedor, Á. J., 2023, “Enhancing Breast Cancer Diagnosis with Deep Learning and Evolutionary Algorithms: A Comparison of Approaches Using Different Thermographic Imaging Treatments,” *Multimed Tools Appl.*
- [130] Mishra, V., Rath, S. K., and Mohapatra, D. P., 2023, “Thermograms-Based Detection of Cancerous Tumors in Breasts Applying Texture Features,” *Quantitative InfraRed Thermography Journal*, **0**(0), pp. 1–26.

- [131] Sayed, B. A., Eldin, A. S., Elzanfaly, D. S., and Ghoneim, A. S., 2023, "A Comprehensive Review of Breast Cancer Early Detection Using Thermography and Convolutional Neural Networks," *2023 International Conference on Computer and Applications (ICCA)*, pp. 1–6.
- [132] Dihmani, H., Bouattane, O., and Grief, O. S., 2022, "A Review on Suspicious-Regions Segmentation Methods in Breast Thermogram Image," *2022 2nd International Conference on Innovative Research in Applied Science, Engineering and Technology (IRASET)*, pp. 1–5.
- [133] Alshehri, A., and AlSaeed, D., 2022, "Breast Cancer Detection in Thermography Using Convolutional Neural Networks (CNNs) with Deep Attention Mechanisms," *Applied Sciences*, **12**(24), p. 12922.
- [134] Roslidar, R., Rahman, A., Muharar, R., Syahputra, M. R., Arnia, F., Syukri, M., Pradhan, B., and Munadi, K., 2020, "A Review on Recent Progress in Thermal Imaging and Deep Learning Approaches for Breast Cancer Detection," *IEEE Access*, **8**, pp. 116176–116194.
- [135] Torghabeh, F. A., Modaresnia, Y., and Hosseini, S. A., 2023, "An Efficient Approach for Breast Abnormality Detection through High-Level Features of Thermography Images," *2023 13th International Conference on Computer and Knowledge Engineering (ICCKE)*, pp. 054–059.
- [136] Santos, L. C., de Cassia Fernandes de Lima, R., de Paiva, A. C., Conci, A., and Espindola, N. A., 2023, "A Computing Platform to Analyze Breast Abnormalities Using Infrared Images," *Med Biol Eng Comput*, **61**(2), pp. 305–315.
- [137] Hakim, A., and Awale, R. N., 2022, "Identification of Breast Abnormality from Thermograms Based on Fractal Geometry Features," *IOT with Smart Systems*, T. Senjyu, P. Mahalle, T. Perumal, and A. Joshi, eds., Springer Nature, Singapore, pp. 393–401.
- [138] Periyasamy, S., Prakasrao, A., Menaka, M., Venkatraman, B., and Jayashree, M., 2022, "Support Vector Machine Based Methodology for Classification of Thermal Images Pertaining to Breast Cancer," *Journal of Thermal Biology*, **110**, p. 103337.
- [139] Bansal, R., Collison, S., Krishnan, L., Aggarwal, B., Vidyasagar, M., Kakileti, S. T., and Manjunath, G., 2023, "A Prospective Evaluation of Breast Thermography Enhanced by a Novel Machine Learning Technique for Screening Breast Abnormalities in a General Population of Women Presenting to a Secondary Care Hospital," *Front. Artif. Intell.*, **5**.
- [140] Aggarwal, A. K., Alpana, and Pandey, M., 2022, "Deep Learning Based Breast Cancer Classification on Thermogram," *2022 International Conference on Computing, Communication, and Intelligent Systems (ICCCIS)*, pp. 769–774.
- [141] Shojaedini, S. V., Abedini, M., and Monajemi, M., 2023, "Generative Adversarial Network: A Statistical-Based Deep Learning Paradigm to Improve Detecting Breast Cancer in Thermograms," *Med Biol Eng Comput*.
- [142] D’Alessandro, G., Tavakolian, P., and Sfarra, S., 2024, "A Review of Techniques and Bio-Heat Transfer Models Supporting Infrared Thermal Imaging for Diagnosis of Malignancy," *Applied Sciences*, **14**(4), p. 1603.
- [143] Venkatapathy, G., Mittal, A., Gnanasekaran, N., and Desai, V. H., 2023, "Inverse Estimation of Breast Tumor Size and Location with Numerical Thermal Images of Breast Model Using Machine Learning Models," *Heat Transfer Engineering*, **44**(15), pp. 1433–1451.
- [144] Perez-Raya, I., Gutierrez, C., and Kandlikar, S., 2024, "A Transformative Approach for Breast Cancer Detection Using Physics-Informed Neural Network and Surface Temperature Data," *Journal of Heat Transfer*, p. Accepted.
- [145] Mukhmetov, O., Zhao, Y., Mashekova, A., Zarikas, V., Ng, E. Y. K., and Aidossov, N., 2023, "Physics-Informed Neural Network for Fast Prediction of Temperature Distributions in

- Cancerous Breasts as a Potential Efficient Portable AI-Based Diagnostic Tool,” *Computer Methods and Programs in Biomedicine*, **242**, p. 107834.
- [146] Sudarsan, N., Arathy, K., Antony, L., Sudheesh, R. S., Muralidharan, M. N., Satheesan, B., and Ansari, S., 2021, “A Computational Method for the Estimation of the Geometrical and Thermophysical Properties of Tumor Using Contact Thermometry,” *Journal of Medical Devices*, **15**(031012).
- [147] Mukhmetov, O., Mashekova, A., Zhao, Y., Ng, E., Midlenko, A., Fok, S., and Teh, S. L., 2021, “Inverse Thermal Modeling and Experimental Validation for Breast Tumor Detection by Using Highly Personalized Surface Thermal Patterns and Geometry of the Breast,” *Proceedings of the Institution of Mechanical Engineers, Part C: Journal of Mechanical Engineering Science*, **235**(19), pp. 3777–3791.
- [148] Mashekova, A., Zhao, Y., Ng, E. Y. K., Zarikas, V., Fok, S. C., and Mukhmetov, O., 2022, “Early Detection of the Breast Cancer Using Infrared Technology – A Comprehensive Review,” *Thermal Science and Engineering Progress*, **27**, p. 101142.
- [149] Recinella, A. N., Gonzalez-Hernandez, J.-L., Kandlikar, S. G., Dabydeen, D., Medeiros, L., and Phatak, P., 2020, “Clinical Infrared Imaging in the Prone Position for Breast Cancer Screening—Initial Screening and Digital Model Validation,” *Journal of Engineering and Science in Medical Diagnostics and Therapy*, **3**(1), p. 011005.
- [150] Gonzalez-Hernandez, J.-L., Recinella, A. N., Kandlikar, S. G., Dabydeen, D., Medeiros, L., and Phatak, P., 2020, “An Inverse Heat Transfer Approach for Patient-Specific Breast Cancer Detection and Tumor Localization Using Surface Thermal Images in the Prone Position,” *Infrared Physics & Technology*, **105**, p. 103202.
- [151] Etehadtavakol, M., and Ng, E. Y. K., 2020, “Survey of Numerical Bioheat Transfer Modelling for Accurate Skin Surface Measurements,” *Thermal Science and Engineering Progress*, **20**, p. 100681.
- [152] Al Husaini, M. A. S., Habaebi, M. H., Suliman, F. M., Islam, M. R., Elsheikh, E. A. A., and Muhaisen, N. A., 2023, “Influence of Tissue Thermophysical Characteristics and Situ-Cooling on the Detection of Breast Cancer,” *Applied Sciences*, **13**(15), p. 8752.
- [153] Silva, L., Seixas, F., Fontes, C., Muchaluat-Saade, D., and Conci, A., 2020, “A Computational Method for Breast Abnormality Detection Using Thermographs,” *2020 IEEE 33rd International Symposium on Computer-Based Medical Systems (CBMS)*, pp. 469–474.
- [154] Mukhmetov, O., Mashekova, A., Zhao, Y., Midlenko, A., Ng, E. Y. K., and Fok, S. C., 2021, “Patient/Breast-Specific Detection of Breast Tumor Based on Patients’ Thermograms, 3D Breast Scans, and Reverse Thermal Modelling,” *Applied Sciences*, **11**(14), p. 6565.
- [155] Bezerra, L. A., Ribeiro, R. R., Lyra, P. R. M., and Lima, R. C. F., 2020, “An Empirical Correlation to Estimate Thermal Properties of the Breast and of the Breast Nodule Using Thermographic Images and Optimization Techniques,” *International Journal of Heat and Mass Transfer*, **149**, p. 119215.
- [156] Benfenati, A., Causin, P., Lupieri, M., and Naldi, G., 2020, “Regularization Techniques for Inverse Problem in DOT Applications,” *J. Phys.: Conf. Ser.*, **1476**(1), p. 012007.
- [157] Howell, K., Dudek, K., and Soroko, M., 2020, “Thermal Camera Performance and Image Analysis Repeatability in Equine Thermography,” *Infrared Physics & Technology*, **110**, p. 103447.
- [158] Vollmer, M., and Möllmann, K.-P., 2018, *Infrared Thermal Imaging: Fundamentals, Research and Applications*, Wiley-VCH Verlag GmbH & Co. KGaA, Weinheim, Germany.
- [159] Rogalski, A., 2022, “Scaling Infrared Detectors—Status and Outlook,” *Rep. Prog. Phys.*, **85**(12), p. 126501.

- [160] Bhan, R. K., and Dhar, V., 2019, "Recent Infrared Detector Technologies, Applications, Trends and Development of HgCdTe Based Cooled Infrared Focal Plane Arrays and Their Characterization," *Opto-Electronics Review*, **27**(2), pp. 174–193.
- [161] Rogalski, A., 2017, "Next Decade in Infrared Detectors," *Electro-Optical and Infrared Systems: Technology and Applications XIV*, D.A. Huckridge, R. Ebert, and H. Bürsing, eds., SPIE, Warsaw, Poland, p. 100.
- [162] Lawson, R., 1956, "Implications of Surface Temperatures in the Diagnosis of Breast Cancer," *Canadian Medical Association Journal*, **75**(4), p. 309.
- [163] Lawson, R. N., Saunders, A. L., and Cowen, R. D., 1956, "Breast Cancer and Heptaldehyde," *Can Med Assoc J*, **75**(6), pp. 486–488.
- [164] Lawson, R. N., 1958, "A New Infrared Imaging Device," *Can Med Assoc J*, **79**(5), pp. 402–403.
- [165] Lawson, R. N., and Chughtai, M. S., 1963, "Breast Cancer and Body Temperature," *Can Med Assoc J*, **88**(2), pp. 68–70.
- [166] Williams, K. L., Williams, F. L., and Handley, R. S., 1960, "INFRA-RED RADIATION THERMOMETRY IN CLINICAL PRACTICE," *The Lancet*, **276**(7157), pp. 958–959.
- [167] Williams, K. L., Williams, F. J. L., and Handley, R. S., 1961, "INFRA-RED THERMOMETRY IN THE DIAGNOSIS OF BREAST DISEASE," *The Lancet*, **278**(7217), pp. 1378–1381.
- [168] Williams, K. L., 1964, "Infrared Thermometry as a Tool in Medical Research," *Annals of the New York Academy of Sciences*, **121**(1), pp. 99–112.
- [169] Williams, K. L., 1964, "Temperature Measurement in Breast Disease\*," *Annals of the New York Academy of Sciences*, **121**(1), pp. 272–281.
- [170] Gershon-cohen, J., Haberman-brueschke, J. A. D., and Brueschke, E. E., 1965, "MEDICAL THERMOGRAPHY: A SUMMARY OF CURRENT STATUS," *Radiologic Clinics of North America*, **3**(3), pp. 403–431.
- [171] Gershon-Cohen, J., 1967, "Medical Thermography," *J SMPTE*, **76**(11), pp. 1085–1088.
- [172] Dodd, G. D., Zermeno, A., Marsh, L., Boyd, D., and Wallace, J. D., 1969, "New Developments in Breast Thermography. High Spatial Resolution," *Cancer*, **24**(6), pp. 1212–1221.
- [173] Draper, J. W., and Boag, J. W., 1971, "The Calculation of Skin Temperature Distributions in Thermography," *Phys. Med. Biol.*, **16**(2), p. 201.
- [174] Isard, H. J., Ostium, B. J., Shilo, R., and Woolf, R. M., 1969, "Thermography in Breast Carcinoma," *Plastic and Reconstructive Surgery*, **44**(6), p. 614.
- [175] Jones, C. H., 1969, "Interpretation Problems in Thermography of the Female Breast," *Bibl Radiol*, **5**, pp. 96–108.
- [176] Davison, T. W., Ewing, K. L., Ferguson, J., Chapman, M., Can, A., and Voorhis, C. C., 1972, "Detection of Breast Cancer by Liquid Crystal Thermography. A Preliminary Report," *Cancer*, **29**(5), pp. 1123–1132.
- [177] Hitchcock, C. R., Hickok, D. F., Soucheray, J., Moulton, T., and Baker, R. C., 1968, "Thermography in Mass Screening for Occult Breast Cancer," *JAMA*, **204**(6), pp. 419–422.
- [178] Haberman, J. D., 1968, "The Present Status of Mammary Thermography," *CA: A Cancer Journal for Clinicians*, **18**(6), pp. 314–321.
- [179] Isard, H. J., Becker, W., Shilo, R., and Ostrum, B. J., 1972, "Breast Thermography after Four Years and 10,000 Studies," *American Journal of Roentgenology*, **115**(4), pp. 811–821.
- [180] BRASFIELD, R. D., SHERMAN, R. S., and LAUGHLIN, J. S., 1965, "THE ROLE OF THERMOGRAPHY IN THE DIAGNOSIS OF CANCER," *Prog Clin Cancer*, **10**, pp. 258–263.

- [181] Swearingen, A. G., 1965, "Thermography: Report of the Radiographic and Thermographic Examinations of the Breasts of 100 Patients," *Radiology*, **85**(5), pp. 818–824.
- [182] Notter, G., and Melander, O., 1966, "Thermographische Untersuchung bei Erkrankungen der Brustdrüse," *Rofo*, **105**(11), pp. 657–664.
- [183] Harris, D. L., Greening, W. P., and Aichroth, P. M., 1966, "Infra-Red in the Diagnosis of a Lump in the Breast.," *Br J Cancer*, **20**(4), pp. 710–721.
- [184] Gershon-Cohen, J., 1967, "Mammography, Thermography and Xerography," *CA: A Cancer Journal for Clinicians*, **17**(3), pp. 108–112.
- [185] Hoffman, R. L., 1967, "Thermography in the Detection of Breast Malignancy," *American Journal of Obstetrics and Gynecology*, **98**(5), pp. 681–686.
- [186] Wallace, J. D., and Dodd, G. D., 1968, "Thermography in the Diagnosis of Breast Cancer," *Radiology*, **91**(4), pp. 679–685.
- [187] Dodd, G. D., Wallace, J. D., Freundlich, I. M., Marsh, L., and Zermino, A., 1969, "Thermography and Cancer of the Breast," *Cancer*, **23**(4), pp. 797–802.
- [188] Lilienfeld, A. M., Barnes, J. M., Barnes, R. B., Brasfield, R., Connell, J. F., Diamond, E., Gershon-Cohen, J., Haberman, J., Isard, H. J., Lane, W. Z., Lattes, R., Miller, J., Seaman, W., and Sherman, R., 1969, "An Evaluation of Thermography in the Detection of Breast Cancer. A Cooperative Pilot Study," *Cancer*, **24**(6), pp. 1206–1211.
- [189] Draper, J. W., and Jones, C. H., 1969, "Thermal Patterns of the Female Breast," *BJR*, **42**(498), pp. 401–410.
- [190] Williams, K. L., 1969, "Thermography in the Prognosis of Breast Cancer," *Bibl Radiol*, **5**, pp. 62–67.
- [191] Jones, C. H., and Draper, J. W., 1970, "A Comparison of Infrared Photography and Thermography in the Detection of Mammary Carcinoma," *British Journal of Radiology*, **43**(512), pp. 507–516.
- [192] Nathan, B. E., Galasko, C. S. B., and Pallett, J. E., 1970, "Thermography in Breast Cancer," *British Journal of Surgery*, **57**(7), pp. 518–520.
- [193] FARRELL, C., WALLACE, J. D., and MANSFIELD, C. M., 1971, "The Use of Thermography in Detection of Metastatic Breast Cancer," *American Journal of Roentgenology*, **111**(1), pp. 148–152.
- [194] Nathan, B. E., Burn, J. I., and MacErlean, D. P., 1972, "Value Of Mammary Thermography In Differential Diagnosis," *The British Medical Journal*, **2**(5809), pp. 316–317.
- [195] Gautherie, M., 1968, "Indirect determination, by infrared thermometry, of thermal properties of human tissue in vivo," *C R Acad Hebd Seances Acad Sci D*, **267**(25), pp. 2203–2206.
- [196] Gros, C., and Gautherie, M., 1968, "Infrared thermometric study of the development in time of human skin temperature in relation to environmental temperature. Concept of cutaneous thermal adaptation," *Rev Fr Etud Clin Biol*, **13**(7), pp. 697–703.
- [197] Gautherie, M., 1969, "Study, by infra-red thermometry, of the thermal properties of human tissues in vivo. Influence of temperature and vascularisation," *Rev Fr Etud Clin Biol*, **14**(9), pp. 885–901.
- [198] Gros, C., Gautherie, M., Bourjat, P., and Vrousos, C., 1969, "Thermography of Breast Diseases," *Bibl Radiol*, **5**, pp. 68–81.
- [199] Gros, C., Gautherie, M., Bourjat, P., Warter, F., and Waille, Y., 1971, "Thermography of irradiated breast cancers," *Bull Cancer*, **58**(4), pp. 445–466.
- [200] Gros, C., Gautherie, M., Archer, F., Haehnel, P., and Colin, C., 1971, "Thermographic classification of breast neoplasms," *Bull Cancer*, **58**(3), pp. 351–361.

- [201] Gautherie, M., Bourjat, P., Gros, C., and Quenneville, Y., 1972, "HEAT PRODUCTION IN BREAST-CANCER. 1. MEASUREMENT BY INTRA-TUMOR THERMOGRAPHY AND CUTANEOUS INFRA-RED THERMOGRAPHY," *REVUE EUROPEENNE D ETUDES CLINIQUES ET BIOLOGIQUE*, **17**(8), pp. 776-+.
- [202] Gautherie, M., QUENNEVILLE, Y., JATTEAU, M., and OTT, J., 1972, "ACCURATE MEASUREMENTS OF SKIN TEMPERATURES BY INFRARED THERMOGRAPHY," *PATHOLOGIE BIOLOGIE*, **20**(11-1), pp. 559-+.
- [203] Gros, C., Gautherie, M., Bourjat, P., and Girardie, J., 1972, "NECESSITY OF COMPLEMENTARY INVESTIGATION METHODS FOR EARLY DIAGNOSIS OF BREAST CANCER," *NECESSITY OF COMPLEMENTARY INVESTIGATION METHODS FOR EARLY DIAGNOSIS OF BREAST CANCER*.
- [204] Gautherie, M., Gros, C., Bourjat, P., and Quenneville, Y., 1973, "Thermogenic capacity of breast carcinomas. II. Variation during hormonal tests," *Biomedicine*, **18**(5), pp. 421-428.
- [205] Gros, C., Gautherie, M., Bourjat, P., and Metzger, L., 1973, "Thermographic semiology of gynecomastia," *Ann Radiol (Paris)*, **16**(11), pp. 667-679.
- [206] Bourjat, P., Gautherie, M., and Grosshans, E., 1975, "Diagnosis, Follow-up and Prognosis of Malignant Melanomas by Thermography," *Bibl Radiol*, (6), pp. 115-127.
- [207] Gautherie, M., Armand, M. O., and Gros, C., 1975, "Heat production by breast neoplasms. IV. Influence of growth rate and probability of lymphatic dissemination during spontaneous development," *Biomedicine*, **22**(4), pp. 328-336.
- [208] Gautherie, M., Haehnel, P., and Gros, C., 1975, "Thermogenesis of breast cancers. V. The effects of <sup>60</sup>Co radiotherapy and the correlations with expectations of a cure," *Biomedicine*, **22**(5), pp. 416-427.
- [209] Gautherie, M., Qenneville, Y., and Gros, C. H., 1975, "Thermogenesis of mammary epitheliomas. III. Study, by means of fluvography, of the termal conductivity of mammary tissue and of the influence of tumor vascularization," *Biomedicine*, **22**(3), pp. 237-245.
- [210] Gautherie, M., Quenneville, Y., Rempp, C., and Gros, C., 1975, "Comparative informative value of telethermography (infrared) and contact thermography (liquid crystals) in the study of the breast," *J Radiol Electrol Med Nucl*, **56 suppl 1**, pp. 316-318.
- [211] Gros, C., Gautherie, M., and Bourjat, P., 1975, "Prognosis and Post-Therapeutic Follow-up of Breast Cancers by Thermography," *Bibl Radiol*, (6), pp. 77-90.
- [212] Gautherie, M., and Gros, C. H., 1976, "Contribution of Infrared Thermography to Early Diagnosis, Pretherapeutic Prognosis, and Post-Irradiation Follow-up of Breast Carcinomas," *Laboratory of Electroradiology, Faculty of Medicine, Louis Pasteur University, Strasbourg, France*.
- [213] Gautherie, M., Quenneville, Y., and Cross, C., 1976, *Metabolic Heat Production. Growth Rate and Prognosis of Early Carcinomas. Functional Explorations in Senology*, European Press, Ghenf, Belgien.
- [214] Gros, C., Gautherie, M., and Warter, F., 1976, "Thermographic prognosis of early breast epitheliomas," *J Radiol Electrol Med Nucl*, **57**(8-9), pp. 571-573.
- [215] Gautherie, M., and Gros, C. M., 1980, "Breast Thermography and Cancer Risk Prediction," *Cancer*, **45**(1), pp. 51-56.
- [216] Gautherie, M., Haehnel, P., Walter, J. P., and Keith, L., 1982, "Long-Term Assessment of Breast Cancer Risk by Liquid-Crystal Thermal Imaging," *Prog Clin Biol Res*, **107**, pp. 279-301.
- [217] Baker, L. H., 1982, "Breast Cancer Detection Demonstration Project: Five-Year Summary Report," *CA: a cancer journal for clinicians*, **32**(4), p. 194.

- [218] Moskowitz, M., Milbrath, J., Gartside, P., Zermeno, A., and Mandel, D., 1976, "Lack of Efficacy of Thermography as a Screening Tool for Minimal and Stage I Breast Cancer," *New England Journal of Medicine*, **295**(5), pp. 249-252,.
- [219] Moskowitz, M., 1985, "Thermography as a Risk Indicator of Breast Cancer. Results of a Study and a Review of the Recent Literature," *The Journal of reproductive medicine*, **30**(6), pp. 451-459,.
- [220] Lapayowker, M. S., Barash, I., Byrne, R., Chang, C. H. J., Dodd, G., Farrell, C., Haberman, J. D., Isard, H. J., and Threatt, B., 1976, "Criteria for Obtaining and Interpreting Breast Thermograms," *Cancer*, **38**(5), pp. 1931–1935.
- [221] Goldsmith, M. F., 1984, "In the Hot Seat: Thermography for Breast Cancer Diagnosis," *JAMA*, **251**(6), pp. 693–695.
- [222] Haberman, J. D., Goin, J. E., Love, T. J., Ohnsorg, F. R., and Berry, H., 1979, "Computer Techniques In Breast Cancer Detection by Absolute Temperature Thermography," *COMPSAC 79. Proceedings. Computer Software and The IEEE Computer Society's Third International Applications Conference, 1979.*, pp. 559–564.
- [223] Goin, J. E., and Haberman, J. D., 1983, "Automated Breast Cancer Detection by Thermography : Performance Goal and Diagnostic Feature Identification," *Pattern Recognition*, **16**(2), pp. 125–129.
- [224] Kennedy, D. A., Lee, T., and Seely, D., 2009, "A Comparative Review of Thermography as a Breast Cancer Screening Technique," *Integrative Cancer Therapies*, **8**(1), pp. 9–16.
- [225] Devices, C., and Health, R., 2019, "FDA Warns Thermography Should Not Be Used in Place of Mammography to Detect, Diagnose, or Screen for Breast Cancer: FDA Safety Communication," FDA.
- [226] Kozlowski, L. J., and Kosonocky, W. F., 2010, "Infrared Dector Arrays," *Handbook of Optics. Vol. 2: Design, Fabrication, and Testing; Sources and Detectors; Radiometry and Photometry*, M. Bass, and Optical Society of America, eds., McGraw-Hill, New York.
- [227] Williams, T. L., 2009, *Thermal Imaging Cameras: Characteristics and Performance*, CRC Press, Boca Raton.
- [228] Rogalski, A., and Chrzanowski, K., 2017, "Infrared Devices and Techniques," *Handbook of Optoelectronics*, CRC Press.
- [229] Rogalski, A., Kopytko, M., and Martyniuk, P., 2018, "Infrared Detector Characterization," *Antimonide-Based Infrared Detectors: A New Perspective*, SPIE.
- [230] Wang, L., Xu, Z., Xu, J., Dong, F., Wang, F., Bai, Z., Zhou, Y., Chai, X., Li, H., Ding, R., Chen, J., and He, L., 2020, "Fabrication and Characterization of InAs/GaSb Type-II Superlattice Long-Wavelength Infrared Detectors Aiming High Temperature Sensitivity," *Journal of Lightwave Technology*, **38**(21), pp. 6129–6134.
- [231] Francis, S. V., Sasikala, M., Bhavani Bharathi, G., and Jaipurkar, S. D., 2014, "Breast Cancer Detection in Rotational Thermography Images Using Texture Features," *Infrared Physics & Technology*, **67**, pp. 490–496.
- [232] Francis, S. V., Sasikala, M., and Jaipurkar, S. D., 2017, "Detection of Breast Abnormality Using Rotational Thermography," *Application of Infrared to Biomedical Sciences*, E.Y. Ng, and M. Etehadtavakol, eds., Springer, Singapore, pp. 133–158.
- [233] Sella, T., Sklair-Levy, M., Cohen, M., Rozin, M., Shapiro-Feinberg, M., Allweis, T. M., Libson, E., and Izhaky, D., 2013, "A Novel Functional Infrared Imaging System Coupled with Multiparametric Computerised Analysis for Risk Assessment of Breast Cancer," *European radiology*, **23**(5), pp. 1191-1198,.
- [234] "Http://Www.Notouchbreastscan.Com/Thermography.Html" [Online]. Available: <http://www.notouchbreastscan.com/thermography.html>. [Accessed: 31-Mar-2024].

- [235] VENKATARAMANI, K., JABBIREDDY, S., MADHU, H. J., and KAKILETI, S. T., 2018, "Contour-Based Determination of Malignant Tissue in a Thermal Image."
- [236] Hakim, A., and Awale, R. N., 2020, "Thermal Imaging - An Emerging Modality for Breast Cancer Detection: A Comprehensive Review," *J Med Syst*, **44**(8), p. 136.
- [237] Gautherie, M., Haehnel, P., Walter, J. P., and Keith, L. G., 1987, "Thermovascular Changes Associated with in Situ and Minimal Breast Cancers. Results of an Ongoing Prospective Study after Four Years," *J Reprod Med*, **32**(11), pp. 833–842.
- [238] Singh, D., and Singh, A. K., 2020, "Role of Image Thermography in Early Breast Cancer Detection- Past, Present and Future," *Computer Methods and Programs in Biomedicine*, **183**, p. 105074.
- [239] Abed, A. H., Shaaban, E. M., Jena, O. P., and Elngar, A. A., 2022, "A Comprehensive Survey on Breast Cancer Thermography Classification Using Deep Neural Network," *Machine Learning and Deep Learning in Medical Data Analytics and Healthcare Applications*, CRC Press.
- [240] Goodfellow, I., Bengio, Y., and Courville, A., 2016, *Deep Learning*, The MIT Press, Cambridge, Massachusetts.
- [241] Gonçalves, C. B., Leles, A. C. Q., Oliveira, L. E., Guimaraes, G., Cunha, J. R., and Fernandes, H., 2019, "Machine Learning and Infrared Thermography for Breast Cancer Detection," *Proceedings*, **27**(1), p. 45.
- [242] Zavvar, T., Ridhawi, I. A., and Abbas, A., 2023, "Thermography-Based Early-Stage Breast Cancer Detection Using SVM," *2023 Fourth International Conference on Intelligent Data Science Technologies and Applications (IDSTA)*, pp. 27–34.
- [243] Yousefi, B., Maldague, X. P. V., and Hassanipour, F., 2023, "Diagnostic Biomarker for Breast Cancer Applying Rayleigh Low-Rank Embedding Thermography," *Engineering Proceedings*, **51**(1), p. 38.
- [244] Tsietsos, D., Yahya, A., Samikannu, R., Tariq, M. U., Babar, M., Qureshi, B., and Koubaa, A., 2023, "Multi-Input Deep Learning Approach for Breast Cancer Screening Using Thermal Infrared Imaging and Clinical Data," *IEEE Access*, **11**, pp. 52101–52116.
- [245] Trongtirakul, T., Agaian, S., and Oulefki, A., 2023, "Automated Tumor Segmentation in Thermographic Breast Images," *Mathematical Biosciences and Engineering*, **20**(9), pp. 16786–16806.
- [246] Queiroz, K. F. F. da C., and Lima, R. de C. F. de, 2023, "Smart Screening System for Breast Cancer: The Use of Thermographic Images, Evolutionary Algorithms, and Oversampling," *Biomed. Phys. Eng. Express*, **9**(5), p. 055027.
- [247] Ortiz, A. R., Secco, L. G., Zangaro, R. A., and Alves, L. P., 2023, "Thermography Applied to Breast Cancer Diagnosis: Proposal for a New Methodological Approach," *Res. Biomed. Eng.*, **39**(1), pp. 297–310.
- [248] Nogales, A., Pérez-Lara, F., Morales, J., and García-Tejedor, Á. J., 2023, "How Do Thermography Colors Influence Breast Cancer Diagnosis? A Hybrid Model of Convolutional Networks with a Weighted Average Evolutionary Algorithm," *Intelligent Systems and Applications*, K. Arai, ed., Springer International Publishing, Cham, pp. 271–281.
- [249] Mishra, V., Rath, S., and Rath, S. K., 2023, "Feature Analysis for Detection of Breast Cancer Thermograms Using Dimensionality Reduction Techniques," *Proceedings of the International Health Informatics Conference*, S. Jain, S. Groppe, and N. Mihindukulasooriya, eds., Springer Nature, Singapore, pp. 311–321.
- [250] Kakileti, S. T., Shrivastava, R., and Manjunath, G., 2023, "Robust Data-Driven Region of Interest Segmentation for Breast Thermography," *Handbook of Dynamic Data Driven*

- Applications Systems: Volume 2*, F. Darema, E.P. Blasch, S. Ravela, and A.J. Aved, eds., Springer International Publishing, Cham, pp. 683–703.
- [251] Husaini, M. A. S. A., Habaebi, M. H., and Islam, M. R., 2023, "Utilizing Deep Learning for the Real-Time Detection of Breast Cancer through Thermography," *2023 9th International Conference on Computer and Communication Engineering (ICCCCE)*, pp. 270–273.
- [252] Hakim, A., and Awale, R. n., 2023, "Harnessing the Power of Machine Learning for Breast Anomaly Prediction Using Thermograms," *International Journal of Medical Engineering and Informatics*, **15**(1), pp. 1–22.
- [253] Hakim, A., and Awale, R. N., 2023, "Designing a Three-Layer Back Propagation Artificial Neural Network for Breast Thermogram Classification," *IETE Journal of Research*, **69**(7), pp. 4053–4065.
- [254] Gupta, K. K., Ritu Vijay, Pahadiya, P., Saxena, S., and Gupta, M., 2023, "Novel Feature Selection Using Machine Learning Algorithm for Breast Cancer Screening of Thermography Images," *Wireless Pers Commun*, **131**(3), pp. 1929–1956.
- [255] Gomathi, P., Muniraj, C., and Periasamy, P. S., 2023, "Digital Infrared Thermal Imaging System Based Breast Cancer Diagnosis Using 4D U-Net Segmentation," *Biomedical Signal Processing and Control*, **85**, p. 104792.
- [256] Gamal, S., Atef, H., Youssef, D., Ismail, T., and El-Azab, J., 2023, "Early Breast Cancer Screening from Thermography via Deep Pre-Trained Edge Detection with Extreme Gradient Boosting," *2023 Intelligent Methods, Systems, and Applications (IMSA)*, pp. 430–433.
- [257] Gade, A., Dash, D. K., Kumari, T. M., Ghosh, S. K., Tripathy, R. K., and Pachori, R. B., 2023, "Multiscale Analysis Domain Interpretable Deep Neural Network for Detection of Breast Cancer Using Thermogram Images," *IEEE Transactions on Instrumentation and Measurement*, **72**, pp. 1–13.
- [258] de Freitas Barbosa, V. A., Félix da Silva, A., de Santana, M. A., Rabelo de Azevedo, R., Fernandes de Lima, R. de C., and dos Santos, W. P., 2023, "Deep-Wavelets and Convolutional Neural Networks to Support Breast Cancer Diagnosis on Thermography Images," *Computer Methods in Biomechanics and Biomedical Engineering: Imaging & Visualization*, **11**(3), pp. 895–913.
- [259] da Queiroz, K. F. F. C., de Queiroz Júnior, J. R. A., Dourado, H., and de Lima, R. de C. F., 2023, "Automatic Segmentation of Region of Interest for Breast Thermographic Image Classification," *Res. Biomed. Eng.*, **39**(1), pp. 199–208.
- [260] Chebbah, N. K., Ouslim, M., and Benabid, S., 2023, "New Computer Aided Diagnostic System Using Deep Neural Network and SVM to Detect Breast Cancer in Thermography," *Quantitative InfraRed Thermography Journal*, **20**(2), pp. 62–77.
- [261] Brasileiro, F. R. S., Sampaio Neto, D. D., Silva Filho, T. M., Souza, R. M. C. R. de, and Araújo, M. C. de, 2023, "Classifying Breast Lesions in Brazilian Thermographic Images Using Convolutional Neural Networks," *Neural Comput & Applic*, **35**(26), pp. 18989–18997.
- [262] Araujo, A. S., Milena H.S., I., Sánchez, Á., Muchaluat-Saade, D. C., and Conci, A., 2023, "Utilizing Infrared Thermography for Assessing Breast Cancer Treatment Progression," *2023 30th International Conference on Systems, Signals and Image Processing (IWSSIP)*, pp. 1–5.
- [263] Alshehri, A., and AlSaeed, D., 2023, "Breast Cancer Diagnosis in Thermography Using Pre-Trained VGG16 with Deep Attention Mechanisms," *Symmetry*, **15**(3), p. 582.

- [264] Aidossov, N., Zarikas, V., Zhao, Y., Mashekova, A., Ng, E. Y. K., Mukhmetov, O., Mirasbekov, Y., and Omirbayev, A., 2023, "An Integrated Intelligent System for Breast Cancer Detection at Early Stages Using IR Images and Machine Learning Methods with Explainability," *SN COMPUT. SCI.*, **4**(2), p. 184.
- [265] Aidossov, N., Zarikas, V., Mashekova, A., Zhao, Y., Ng, E. Y. K., Midlenko, A., and Mukhmetov, O., 2023, "Evaluation of Integrated CNN, Transfer Learning, and BN with Thermography for Breast Cancer Detection," *Applied Sciences*, **13**(1), p. 600.
- [266] Yadav, S. S., and Jadhav, S. M., 2022, "Thermal Infrared Imaging Based Breast Cancer Diagnosis Using Machine Learning Techniques," *Multimed Tools Appl*, **81**(10), pp. 13139–13157.
- [267] Vigil, N., Nouri, B. M., Fernandes, H. C., Ibarra-Castanedo, C., Maldague, X. P. V., and Yousefi, B., 2022, "Convex Factorization Embedding Thermography for Breast Cancer Diagnostic," *IEEE Open Journal of Instrumentation and Measurement*, **1**, pp. 1–8.
- [268] Torres-Galván, J. C., Guevara, E., Kolosovas-Machuca, E. S., Ocegüera-Villanueva, A., Flores, J. L., and González, F. J., 2022, "Deep Convolutional Neural Networks for Classifying Breast Cancer Using Infrared Thermography," *Quantitative InfraRed Thermography Journal*, **19**(4), pp. 283–294.
- [269] Singh, D., Singh, A. K., and Tiwari, S., 2022, "Early Thermographic Screening of Breast Abnormality in Women with Dense Breast by Thermal, Fractal, and Statistical Analysis," *Artificial Intelligence over Infrared Images for Medical Applications and Medical Image Assisted Biomarker Discovery*, S.T. Kakileti, M. Gabrani, G. Manjunath, M. Rosen-Zvi, N. Braman, R.G. Schwartz, A.F. Frangi, P.-C. Chung, C. Weight, and V. Jagadish, eds., Springer Nature Switzerland, Cham, pp. 20–33.
- [270] Sharma, R., Ballabh Sharma, J., Maheshwari, R., and Agarwal, P., 2022, "Thermogram Adaptive Efficient Model for Breast Cancer Detection Using Fractional Derivative Mask and Hybrid Feature Set in the IoT Environment," *Computer Modeling in Engineering & Sciences*, **130**(2), pp. 923–947.
- [271] Mohamed, E. A., Rashed, E. A., Gaber, T., and Karam, O., 2022, "Deep Learning Model for Fully Automated Breast Cancer Detection System from Thermograms," *PLOS ONE*, **17**(1), p. e0262349.
- [272] Mohamed, E. A., Gaber, T., Karam, O., and Rashed, E. A., 2022, "A Novel CNN Pooling Layer for Breast Cancer Segmentation and Classification from Thermograms," *PLOS ONE*, **17**(10), p. e0276523.
- [273] Mammoottil, M. J., Kulangara, L. J., Cherian, A. S., Mohandas, P., Hasikin, K., and Mahmud, M., 2022, "Detection of Breast Cancer from Five-View Thermal Images Using Convolutional Neural Networks," *Journal of Healthcare Engineering*, **2022**, p. e4295221.
- [274] M. Alqhtani, S., 2022, "BreastCNN: A Novel Layer-Based Convolutional Neural Network for Breast Cancer Diagnosis in DMR-Thermogram Images," *Applied Artificial Intelligence*, **36**(1), p. 2067631.
- [275] Kakileti, S. T., Shrivastava, R., Manjunath, G., Vidyasagar, M., and Graewingholt, A., 2022, "Automated Vascular Analysis of Breast Thermograms with Interpretable Features," *JMI*, **9**(4), p. 044502.
- [276] Gupta, K. K., Vijay, R., Pahadiya, P., and Saxena, S., 2022, "Use of Novel Thermography Features of Extraction and Different Artificial Neural Network Algorithms in Breast Cancer Screening," *Wireless Pers Commun*, **123**(1), pp. 495–524.
- [277] Gupta, K. K., Vijay, R., and Pahadiya, P., 2022, "Detection of Abnormality in Breast Thermograms Using Canny Edge Detection Algorithm for Thermography Images," *International Journal of Medical Engineering and Informatics*, **14**(1), pp. 31–42.

- [278] Gupta, K. K., Rituvijay, Pahadiya, P., and Saxena, S., 2022, "Detection of Cancer in Breast Thermograms Using Mathematical Threshold Based Segmentation and Morphology Technique," *Int J Syst Assur Eng Manag*, **13**(1), pp. 421–428.
- [279] Gonçalves, C. B., Souza, J. R., and Fernandes, H., 2022, "CNN Architecture Optimization Using Bio-Inspired Algorithms for Breast Cancer Detection in Infrared Images," *Computers in Biology and Medicine*, **142**, p. 105205.
- [280] Garyali, P., Ranjbar, I., and Movahedi, S., 2022, "A Novel Thermography-Based Artificial Intelligence-Powered Solution for Screening Breast Cancer," *Artificial Intelligence over Infrared Images for Medical Applications and Medical Image Assisted Biomarker Discovery*, S.T. Kakileti, M. Gabrani, G. Manjunath, M. Rosen-Zvi, N. Braman, R.G. Schwartz, A.F. Frangi, P.-C. Chung, C. Weight, and V. Jagadish, eds., Springer Nature Switzerland, Cham, pp. 34–44.
- [281] Elouerghi, A., Bellarbi, L., Khomsi, Z., Jbari, A., Errachid, A., and Yaakoubi, N., 2022, "A Flexible Wearable Thermography System Based on Bioheat Microsensors Network for Early Breast Cancer Detection: IoT Technology," *Journal of Electrical and Computer Engineering*, **2022**, p. e5921691.
- [282] Dey, S., Roychoudhury, R., Malakar, S., and Sarkar, R., 2022, "Screening of Breast Cancer from Thermogram Images by Edge Detection Aided Deep Transfer Learning Model," *Multimed Tools Appl*, **81**(7), pp. 9331–9349.
- [283] de Santana, M. A., de Freitas Barbosa, V. A., de Cássia Fernandes de Lima, R., and dos Santos, W. P., 2022, "Combining Deep-Wavelet Neural Networks and Support-Vector Machines to Classify Breast Lesions in Thermography Images," *Health Technol.*, **12**(6), pp. 1183–1195.
- [284] Chatterjee, S., Biswas, S., Majee, A., Sen, S., Oliva, D., and Sarkar, R., 2022, "Breast Cancer Detection from Thermal Images Using a Grunwald-Letnikov-Aided Dragonfly Algorithm-Based Deep Feature Selection Method," *Computers in Biology and Medicine*, **141**, p. 105027.
- [285] Araujo, A. S., Issa, M. H. S., Sánchez, Á., Muchaluat-Saade, D. C., and Conci, A., 2022, "Using Thermography for Breast Cancer Neoadjuvant Treatment," *2022 29th International Conference on Systems, Signals and Image Processing (IWSSIP)*, pp. 1–4.
- [286] Alsaedi, D., Melnikov, A., Muzaffar, K., Mandelis, A., and Ramahi, O. M., 2022, "A Microwave-Thermography Hybrid Technique for Breast Cancer Detection," *IEEE Journal of Electromagnetics, RF and Microwaves in Medicine and Biology*, **6**(1), pp. 153–163.
- [287] Allugunti, V. R., 2022, "Breast Cancer Detection Based on Thermographic Images Using Machine Learning and Deep Learning Algorithms," *Int. J. Eng. Comput. Sci.*, **4**(1), pp. 49–56.
- [288] Al Husaini, M. A. S., Habaebi, M. H., Gunawan, T. S., Islam, M. R., Elsheikh, E. A. A., and Suliman, F. M., 2022, "Thermal-Based Early Breast Cancer Detection Using Inception V3, Inception V4 and Modified Inception MV4," *Neural Comput & Applic*, **34**(1), pp. 333–348.
- [289] Zou, Y., Zhang, L., Liu, C., Wang, B., Hu, Y., and Chen, Q., 2021, "Super-Resolution Reconstruction of Infrared Images Based on a Convolutional Neural Network with Skip Connections," *Optics and Lasers in Engineering*, **146**, p. 106717.
- [290] Tiwari, D., Dixit, M., and Gupta, K., 2021, "Deep Multi-View Breast Cancer Detection: A Multi-View Concatenated Infrared Thermal Images Based Breast Cancer Detection System Using Deep Transfer Learning," *TS*, **38**(6), pp. 1699–1711.
- [291] Sánchez-Cauce, R., Pérez-Martín, J., and Luque, M., 2021, "Multi-Input Convolutional Neural Network for Breast Cancer Detection Using Thermal Images and Clinical Data," *Computer Methods and Programs in Biomedicine*, **204**, p. 106045.

- [292] Roslidar, R., Syaryadhi, M., Saddami, K., Pradhan, B., Arnia, F., Syukri, M., Munadi, K., Doctoral Program, School of Engineering, Universitas Syiah Kuala, Banda Aceh, Indonesia, Department of Electrical and Computer Engineering, Universitas Syiah Kuala, Indonesia, Telematics Research Center, Universitas Syiah Kuala, Banda Aceh, Indonesia, Centre for Advanced Modelling and Geospatial Information Systems (CAMGIS), Faculty of Engineering and IT, University of Technology Sydney, Ultimo, Australia, Center of Excellence for Climate Change Research, King Abdulaziz University, Jeddah, Saudi Arabia, Earth Observation Center, Institute of Climate Change, Universiti Kebangsaan Malaysia, Bangi, Malaysia, Medical Faculty, Universitas Syiah Kuala, Banda Aceh, Indonesia, and Tsunami and Disaster Mitigation Research Center, Universitas Syiah Kuala, Banda Aceh, Indonesia, 2021, "BreaCNet: A High-Accuracy Breast Thermogram Classifier Based on Mobile Convolutional Neural Network," *MBE*, **19**(2), pp. 1304–1331.
- [293] Resmini, R., Silva, L., Araujo, A. S., Medeiros, P., Muchaluat-Saade, D., and Conci, A., 2021, "Combining Genetic Algorithms and SVM for Breast Cancer Diagnosis Using Infrared Thermography," *Sensors*, **21**(14), p. 4802.
- [294] Resmini, R., Faria da Silva, L., Medeiros, P. R. T., Araujo, A. S., Muchaluat-Saade, D. C., and Conci, A., 2021, "A Hybrid Methodology for Breast Screening and Cancer Diagnosis Using Thermography," *Computers in Biology and Medicine*, **135**, p. 104553.
- [295] Pereira, J. M. S., Santana, M. A., Gomes, J. C., de Freitas Barbosa, V. A., Valença, M. J. S., de Lima, S. M. L., and dos Santos, W. P., 2021, "Feature Selection Based on Dialectics to Support Breast Cancer Diagnosis Using Thermographic Images," *Res. Biomed. Eng.*, **37**(3), pp. 485–506.
- [296] Lahane, S. R., Chavan, P. N., and Madankar, P. M., 2021, "Classification of Thermographic Images for Breast Cancer Detection Based on Deep Learning," *Annals of the Romanian Society for Cell Biology*, **25**(6), pp. 3459–3466.
- [297] Houssein, E. H., Emam, M. M., and Ali, A. A., 2021, "An Efficient Multilevel Thresholding Segmentation Method for Thermography Breast Cancer Imaging Based on Improved Chimp Optimization Algorithm," *Expert Systems with Applications*, **185**, p. 115651.
- [298] Arul Edwin Raj, A. M., Sundaram, M., and Jaya, T., 2021, "Thermography Based Breast Cancer Detection Using Self-Adaptive Gray Level Histogram Equalization Color Enhancement Method," *International Journal of Imaging Systems and Technology*, **31**(2), pp. 854–873.
- [299] Tayel, M. B., and Elbagoury, A. M., 2020, "Automatic Breast Thermography Segmentation Based on Fully Convolutional Neural Networks," *International Journal of Research and Review*, **7**(10), p. 10.
- [300] Tayel, M. B., and Elbagoury, A. M., 2020, "An Efficient and Reliable Method for Regional Analysis of Breast Thermographic Images," *GSJ*, **8**(9).
- [301] Silva, T. A. E. da, Silva, L. F. da, Muchaluat-Saade, D. C., and Conci, A., 2020, "A Computational Method to Assist the Diagnosis of Breast Disease Using Dynamic Thermography," *Sensors*, **20**(14), p. 3866.
- [302] Pereira, J. M. S., Santana, M. A., Lima, R. C. F., Lima, S. M. L., and Santos, W. P., 2020, "Method for Classification of Breast Lesions in Thermographic Images Using Elm Classifiers," *Understanding a cancer diagnosis*, **1**, pp. 117–132.
- [303] Pereira, J. M. S., Santana, M. A., Lima, R. C. F., and Santos, W. P., 2020, "Lesion Detection in Breast Thermography Using Machine Learning Algorithms without Previous Segmentation," *Understanding a cancer diagnosis*, **1**, pp. 81–94.
- [304] Mahmoud, A., 2020, "Automatic Breast Thermography Images Classification Based on Deep Neural Networks," *Annals of Optimization Theory and Practice*, **3**(2), pp. 71–79.

- [305] Lennox, N., and Haskins, B., 2020, "Contrasting Classifiers for the Detection of Breast Cancer Using Thermographic Images," *Proceedings of the 2nd International Conference on Intelligent and Innovative Computing Applications*, Association for Computing Machinery, New York, NY, USA, pp. 1–9.
- [306] Hamidpour, S. S. F., Firouzmand, M., Navid, M., Eghbal, M., and Alikhassi, A., 2020, "Extraction of Vessel Structure in Thermal Images to Help Early Breast Cancer Detection," *Computer Methods in Biomechanics and Biomedical Engineering: Imaging & Visualization*, **8**(1), pp. 103–108.
- [307] Flores, J. L., Gonzalez, F. J., Cruz, A., Navarro, N. E., and Ocegüera, A., 2020, "Automatic Analysis of Breast Thermograms by Convolutional Neural Networks," *Applications of Digital Image Processing XLIII*, SPIE, pp. 396–403.
- [308] Farooq, M. A., and Corcoran, P., 2020, "Infrared Imaging for Human Thermography and Breast Tumor Classification Using Thermal Images," *2020 31st Irish Signals and Systems Conference (ISSC)*, IEEE, Letterkenny, Ireland, pp. 1–6.
- [309] Cruz-Alejo, J. de la, Guillermo, I. C. A., Vázquez, M. B. A., and Contreras, E. E., 2020, "Detection of Breast Cancer in Infrared Thermographies Using Stochastic Techniques in a FPGA Platform," *Journal of Bioinformatics and Systems Biology*, **3**(3), pp. 45–57.
- [310] Cabioğlu, Ç., and Oğul, H., 2020, "Computer-Aided Breast Cancer Diagnosis from Thermal Images Using Transfer Learning," *Bioinformatics and Biomedical Engineering*, I. Rojas, O. Valenzuela, F. Rojas, L.J. Herrera, and F. Ortuño, eds., Springer International Publishing, Cham, pp. 716–726.
- [311] AlFayez, F., El-Soud, M. W. A., and Gaber, T., 2020, "Thermogram Breast Cancer Detection: A Comparative Study of Two Machine Learning Techniques," *Applied Sciences*, **10**(2), p. 551.
- [312] Usha, N., Sriraam, N., Kavya, N., Sharath, D., Prabha, R., Hiremath, B., Venkataraman, B., and Menaka, M., 2019, "Feature Selection and Classification for Analysis of Breast Thermograms," *2019 2nd International Conference on Signal Processing and Communication (ICSPC)*, pp. 276–280.
- [313] Sathish, D., Kamath, S., Prasad, K., and Kadavigere, R., 2019, "Role of Normalization of Breast Thermogram Images and Automatic Classification of Breast Cancer," *Vis Comput*, **35**(1), pp. 57–70.
- [314] Rodrigues, A. L., de Santana, M. A., Azevedo, W. W., Bezerra, R. S., Barbosa, V. A. F., de Lima, R. C. F., and dos Santos, W. P., 2019, "Identification of Mammary Lesions in Thermographic Images: Feature Selection Study Using Genetic Algorithms and Particle Swarm Optimization," *Res. Biomed. Eng.*, **35**(3), pp. 213–222.
- [315] Ramya Devi, R., and Anandhamala, G. S., 2019, "Analysis of Breast Thermograms Using Asymmetry in Infra-Mammary Curves," *J Med Syst*, **43**(6), p. 146.
- [316] Mambou, S., Krejcar, O., Maresova, P., Selamat, A., and Kuca, K., 2019, "Novel Four Stages Classification of Breast Cancer Using Infrared Thermal Imaging and a Deep Learning Model," *Bioinformatics and Biomedical Engineering*, I. Rojas, O. Valenzuela, F. Rojas, and F. Ortuño, eds., Springer International Publishing, Cham, pp. 63–74.
- [317] Lennox, N., and Haskins, B., 2019, "Comparison of Segmentation Methods for the Detection of Breast Cancer Using Thermal Images," *2019 International Multidisciplinary Information Technology and Engineering Conference (IMITEC)*, pp. 1–8.
- [318] Kiyet, S., Aslankaya, M. Y., Taskiran, M., and Bolat, B., 2019, "Breast Cancer Detection From Thermography Based on Deep Neural Networks," *2019 Innovations in Intelligent Systems and Applications Conference (ASYU)*, pp. 1–5.

- [319] Khan, A. A., and Shatru Arora, A., 2019, "Classification in Thermograms for Breast Cancer Detection Using Texture Features with Feature Selection Method and Ensemble Classifier," *2019 International Conference on Issues and Challenges in Intelligent Computing Techniques (ICICT)*, pp. 1–6.
- [320] Gogoi, U. R., Majumdar, G., Bhowmik, M. K., and Ghosh, A. K., 2019, "Evaluating the Efficiency of Infrared Breast Thermography for Early Breast Cancer Risk Prediction in Asymptomatic Population," *Infrared Physics & Technology*, **99**, pp. 201–211.
- [321] Fernández-Ovies, F. J., Santiago Alférez-Baquero, E., de Andrés-Galiana, E. J., Cernea, A., Fernández-Muñiz, Z., and Fernández-Martínez, J. L., 2019, "Detection of Breast Cancer Using Infrared Thermography and Deep Neural Networks," *Bioinformatics and Biomedical Engineering*, I. Rojas, O. Valenzuela, F. Rojas, and F. Ortuño, eds., Springer International Publishing, Cham, pp. 514–523.
- [322] Ahmed, A., Ali, M., and Selim, M., 2019, "Bio-Inspired Based Techniques for Thermogram Breast Cancer Classification," *International Journal of Intelligent Engineering and Systems*, **12**(2), pp. 114–124.
- [323] Silva, L. F., Saade, D. C. M., Sequeiros, G. O., Silva, A. C., Paiva, A. C., Bravo, R. S., and Conci, A., 2014, "A New Database for Breast Research with Infrared Image," *j med imaging hlth inform*, **4**(1), pp. 92–100.
- [324] Bhowmik, M. K., Gogoi, U. R., Majumdar, G., Bhattacharjee, D., Datta, D., and Ghosh, A. K., 2018, "Designing of Ground-Truth-Annotated DBT-TU-JU Breast Thermogram Database Toward Early Abnormality Prediction," *IEEE J. Biomed. Health Inform.*, **22**(4), pp. 1238–1249.
- [325] Hossam, A., Harb, H. M., and Abd El Kader, H. M., 2018, "AUTOMATIC IMAGE SEGMENTATION METHOD FOR BREAST CANCER ANALYSIS USING THERMOGRAPHY," *JES. Journal of Engineering Sciences*, **46**(No 1), pp. 12–32.
- [326] de Freitas Oliveira Baffa, M., and Grassano Lattari, L., 2018, "Convolutional Neural Networks for Static and Dynamic Breast Infrared Imaging Classification," *2018 31st SIBGRAPI Conference on Graphics, Patterns and Images (SIBGRAPI)*, pp. 174–181.
- [327] He, K., Zhang, X., Ren, S., and Sun, J., 2016, "Deep Residual Learning for Image Recognition," pp. 770–778.
- [328] Simonyan, K., and Zisserman, A., 2015, "Very Deep Convolutional Networks for Large-Scale Image Recognition."
- [329] Szegedy, C., Vanhoucke, V., Ioffe, S., Shlens, J., and Wojna, Z., 2016, "Rethinking the Inception Architecture for Computer Vision," pp. 2818–2826.
- [330] Pennes, H. H., 1948, "Analysis of Tissue and Arterial Blood Temperatures in the Resting Human Forearm," *Journal of applied physiology*, **1**(2), pp. 93-122,.
- [331] Bhowmik, A., Singh, R., Repaka, R., and Mishra, S. C., 2013, "Conventional and Newly Developed Bioheat Transport Models in Vascularized Tissues: A Review," *Journal of Thermal Biology*, **38**(3), pp. 107–125.
- [332] Haemmerich, D., 2022, "1 - Mathematical Modeling of Heat Transfer in Biological Tissues (Bioheat Transfer)," *Principles and Technologies for Electromagnetic Energy Based Therapies*, P. Prakash, and G. Srimathveeravalli, eds., Academic Press, pp. 1–24.
- [333] Silva, M., Freitas, B., Andrade, R., Espregueira-Mendes, J., Silva, F., Carvalho, Ó., and Flores, P., 2020, "Computational Modelling of the Bioheat Transfer Process in Human Skin Subjected to Direct Heating and/or Cooling Sources: A Systematic Review," *Ann Biomed Eng*, **48**(6), pp. 1616–1639.
- [334] Shrivastava, D., 2018, *Theory and Applications of Heat Transfer in Humans*, John Wiley & Sons, Incorporated, Newark, UNITED KINGDOM.

- [335] Bazett, H. C., Love, L., Newton, M., Eisenberg, L., Day, R., and Forster, R., 1948, "Temperature Changes in Blood Flowing in Arteries and Veins in Man," *Journal of Applied Physiology*, **1**(1), pp. 3-19,.
- [336] Bazett, H. C., Mendelson, E. S., Love, L., and Libet, B., 1948, "Precooling of Blood in the Arteries, Effective Heat Capacity and Evaporative Cooling as Factors Modifying Cooling of the Extremities," *Journal of Applied Physiology*, **1**(2), pp. 169-182,.
- [337] Wissler, E. H., 1961, "Steady-State Temperature Distribution in Man," *Journal of Applied Physiology*, **16**(4), pp. 734-740.
- [338] Ponder, E., 1962, "The Coefficient of Thermal Conductivity of Blood and of Various Tissues," *J Gen Physiol*, **45**(3), pp. 545-551.
- [339] Dodd, G. D., and Wallace, J. D., 1968, "The Venous Diameter Ratio in the Radiographic Diagnosis of Breast Cancer," *Radiology*, **90**(5), pp. 900-904.
- [340] Birch, J., Brånemark, P.-I., and Nilsson, K., 1969, "The Vascularization of a Free Full Thickness Skin Graft:III. An Infrared Thermographic Study," *Scandinavian Journal of Plastic and Reconstructive Surgery*, **3**(1), pp. 18-22.
- [341] Priebe, L., and Betz, E., 1969, "Heat transport in homogeneously and isotropically perfused tissue," *Arztl Forsch*, **23**(1), pp. 18-30.
- [342] Wulff, W., 1974, "The Energy Conservation Equation for Living Tissue," *IEEE Transactions on Biomedical Engineering*, **BME-21**(6), pp. 494-495.
- [343] Chen, M. M., and Holmes, K. R., 1980, "Microvascular Contributions in Tissue Heat Transfer," *Annals of the New York Academy of Sciences*, **335**(1), pp. 137-150.
- [344] Xuan, Y., and Roetzel, W., 1997, "Bioheat Equation of the Human Thermal System," *Chemical Engineering & Technology*, **20**(4), pp. 268-276.
- [345] Weinbaum, S., Jiji, L. M., and Lemons, D. E., 1984, "Theory and Experiment for the Effect of Vascular Microstructure on Surface Tissue Heat Transfer—Part I: Anatomical Foundation and Model Conceptualization," *Journal of Biomechanical Engineering*, **106**(4), pp. 321-330.
- [346] Weinbaum, S., Jiji, L. M., and Lemons, D. E., 1984, "Theory and Experiment for the Effect of Vascular Temperature on Surface Tissue Heat Transfer—Part 2: Model Formulation and Solution," *ASME J. Biomech. Eng*, **106**(4), pp. 331-341.
- [347] Nakayama, A., and Kuwahara, F., 2008, "A General Bioheat Transfer Model Based on the Theory of Porous Media," *International Journal of Heat and Mass Transfer*, **51**(11), pp. 3190-3199.
- [348] Mahjoob, S., and Vafai, K., 2009, "Analysis of Bioheat Transport Through a Dual Layer Biological Media," *Journal of Heat Transfer*, **132**(031101).
- [349] Wang, L., and Fan, J., 2010, "Modeling Bioheat Transport at Macroscale," *Journal of Heat Transfer*, **133**(011010).
- [350] Wang, Y.-P., Cheng, R.-H., He, Y., and Mu, L.-Z., 2022, "Thermal Analysis of Blood Flow Alterations in Human Hand and Foot Based on Vascular-Porous Media Model," *Front. Bioeng. Biotechnol.*, **9**.
- [351] He, Z.-Z., and Liu, J., 2017, "A Coupled Continuum-Discrete Bioheat Transfer Model for Vascularized Tissue," *International Journal of Heat and Mass Transfer*, **107**, pp. 544-556,.
- [352] He, Z.-Z., and Liu, J., 2016, "An Efficient Parallel Numerical Modeling of Bioheat Transfer in Realistic Tissue Structure," *International Journal of Heat and Mass Transfer*, **95**, pp. 843-852,.
- [353] Tang, Y., Mu, L., and He, Y., 2020, "Numerical Simulation of Fluid and Heat Transfer in a Biological Tissue Using an Immersed Boundary Method Mimicking the Exact Structure of the Microvascular Network," *Fluid Dynamics & Materials Processing*, **16**(2), pp. 281-296.

- [354] Rubenstein, D. A., Frame, M. D., and Yin, W., 2012, *Biofluid Mechanics: An Introduction to Fluid Mechanics, Macrocirculation, and Microcirculation*, Elsevier Academic Press, Amsterdam ; Boston.
- [355] Weinbaum, S., and Jiji, L. M., 1985, "A New Simplified Bioheat Equation for the Effect of Blood Flow on Local Average Tissue Temperature," *Journal of Biomechanical Engineering*, **107**(2), pp. 131–139.
- [356] Ambreen, T., and Kim, M.-H., 2020, "Influence of Particle Size on the Effective Thermal Conductivity of Nanofluids: A Critical Review," *Applied Energy*, **264**, p. 114684.
- [357] Xie, H., Fujii, M., and Zhang, X., 2005, "Effect of Interfacial Nanolayer on the Effective Thermal Conductivity of Nanoparticle-Fluid Mixture," *International Journal of Heat and Mass Transfer*, **48**(14), pp. 2926–2932.
- [358] Wang, M., Wang, J., Pan, N., Chen, S., and He, J., 2006, "Three-Dimensional Effect on the Effective Thermal Conductivity of Porous Media," *J. Phys. D: Appl. Phys.*, **40**(1), p. 260.
- [359] Rojas-Altamirano, G., Vargas, R. O., Escandón, J. P., Mil-Martínez, R., and Rojas-Montero, A., 2022, "Calculation of Effective Thermal Conductivity for Human Skin Using the Fractal Monte Carlo Method," *Micromachines*, **13**(3), p. 424.
- [360] Shen, H., Ye, Q., and Meng, G., 2017, "Anisotropic Fractal Model for the Effective Thermal Conductivity of Random Metal Fiber Porous Media with High Porosity," *Physics Letters A*, **381**(37), pp. 3193–3196.
- [361] Samantray, P. K., Karthikeyan, P., and Reddy, K. S., 2006, "Estimating Effective Thermal Conductivity of Two-Phase Materials," *International Journal of Heat and Mass Transfer*, **49**(21), pp. 4209–4219.
- [362] Benveniste, Y., 1986, "On the Effective Thermal Conductivity of Multiphase Composites," *Z. angew. Math. Phys.*, **37**(5), pp. 696–713.
- [363] Wang, J., Carson, J. K., North, M. F., and Cleland, D. J., 2006, "A New Approach to Modelling the Effective Thermal Conductivity of Heterogeneous Materials," *International Journal of Heat and Mass Transfer*, **49**(17), pp. 3075–3083.
- [364] Yu, B., Zou, M., and Feng, Y., 2005, "Permeability of Fractal Porous Media by Monte Carlo Simulations," *International Journal of Heat and Mass Transfer*, **48**(13), pp. 2787–2794.
- [365] Yu, B., and Li, J., 2001, "Some Fractal Characters of Porous Media," *Fractals*, **09**(03), pp. 365–372.
- [366] Yu, B., and Cheng, P., 2002, "A Fractal Permeability Model for Bi-Dispersed Porous Media," *International Journal of Heat and Mass Transfer*, **45**(14), pp. 2983–2993.
- [367] Freundlich, I. M., Wallace, J. D., and Dodd, G. D., 1968, "Thermography and the Venous Diameter Ratio in the Detection of the Nonpalpable Breast Carcinoma," *Am J Roentgenol Radium Ther Nucl Med*, **102**(4), pp. 927–932.
- [368] Gullino, P. M., and Grantham, F. H., 1962, "Studies on the Exchange of Fluids Between Host and Tumor. III. Regulation of Blood Flow in Hepatomas and Other Rat Tumors," *JNCI: Journal of the National Cancer Institute*, **28**(1), pp. 211–229.
- [369] Gullino, P. M., Clark, S. H., and Grantham, F. H., 1964, "The Interstitial Fluid of Solid Tumors," *Cancer Research*, **24**(5), pp. 780–797.
- [370] Said Camilleri, J., Farrugia, L., Curto, S., Rodrigues, D. B., Farina, L., Caruana Dingli, G., Bonello, J., Farhat, I., and Sammut, C. V., 2022, "Review of Thermal and Physiological Properties of Human Breast Tissue," *Sensors*, **22**(10), p. 3894.
- [371] Özişik, M. N., Orlande, H. R. B., Colaço, M. J., and Cotta, R. M., 2017, *Finite Difference Methods in Heat Transfer*, CRC Press.

- [372] Kollmannsberger, S., D'Angella, D., Jokeit, M., and Herrmann, L., 2021, *Deep Learning in Computational Mechanics: An Introductory Course*, Springer International Publishing, Cham.
- [373] Oommen, V., and Srinivasan, B., 2022, "Solving Inverse Heat Transfer Problems Without Surrogate Models: A Fast, Data-Sparse, Physics Informed Neural Network Approach," *Journal of Computing and Information Science in Engineering*, **22**(041012).
- [374] Cai, S., Wang, Z., Wang, S., Perdikaris, P., and Karniadakis, G. E., 2021, "Physics-Informed Neural Networks for Heat Transfer Problems," *Journal of Heat Transfer*, **143**(060801).
- [375] Osman, M. M., and Afify, E. M., 1984, "Thermal Modeling of the Normal Woman's Breast," *J Biomech Eng*, **106**(2), pp. 123–130.
- [376] Keller, K. H., and Seiler, L., 1971, "An Analysis of Peripheral Heat Transfer in Man.," *Journal of Applied Physiology*, **30**(5), pp. 779–786.
- [377] Osman, M. M., and Afify, E. M., 1988, "Thermal Modeling of the Malignant Woman's Breast," *Journal of Biomechanical Engineering*, **110**(4), pp. 269–276.
- [378] Sudharsan, N. M., Ng, E. Y. K., and Teh, S. L., 1999, "Surface Temperature Distribution of a Breast With and Without Tumour," *Computer Methods in Biomechanics and Biomedical Engineering*, **2**(3), pp. 187–199.
- [379] Ng, E. Y. K., and Kee, E. C., 2008, "Advanced Integrated Technique in Breast Cancer Thermography," *Journal of Medical Engineering & Technology*, **32**(2), pp. 103–114.
- [380] Das, K., and Mishra, S. C., 2015, "Simultaneous Estimation of Size, Radial and Angular Locations of a Malignant Tumor in a 3-D Human Breast – A Numerical Study," *Journal of Thermal Biology*, **52**, pp. 147–156.
- [381] Figueiredo, A. A. A., Fernandes, H. C., Malheiros, F. C., and Guimaraes, G., 2020, "Influence Analysis of Thermophysical Properties on Temperature Profiles on the Breast Skin Surface," *International Communications in Heat and Mass Transfer*, **111**, p. 104453.
- [382] González, F. J., 2007, "Thermal Simulation of Breast Tumors," *Revista mexicana de física*, **53**(4), pp. 323–326.
- [383] Hu, L., Gupta, A., Gore, J. P., and Xu, L. X., 2004, "Effect of Forced Convection on the Skin Thermal Expression of Breast Cancer," *Journal of Biomechanical Engineering*, **126**(2), pp. 204–211.
- [384] Zhang, H., 2008, "Lattice Boltzmann Method for Solving the Bioheat Equation," *Phys. Med. Biol.*, **53**(3), pp. N15–N23.
- [385] Amri, A., Pulko, S. H., and Wilkinson, A. J., 2016, "Potentialities of Steady-State and Transient Thermography in Breast Tumour Depth Detection: A Numerical Study," *Computer Methods and Programs in Biomedicine*, **123**, pp. 68–80.
- [386] Francis, J. E., Roggli, R., Love, T. J., and Robinson, C. P., 1979, "Thermography as a Means of Blood Perfusion Measurement," *Journal of Biomechanical Engineering*, **101**(4), pp. 246–249.
- [387] Figueiredo, A. A. A., do Nascimento, J. G., Malheiros, F. C., da Silva Ignacio, L. H., Fernandes, H. C., and Guimaraes, G., 2019, "Breast Tumor Localization Using Skin Surface Temperatures from a 2D Anatomic Model without Knowledge of the Thermophysical Properties," *Computer Methods and Programs in Biomedicine*, **172**, pp. 65–77.
- [388] Hassiotou, F., and Geddes, D., 2013, "Anatomy of the Human Mammary Gland: Current Status of Knowledge," *Clinical Anatomy*, **26**(1), pp. 29–48.
- [389] Barros, T. C., and Figueiredo, A. A. A., 2023, "Three-Dimensional Numerical Evaluation of Skin Surface Thermal Contrast by Application of Hypothermia at Different Depths and Sizes of the Breast Tumor," *Computer Methods and Programs in Biomedicine*, **236**, p. 107562.

- [390] Jiang, L., Zhan, W., and Loew, M. H., 2010, "Modeling Static and Dynamic Thermography of the Human Breast under Elastic Deformation," *Phys. Med. Biol.*, **56**(1), p. 187.
- [391] Bezerra, L. A., Oliveira, M. M., Rolim, T. L., Conci, A., Santos, F. G. S., Lyra, P. R. M., and Lima, R. C. F., 2013, "Estimation of Breast Tumor Thermal Properties Using Infrared Images," *Signal Processing*, **93**(10), pp. 2851–2863.
- [392] Ng, E.-K., and Sudharsan, N. M., 2001, "Effect of Blood Flow, Tumour and Cold Stress in a Female Breast: A Novel Time-Accurate Computer Simulation," *Proc Inst Mech Eng H*, **215**(4), pp. 393–404.
- [393] Figueiredo, A. A. A., Menegaz, G. L., Fernandes, H. C., and Guimaraes, G., 2018, "Thermographic Computational Analyses of a 3D Model of a Scanned Breast," *Medical Image Computing and Computer Assisted Intervention – MICCAI 2018*, A.F. Frangi, J.A. Schnabel, C. Davatzikos, C. Alberola-López, and G. Fichtinger, eds., Springer International Publishing, Cham, pp. 885–892.
- [394] Mukhmetov, O., Igal, D., Mashekova, A., Zhao, Y., Ng, E. Y. K., Fok, S. C., and Teh, S. L., 2021, "Thermal Modeling for Breast Tumor Detection Using Thermography," *International Journal of Thermal Sciences*, **161**, p. 106712.
- [395] Gonzalez-Hernandez, J.-L., Kandlikar, S. G., Dabydeen, D., Medeiros, L., and Phatak, P., 2018, "Generation and Thermal Simulation of a Digital Model of the Female Breast in Prone Position," *Journal of Engineering and Science in Medical Diagnostics and Therapy*, **1**(4), p. 041006.
- [396] Gonzalez-Hernandez, J. L., 2019, "A Patient-Specific Approach for Breast Cancer Detection and Tumor Localization Using Infrared Imaging," Theses.
- [397] Lozano, A., Hayes, J. C., Compton, L. M., Azarnoosh, J., and Hassanipour, F., 2020, "Determining the Thermal Characteristics of Breast Cancer Based on High-Resolution Infrared Imaging, 3D Breast Scans, and Magnetic Resonance Imaging," *Sci Rep*, **10**(1), p. 10105.
- [398] Perez-Raya, I., and Kandlikar, S. G., 2023, "Thermal Modeling of Patient-Specific Breast Cancer With Physics-Based Artificial Intelligence," *ASME Journal of Heat and Mass Transfer*, **145**(3), p. 031201.
- [399] Hossain, S., and Mohammadi, F. A., 2016, "Tumor Parameter Estimation Considering the Body Geometry by Thermography," *Computers in Biology and Medicine*, **76**, pp. 80–93.
- [400] Saniei, E., Setayeshi, S., Akbari, M. E., and Navid, M., 2016, "Parameter Estimation of Breast Tumour Using Dynamic Neural Network from Thermal Pattern," *Journal of Advanced Research*, **7**(6), pp. 1045–1055.
- [401] Owens, A., 2020, "A Patient-Specific Infrared Imaging Technique for Adjunctive Breast Cancer Screening: A Clinical and Simulation - Based Approach," Theses.
- [402] Moré, J. J., 1978, "The Levenberg-Marquardt Algorithm: Implementation and Theory," *Numerical Analysis*, G.A. Watson, ed., Springer, Berlin, Heidelberg, pp. 105–116.
- [403] Goshtasby, A., 2012, *Image Registration: Principles, Tools and Methods*, Springer, London.
- [404] Solomon, C., and Breckon, T., 2011, *Fundamentals of Digital Image Processing: A Practical Approach with Examples in Matlab*, Wiley-Blackwell, Chichester, West Sussex ; Hoboken, NJ.
- [405] Szeliski, R., 2011, *Computer Vision*, Springer London, London.
- [406] Ozisik, M. N., 2020, *Inverse Heat Transfer: Fundamentals and Applications*, Routledge, New York.

- [407] Trobec, R., Bulić, P., Robič, B., and Slivnik, B., 2018, *Introduction to Parallel Computing: From Algorithms to Programming on State-of-the-Art Platforms*, Springer International Publishing : Imprint: Springer, Cham.
- [408] 2009, "ANSYS FLUENT 12.0 UDF Manual - 7. Parallel Considerations" [Online]. Available: <https://www.afs.enea.it/project/neptunius/docs/fluent/html/udf/node212.htm>. [Accessed: 15-Mar-2024].
- [409] Hsia, H. C., and Thomson, J. G., 2003, "Differences in Breast Shape Preferences between Plastic Surgeons and Patients Seeking Breast Augmentation," *Plastic and Reconstructive Surgery*, **112**(1), p. 312.
- [410] Swanson, E., 2017, "A Measurement System and Ideal Breast Shape," *Evidence-Based Cosmetic Breast Surgery*, Springer International Publishing, Cham, pp. 19–31.
- [411] Pratama, D. A., Bakar, M. A., Ibrahim, N. F., Idris, R., and Mohamed, N., 2023, "Physical Restriction Neural Networks with Restarting Strategy for Solving Mathematical Model of Thermal Heat Equation for Early Diagnose Breast Cancer," *Results in Applied Mathematics*, **19**, p. 100384.
- [412] Figueiredo, A. A. A., Fernandes, H. C., and Guimaraes, G., 2018, "Experimental Approach for Breast Cancer Center Estimation Using Infrared Thermography," *Infrared Physics & Technology*, **95**, pp. 100–112.
- [413] Figueiredo, A. A. A., Nascimento, J. G., Malheiros, F. C., Silva Ignacio, L. H., Fernandes, H. C., and Guimaraes, G., 2019, "Breast Tumor Localization Using Skin Surface Temperatures from a 2D Anatomic Model without Knowledge of the Thermophysical Properties," *Computer Methods and Programs in Biomedicine*, **172**, pp. 65–77.
- [414] Gershenson, M., and Gershenson, J., 2023, "Dynamic Vascular Imaging Using Active Breast Thermography," *Sensors*, **23**(6), p. 3012.
- [415] Gutierrez, C., Owens, A., Medeiros, L., Dabydeen, D., Sritharan, N., Phatak, P., and Kandlikar, S. G., 2024, "Breast Cancer Detection Using Enhanced IRI-Numerical Engine and Inverse Heat Transfer Modeling: Model Description and Clinical Validation," *Sci Rep*, **14**(1), p. 3316.
- [416] Sritharan, N., Gutierrez, C., Perez-Raya, I., Gonzalez-Hernandez, J.-L., Owens, A., Dabydeen, D., Medeiros, L., Kandlikar, S. G., and Phatak, P., 2023, "Inverse Modeling with Surface Temperature Accurately Detects the Presence of Breast Cancer."
- [417] Duck, F. A., 2013, *Physical Properties of Tissues: A Comprehensive Reference Book*, Academic Press.
- [418] Hebda, T., and Czar, P., 2013, *Handbook of Informatics for Nurses & Healthcare Professionals*, Pearson, Boston.
- [419] Dantuma, M., Dommelen, R. van, and Manohar, S., 2019, "Semi-Anthropomorphic Photoacoustic Breast Phantom," *Biomed. Opt. Express*, BOE, **10**(11), pp. 5921–5939.
- [420] Dantuma, M., Kruitwagen, S., Julia, J. O., Meerdervoort, R. P. P. van, and Manohar, S., 2021, "Tunable Blood Oxygenation in the Vascular Anatomy of a Semi-Anthropomorphic Photoacoustic Breast Phantom," *JBO*, **26**(3), p. 036003.
- [421] Arpine, G., Bunker, M. J., Fluvio, L., Sims, R., Inziello, J., Stubbs, J., Mukhtar, R., Tatiana, K., and Link to external site, this link will open in a new window, 2021, "Applications of 3D Printing in Breast Cancer Management," *3D Printing in Medicine*, **7**(1).